

**INVESTIGATION OF SURFACE INHOMOGENEITY AND ESTIMATION OF THE  
GOES SKIN TEMPERATURE ASSIMILATION ERRORS OF THE MM5 IMPLIED  
BY THE INHOMOGENEITY OVER HOUSTON METROPOLITAN AREA**

A Dissertation

by

SANG-OK HAN

Submitted to the Office of Graduate Studies of  
Texas A&M University  
in partial fulfillment of the requirements for the degree of

DOCTOR OF PHILOSOPHY

August 2004

Major Subject: Meteorology

**INVESTIGATION OF SURFACE INHOMOGENEITY AND ESTIMATION OF THE  
GOES SKIN TEMPERATURE ASSIMILATION ERRORS OF THE MM5 IMPLIED  
BY THE INHOMOGENEITY OVER HOUSTON METROPOLITAN AREA**

A Dissertation

by

SANG-OK HAN

Submitted to the Office of Graduate Studies of  
Texas A&M University  
in partial fulfillment of the requirements for the degree of  
DOCTOR OF PHILOSOPHY

Approved as to style and content by:

---

John W. Nielsen-Gammon  
(Chair of Committee)

---

Gerald R. North  
(Member)

---

Fuqing Zhang  
(Member)

---

Anthony Cahill  
(Member)

---

Richard Orville  
(Head of Department)

August 2004

Major Subject: Meteorology

## ABSTRACT

Investigation of Surface Inhomogeneity and Estimation of the GOES Skin Temperature Assimilation Errors of the MM5 Implied by the Inhomogeneity Over Houston Metropolitan Area. (August 2004)

Sang-Ok Han, B.S., Seoul National University;

M.S., Texas A&M University

Chair of Advisory Committee: Dr. John W. Nielsen-Gammon

This study developed a parameterization method to investigate the impacts of inhomogeneous land surfaces on mesoscale model simulations using a high-resolution 1-d PBL model. Then, the 1-d PBL model was used to investigate the inhomogeneity-caused model errors in applying the GOES satellite skin temperature assimilation technique into the MM5 over the Houston metropolitan area (HOU). In order to investigate the surface inhomogeneity impacts on the surface fluxes and PBL variables over HOU, homo- and inhomogeneous 1-d PBL model simulations were performed over HOU and compared to each other. The 1-d PBL model was constructed so that the surface inhomogeneities were able to be represented within model grid elements using a methodology similar to Avissar and Pielke (1989). The surface inhomogeneities over HOU were defined using 30-m resolution land cover data produced by Global Environment Management (GEM), Inc. The inhomogeneity parameterization method developed in the 1-d model was applied to a standard MM5 simulation to test the applicability of the parameterization to 3-d mesoscale model simulations.

From the 1-d simulations it was inferred that the surface inhomogeneities would enhance the sensible heat flux by about 36 % and reduce the latent heat flux by about 25 %, thereby inducing the warmer (0.7 %) and drier (-1.0 %) PBL and the colder and moister PBL top induced by greater turbulent diffusivities. The 3-d application of the inhomogeneity parameterization indicated consistent results with the 1-d in general, with additional effects of advection and differential local circulation.

The original GOES simulation was warmer compared to observations over HOU than over surrounding areas. The satellite data assimilation itself would lead to a warm bias

due to erroneous estimation of gridpoint-mean skin temperature by the satellite, but 1-d simulations indicate that the impact of this error should be much weaker than what was observed. It seems that, unless the already existing warm and dry bias of the MM5 is corrected, the inhomogeneity parameterization in the MM5 would adversely affect the MM5 performance. Therefore, consideration of the surface inhomogeneities in the urban area needs to be confined to the GOES skin temperature retrieval errors at the moment.

## **DEDICATION**

This dissertation is dedicated to my mother and son, Isaac Han. My mother has sacrificed all through her life for her sons and daughters. She always prays so that her children can have a better life. My son made my life so joyful. He is so cute and precious.

## ACKNOWLEDGMENTS

I wish to express my sincere thanks to my advisor Dr. John W. Nielsen-Gammon for his guidance, support, and encouragement to finish this study. I was supported financially from him for the last 6 years. I would also like to thank the other committee members, Dr. Gerald R. North, Dr. Fuqing Zhang, and Dr. Anthony Cahill for their advice and suggestions.

I thank Eun-Kyoung Seo for being beside me all the time as my wife and academic colleague. I also give my thanks to those who showed their concern about me: my family, friends, and my brothers and sisters in the HANSARANG church. I thank my GOD Jesus Christ for His grace and His blessings during my time here at Texas A&M University.

## TABLE OF CONTENTS

	Page
ABSTRACT.....	iii
DEDICATION.....	v
ACKNOWLEDGMENTS.....	vi
TABLE OF CONTENTS.....	vii
LIST OF TABLES.....	xi
LIST OF FIGURES.....	xiii
 CHAPTER	
I INTRODUCTION AND BACKGROUND.....	1
1. Introduction.....	1
2. Literature review.....	5
3. Hypothesis.....	8
II INVESTIGATION ON RELATIVE MM5 PERFORMANCE IN INHOMOGENEOUS HOUSTON URBAN AREA COMPARED TO THAT IN HOMOGENEOUS SURROUNDING AREAS.....	10
1. Introduction.....	10
2. Description on MM5 simulation.....	11
3. Description on MTP data.....	13
4. Description on HDT sonde data.....	17
5. Preparation of verification data from MTP, sonde, and NGMM5 data files.....	17
6. Selection of verification data sample.....	20
7. Comparison of NGMM5 biases against MTP.....	24
a. PBL height bias.....	24
b. Potential temperature biases.....	28
8. Potential temperature biases of NGMM5 and MTP against sonde soundings at HDT.....	30

CHAPTER	Page
III INVESTIGATION ON SUBGRID-SCALE SURFACE INHOMOGENEITY IN THE HOU USING 1-D PBL MODEL .....	36
1. Introduction .....	36
2. Description of 1-d PBL model .....	36
a. Vertical structure of the 1-d PBL model .....	37
b. Slab model.....	38
c. Prediction for nocturnal regime .....	41
d. Prediction for free convection regime .....	44
e. Computational details .....	46
3. Experiment design .....	46
a. Specification of surface characteristics.....	47
b. Distribution of surface characteristics .....	50
c. Other aspects of the simulations .....	52
d. Methodology of inhomogeneous simulation (IN1D) .....	58
4. Comparative study using the simulation results .....	59
a. Distribution of time-averaged variable difference in HOU area .....	59
b. Time variation of HOU area mean variables.....	68
c. Comparison of HOU area mean PBL atmosphere.....	72
5. Discussion .....	80
a. Consideration of fundamental causes of inhomogeneity impacts .....	80
b. Turbulence characteristics from the perspective of grid- mean bulk Richardson number .....	81
c. Sensitivity of inhomogeneity impacts to each surface parameter.....	82
d. Implication of the frictional velocity ( $U_*$ ) and temperature ( $T_*$ ) impacts.....	86
e. Relative importance of area coverage and different surface characteristics .....	91
f. Sensitivity of wind speed .....	92
g. Percent difference of the IN1D with respect to CLIM .....	97
IV ESTIMATION OF GOES SKIN TEMPERATURE ERROR OVER HOUSTON URBAN AREA.....	99
1. Introduction .....	99
2. Brief description of the GOES satellite data assimilation technique .....	100



CHAPTER	Page
a. Calculation of observed soil moisture availability .....	100
b. Land Surface Temperature (LST) retrieval equation of the Physical Split-Window algorithm .....	101
3. Estimation of GOES skin temperature error .....	103
a. Method.....	103
b. Results .....	106
4. Investigation of model impacts caused by the GOES skin temperature error.....	110
a. Method.....	110
b. Results .....	111
5. GOES assimilation errors associated with linear interpolation of hourly ground temperature into model time step.....	117
a. Method.....	117
b. Results from homogeneous simulation .....	118
c. Results from inhomogeneous simulation.....	121
6. GOES assimilation errors caused by using the model without surface inhomogeneity parameterization .....	124
a. Method.....	124
b. Results .....	125
 V PRELIMINARY APPLICATION OF THE INHOMOGENEITY PARAMETERIZATION INTO A STANDARD MM5 SIMULATION IN USE OF MRF PBL SCHEME.....	 130
1. Introduction .....	130
2. Method of the inhomogeneity parameterization .....	131
3. Description of MRF PBL scheme .....	133
a. Determination of diffusivity profiles .....	133
b. Determination of boundary layer depth.....	135
c. Diffusivities for heat and water vapor .....	136
4. Simulation aspects.....	137
a. Configuration of MM5 .....	137
b. Simulation case.....	137
5. Comparison of simulation results between the INHOMO and HOMO.....	139
a. Spatial distribution of simulated PBL variables .....	139
b. Comparison of surface variables at HDT as function of time.....	155
c. Comparison of variable profiles at HDT .....	159
d. Illustration of the PBL atmospheric differences in cross sections .....	164

CHAPTER	Page
VI CONCLUSIONS.....	169
REFERENCES .....	174
VITA.....	180

## LIST OF TABLES

TABLE		Page
1	Key model settings for the MM5 simulations during the ozone episode (Aug. 25 – Sep. 1, 2000). .....	14
2	Area coverage (%) of MM5 landuse types included in each area and verification data point numbers of each area.....	24
3	Specified model surface parameter values for each of 10 land cover types. The abbreviated column headings are explained in the text.....	50
4	Differences of surface wind speed between the homogeneous 1-d simulation with idealized geostrophic winds (G1PBL, G2PBL, and G3PBL defined in the text) and the homogeneous 1-d with the balance assumption (BAPBL) during the stable (0400 UTC – 1400 UTC) and convective (1600 UTC – 2300 UTC) regimes. ....	58
5	Characteristic features of inhomogeneous 1-d simulations.....	60
6	Initiation and end time of free convective regime from 121 simulations of IN1D and HO1D indicated by number of hours UTC into the integration. ....	61
7	Specification of surface parameters used in sensitivity runs. Column headings are defined on pages 47 and 50. ....	84
8	The 4m wind speed and the percent impact of wind speed sensitivity runs of sensible and latent heat fluxes averaged for the stable (parentheses) and convective regime. Each row represents each sensitivity run with different initial wind speed. ....	94
9	The HOU-area-averaged percent differences of IN1D simulations with respect to CLIM simulation.....	98
10	Specified transmittance at the surface and coefficient values used in computation of skin temperature retrieval error for GOES-8 Imager channels 4 and 5. ....	104
11	HOU-area-averaged soil moisture availability and percent difference of the GOES assimilation soil moisture availability from the model value. ....	111

TABLE	Page
12	Percent errors induced by inhomogeneous ground temperature in the 1-d PBL model of the GOES skin temperature assimilation technique (GERR). .... 117
13	Percent errors of sensible (SHFLX) and latent (LHFLX) heat fluxes, surface layer potential temperature (4mTh), specific humidity (4mQ) and wind speed (4mWind), and ground temperature (Tg). Bold and plain numerals indicate errors obtained from inhomo- and homogeneous simulations, respectively..... 124
14	Percent errors of sensible (SHFLX) and latent (LHFLX) heat fluxes, surface layer potential temperature (4mTh), specific humidity (4mQ) and wind speed (4mWind), and ground temperature (Tg) for two assimilation errors and their combination designated by Model error, GOES error, and Total error, respectively, in the first column. . .... 129
15	MM5 model parameter settings used in the inhomogeneity test run..... 138

## LIST OF FIGURES

FIGURE		Page
1	1. Configuration of NGMM5 model domains. The grid sizes of the four domains are 108 km, 36 km, 12 km, and 4 km from the domain A, B, C, and D, respectively. ....	12
2	The 11 locations of reference MM5 soundings designated by asterisk marks. ....	16
3	MTP scan points selected for flight altitudes of about 2000 ft (0.61 km). The square box in the figure represents Houston urban area. ....	19
4	The NGMM5 and MTP PBL height statistics as function of critical lapse rate represented by (a) F-variance test value between MTP and NGMM5, (b) Kurtosis of the NGMM5 PBL height biases, (c) Skewness of NGMM5 PBL height biases, (d) NGMM5 PBL height mean biases, and (e) standard deviation of the NGMM5 PBL height biases, during the Regime-I. ....	22
5	The same as Figure 4 except for the Regime-II. ....	23
6	PBL heights of the NGMM5 (dotted) and MTP (solid) for the selected data sample of the ozone Regime-I (Aug. 25 - Aug. 29, 2000). ....	25
7	The 7 sub-areas with about equal area coverage representing the Houston urban area (HOU) and 6 surrounding areas (NW, N, NE, W, SW, and S). ....	25
8	Bar graphs comparing statistics of NGMM5 PBL height biases against MTP among the 7 sub-areas in Figure 7, combined SUR areas, and total area: (a) PBL height mean bias, (b) standard deviation of the PBL height biases, and (c) significance of mean bias difference between HOU and each of SUR and combined areas. In the graphs "Total" denotes entire sample and "SUR TOT" represents combined SUR areas. ....	27
9	Bar graphs comparing statistics of NGMM5 layer-averaged potential temperature biases, 450 m – 950 m lower layer (a – c) and 2000 m – 2500 m upper layer (d – f) against MTP among the 7 sub-areas in Figure 7, combined SUR areas, and total area: (a) and (d) PBL potential temperature mean bias, (b) and (e) standard deviation of biases, and (c) and (f) significance of mean bias difference between HOU and each of SUR and combined areas. In the graphs	

FIGURE	Page
“Total” denotes entire sample and “SUR TOT” represents combined SUR areas. ....	29
10 Potential temperature soundings of the sondes (dotted) and NGMM5 (solid) at HDT between 1500 UTC and 0000 UTC during the ozone Regime-I (Aug. 25 - Aug. 29, 2000). ....	31
11 Bar graph exhibiting the potential temperature mean biases of the NGMM5 (blue) and standard deviations of the biases (red) against sonde observations between 1500 UTC and 2300 UTC at HDT during the ozone Regime-I (Aug. 25 – Aug. 29). ....	32
12 Profiles of (a-d) MTP potential temperature biases against sonde soundings and (e) those mean bias at HDT. Observation times are indicated in each figure. ....	34
13 Bar graph exhibiting MTP potential temperature mean biases against sonde soundings between 1500 UTC and 2300 UTC at the HDT at height levels from 50 m to 3000 m above ground during ozone Regime-I (Aug. 25 – Aug. 29). ....	35
14 (a) Distribution of 10 land cover types in the HOU area. Boxes A and B designate forest and downtown areas, respectively, and (b) land cover classification of the eight counties (Brazoria, Chambers, Fort Bend, Galveston, Harris, Liberty, Montgomery, and Waller) around Houston, Texas. ....	48
15 Graph indicating the Fractional Area Coverage (FAC) for each of 10 land cover types averaged in the HOU area. ....	49
16 Distributions of Fractional Areal Coverage (FAC) of (a) broad leaf forest, (b) coniferous forest, (c) mixed forest, (d) grass, (e) wet land, (f) water body, (g) barren land, (h) roads, (i) impervious flat, and (j) impervious structure within 4 km grids in the HOU area. ....	51
17 Distribution of 4 km grid-mean surface parameter values in the HOU area: (a) SLMO, (b) ALBD (%), (c) SFZ0 (m), (d) SFEM, and (e) CAPG (*3.293e+6 J/K/m <sup>3</sup> ). ....	53

FIGURE	Page	
18	Distribution of 4 km grid-mean standard deviations of each surface parameter value in the HOU area: (a) SLMO, (b) ALBD (%), (c) SFZ0 (m), (d) SFEM, and (e) CAPG ( $*3.293e+6$ J/K/m <sup>3</sup> ). . . . .	54
19	Profiles of (a) potential temperature, (b) specific humidity, (c) u-wind, and (d) v-wind used as the atmospheric initial conditions of the 1-d PBL simulations. . . . .	55
20	Distribution of the stable regime (0400 UTC - 1400 UTC) time-averaged differences (IN1D - HO1D) of (a) ground temperature, (b) 4m potential temperature, (c) 4m wind speed, (d) 4m specific humidity, (e) sensible heat flux, and (f) latent heat flux in HOU. Contour units are in each figure title. . . . .	62
21	Same as Figure 20 but for the convective regime between 1600 UTC and 2300 UTC. . . . .	66
22	HOU-area-averaged sensible and latent heat fluxes in the surface layer as function of forecasting time: sensible heat fluxes at the (a) bottom (SHFLX) and (b) top (SHFLXT), latent heat fluxes at the (c) bottom (LHFLX) and (d) top (LHFLXT). Solid and dotted lines represent the IN1D and HO1D, respectively. The positive sign represents upward direction of the fluxes. . . . .	69
23	HOU-area-averaged (a) ground temperature, (b) 4m potential temperature, (c) 4m wind speed, and (d) 4m specific humidity for the IN1D (solid) and HO1D (dotted) as function of forecasting time. . . . .	71
24	Profiles of HOU-area-averaged potential temperature for the IN1D (solid) and HO1D (dotted) from 1300 UTC to 0000 UTC. The x-axis is in K and y-axis is in km. . . . .	73
25	The same as Figure 24 but for specific humidity. . . . .	74
26	The same as Figure 24 but for wind speed. . . . .	75
27	Distributions of differences (IN1D - HO1D) of the PBL-averaged (a) potential temperature, (b) specific humidity, (c) wind speed and (d) PBL height at 2100 UTC in HOU. The minimum and maximum values in the domain are indicated at the bottom of each figure. Units are indicated in each figure title. . . . .	78

FIGURE	Page
28	Time variation of the HOU-area-averaged PBL height for the IN1D (solid) and HO1D (dotted) from 1500 UTC to 2300 UTC during the convective regime. .... 79
29	HOU-area-averaged grid-mean bulk Richardson number for the IN1D (solid) and HO1D (dotted) as function of forecasting time. .... 83
30	Comparisons of (a) ground temperatures and (b) 4 m potential temperatures from 5 different settings of surface inhomogeneities during the stable regime with respect to homogeneous and inhomogeneous (all surface params) runs. Each line indicated in panel denotes each inhomogeneity setting. .... 85
31	The same as Figure 30 but for the convective regime. .... 87
32	Bargraph showing the relative sensitivities of surface variables to the inhomogeneity defined by a single parameter with the fractional area coverage for each of 10 land cover types being given by 0.1. (a) stable regime and (b) convective regime. .... 88
33	Distribution of $U^*$ and $T^*$ differences between homogeneous and inhomogeneous representation of surface roughness length in HOU for each regime: (a) and (b) for stable regime, (c) and (d) for convective regime in HOU. .... 90
34	Percent impact distribution in the A-F space (defined in the text) of (a) sensible and (b) latent heat fluxes in the stable regime, and (c) sensible and (d) latent heat fluxes in the convective regime. .... 93
35	Inhomogeneity impacts of sensible and latent heat fluxes for (a) and (b) stable and (c) and (d) convective regimes as function of initial wind speeds. The impacts are defined as the wind speed sensitivity runs minus homogeneous CLIM. .... 95
36	Distributions of ground temperature difference (IN1D - HO1D) in HOU from 0100 UTC to 0000 UTC. Contour intervals are 0.5 K. .... 105
37	Histograms representing densities of the IN1D subgrid-scale ground temperatures with 0.2 K bin size in the HOU area. .... 107



FIGURE	Page
38	Distribution of the GOES skin temperature retrieval error induced by the inhomogeneous ground temperature within grid elements in the HOU area. Contour lines are in 0.01 K interval (0100 UTC - 1200 UTC) and 0.04 K interval (1300 UTC - 0000 UTC). ..... 108
39	Distribution of time-averaged (between 1600 UTC and 2300 UTC during the convective regime) errors caused by the GOES ground temperature retrieval error in HOU: (a) ground temperature, (b) 4m potential temperature, (c) 4m wind speed, (d) 4m specific humidity, (e) sensible heat flux, and (f) latent heat flux. The maximum and minimum values in the domain are indicated at the bottom of each figure. .... 112
40	The HOU-area-averaged sensible and latent heat flux errors caused by GOES ground temperature retrieval error as function of forecasting time: (a) SHFLX error at the surface layer bottom, (b) those at the top, (c) LHFLX error at the surface layer bottom, and (d) those at the top. .... 114
41	The HOU-area-averaged surface variable errors caused by GOES ground temperature retrieval error as function of forecasting time: (a) potential ground temperature, (b) 4m potential temperature, (c) 4m wind speed, and (d) 4m specific humidity. .... 115
42	Error profiles of HOU-area-averaged PBL variables induced by GOES ground temperature retrieval error at 22 UTC: (a) potential temperature, (b) specific humidity, and (c) wind speed. .... 116
43	The GOES skin temperature assimilation errors of the homogeneous 1-d PBL model caused by the linear interpolation of hourly observed ground temperatures in HOU: (a) sensible heat flux ( $\text{W m}^{-2}$ ), (b) surface layer potential temperature (K), (c) latent heat flux ( $\text{W m}^{-2}$ ), and (d) surface layer specific humidity (g/kg). The errors are averaged in time between 1800 UTC and 2200 UTC. .... 119
44	The HOU-area-averaged GOES skin temperature assimilation error of the homogeneous 1-d PBL model caused by the linear interpolation of the observed hourly ground temperature: (a) sensible heat flux ( $\text{W m}^{-2}$ ), (b) surface layer potential temperature (K), (c) latent heat flux ( $\text{W m}^{-2}$ ), and (d) surface layer specific humidity (g/kg). .... 120
45	The same as Figure 43 but for the inhomogeneous runs. .... 122

FIGURE	Page
46	The same as Figure 44 but for the inhomogeneous 1-d model assimilation. .... 123
47	The GOES skin temperature assimilation errors of the homogeneous 1-d PBL model caused by the model ground temperature error in HOU: (a) sensible heat flux ( $W m^{-2}$ ), (b) surface layer potential temperature (K), (c) latent heat flux ( $W m^{-2}$ ), and (d) surface layer specific humidity (g/kg). The errors are averaged in time between 1800 UTC and 2200 UTC. .... 126
48	The HOU-area-averaged GOES skin temperature assimilation error of the homogeneous 1-d PBL model caused by the model ground temperature error: (a) sensible heat flux ( $W m^{-2}$ ), (b) surface layer potential temperature (K), (c) latent heat flux ( $W m^{-2}$ ), and (d) surface layer specific humidity (g/kg). .... 127
49	Location of the HOU urban grids in the 4 km domain of the MM5. .... 132
50	Temperature contour plots of the HOMO (left) and INHOMO (right) and those differences (center), INHOMO - HOMO, at 15 m lowest sigma level (upper), 1160 m sigma8575 level (middle), and 2570 m sigma7050 level (lower) at 1500 UTC. Contour intervals are 1 K and 0.1 K for the temperature and difference, respectively. .... 140
51	The same as Figure 50 but for at 1800 UTC. .... 141
52	The same as Figure 50 but for at 2100 UTC. .... 142
53	The same as Figure 50 but for at 0000 UTC. .... 144
54	Dewpoint temperature contour plots of the HOMO (left) and INHOMO (right) and those differences (center), INHOMO - HOMO, at 15 m lowest sigma level (upper), 1160 m sigma8575 level (middle), and 2570 m sigma7050 level (lower) at 1500 UTC. Contour intervals are 1 K for the lowest level and 0.5 K at sigma8575 and sigma7050 levels. Contour interval of the difference is 0.2 K. .... 146
55	The same as Figure 54 but for at 1800 UTC. .... 147
56	The same as Figure 54 but for at 2100 UTC. .... 148

FIGURE	Page
57	The same as Figure 54 but for at 0000 UTC. .... 149
58	Wind barb plots of the HOMO (left), INHOMO (right), and those wind vector and speed difference (center), INHOMO - HOMO, at 15 m lowest sigma level (upper), 1160 m sigma8575 level (middle), and 2570 m sigma7050 level (lower) at 1500 UTC. Wind barbs are in knots and the wind speed differences are in 0.2 m/s intervals. .... 150
59	The same as Figure 58 but for at 1800 UTC. .... 151
60	The same as Figure 58 but for at 2100 UTC. .... 153
61	The same as Figure 58 but for at 0000 UTC. .... 154
62	Plots comparing HOU-area-average of (a) ground temperature and lowest sigma level (b) temperature, (c) dewpoint temperature, and (d) wind speed and (e) PBL height between the INHOMO (solid) and HOMO (dashed). X-axes indicate time in UTC expressed by "date/UTC". Y-axes indicate values of each variable with units appearing in each figure title. .... 156
63	Plots comparing HOU-area-average of (a) sensible heat flux and (b) latent heat flux between the INHOMO (solid) and HOMO (dashed). X-axes indicate the time expressed by "date/UTC" and y-axes indicate values with units appearing in the figure titles. .... 158
64	Profile plots comparing potential temperature between INHOMO (solid) and HOMO (dashed) at HDT from 1600 UTC to 0000 UTC. The x-axes are in degree K and y-axes are in mb. .... 160
65	The same as Figure 64 but for Relative Humidity. The x-axes are in percent and y-axes are in mb. .... 161
66	The same as Figure 64 but for wind speed. The x-axes are in m/s and y-axes are in mb. .... 162
67	Graph indicating the location of cross section presented in Figures 68, 69, and 70. .... 165

FIGURE		Page
68	Cross section plots of relative humidity in color, potential temperature (K) in red lines, and section plane tangential winds (m/s) in arrow for the HOMO and INHOMO, and those variable differences at 1600 UTC (upper), 1700 UTC (middle), and 1800 UTC (lower). Color bars in each panel designate the relative humidity. ....	166
69	The same as Figure 68 but for at 1900 UTC (upper), 2000 UTC (middle), and 2100 UTC (lower). ....	167
70	The same as Figure 68 but for at 2200 UTC (upper), 2300 UTC (middle), and 0000 UTC (lower). ....	168

## CHAPTER I

### INTRODUCTION AND BACKGROUND

#### 1. Introduction

In the hot humid summertime, when the large-scale wind is weak, high ozone is most probable in southeast Texas. The ozone is formed by the photochemical reaction of Volatile Organic Compounds (VOC<sub>s</sub>) and Nitrogen Oxides (NO<sub>x</sub>) and transported in the air through wind advection and diffusion processes. Assuming the emission and background ozone are unchanged, the variability of ozone in southeast Texas is attributed mainly to the effects of thermally driven local atmospheric circulations around the area.

Under weak large-scale wind circumstances, the Houston metropolitan area winds are dominated by the land-sea breeze which is driven by land-sea thermal contrasts along the coasts of the Gulf of Mexico and Galveston Bay. The Texas Natural Resource Conservation Commission (TNRCC), which is now named the Texas Commission on Environmental Quality (TCEQ), documented that the land-sea breeze cycle causes the recirculation of pollutants in the Houston metropolitan area (Allen et al., 2002). Based on numerical simulations with the Penn State/NCAR Mesoscale Model, Version 5 (MM5), Orville et al. (2001) indicated that the city-breeze of Houston, which is caused by the heat-island effect, combines with the sea-breeze to draw ozone and ozone precursors from the heavily industrialized area of the Houston Ship Channel into the Houston area.

Since the Houston-Galveston (HG) area is classified as a severe nonattainment area under the Federal Clean Air Act Amendments (FCAA) for 1990, Texas government is required to take measures to comply with the National Ambient Air Quality Standards for ozone. With the purpose of identifying the meteorological and chemical processes that cause the high ozone problem in the HG area, the TEXas Air Quality Study (TEXAQS) 2000 was conducted in the summer of 2000. The Aug. 25 – Sep. 1, 2000 ozone episode occurred during the TEXAQS 2000 field campaign, and this episode has become the primary test case for regulatory strategies.

---

The journal model is *the Monthly Weather Review*.

TCEQ uses a photochemical grid model to assess the air quality benefits of emission reduction and determine the effectiveness of proposed air quality regulations. To run the photochemical grid model, 3-d meteorological data are needed as inputs. However, due to the lack of spatial and temporal resolution of 3-d meteorological observations, it is necessary to use meteorological model outputs. Therefore, the performance of the photochemical model is strongly dependent on the meteorological model performance. Since the MM5 has been designated as the meteorological model to provide the inputs for the photochemical grid model, an optimal MM5 model configuration is sought for the Aug. 25 – Sep. 1, 2000 ozone episode.

In order to achieve acceptable performance of the MM5 as a driver meteorological model for the photochemical model of regulatory purpose, Nielsen-Gammon (2002a) of TAMU has run the MM5 in a retrospective manner, nudging with some special observations obtained during TEXAQS 2000. In the retrospective MM5 runs during the TEXAQS 2000 campaign Nielsen-Gammon (2002a) improved the model PBL atmosphere using time-variable landuse characteristics and nudging the model PBL variables to the special observations. From the verification of the 4-km grid domain encompassing the Houston metropolitan area, he indicated that the wrong representative surface characteristics in the model contributed to the inability of representing the real PBL atmosphere around the area. He also addressed problems with the MM5 PBL scheme in simulating the Low Level Jet (LLJ), occurring in stable atmospheric conditions of nighttime.

Recently the GOES satellite-derived skin temperature data assimilation technique (McNider et al., 1994) was applied to the MM5 simulation successfully. The technique uses satellite-observed skin temperature in order to obtain model soil moisture availability. In previous MM5 model simulations, urban-scale wind patterns were driven by arbitrarily-specified land use variations, especially variations of soil moisture. The GOES skin temperature data assimilation brought much improved model performance.

In spite of the improved performance of the MM5 simulation brought both by nudging special ground observations and by adopting the GOES skin temperature assimilation technique, there still exist potential errors in the representation of energy exchange between land-surface and atmosphere in the model. The issue is raised because the MM5 simulation for the ozone episode is applied over the Houston metropolitan area which has highly

heterogeneous surface properties. In the model, the land-surface provides bottom boundary conditions by exchanging momentum, sensible and latent heat flux with the Planetary Boundary Layer (PBL) above the surface. Thus, the PBL and land-surface are coupled together through the feedback processes of fluxes during the model integration. Therefore, an accurate land-surface scheme is important for the success of PBL simulations. The land-surface scheme in use by both the MM5 simulation of the ozone episode and the GOES skin temperature assimilation is the simplest slab model developed by Blackadar (Zhang and Anthes, 1982) following the force-restore method (Deardorff, 1977) for calculation of surface temperature using the surface energy budget relation. The slab model only requires, as specified surface parameters, soil moisture availability, surface albedo, surface emissivity, thermal inertia, and roughness length. All the parameters are model grid-averaged representative values specified according to the 24 USGS land-use categories.

This study tries to assess the impact of homogeneous representation of the surface properties in the MM5 on its PBL atmosphere when the model is applied in the very heterogeneous Houston metropolitan area. The area is believed to have high heterogeneity of surface properties even within the 4-km grid size of the nested domain encompassing the HG area. The heterogeneity of the area is attributed to the distribution of residential areas, commercial buildings, paved roads, small lakes, parks, parking lots, trees, and so on. A more correct treatment of the land surface ought to yield an even better simulation.

Also, this study examines the GOES satellite-retrieved skin temperature error implied by the surface heterogeneity and its impact on the GOES skin temperature assimilation. The physical split-window retrieval algorithm (Suggs et al., 1998) used to retrieve skin temperature and precipitable water from GOES infrared measurements makes use of MM5 outputs to calculate the first guess upwelling radiation for each IR channel. While the actual upwelling radiation observed by the satellite represents the volumetric mean of the pixel area, the first-guess radiation of a 4-km grid box is the grid area-averaged mean calculated by using a radiative transfer model with the ground temperature being represented by grid area mean value. Therefore, considering the Planck function used in the radiative transfer model is a non-linear function of ground temperature, the average of surface radiation is different from the radiation calculated from the grid-averaged ground temperature.

The immediate goal of this study is to reduce the MM5 simulation errors induced by the land surface heterogeneity in the Houston urban area during the Aug. 25 – Sep. 1, 2000 ozone episode. In pursuit of the goal, 30m resolution land cover data over the HG area will be investigated to characterize the fractional area coverage (FAC) of land-cover types within each grid element of the 4km nested domain of the MM5. Then, realistic land-surface parameter values will be obtained based on the FACs for each grid element. A 1-d PBL model which has the same land-surface scheme as the MM5 is constructed and used as a surrogate for the MM5 in order to examine the difference of surface fluxes between homogeneous and heterogeneous representation of a grid surface and its impact on the model atmosphere. The 1-d model is constructed so that any number of land-cover types can be represented and thus the subgrid-scale heterogeneity can be taken account of within a grid element. This makes it possible to compute the energy and moisture exchange between the land surface and atmosphere more realistically. Land-surface temperature distributions produced from the 1-d model will be used in estimation of the satellite skin temperature retrieval error.

This chapter is devoted to a literature review in the context of PBL model deficiencies regarding its representation of surface characteristics. Then, the hypothesis that this study is based on is suggested.

In chapter II, using the MM5 outputs and Microwave Temperature Profiler (MTP) data during the ozone episode, the MM5 performances in two areas, urban Houston and the rest of the 4-km model domain, will be compared with each other. From this comparative verification the potential model errors associated with urban land surface characteristics will be clarified.

In chapter III, a 1-d PBL model will be used to investigate the characteristic features of surface inhomogeneity in the Houston urban area. A parameterization technique for realization of observed inhomogeneous surface characteristics in the 1-d model is developed and the simulation results will be compared with those without the parameterization. From the comparison study how the surface inhomogeneity brings its impacts on model simulations will be explained.



In chapter IV, the GOES satellite-derived skin temperature errors associated with the inhomogeneous surface is estimated using a simple methodology and the ground temperature distribution simulated by the 1-d model in chapter III.

In chapter V, the parameterization technique developed in the 1-d PBL model is applied into the standard MM5 (version 3.4) simulation and the results is compared to the simulations without the parameterization.

In chapter VI, the summary of key results of the previous chapters and conclusive remarks are provided.

## 2. Literature review

Differential heating of the earth surface is the driving force of the air motions above it. In the case of mesoscale circulations such as sea-land breeze, mountain-valley flow, and other nonclassical mesoscale circulations (Segal and Arritt 1992), the surface contrast plays the crucial role in driving the thermally induced flows within the PBL. The impact of the microscale land surface on the atmospheric circulation is an ongoing topic of atmospheric research. So far it seems that study on that topic is rare due to the difficulty in obtaining sufficient observations on that scale.

In a model, the land surface provides bottom boundary conditions by exchanging momentum, sensible and latent heat flux with the Planetary Boundary Layer (PBL) above the surface. Thus, the PBL and land surface are coupled together through the feedback processes of fluxes during the model integration. Therefore, an accurate land-surface scheme is important for the success of PBL simulations. Land-surface schemes range from simple one layer models (Manabe, 1969) to sophisticated ones such as soil-canopy models (e.g., Dickinson et al., 1986; Sellers et al., 1986). The sophisticated ones require many model parameters to be specified: for example, albedo of the canopy, fractional cover of vegetation, canopy roughness length, leaf area index, stomatal resistance, total rooting depth, soil texture index, soil porosity, saturated hydraulic conductivity, and so on. While the simplest level of land-surface scheme predicts just topsoil temperature, most sophisticated ones predict the soil temperature and moisture. An inter-comparison of various land-surface schemes is well documented by Chen et al. (1997).

Most numerical PBL schemes coupled with a land-surface scheme compute turbulent surface fluxes based on the surface similarity theory that takes into accounts the atmospheric stability and representative surface characteristics. Due to the dominant influence of friction in the surface layer where the fluxes are considered constant, the physical length scale can not be treated equally as in the upper layers of the PBL (Ekman layer). The Monin-Obukhov length ( $L$ ) scale is usually adopted in expressing the gradient of the mean atmospheric parameters in the surface layer. Thus, the atmospheric profiles in the surface layer are expressed as a universal function of nondimensionalized Monin-Obukhov length ( $z/L$ , nondimensional stability parameter, where  $z$  is height above the surface), which is called the Monin-Obukhov similarity (Monin and Obukhov, 1954). Then, the surface fluxes can be calculated based on a flux-profile relationship (Businger et al., 1971). Because the independent Monin-Obukhov length is determined by the frictional velocity and the ground heat flux, the characteristic of the ground surface is crucial factor for the determination of the surface fluxes.

The surface characteristics for use in the MM5 slab models include roughness, soil moisture availability, emissivity, thermal capacity of the soil, and surface albedo. The slab model in the MM5 predicts ground temperature using a prognostic representation of surface energy balance in the thin soil layer (slab).

Most 3-d mesoscale models including MM5 are constrained to using a homogeneous surface in each grid box for the parameterization of the turbulent processes in the PBL. This induces errors in accurately expressing the surface fluxes from a grid element where subgrid-scale heterogeneity is obvious. Because the surface fluxes are nonlinearly related to the atmospheric stability and surface characteristics (Avissar 1992), actual surface fluxes are different from those calculated using the representative grid-mean surface characteristics for a grid element with heterogeneous surface. According to Mahrt (1987) surface-flux errors can be introduced by exchange coefficients obtained from grid-mean variables instead of spatially averaging the local exchange coefficients within the grid. This is because the flux formulations in the model are based on the relationship between local fluxes and local gradients but the model relies on grid-averaged values.

Thus, it seems that the turbulent surface flux errors can be reduced by better treating the land-surface heterogeneity. Avissar and Pielke (1989), Pielke et al. (1991), and Dalu and

Pielke (1993) suggested the errors related to the surface heterogeneity can be minimized by obtaining the fluxes by averaging proportionately according to the PDF of surface characteristics within the grid. In realizing their idea, Avissar and Pielke (1989) regrouped similar land patches at different places within the grid element into subgrid classes. For each class the surface fluxes to the atmosphere are assessed independently. Then the grid-mean fluxes between the land surface and atmosphere are obtained by averaging in proportion to the fractional area coverage of the subgrid classes.

For large-scale models like GCMs, subgrid-scale atmospheric forcings might be important in adequately representing the surface fluxes. In an effort to consider the subgrid-scale atmospheric forcing experienced by the surface, Seth and Giorgi (1994) developed the explicit subgrid method. They broke down the atmospheric grid cell into subgrid cells corresponding to surface patches. Then, by using a physically meaningful function, atmospheric forcings are distributed explicitly to the subgrid cells. They showed that the subgrid-scale atmospheric forcings resulted in a shift of energy partitioning toward increasing the Bowen ratio in the surface layer.

Recently, numerical studies on the PBL affected by surface heterogeneity began to adopt the Large Eddy Simulation (LES) technique (Avissar and Schmidt, 1998; Gopalakrishnan and Avissar, 2000; Lin and Glendening, 2002). From their LES study, Avissar and Schmidt (1998) concluded that as long as the “patchiness” of the landscape has a characteristic length scale smaller than 5-10 km, the Avissar and Pielke’s (1989) mosaic type of land-surface scheme can be applied to represent the land surface in atmospheric models.

The explicit subgrid method of Seth and Giorgi (1994) is more realistic but computationally more expensive than Avissar and Pielke’s method. Because subgrid-scale atmospheric forcings are not distinct and can be assumed well mixed for a mesoscale model with grid size of several kilo-meters, Avissar and Pielke’s method seems to be a good choice to minimize the land-surface heterogeneity-caused errors of surface flux computations in a mesoscale model. Many numerical studies that examined the response of PBL atmosphere to heterogeneous surface fluxes were conducted based on the idea similar to Avissar and Pielke’s: Wetzel and Boone (1995), Molders and Raabe (1996), Doran and Zhong (1995), Doran et al. (1995), Zhong and Doran (1995), Ronda et al. (2002), Chen et al. (2003), Essery et al. (2003), LeMone et al. (2003) and so on. This study adopts Avissar and Pielke’s method

as done in the previous studies but is different from those studies in that subgrid-scale atmospheric forcings in the surface layer only are considered as well.

### 3. Hypothesis

In meteorological models, the surface fluxes (exchange of energy, momentum, and moisture between the land-surface and atmosphere) are diagnosed at every model time step in such a way as to obtain energy balance at the thin model land-surface interface. The diagnosed surface fluxes are mostly nonlinear functions of the land-surface properties and atmospheric stability. By feedback processes the land surface and atmosphere interact nonlinearly during model integration.

In a grid model the atmospheric and land-surface variables are represented by grid-averaged mean values. The surface flux calculations typically use the grid-averaged mean values of atmospheric forcing and land-surface properties. As mentioned by Mahrt (1987) the problem with using the grid-averaged values in the flux calculation is that the model uses flux formulations based on the relationship between local fluxes and the local atmospheric and land-surface variables. Furthermore, due to the nonlinearity of the flux formulations, it is obvious that mean surface flux in a grid box is different from the flux calculated from the grid mean variables.

We hypothesize that the errors caused by homogeneous representation of land-surfaces in MM5 model simulation can be understood to some extent by using a 1-d PBL model that has the same land-surface scheme as the MM5. By comparing two 1-d PBL simulations implemented with same model-driving forcings but for land surface representation, one with a homogeneous representation and the other with a heterogeneous subgrid-scale land-surface, relative differences between the two simulations can be obtained. Then, the difference is regarded as the errors caused by homogeneous representation of the land surface in mesoscale models including the MM5.

When we deal with the 4-km grid domain of MM5 in a highly heterogeneous urban area, partitioning the grid elements into smaller patches is difficult and practically impossible within the MM5 model system itself. Presently the MM5 system has not been applied with a grid size of several hundred meters, and the parameterizations have not been designed for that small grid spacing. Therefore, the 1-d PBL model can be a useful tool to infer the

difference between the homogeneous and heterogeneous representation of land-surface properties in MM5 simulations. The methodology adopted here is the same as Avissar and Pielke (1989) except that subgrid-scale atmospheric forcings are added.

For the same reason as the flux calculations between the land-surface and atmosphere, the skin temperature retrieval by GOES satellite measurement could have errors associated with heterogeneity of land surface when the retrieved skin temperature is used for obtaining soil moisture availability in the MM5 simulations. Using subgrid-scale ground temperatures generated by the 1-d PBL run the skin temperature retrieval error can be estimated with the assumptions that the model atmosphere is homogeneous and the heterogeneity is given only by the land surfaces within a grid element of the MM5.

**CHAPTER II**

**INVESTIGATION ON RELATIVE MM5 PERFORMANCE IN INHOMOGENEOUS  
HOUSTON URBAN AREA COMPARED TO THAT IN HOMOGENEOUS  
SURROUNDING AREAS**

1. Introduction

Systematic MM5 model errors associated with interaction between land surface and atmosphere were documented consistently in previous studies (Chen and Dudhia, 2001a; Pyles et al., 2002; Colle and Olson, 2002; Zhong and Fast, 2002). Those systematic errors include near-surface warm and dry biases over land and high bias in surface sensible heat fluxes. Because those errors are associated with PBL physics, land-surface processes, and model dynamics in complex ways, it is a challenging task to resolve the problem in MM5 modeling. As a reason for the slower development of convective mixed layer in the MM5 despite its high bias in surface sensible heat fluxes, Chen and Dudhia (2001b) presumed that some effects induced by small-scale heterogeneity that the MM5 failed to capture might cause the model error. Zhong and Fast (2002) explained that improved model parameterization of longwave radiation and turbulent mixing would be necessary for accurate local forecasting. While the systematic model errors are usually found to be common in the whole model domain the magnitude of the errors can be variable from grid point to grid point depending on surface characteristics in the model domain.

This chapter provides verification statistics in the Houston urban (HOU) area compared to the surrounding (SUR) area for the MM5 simulations during the ozone episode (Aug. 25 – Sep. 1, 2000). The difference of verification statistics between HOU and SUR is hypothesized as partly being caused by different surface characteristics when the areas are under same environmental weather conditions. Among the differences in the surface characteristics between HOU and SUR is subgrid-scale inhomogeneity of surface characteristics in HOU. Given the systematic model errors associated with improper specification of surface parameter values the errors can be reduced by tuning the specification of the surface parameter values. Especially, appropriate values of roughness

length and moisture availability parameters are important to properly represent model flux parameterization (Oncley and Dudhia, 1995). However, the errors caused by subgrid-scale inhomogeneity remain unsolved.

The MM5 outputs used in this verification are from retrospective runs tuned very carefully making use of variety of observations and GOES satellite assimilation by J. Nielsen-Gammon at Texas A&M University (TAMU). Aside from the sea breeze, the weather conditions during the ozone episode can be regarded as homogeneous in the HG area of the verification model domain. Most days during the ozone episode were experiencing clear sky conditions free of rain with some exceptions of isolated shower activity (Aug. 25, Aug. 27, Aug. 29) and thunderstorms (Aug. 31, Sep. 1) which were brief. The observations used are Microwave Temperature Profiler (MTP) and sondes launched at Houston Downtown (HDT).

## 2. Description on MM5 simulation

The MM5 system used in this verification study was configured with 4 domains (Fig. 1): 108 km outermost, 36 km nested, 12 km nested, and 4 km innermost domains. While the outer 3 domains interact in 2-way, the innermost 4 km domain was 1-way nested. The 4-km domain encompassing the HG area is the target domain of this study.

Using the variety of observations during the TEXAQS 2000 MM5 retrospective simulations for the ozone episode (August 25, - September 1, 2000) were tuned extensively by Nielsen-Gammon to meet the requirement needed for use of the model as a chemistry grid model driver. The 108-, 36-, and 12-km outer domain grids were nudged to Eta Data Assimilation System (EDAS) analyses. This type of data assimilation is called analysis nudging. On the 4-km target domain observations were directly assimilated to alter the simulations. This type of data assimilation is called observation nudging.

In an effort to correct for the larger-scale biases as well as systematic errors in the diurnal wind cycle, wind profiler data was utilized for the observation nudging in the 4-km domain. Five profilers were available during the ozone episode and the data is available between about 150 m and 2000-3500 m. Vertical resolution of the data was

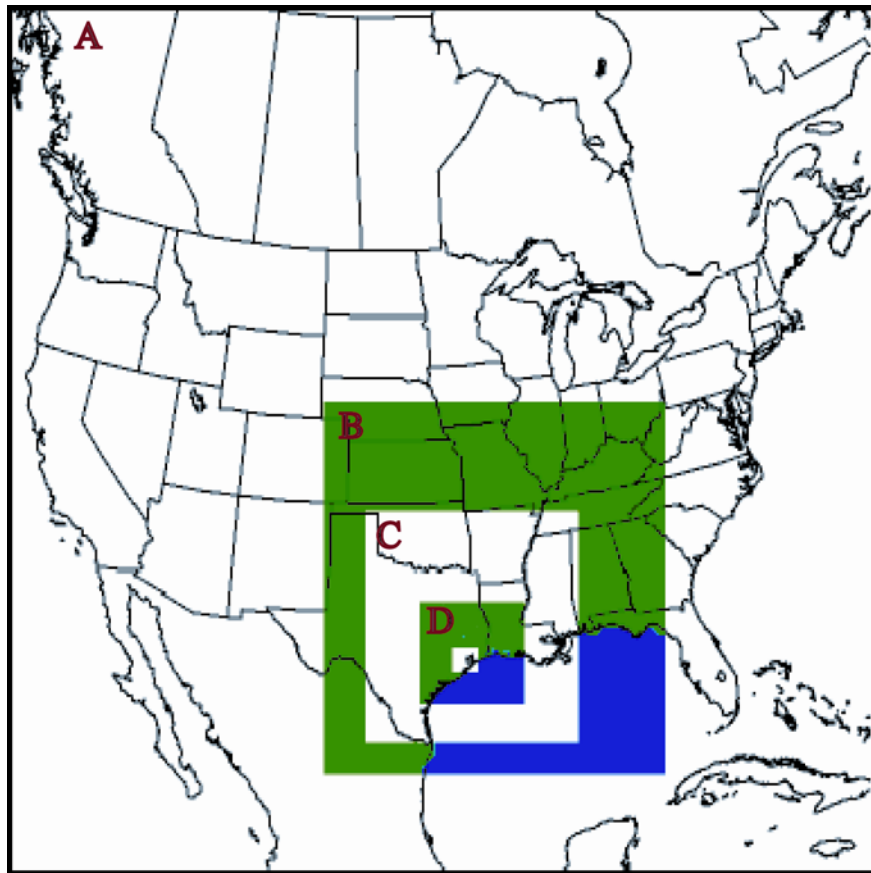


Figure 1. Configuration of NGMM5 model domains. The grid sizes of the four domains are 108 km, 36 km, 12 km, and 4 km from the domain A, B, C, and D, respectively.



sufficient for model levels within the interval. Four parameters to control the observational nudging characteristics in the MM5 were determined after considering profiler data characteristics and the circulation features to be simulated: 1) time interval, 240 minutes, 2) vertical radius of influence, 0.001, 3) horizontal radius of influence, 150 km, and 4) nudging strength, 0.0004. Details of wind profiler data nudging are found in a Nielsen-Gammon report (2002b).

Recently, Nielsen-Gammon applied the GOES satellite assimilation technique to the MM5 simulations along with the observation nudging explained above on the 4-km domain. The GOES satellite assimilation technique originally developed by McNider (1994) is state-of-the-art technology for the purpose of obtaining soil moisture availability using time variation of satellite-observed skin temperature. Compared to previous simulations without the GOES satellite assimilation new simulations brought much improvement in model performance. The application of the satellite assimilation to an MM5 simulation of 4-km grid size was done for the first time with these runs. The theoretical background on which the technology is based will be explained later in another chapter. The key model settings are listed in Table 1. Hereafter, the 4-km model domain applied with both the observation nudging and GOES satellite assimilation technique is called NGMM5.

### 3. Description on MTP data

The verification study comparing the MM5 performance between two areas, horizontally adjacent to each other within the mesoscale range, requires much denser observations not only in time but also in space than conventional observations such as synoptic surface and radiosonde measurements. Particularly, when an urban area such as Houston metropolitan of this study is compared with the surrounding rural area, dense observations are essential because of large variability of the surface characteristics within such a small horizontal distance in the urban area. Further, the surface characteristics with such small scale inhibit the representativeness of the surface meteorological measurements from the local air quality network. Verification data must span the full range of urban conditions in order that mean urban atmosphere can be reliably determined.

Table 1. Key model settings for the MM5 simulations during the ozone episode (Aug. 25 – Sep. 1, 2000).

<b>Model aspects</b>	<b>Setting</b>
Model version	3.4
Grid spacing	4 km, 12 km, 36 km, 108 km
Innermost nesting	One-way
Radiation scheme	RRTM
Radiation update frequency	30 minute
Cumulus parameterization	Grell (none on fine nest)
Cloud physics	Simple ice
PBL scheme	MRF
Soil scheme	5-layer
Shallow convection scheme	Yes
Coriolis force	3-d
Land use	25-category USGS
Soil moisture	Updated by GOES assimilation for 4 km domain

During TEXAQS 2000 the Microwave Temperature Profiler (MTP) instrument on the NCAR Electra aircraft was operated by M.J. Mahoney of the California Institute of Technology. This instrument was designed to produce vertical profiles of temperature along the flight track of the aircraft. Such profiles are inherently unbiased by surface inhomogeneities.

The MTP instrument is a passive microwave instrument that scans forward from the aircraft with multiple scan angles. The multiple scan angles provide information on the vertical structure of observed radiance along the flight track. Then, the observed radiances and those theoretically obtained from a set of reference temperature profiles are ingested into a statistical retrieval algorithm to retrieve the vertical structure of temperature.

In the past, the MTP has been largely used on high-altitude (10 – 12 km) aircraft to study the upper troposphere, the tropopause, and the lower stratosphere: for example, atmospheric wave phenomena (Dornbrack et al., 2002), clear-air turbulence (CAT) analyses (Gary, 1981; Gary, 1984), and aerosol and chemical species (Kondo et al., 1999). The TEXAQS 2000 field program was the first use of the instrument at low levels in the atmosphere.

The MTP measures the natural thermal emission (radiance or brightness temperature) from oxygen molecules at three frequencies (55.51, 56.65 and 58.79 GHz). In order to obtain a vertical temperature profile along the flight track, the measured microwave brightness temperatures, or observables, are related to an actual physical temperature profile by a linear multiple regression. In establishing the regression, forward radiative calculations for hundreds of radiosondes representing the time and location of the MTP measurement are performed. Based on the calculations the statistical retrieval coefficients are calculated. Once the retrieval coefficients are determined, then the measured brightness temperatures can be converted to a vertical temperature profile.

Thus, the accuracy of the retrieval depends on the representativeness of the reference temperature profiles. Because the Electra typically flew between 1500 UTC and 2300 UTC, the referencing soundings needed to include the variability in PBL depth during the flight time period. Also, the soundings are required to be representative of meteorological conditions found not only at inland locations but also offshore or along the immediate coast.

In order to meet these requirements, soundings from MM5 simulations were used as the referencing soundings for the temperature retrievals. Model soundings were extracted at 1500 UTC, 1700 UTC, 1900 UTC, 2100 UTC, and 2300 UTC on each of the days during the ozone episode in which the aircraft flew. Through careful examination of the three-dimensional temperature structure in the MM5 simulations, reference sounding sites (Fig. 2) were identified to represent conditions far offshore, near to shore, over Galveston Bay, along the eastern and western shores of Galveston Bay, near Houston, and at more distant locations to the southwest, northwest, and northeast.

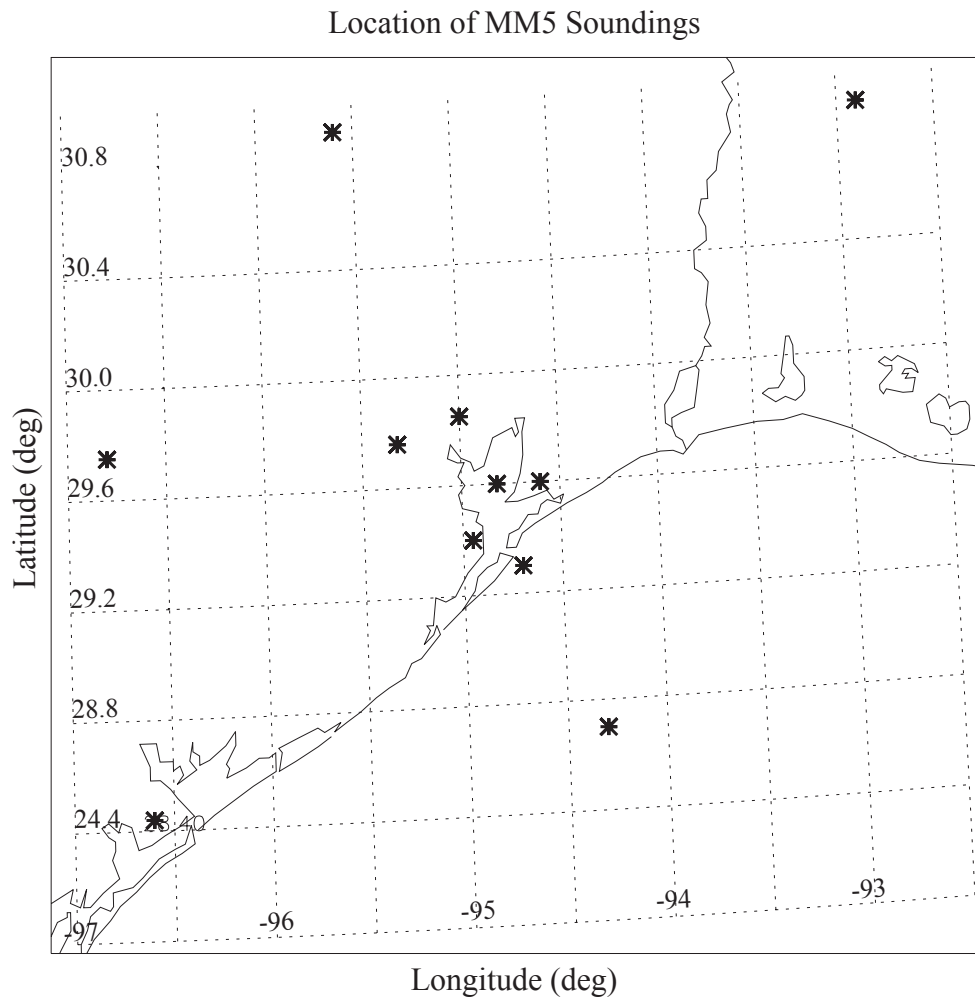


Figure 2. The 11 locations of reference MM5 soundings designated by asterisk marks.

In order to minimize the possibility that the MTP retrievals would reproduce biases in PBL structure caused by a particular MM5 PBL scheme, soundings were constructed from two MM5 runs for the ozone episode, one with the MRF PBL scheme and the other with the Gayno-Seaman scheme. Thus, the range of model-simulated structures were expected to allow the MTP retrievals to accurately reflect true atmospheric conditions. Notice that the outputs used as reference soundings were from both MM5 driver runs which were applied with wind profiler observation nudging only. MTP data available during the ozone episode are on August 25, 27, 28, 30, and September 1, 2000.

The accuracy of the MTP observation depends on the retrieval algorithm. Due to lack of investigation on MTP data accuracy within the PBL, the verification statistics using the MTP data can not be interpreted as representing absolute model performance at this time. However, comparison of the verification statistics between HOU and SUR can be useful in identifying model errors associated with the surface characteristics in HOU area. This comparison was possible and meaningful thanks to the enormous MTP data coverage in the model domain, and not possible from the spatially isolated sonde observations.

#### 4. Description on HDT sonde data

During TEXAQS 2000 one of the three sonde launch sites was at downtown Houston (HDT). The latitude and longitude of the HDT are 29.77N and 95.36W. The elevation of the site is 14 m MSL. The sondes were Airsondes and were bought from Atmospheric Instrumentation Research, Inc. During the ozone episode (Aug. 25 – Sep. 1, 2000) 36 soundings were launched and data from the soundings are available for this study.

#### 5. Preparation of verification data from MTP, sonde, and NGMM5 data files

The MTP raw data set consists of series of retrieved vertical temperatures along the flight tracks. Investigation of the raw data set revealed that the MTP-retrieved temperatures are not as good for characterizing the PBL during higher altitude flights. There is also substantial scan-to-scan variability in the retrieved temperature, probably due to the variable microwave emissivity from the ground. Therefore, we selected MTP potential temperatures from flight tracks of about 2000 ft (0.61 km) and applied a 3-scan moving average for the verification purpose of this study. The selected flight tracks are illustrated in Figure 3. Each

scan spans about 15 seconds and the aircraft speed is about 100 m/s. Therefore, 3-scan sets are separated by 4.5 km.

The MTP potential temperatures at variable heights from scan-to-scan are interpolated onto fixed height levels. The levels used in this verification study are: 50 m, 150 m, 250 m, 350 m, 450 m, 550 m, 650 m, 750 m, 850 m, 950 m, 1050 m, 1150 m, 1250 m, 1350 m, 1450 m, 1550 m, 1750 m, 2000 m, 2250 m, 2500 m, 2750 m, and 3000 m. At those heights the verification statistics will be calculated.

The NGMM5 potential temperatures were computed on model grids. Then, the potential temperatures were interpolated to the verification heights vertically and the MTP scan points horizontally. The spatial interpolation was performed by a weighted average of 4 grid points surrounding a MTP scan point. The NGMM5 outputs are available in 1-h interval and any MTP scan times fall between model output times. Therefore, in order to match the model potential temperatures with those of MTP, time interpolation of the model data to the MTP times was performed.

In order to compare the MTP and NGMM5 with the HDT sonde observation, potential temperature profiles at HDT were obtained at the same heights as for MTP and NGMM5. The model potential temperatures were interpolated horizontally and temporarily to match the location and time of the HDT soundings.

## MTP Flight Tracks (Scan Points)

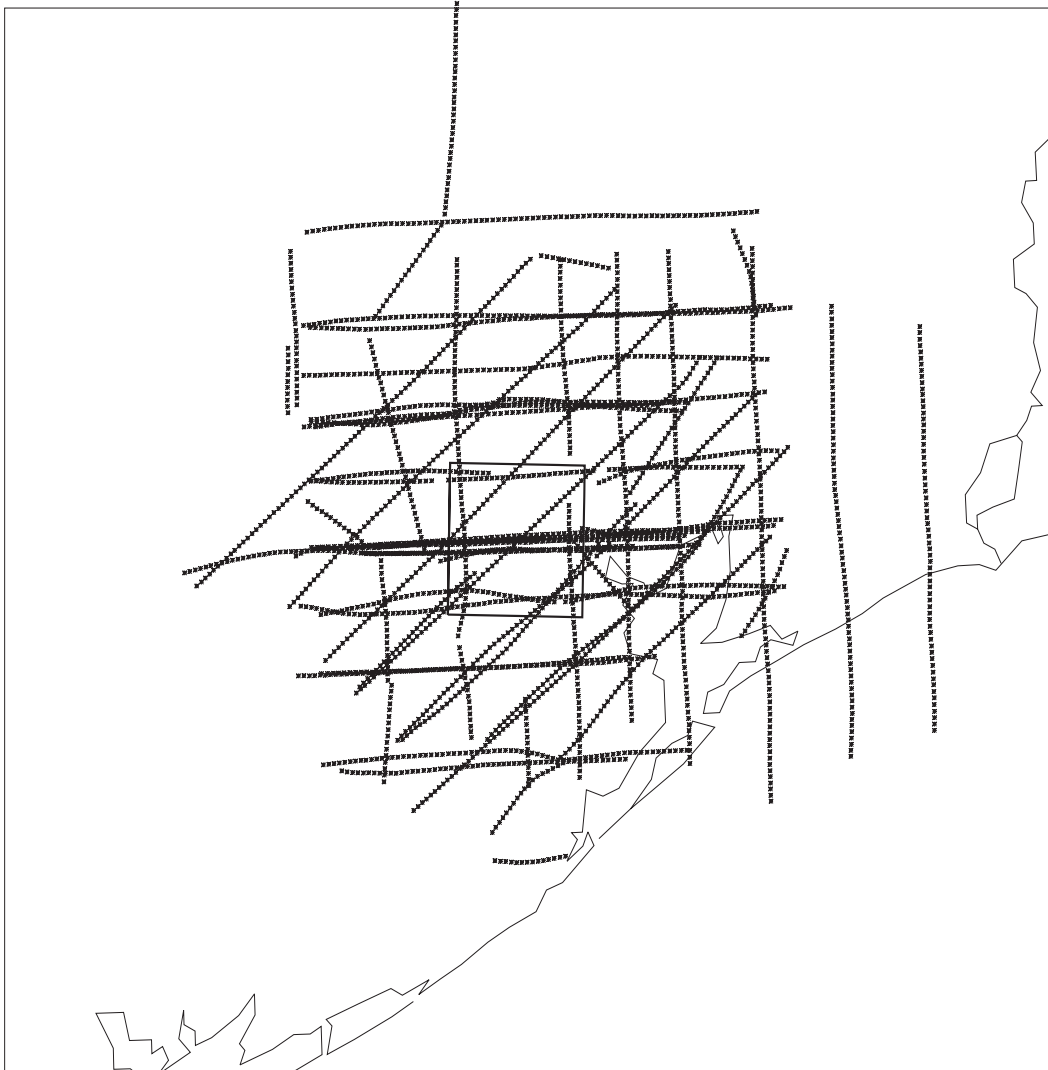


Figure 3. MTP scan points selected for flight altitudes of about 2000 ft (0.61 km). The square box in the figure represents Houston urban area.

## 6. Selection of verification data sample

So as to compare PBL heights obtained from the NGMM5 and MTP, a PBL height definition was applied to both data sets. Since the MTP data is available for only temperatures, a temperature profile definition (Coulter, 1979) is chosen as only method of obtaining PBL heights from both MTP and NGMM5 data set. The original definition is that height at which the temperature profile first become less than adiabatic is defined as the PBL height. In general, the PBL heights determined by the temperature profile definition are consistently lower than those obtained by other methods such as lidar and sodar results (Coulter, 1979). Lower-height bias of temperature profile definition is also indicated in recent study on comparison of mixed layer heights by C. Smith (2004, personal communication). Owing to the consistent lower-height biases, differences of PBL heights between MTP and NGMM5 are believed to be statistically meaningful as long as the PBL heights to be compared are calculated using the same temperature profile definition.

Based on the temperature profile definition an algorithm to calculate the PBL height was developed. In the algorithm, potential temperature lapse rates are checked by increasing height from ground level. According to the definition the height at which the lapse rate first become greater than zero (critical lapse rate) is supposed to be the PBL height indicated by the potential temperature profile. However, the zero critical lapse rate does not consider entrainment at the PBL top caused by overshooting of thermals. Intuitively we expect that the critical lapse rate exists somewhere between zero and 2 K/km rather than zero considering the entrainment effect near the PBL top.

In this study the critical lapse rate was determined so that the PBL height samples from both MTP and NGMM5 have similar variance. First, the MTP data was classified into two parts corresponding to Regime-I (Aug. 25 – Aug. 29) and Regime-II (Aug. 30 – Sep. 1) of the ozone episode because both MTP and NGMM5 data indicated substantial differences between Regime-I and Regime-II because of difference in large-scale winds. Then, 140 paired samples of the MTP and NGMM5 PBL heights were obtained with respect to each of 140 critical lapse rate values ranging from 0.1 K/km to 1.5 K/km and from 0.6 K/km to 2.0 K/km for the Regime-I and II, respectively. In the samples the MTP scan points over water and with PBL heights less than 800 m were excluded purposely to get statistical results as



significant as possible since those points are suspected to be contaminated significantly due to surface emission. The sample data was confined in time to between 1500 UTC and 0000 UTC.

Using the samples, F-variance test values between the MTP and NGMM5 PBL heights were computed with respect to each critical lapse rate value for the Regime-I and II. F-variance test values range between 0 and 1 and indicate significance of variance similarity between two data samples. A value closer to 1 indicates greater similarity of variance between two data. Figures 4a and 5a illustrate the F-variance test values between MTP and NGMM5 PBL heights as function of critical lapse rate for Regime-I and II, respectively. The statistical characteristics of NGMM5 PBL height biases for the paired samples are indicated by values of kurtosis, skewness, mean, and standard deviation with respective to the critical values as shown in figures 4 and 5 (b, c, d, and e). The kurtosis value signifies the degree of peakedness of a distribution with a positive value indicating a distribution with a high peak, a negative value indicating a flat-topped distribution, and a zero value indicating a normal distribution. The skewness value signifies the degree of asymmetry of a distribution with a positive value indicating right-skewedness, a negative value left-skewedness, and values near zero an approximately normal distribution.

The critical lapse rate that produces both a peak F-variance test value and maximum number of samples was determined as the critical lapse rate to be used in the PBL height calculation for this study. The determined critical values are 0.63 K/km and 1.08 K/km for Regime-I and II, respectively as indicated by thin vertical lines in figures 4 and 5.

For Regime-I, the NGMM5 PBL height biases are seen to be nearly normal-distributed at the determined critical lapse rate value as indicated by kurtosis and skewness values close to zero. For Regime-II, the NGMM5 PBL height biases are significantly left-skewed in distribution at the determined critical lapse rate value as indicated by a skewness value of about  $-1.2$ .

Because the statistical characteristics of the PBL height biases are significantly different between the Regime-I and II, only the MTP scan points included in the Regime-

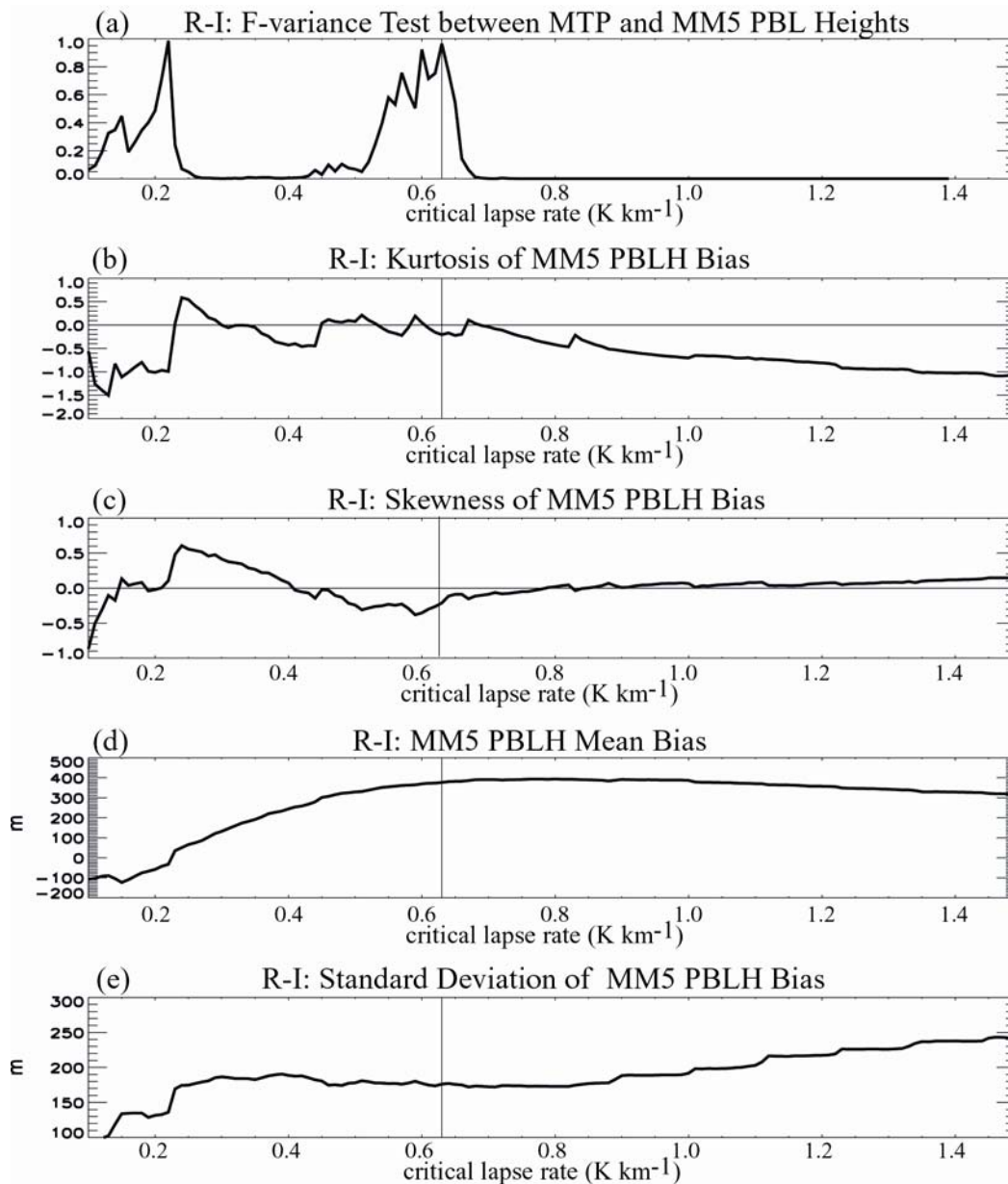


Figure 4. The NGMM5 and MTP PBL height statistics as function of critical lapse rate represented by (a) F-variance test value between MTP and NGMM5, (b) Kurtosis of the NGMM5 PBL height biases, (c) Skewness of NGMM5 PBL height biases, (d) NGMM5 PBL height mean biases, and (e) standard deviation of the NGMM5 PBL height biases, during the Regime-I.

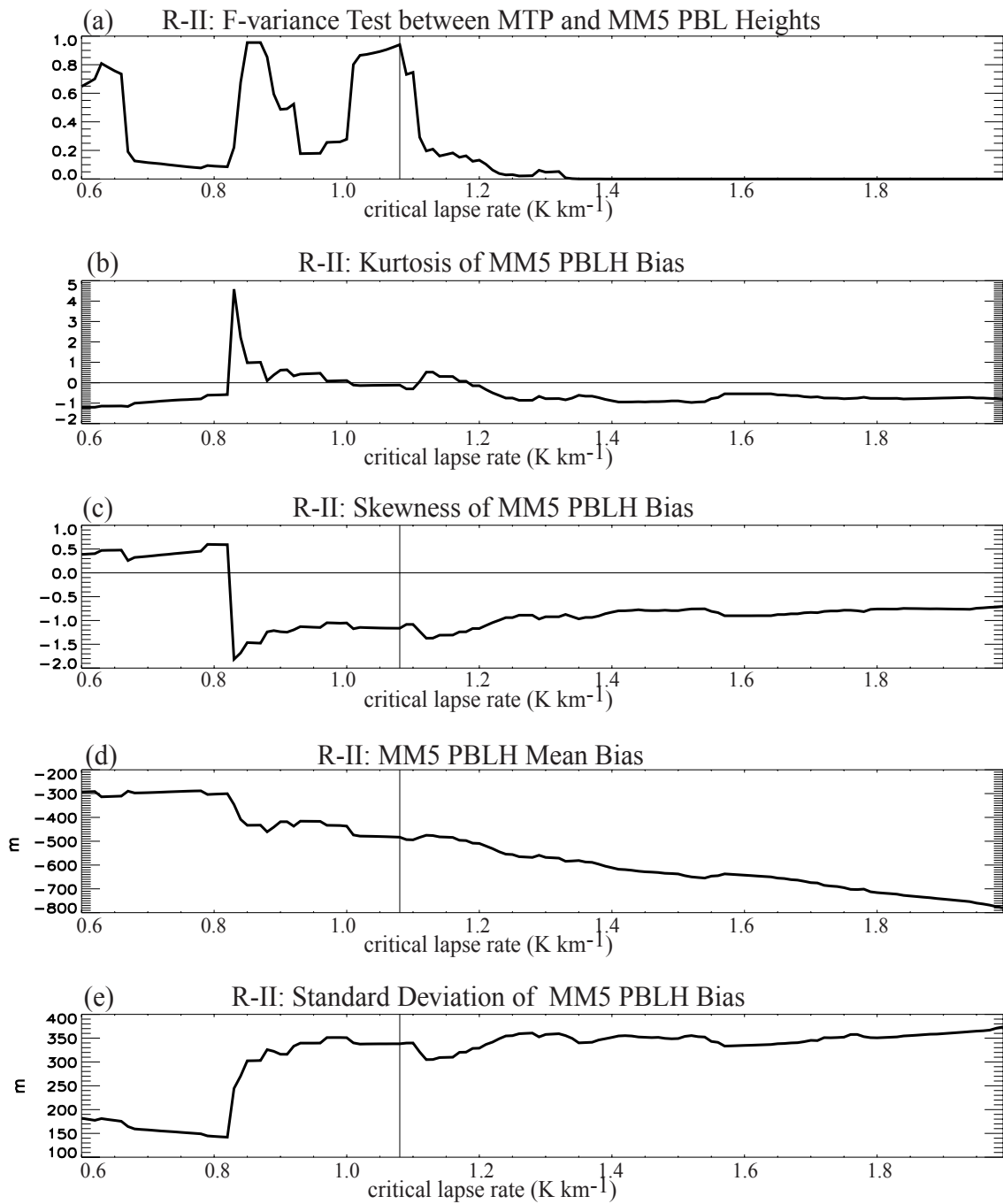


Figure 5. The same as Figure 4 except for the Regime-II.

Table 2. Area coverage (%) of MM5 landuse types included in each area and verification data point numbers of each area.

MM5 land use types	HOU	SUR NW	SUR N	SUR NE	SUR W	SUR SW	SUR S
1, Urban & Built-Up Land	51.0	-	0.9	-	3.6	-	2.7
2, Dryland Cropland & Pasture	39.0	52.9	30.9	34.7	88.2	74.0	92.9
5, Cropland/Grassland Mosaic	4.0	-	7.3	-	5.5	16.8	1.7
7, Grassland	3.0	-	-	-	1.8	-	-
10, Savanna	-	-	-	0.8	-	6.7	-
11, Deciduous Broadleaf Forest	-	-	-	14.9	-	-	0.9
14, Evergreen Needleleaf Forest	3.0	47.1	60.0	49.6	0.9	2.5	1.8
16, Water Body	-	-	0.9	-	-	-	-
Number of data points	38	47	18	4	59	31	11

I data sample of the determined critical lapse rate were utilized in comparison of PBL height and potential temperature biases between the HOU and surrounding areas. The number of total data points in the sample is 240. The PBL heights of the NGMM5 and MTP at the 240 points are illustrated in Figure 6.

## 7. Comparison of NGMM5 biases against MTP

### a. PBL height bias

In order to compare the PBL height biases in HOU to those in surrounding areas, Houston urban and 6 surrounding areas of about equal areal coverage in the model domain are defined as indicated in Figure 7 by 1) HOU, 2) NW, 3) N, 4) NE, 5) W, 6) SW, and 7) S. The HOU area is centered at Houston Downtown. Percent area coverage of the NGMM5 landuse types and number of data points in each area are listed in Table 2.

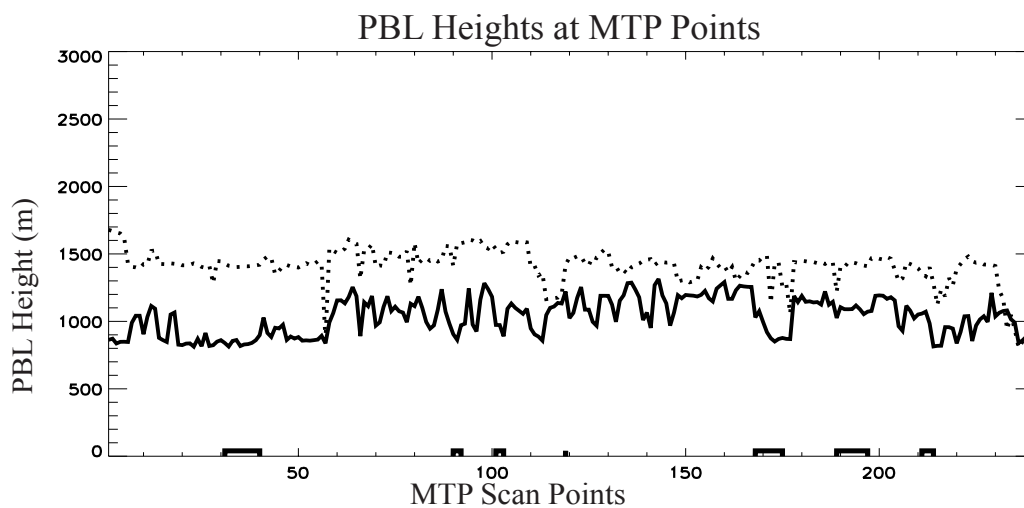


Figure 6. PBL heights of the NGMM5 (dotted) and MTP (solid) for the selected data sample of the ozone Regime-I (Aug. 25 - Aug. 29, 2000).

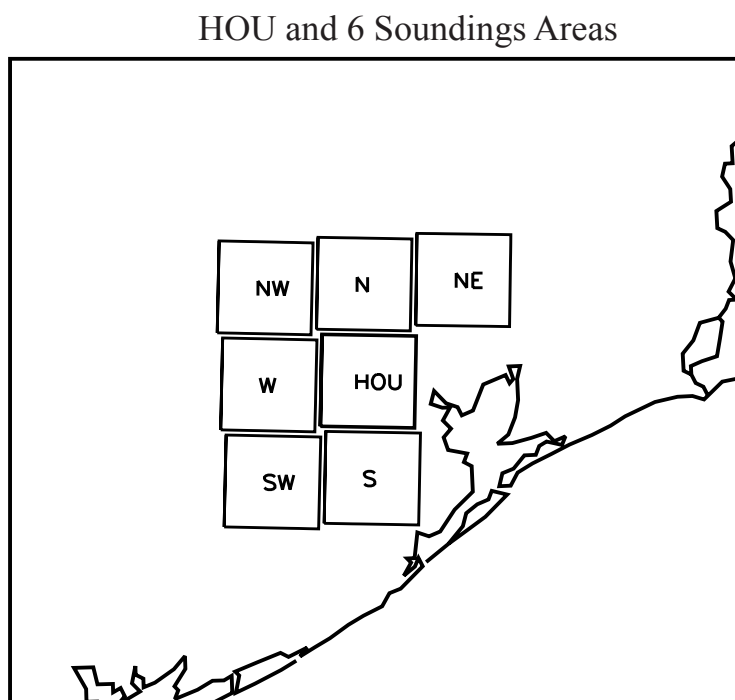


Figure 7. The 7 sub-areas with about equal area coverage representing the Houston urban area (HOU) and 6 surrounding areas (NW, N, NE, W, SW, and S).

In general mean PBL height bias in HOU is greater than SUR areas except for SUR N as indicated in Figure 8a. Mean bias differences between HOU and each of SUR areas range from about 30 m to 130 m. On average the HOU indicated PBL height mean bias 80 m greater than combined SUR areas.

In order to look at whether the bias differences between the HOU and each of SUR areas are statistically significant, statistical T-test values were computed between the HOU biases and those of each SUR area and the results are illustrated in Figure 8c. A T-test value represents the probability that two sample data will show the same sign of mean difference in further samplings. Based on the T-test values, it can be stated that the PBL height biases in HOU are significantly different from those in SUR NW and SW. The T-test values between HOU and NW and between HOU and SW are 100 % and 99.3 %, respectively. The T-test value between HOU and combined SUR total areas is 99.6 % indicating the difference of mean PBL height biases between HOU and combined SUR areas is significant.

The distribution of biases is not seen to be typically different in HOU compared to SUR areas. Standard deviations of biases in each area are illustrated in Figure 8b in order to examine how biases in each area are spread from each mean bias. While individual SUR areas indicated more or less spreads of biases from the mean compared to HOU, on average SUR areas showed greater spread than HOU.

In summary, with significant probability, the NGMM5 in the HOU area is seen to have greater PBL height bias by about 80 m than the SUR areas. Further the biases in the HOU area are less spread from the mean than the combined total SUR areas.

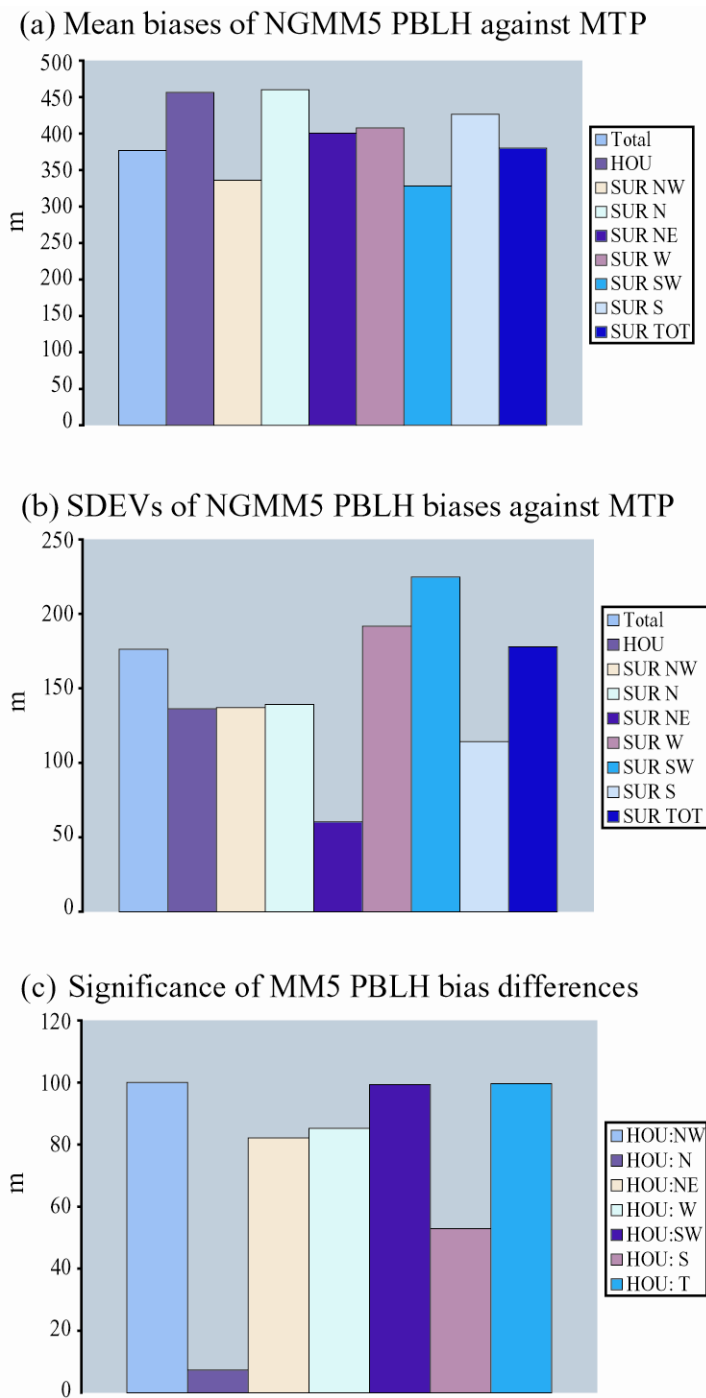


Figure 8. Bar graphs comparing statistics of NGMM5 PBL height biases against MTP among the 7 sub-areas in Figure 7, combined SUR areas, and total area: (a) PBL height mean bias, (b) standard deviation of the PBL height biases, and (c) significance of mean bias difference between HOU and each of SUR and combined areas. In the graphs "Total" denotes entire sample and "SUR TOT" represents combined SUR areas.

*b. Potential temperature biases*

Using the same data points included in the sample of the PBL height bias calculations, potential temperature biases were computed and compared between the HOU and SUR areas. The potential temperature bias calculations were applied to average values in two atmospheric layers: 1) 450 m – 950 m and 2) 2000 m – 2500 m.

Mean biases of the NGMM5 PBL potential temperatures against the MTP in the HOU, 6 SUR areas, and combined SUR areas are illustrated in figures 9a and 9d. In the lower levels (450 m – 950 m), HOU area NGMM5 is generally experiencing more strongly negative mean biases implying a relatively warmer atmosphere than simulated compared to SUR areas. The biases in the upper levels (2000 m – 2500 m) are not as significant as in the lower levels. While mean biases in HOU and combined SUR areas are  $-0.8$  K and  $-1.5$  K respectively in the lower levels, those of in upper levels are  $-0.5$  K and  $-0.3$  K in HOU and combined SUR areas, respectively. In general, the HOU area indicated a greater negative mean bias in the upper levels implying a relatively colder atmosphere there. The HOU area is about  $-0.2$  K relatively colder than the combined SUR areas in the upper levels.

As shown in Figure 9c by the T-test value explained above, the bias differences are significant between the HOU and SUR NW, W, and SW for the lower levels. When HOU biases are compared to those of combined SUR areas the difference of mean biases between two areas is also statistically significant. For the upper levels the bias differences are not as significant. However, the combined SUR areas indicated a significantly different mean bias than HOU as represented by 98.6 % T-test value (Fig. 9f).

As with the PBL height biases, standard deviations of potential temperatures did not show consistent variations among the areas (Figs. 9b and 9e). However, the combined SUR areas indicated a greater departure of biases from the mean than the HOU area in the lower levels, which is consistent with the result of PBL height biases. In the upper levels, the HOU and combined SUR areas showed similar distribution of biases from the mean.



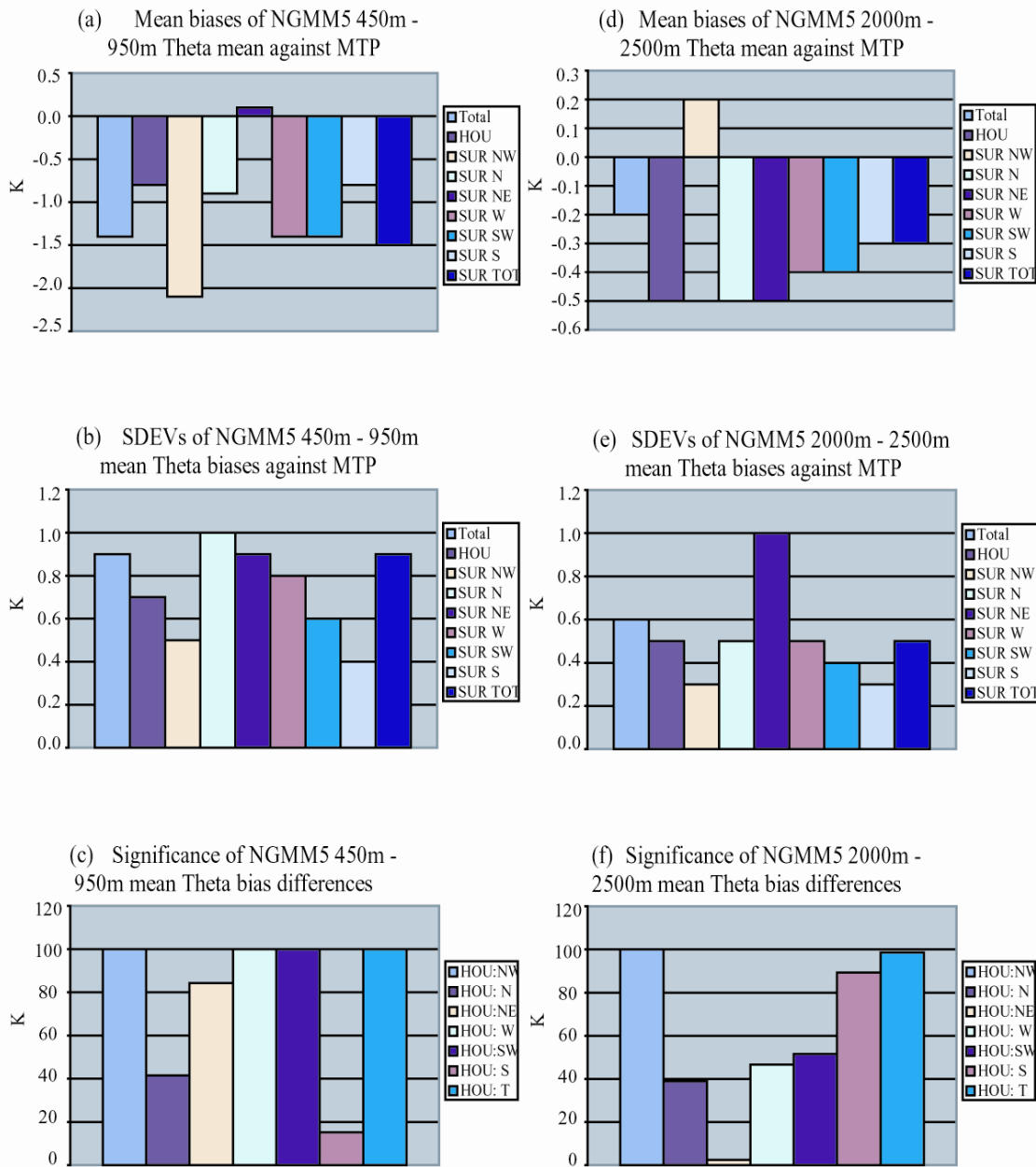


Figure 9. Bar graphs comparing statistics of NGMM5 layer-averaged potential temperature biases, 450 m – 950 m lower layer (a-c) and 2000 m – 2500 m upper layer (d-f) against MTP among the 7 sub-areas in Figure 7, combined SUR areas, and total area: (a) and (d) PBL potential temperature mean bias, (b) and (e) standard deviation of biases, and (c) and (f) significance of mean bias difference between HOU and each of SUR and combined areas. In the graphs “Total” denotes entire sample and “SUR TOT” represents combined SUR areas.

In summary, the HOU area is about 0.7 K warmer in the lower levels (450 m – 950 m) and about –0.2 K colder in the upper levels relative to the combined SUR areas with significant probability. In the lower levels the biases in the combined SUR areas seem to be distributed more broadly than in the HOU area. Notice that the positive relative temperature bias is consistent with the positive relative PBL height bias. However, as can be seen in Figure 6, the MTP indicated lower PBL heights overall than the NGMM5. This is physically inconsistent because a warmer PBL atmosphere would produce higher PBL heights. This inconsistency can be attributed to the crude PBL height estimation algorithm from the MTP data set.

#### 8. Potential temperature biases of NGMM5 and MTP against sonde soundings at HDT

To help understand the true performance of the NGMM5 at HDT we provide mean and standard deviation of the NGMM5 potential temperature biases using soundings launched at HDT during the ozone episode. Among the available soundings, the times between 1500 UTC and 0000 UTC during the Regime-I (Aug. 25 – Aug. 29) were selected so that the soundings are comparable to the MTP data sample used for the comparison of biases in the previous section. Figure 10 presents 12 HDT soundings (dotted) along with those of NGMM5 (solid) selected for the bias calculation.

In general warm biases of the NGMM5 are indicated in most height levels except for 1350 m – 1750 m levels as shown in Figure 11. Near the ground surface below 350 m height level, the warm biases are relatively larger ranging from about 0.7 K to 1.1 K. The other height levels showed warm biases which are close to or less than 0.5 K except for 1350 m – 1750 m levels where cold biases of about –0.5 K are indicated.

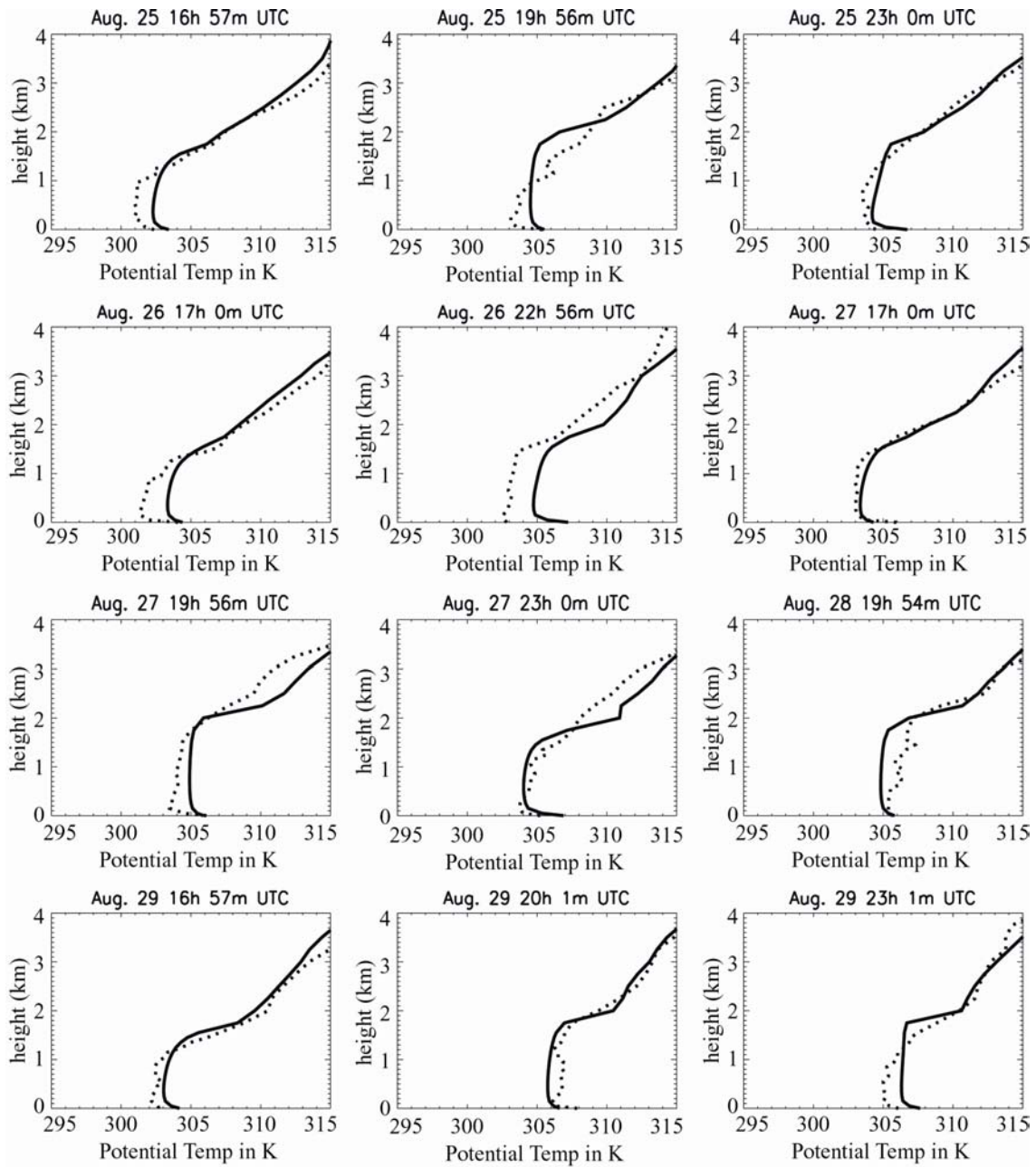
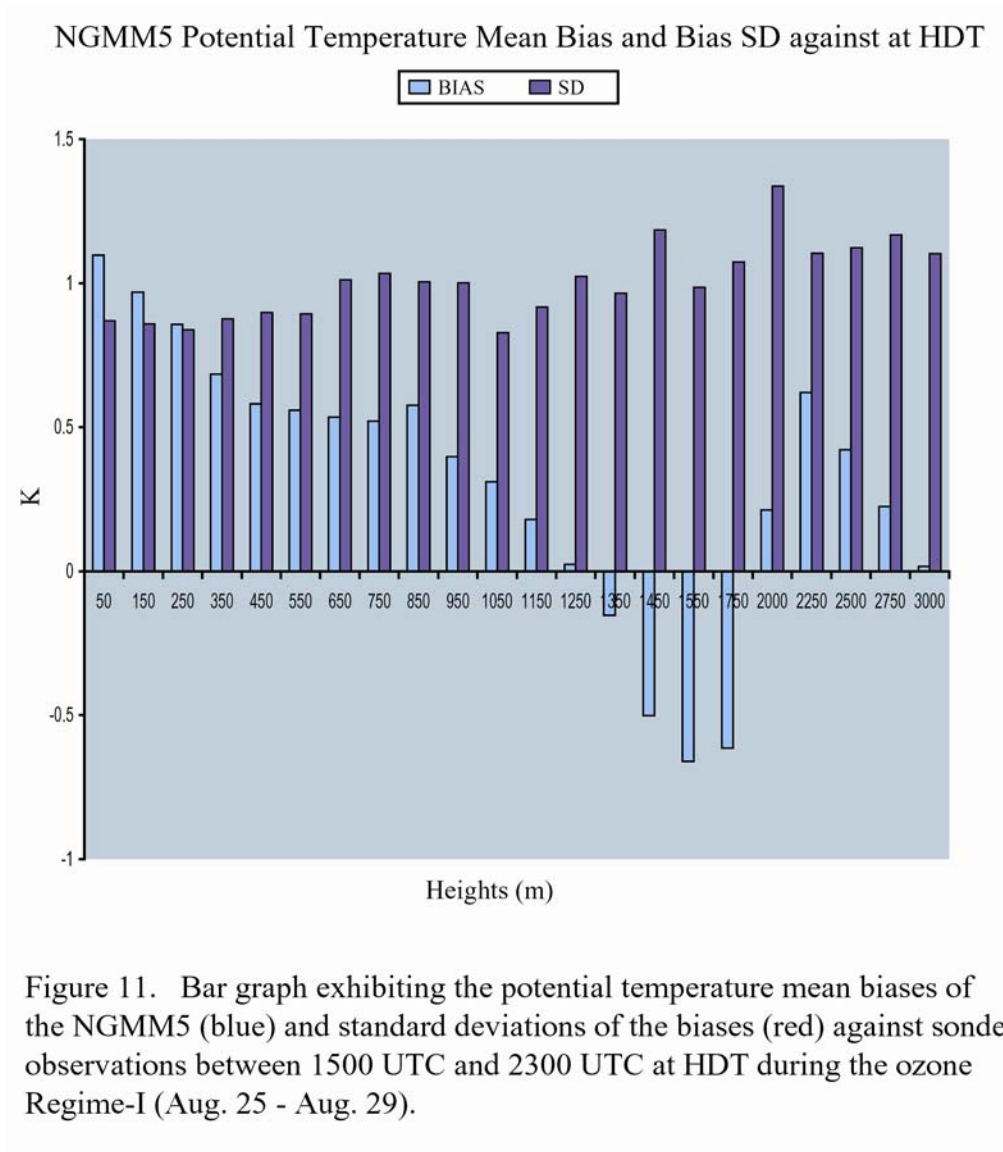


Figure 10. Potential temperature soundings of the sondes (dotted) and NGMM5 (solid) at HDT between 1500 UTC and 0000 UTC during the ozone Regime-I (Aug. 25 - Aug. 29, 2000).



In order to examine the MTP temperature retrieval errors at HDT, MTP scan points which are close to the HDT in time and location were selected and compared to the HDT soundings. The MTP points were so selected that the distance from the HDT is not greater than 0.05 degree latitude, and that MTP times fall between 1500 UTC and 0000 UTC during the Regime-I. Time differences between paired MTP and sonde soundings are not greater than 30 minutes. Time interpolations were not performed. Four MTP soundings met the criteria and the biases at height levels are presented along with mean biases in Figure 12. Using those data, mean biases at each height level are computed and presented in Figure 13. MTP potential temperatures generally indicated warm biases greater than 1.0 K in most height levels except for 450 m – 950 m height levels. The warm biases are relatively significant at height levels below 250 m and between the 1750 m and 2250 m levels at which the biases are greater than 1.5 K. At 450 m – 950 m height levels which are close to the MTP flight level (2000 ft or 0.61 km) the MTP biases are around 0.7 K.

As explained above, at most height levels, both the NGMM5 and MTP indicated warm biases compared to HDT with the MTP showing biases greater than the NGMM5 by about 0.3 K to 1.7 K. This accounts for the cold biases of NGMM5 against MTP, about -0.8 K at 450 m – 950 m levels (Fig. 9a) and about -0.5 K at 2000 m – 2500 m levels (Fig. 9d), in the HDT. Thus, the three comparisons above, NGMM5 against MTP, NGMM5 against sondes, and MTP against sondes are consistent with each other.

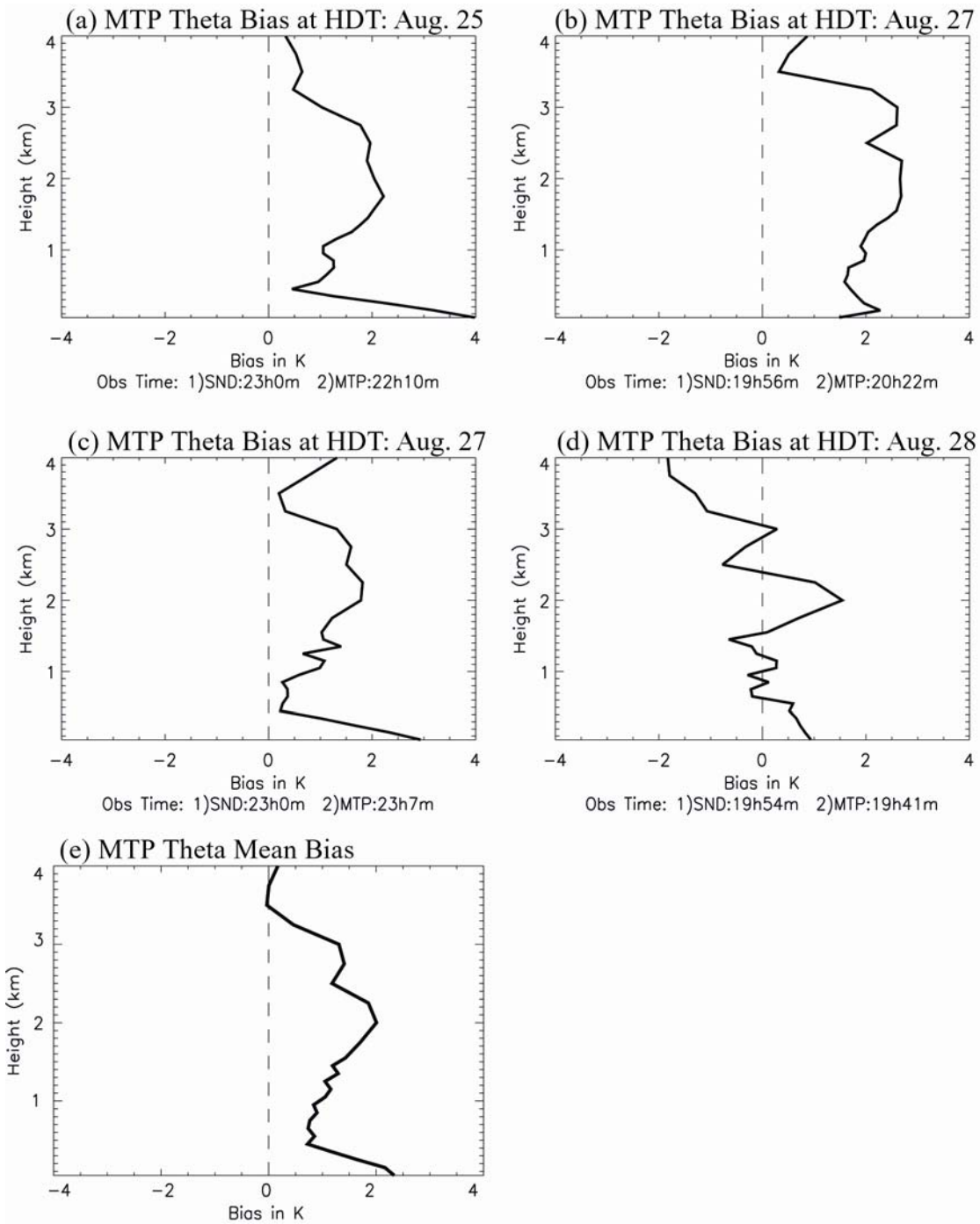
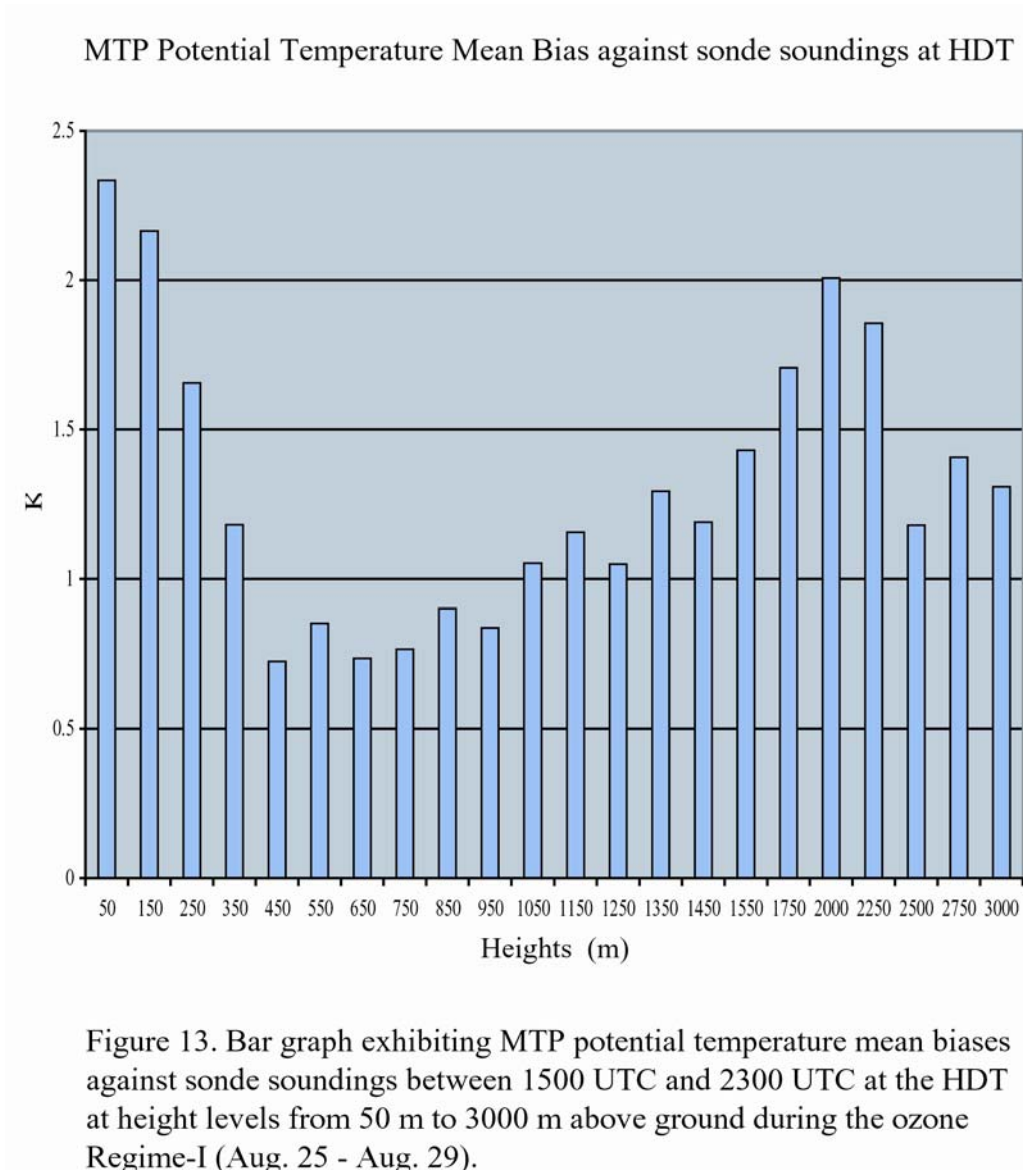


Figure 12. Profiles of (a-d) MTP potential temperature biases against sonde soundings and (e) those mean bias at HDT. Observation times are indicated in each figure.



### CHAPTER III

## INVESTIGATION ON SUBGRID-SCALE SURFACE INHOMOGENEITY IN THE HOU AREA USING 1-D PBL MODEL

### 1. Introduction

In the previous chapter efforts were made to find evidence of MM5 model errors associated with inhomogeneous surface characteristics in the HOU area using MTP and radiosondes. Even though the results indicated to some extent differences between the HOU and SUR areas, the absolute accuracy is still unknown. Due to the inadequacy of the existing observations for studies of surface inhomogeneities on such a small scale, it is very difficult to quantify model errors induced by inhomogeneity of surface characteristics not parameterized in the model.

Instead, in order to study in depth the inhomogeneity impacts in the HOU area we propose to use a 1-d PBL model. The 1-d model is developed so that observed and specified inhomogeneous surface characteristics are able to be represented in the model using methodology similar to Avissar and Pielke (1989).

In this chapter we regard the 1-d model as a surrogate model for the MM5 to examine the impact of inhomogeneous surface characteristics in the HOU area.

### 2. Description of 1-d PBL model

A high-resolution, one-dimensional, moist PBL model was constructed specifically for this study. The 1-d PBL model coding is mostly based on the Zhang and Anthes (1982) paper which followed Blackadar (1976, 1978). The model consists of two modules representing two different regimes of turbulent mixing in the PBL. One is for stable atmospheric stability in night time (nocturnal regime), in which a first-order closure representation of turbulence mixing is utilized. The other is for unstable atmospheric stability in daytime (free convection regime), in which a convective plume model first proposed by Estoque (1968) and later developed by Blackadar (1976, 1978) is made use of. The model equations are as follows:



$$\frac{\partial \theta}{\partial t} = -\frac{1}{\rho} \frac{\partial \overline{\rho w' \theta'}}{\partial z} \quad (1)$$

$$\frac{\partial q}{\partial t} = -\frac{1}{\rho} \frac{\partial \overline{\rho w' q'}}{\partial z} \quad (2)$$

$$\frac{\partial u}{\partial t} = f(v - v_g) - \frac{1}{\rho} \frac{\partial \overline{\rho u' w'}}{\partial z} \quad (3)$$

$$\frac{\partial v}{\partial t} = -f(u - u_g) - \frac{1}{\rho} \frac{\partial \overline{\rho v' w'}}{\partial z} \quad (4)$$

In the equations, the symbols have the conventional meaning recognized in atmospheric science with a prime representing fluctuation from the mean value of the variable. Terms involving primes are parameterized as described below. For surface temperature calculations a predictive slab model is used through an energy budget equation. It should be noticed that cloud physical processes are not included in the model. Therefore, there is no phase change of moisture, and no effect of atmospheric radiation except at the ground. The model details are described in the following.

*a. Vertical structure of the 1-d PBL model*

The model bottom boundary is provided with two soil layers. One is an upper thin soil layer (slab) where the slab model is applied to compute the ground potential temperature. The second is a lower deep soil layer (substrate) where the soil temperature is considered invariant during the model integration period. The atmospheric layers above the ground surface consist of an 8-meter deep surface layer where the Monin-Obukhov similarity theory is applied, and levels above with a vertical depth of 100 m where K-theory or a plume model determined according to the atmospheric stability is used to calculate the turbulent fluxes. While the prognostic variables ( $u, v, \theta$ , and  $q$ ) are defined at half levels, the diagnostic variables such as Richardson number  $Ri$ , the eddy exchange coefficient  $K$ , and the fluxes of heat  $H$ , moisture  $Q$ , and momentum  $\tau$  are defined at the top of each layer. In this study 51 atmospheric layers including the surface layer are used, spanning a total height of 5008 m.

*b. Slab model*

The prognostic representation of surface energy balance in the thin soil layer (slab) is used to compute ground potential temperature,  $\theta_g$ . The energy budget equation is expressed as

$$C_g \frac{\partial \theta_g}{\partial t} = R_n - H_m - H_g - E, \quad (5)$$

where  $C_g$  is the thermal capacity of the slab per unit area,  $R_n$  the net radiation,  $H_m$  the heat flux into the substrate,  $H_g$  the heat flux into the atmosphere, and  $E$  the latent heat flux into the atmosphere. This predictive equation for ground temperature is often referred to as the force-restore method (Deardorff 1977, Dickinson 1988). The  $C_g$  is determined so that the amplitude and phase of the slab temperature are identical to the surface temperature of a real soil layer of uniform thermal conductivity  $k_s$  and volumetric heat capacity  $C_s$ . Considering higher harmonics in addition to the sinusoidal nature of the surface forcing Blackadar (1979) came up with

$$C_g = 0.95 \left( k_s C_s / 2\Omega \right)^{1/2}, \quad (6)$$

where  $\Omega$  is the angular velocity of the earth. The flux terms in the right hand side of the budget are explained in detail as follows:

1) Net radiation

The net radiation,  $R_n$  is the sum of solar radiation  $Q_s$  and net longwave radiation (upward  $I \uparrow$ , downward  $I \downarrow$ ),

$$R_n = Q_s + I \downarrow - I \uparrow. \quad (7)$$

The amount of solar radiation absorbed by the slab is approximated as

$$Q_s = S(1 - A)(\cos \zeta) \tau_s^{\sec \zeta}, \quad (8)$$

where  $S$  is the solar constant,  $A$  the albedo,  $\zeta$  the solar zenith angle,  $\tau_s$  the atmospheric transmissivity, and

$$\cos \zeta = \sin \psi \sin \delta + \cos \psi \cos \delta \cos h, \quad (9)$$

in which  $\psi$  is the latitude of the location,  $\delta$  the solar declination, and  $h$  the local hour angle of the sun (Sellers, 1974). In this model, the downward longwave radiation,  $I \downarrow$ , is specified to be constant and the upward (outgoing) longwave radiation,  $I \uparrow$ , is calculated by

$$I \uparrow = \varepsilon \sigma T_g^4, \quad (10)$$

where  $\varepsilon$  is the slab emissivity,  $\sigma$  the Stefan-Boltzman constant, and  $T_g$  the slab temperature.

## 2) Heat flux to the ground (substrate) $H_m$

This term plays as a restoring forcing in the budget equation. That is, the forcing by the sum of net radiation  $R_n$ , sensible heat flux  $H_g$ , and latent heat flux  $E$  is modified by this term (Deardorff 1977, Dickinson 1988). When the forcing is removed this term restores the ground temperature (slab temperature)  $T_g$  exponentially towards the substrate temperature  $T_m$ . This term is expressed as

$$H_m = K_m C_g (T_g - T_m), \quad (11)$$

where  $T_m$  is the substrate temperature and  $K_m$  the heat transfer coefficient which is expressed as

$$K_m = 1.18 \Omega. \quad (12)$$

## 3) Sensible heat flux $H_g$

The sensible heat flux  $H_g$  is computed from the surface similarity theory and expressed as

$$H_g = -c_{pm} \rho_a k u_* T^*, \quad (13)$$

where  $c_{pm}$  and  $\rho_a$  are the specific heat of moist air at constant pressure and the dry air density respectively, and  $k$  is the Von Karman constant. The friction velocity  $u_*$  and friction temperature  $T_*$  are given by

$$u_* = \text{Max} \left( \frac{kV_a}{\ln \frac{z_a}{z_0} - \psi_m}, u_{*0} \right), \quad (14)$$

$$T_* = \frac{\theta_a - \theta_g}{\ln \frac{z_a}{z_0} - \psi_h}, \quad (15)$$

where  $u_{*0}$  is a background value (0.1 m s<sup>-1</sup> over land and zero over water) and  $V_a$  is the scalar wind speed at the surface layer,  $z_0$  the roughness length,  $z_a$  the surface layer variable height (4 m in this model), and  $\theta_a$  the surface layer potential temperature. The  $\psi_m$  and  $\psi_h$  denote the nondimensional stability parameters for momentum and heat fluxes respectively. The stability parameters come from integrating the gradients of variables which are expressed as a function only of dimensionless height from the roughness length  $z_0$  to  $z_a$ . The nondimensional expression of the gradient is based on Monin-Obukhov (1954) similarity theory. Then, the dimensionless height is expressed as  $\xi = \frac{z}{L}$ , where  $L$  is the Monin-Obukhov length defined by

$$L = -\frac{c_{pm} \rho_a \theta_a u_*^3}{kgH_g}. \quad (16)$$

In this model, the nondimensional functions come from Businger (1971) equations, and the analytical forms for the integral have been provided by Paulson (1970).

#### 4) Latent heat flux $E$

The computation of the latent heat flux  $E$  makes use of the Carlson and Boland (1978) formulation given by

$$E = A_m \rho_a I^{-1} (q_s(T_g) - q_a), \quad (17)$$

where  $q_s$  represents the saturation specific humidity,  $q_a$  the specific humidity at the surface layer, and  $A_m$  the moisture availability of the slab.

$$I^{-1} = ku_* \left[ \ln \left( \frac{ku_* z_a}{K_a} + \frac{z_a}{z_l} \right) - \psi_h \right]^{-1}, \quad (18)$$

where  $z_l$  is the depth of the molecular layer (0.01 m over land and  $z_0$  over water), and  $K_a$  is a background molecular diffusivity equal to  $2.4 \times 10^{-5} m^2 s^{-1}$ . While the roughness length  $z_0$  is specified over land, it is calculated over water as a function of friction velocity (Delson et al. 1971), expressed as

$$z_0 = 0.032 u_*^2 / g + z_{0c}, \quad (19)$$

where  $z_{0c}$  is a background value of  $10^{-4} m$ .

### c. Prediction for nocturnal regime

When the atmospheric stratification is stable and marginally unstable (mostly at night time) the model runs with the module defined as the nocturnal regime. In this regime a first-order closure scheme (K-theory) is used for the computation of turbulent fluxes in which the eddy coefficient  $K$  is defined as a function of Richardson number. The flux calculations at the 8 m surface layer follow the formulations which are based on Monin-Obukhov similarity theory.

There are three types of turbulent mixing in the surface layer of the PBL classified as the nocturnal regime. The determination of the type depends on the sign and magnitude of the bulk Richardson number  $R_{iB}$  defined by

$$R_{iB} = \frac{gz_a}{\theta_a} \frac{\theta_a - \theta_g}{V_a^2}, \quad (20)$$

where  $V_a$  is the scalar wind speed at the surface. The significance of the type-determination is that the nondimensional stability parameters are determined differently according to the types thus resulting in different amount of fluxes.

### 1) Stable type

When the bulk Richardson number  $R_{iB}$  is greater than the critical Richardson number  $R_{ic} = 0.2$ , the surface layer is assumed to be so stable that no turbulence exists. In this case the nondimensional stability parameters are set to zero and the frictional velocity and the surface heat flux are given by

$$u_* = u_{*0}, \quad (21)$$

$$H_g = \text{Max}\left(-c_p \rho_a k u_* T_*, -25 \text{Wm}^{-2}\right), \quad (22)$$

where  $u_{*0}$  is the background value,  $0.1 \text{m}^{-1}$  over land and zero over water.

### 2) Mechanical turbulence case

When the condition  $0 \leq R_{iB} \leq R_{ic} = 0.2$  is satisfied the turbulence in the surface layer is assumed to be mechanically driven. In this case the nondimensional stability parameters are given as follows:

$$\psi_m = \psi_h = -5 \left( \frac{R_{iB}}{1.1 - 5R_{iB}} \right) \ln \frac{z_a}{z_0}. \quad (23)$$

### 3) Forced convection case

In this case the surface layer is marginally unstable with the condition,  $R_{iB} \leq 0$  and  $|z_h/L| \leq 1.5$ , where  $z_h$  is the height of the PBL. In this model, this case is treated as a quasi-neutral case, thus the following approximations are used:

$$\frac{z_a}{L} = R_{iB} \text{ and } \psi_m = \psi_h = 0. \quad (24)$$

Now that the frictional velocity is given in accordance with the turbulent mixing type, the ground stress  $\tau_g$  can be calculated as

$$\tau_g = \rho u_*^2. \quad (25)$$

The surface fluxes are given as expressed in the slab model.

The prediction of variables is made after determining the eddy exchange coefficients, which are assumed to be the same among the coefficients for momentum, heat, and moisture:  $K_m = K_h = K_q$ . In this model, the K-coefficient derived by Blackadar (1976), who followed Mellor and Yamada's (1974) second order closure equations, is used as expressed by

$$K_m = K_0 + S_i (kl)^2 (R_c - R_i) / R_c, \quad (26)$$

where  $K_0$  is a background value (=1.0),  $R_c$  the critical Richardson number (=0.25),  $l$  a length that is presumed to characterize the turbulence containing energy, and  $S_i$  the vertical wind shear at  $i$ -th layer. The Richardson number  $R_i$  is defined as

$$R_i(z_i) = \frac{g}{\theta_{i-1/2}} \frac{\theta_{i+1/2} - \theta_{i-1/2}}{z_{i+1/2} - z_{i-1/2}}. \quad (27)$$

For the stability condition  $R_i > R_c$ , it is assumed that the shear-generated turbulence is suppressed by setting the value of  $K_m$  to  $K_0$ .

Now that the K-coefficients and the surface fluxes have been obtained, the predictions for the surface layer variables are given by

$$\frac{\partial \theta_a}{\partial t} = [K_{h1} (\theta_{3/2} - \theta_a) / (z_{3/2} - z_a) + H_g / (\rho c_p)] / z_1, \quad (28)$$

$$\frac{\partial q_a}{\partial t} = [K_{q1} (q_{3/2} - q_a) / (z_{3/2} - z_a) + Q_g / \rho] / z_1, \quad (29)$$

$$\frac{\partial u_a}{\partial t} = [K_{m1} (u_{3/2} - u_a) / (z_{3/2} - z_a) - \tau_g u_a / (\rho V_a)] / z_1 + f(v_a - v_{ga}), \quad (30)$$

$$\frac{\partial v_a}{\partial t} = \left[ K_{m1} (v_{3/2} - v_a) / (z_{3/2} - z_a) - \tau_g v_a / (\rho V_a) \right] / z_1 - f(u_a - u_{ga}), \quad (31)$$

where subscript  $a$  indicates the variable at the surface layer, first half layer and  $f$  represents the Coriolis parameter.

Above the surface layer the surface flux terms of the above surface prediction equations are substituted for fluxes at the bottom of each layer expressed in the same way as at the top of each layer. Then, an implicit diffusion scheme is utilized for the computation of turbulent flux terms.

*d. Prediction for free convection regime*

Under the strong solar heating associated with clear sky conditions in daytime, a super-adiabatic layer usually occurs in the lowest atmospheric layer. With that condition a buoyant plume model (Estoque, 1968) is suggested in such a way that as the plumes of hot air rise, mixing of heat, momentum, and moisture takes place at each level. In the Blackadar (1979) PBL, the vertical mixing is visualized as taking place between the lowest layer and each layer in the mixed layer, instead of between adjacent layers as in K-theory for the nocturnal regime in this model.

In the surface layer, the rates of change of the prognostic variables are given by

$$\frac{\partial u_a}{\partial t} = f(v_a - v_{ga}) - \left[ \frac{\tau_g u_a}{\rho V_a} - \bar{m} \sum_{i=2}^l (u_a - u_{i-1/2}) \Delta z \right] / z_1, \quad (32)$$

$$\frac{\partial v_a}{\partial t} = -f(u_a - u_{ga}) - \left[ \frac{\tau_g v_a}{\rho V_a} - \bar{m} \sum_{i=2}^l (v_a - v_{i-1/2}) \Delta z \right] / z_1, \quad (33)$$

$$\frac{\partial q_a}{\partial t} = \left[ Q_g - \bar{m} \sum_{i=2}^l (q_a - q_{i-1/2}) \Delta z \right] / (\rho z_1), \quad (34)$$

where, the index  $l$  represents mixing height and  $\Delta z$  is  $i$ -th layer depth. The mixing coefficient  $\bar{m}$  represents the fraction of mass exchange between any level and the surface layer per unit time. By applying heat energy conservation (Blackadar, 1978; Westphal, 1981) it is expressed as



$$\bar{m} = H_1 \left\{ \rho_a c_p (1 - \varepsilon) \int_{z_1}^{z_h} [\theta_a - \theta(z')] dz' \right\}^{-1}, \quad (35)$$

where  $\varepsilon$  is the entrainment coefficient which is the ratio of negative area to positive area. Following the studies by Tennekes (1975), Mahrt and Lenschow (1976), and Stull (1976) the value of 0.2 for the ratio is used in this model.  $H_1$  is the heat flux at the top of the surface layer which is an empirical equation derived by Priestley (1956) and expressed as

$$H_1 = \rho_a c_p z_1 (\theta_a - \theta_{3/2})^{3/2} \left\{ \left( \frac{2g}{27\theta_a} \right)^{1/2} \frac{1}{z_1} [z_1^{-1/3} - (2z_{3/2})^{-1/3}]^{-3/2} \right\}, \quad (36)$$

where  $z_1$  is the depth of the surface layer. Because the heat flux at the top of the surface layer is obtained by above equation, the potential temperature  $\theta_a$  in the surface layer is predicted by

$$\frac{\partial \theta_a}{\partial t} = -(H_1 - H_g) / (\rho_a c_p z_1) \quad (37)$$

For the variables above the surface layer, the prognostic equations are

$$\frac{\partial \alpha_i}{\partial t} = \bar{m} (\alpha_a - \alpha_i), \quad \alpha = \theta, q, \quad (38)$$

$$\frac{\partial \alpha_i}{\partial t} = w \bar{m} (\alpha_a - \alpha_i), \quad \alpha = u, v, \quad (39)$$

where the  $w$  is the weight function for reducing mixing near the top of the mixed layer given by

$$w = 1 - z / z_h. \quad (40)$$

In the free convection regime the nondimensional stability parameters are given as follows

$$\psi_h = -3.23 \left( \frac{z_a}{L} \right) - 1.99 \left( \frac{z_a}{L} \right)^2 - 0.474 \left( \frac{z_a}{L} \right)^3, \quad (41)$$

$$\psi_m = -1.86\left(\frac{z_a}{L}\right) - 1.07\left(\frac{z_a}{L}\right)^2 - 0.249\left(\frac{z_a}{L}\right)^3. \quad (42)$$

In this model  $z_a/L$  is approximated using an explicit function of  $R_{iB}$ ,

$$\frac{z_a}{L} = R_{iB} \ln \frac{z_a}{z_0}. \quad (43)$$

For the variables above the mixed layer the nocturnal module is used again.

#### *e. Computational details*

At every time step the diagnostic part of the model is computed ahead of the prediction. The bulk Richardson number  $R_{iB}$  and the value of  $z_h/L$  are checked to determine the atmospheric regime. Then, according to the regime, the nondimensional stability parameters,  $\psi_m$  and  $\psi_h$  are computed. Then the friction velocity  $u_*$  and friction temperature  $T_*$  are obtained. Next, the terms in the right hand side of the surface energy budget equations are calculated and then as the final diagnostic parameters, the eddy exchange coefficients (K-coefficients) at each level are calculated. The prediction of the variables is in accordance with the regime determined in the preceding diagnostic part.

A Centered-Time and Centered-Space (CTCS) finite-difference approximation is used to express the time and space derivatives for the time integration of the predictive equations. To remove the computational mode which is the characteristic of the CTCS finite-difference, a frequency filter for time integration (Asselin, 1972) is applied every time step. To insure computational stability a small time step,  $\Delta t$ , of 10 s is used except for the surface layer. In the surface layer a shorter time step is required due to the smaller depth of the layer ( $\Delta z = 8m$ ). In this model 0.5 s is chosen.

### 3. Experiment design

Understanding the sensitivity of the 1-d model to surface characteristics is fundamental to simulations in this study and comprises the investigation of the impact of inhomogeneity.

In accordance with that purpose, model input data were prepared and the simulations were designed. The 1-d PBL model experiments consists of three simulations: 1) homogeneous run (HO1D), 2) inhomogeneous run (IN1D), and 3) climatological run (CLIM).

*a. Specification of surface characteristics*

First, we investigated land surface cover types in the HOU area using the 30-m resolution land cover data produced by Global Environment Management (GEM), Inc. using LANDSAT satellite imagery and ancillary data sets. The land cover data is image data with each pixel representing one of 10 land cover types of 30 m size. The GEM classified the land covers in the HOU area into 9 types: 1) broad leaf forest, 2) coniferous forest, 3) mixed forest, 4) grass, 5) wet land, 6) water body, 7) barren land, 8) roads, and 9) impervious. In this study we assumed that the impervious land type can be divided into two types, one with flat surfaces such as parking lot and the other with structures such as buildings.

Figure 14a shows the distribution of land cover types in the HOU area which is the area of interest in this study. Notice that the area is centered at HDT and corresponds to the HOU area defined in the previous chapter. Figure 14b is suggested to compare the surface inhomogeneity over the HOU with those of surrounding areas. A greater variability of surface characteristics over HOU, particularly with respect to impervious surfaces as a significant fraction of the land cover, can be seen from the figure. Figure 15 illustrates fractional area coverage of each land cover type in the HOU area of interest.

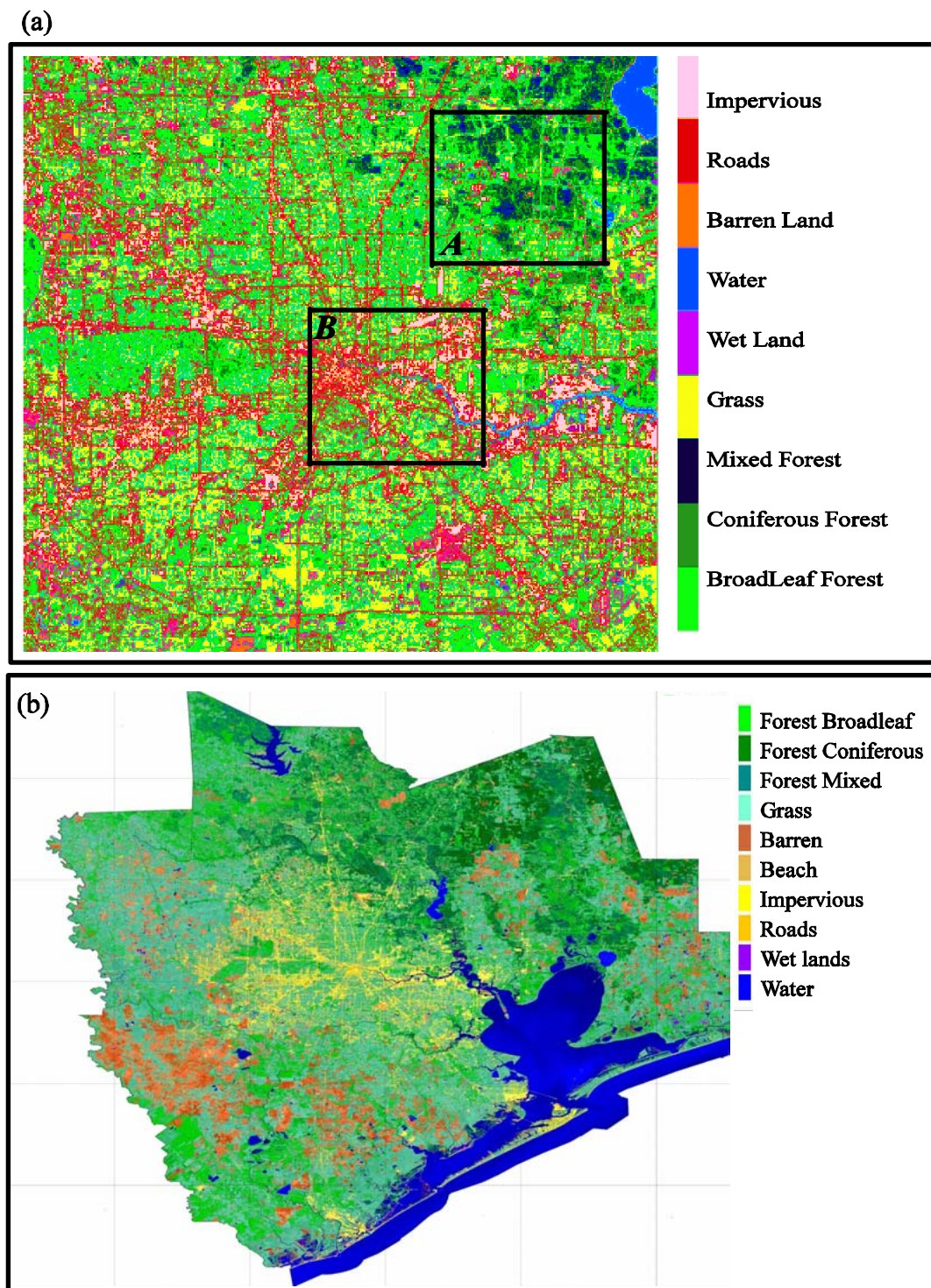


Figure 14. (a) Distribution of 10 land cover types in the HOU area. Boxes A and B designate forest and downtown areas, respectively, and (b) land cover classification of the eight counties (Brazoria, Chambers, Fort Bend, Galveston, Harris, Liberty, Montgomery, and Waller) around Houston, Texas.

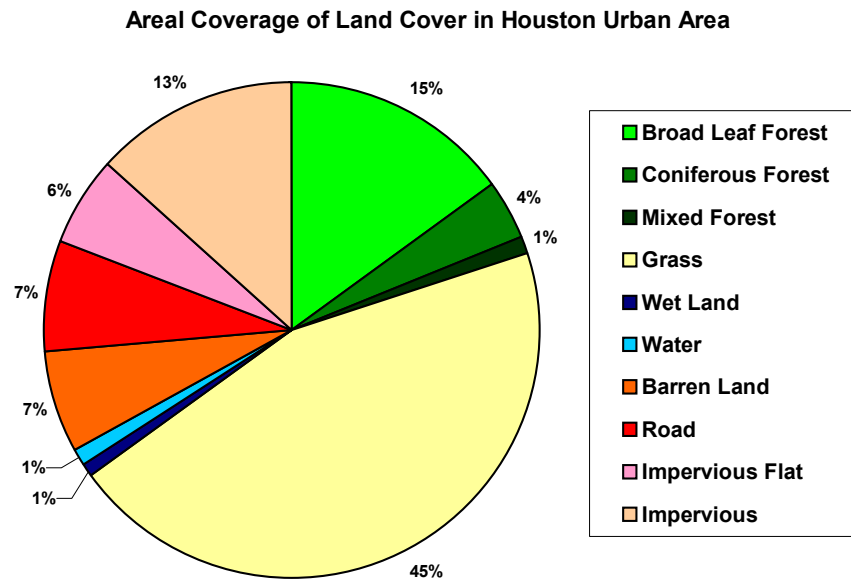


Figure 15. Graph indicating the Fractional Area Coverage (FAC) for each of 10 land cover types averaged in the HOU area.

Secondly, model surface parameter values are specified for each of 10 land cover types. The five model surface parameters are soil moisture availability (SLMO), albedo (ALBD), roughness length (SFZ0), surface emissivity (SFEM), and soil heat capacity (CAPG). The specification of the parameter values is determined from the range of parameter values available from several sources such as the MM5 input table, Oke (1987), and others. Table 3 lists the specified surface parameter values for each of 10 land cover types. Those parameter values are fundamental to this 1-d model study.

Table 3. Specified model surface parameter values for each of 10 land cover types. The abbreviated column headings are explained in the text.

Land Cover Type	HOU FAC	SLMO	ALBD (%)	SFZO (m)	SFEM	CAPG (J/K/m**3)
BroadLeaf Forest	0.15	0.58	11.38	1.6	0.95	2955700.
Coniferous Forest	0.04	0.35	9.81	1.3	0.95	2364560.
Mixed Forest	0.01	0.35	7.79	1.3	0.94	2364560.
Grass	0.45	0.17	16.00	0.2	0.92	1773420.
Wet Land	0.01	0.69	14.30	0.3	0.95	3546840.
Water	0.01	1.00	12.77	0.01	0.98	3546840.
Barren Land	0.07	0.02	21.37	0.15	0.85	1182280.
Roads	0.07	0.	23.76	0.001	0.95	1714306.
Impervious Flat	0.06	0.	25.20	0.01	0.69	754549.
Impervious	0.13	0.	25.20	0.7	0.69	754549.
<b>Area-Weight Mean</b>		<b>0.20</b>	<b>17.6</b>	<b>0.5</b>	<b>0.88</b>	<b>1773422.</b>

*b. Distribution of surface characteristics*

The area of interest (Fig. 14a) is segmented into 121 grid boxes such that each grid box is 4 km by 4 km. Actually, the area of interest had been determined so as to consist of 11 by 11 4-km grids centered at HDT. The reason for this is that the 1-d model is assumed to be a 4 km by 4 km atmospheric column, and the MM5 target domain of this study has 4 km grid spacing.

Within each grid box fractional area coverage (FAC) for each of 10 land cover types was computed by counting the 30m-sized pixels from the GEM image files. The FAC for each land type was obtained by dividing the counted pixel numbers by total number of pixels within the grid box. The FAC for 10 land types in the area of interest is illustrated in Figure 16 with contours.

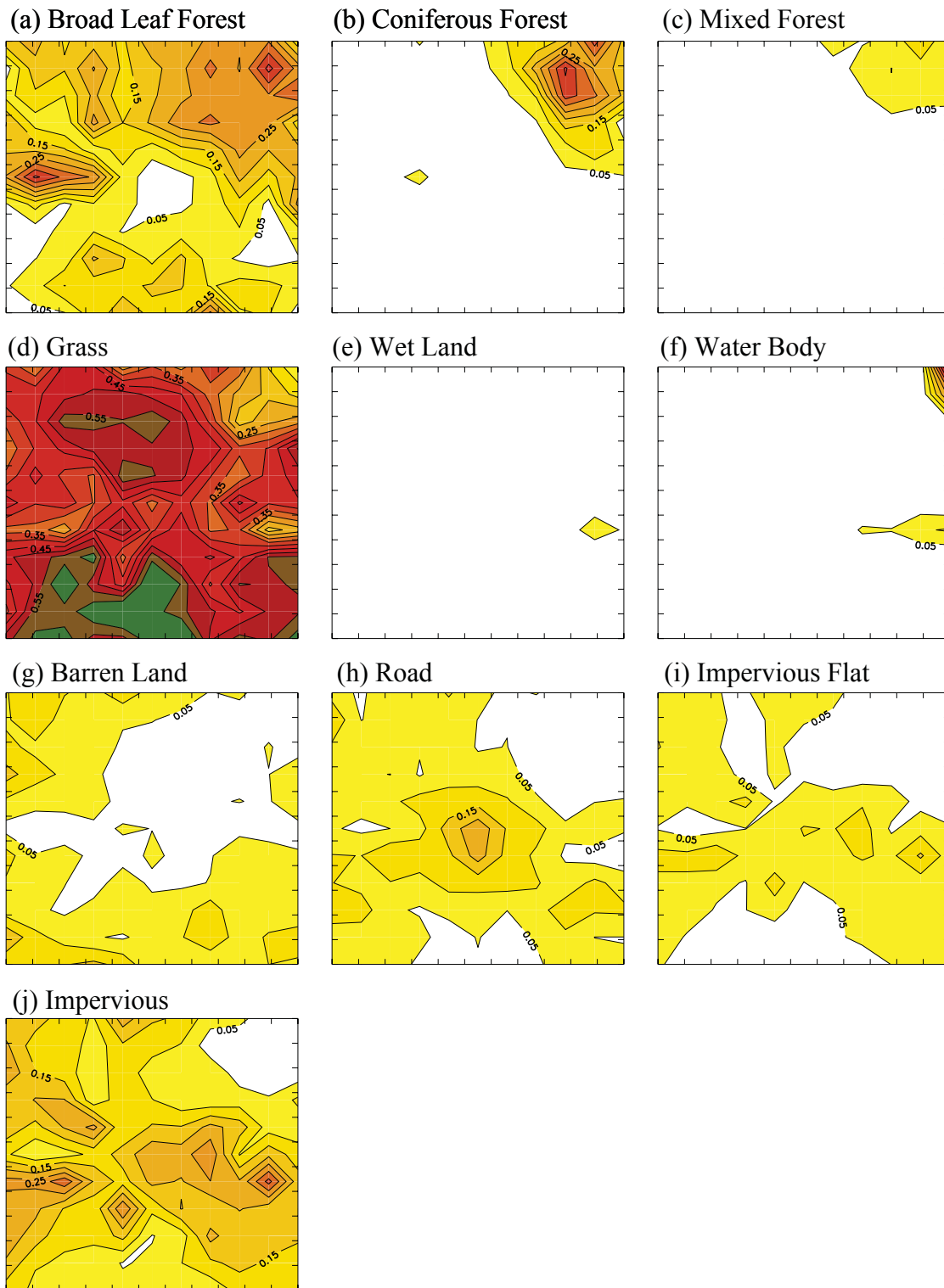


Figure 16. Distributions of Fractional Areal Coverage (FAC) of (a) broad leaf forest, (b) coniferous forest, (c) mixed forest, (d) grass, (e) wet land, (f) water body, (g) barren land, (h) roads, (i) impervious flat, and (j) impervious structure within 4 km grids in the HOU area.

Mean surface parameter values of each grid box were obtained by area-weighted average of 10 land types,

$$\bar{p}_j = \sum_{i=1}^{10} (FAC_i \times P_{i,j}), \quad (44)$$

where  $\bar{p}_j$  is mean value of  $j$ -th surface parameter,  $FAC_i$  is fractional area coverage of  $i$ -th land cover type, and  $P_{i,j}$  represents the surface parameter value specified for  $i$ -th land cover type and  $j$ -th surface parameter. Distributions of the 4 km grid-mean and within-grid standard deviation values of surface parameters over HOU are illustrated in figures 17 and 18, respectively. For all the parameters, the greater grid-mean standard deviations imply a broader distribution of each surface parameter within grids over the areas.

*c. Other aspects of the simulations*

The same initial atmospheric conditions were used for all simulations involved in this study. Standard MM5 output files were used to extract the initial model soundings. First, the MM5 outputs were obtained in the HOU area corresponding to Figure 14. Then, the MM5 sigma level data were vertically interpolated into 1-d model height levels. So as to get one initial sounding the extracted soundings on the 4-km grid boxes in the HOU area were horizontally averaged. The initial soundings of potential temperature, specific humidity, u- and v-wind components are presented in Figure 19. The initial time is 0000 UTC on August 30, 2000.

In order to give the same forcing to all simulations, two forcing terms, shortwave radiation and downward longwave radiation, and surface pressure were prescribed at every model time step. Those terms are assumed to be almost unaffected by the surface inhomogeneity within the 4-km grid box. In the same way as for the initial soundings, those prescribed terms were obtained from the MM5 outputs at one hour interval for 24 forecast hours, then interpolated linearly to the 1-d model time steps. The forecast length for all simulations is 24 hours.



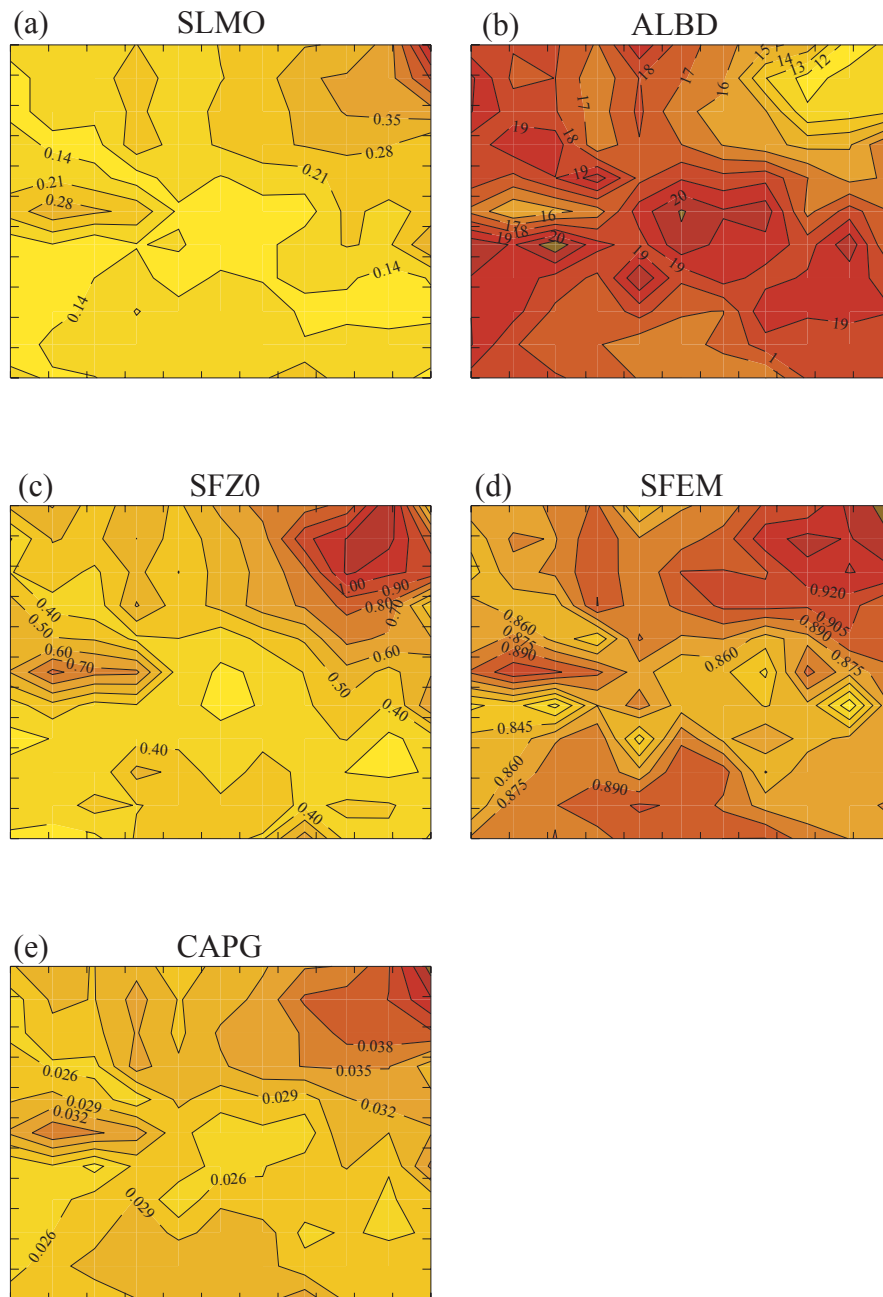


Figure 17. Distribution of 4 km grid-mean surface parameter values in the HOU area: (a) SLMO, (b) ALBD (%), (c) SFZ0 (m), (d) SFEM, and (e) CAPG ( $\times 3.293 \times 10^6$  J/K/m<sup>3</sup>).

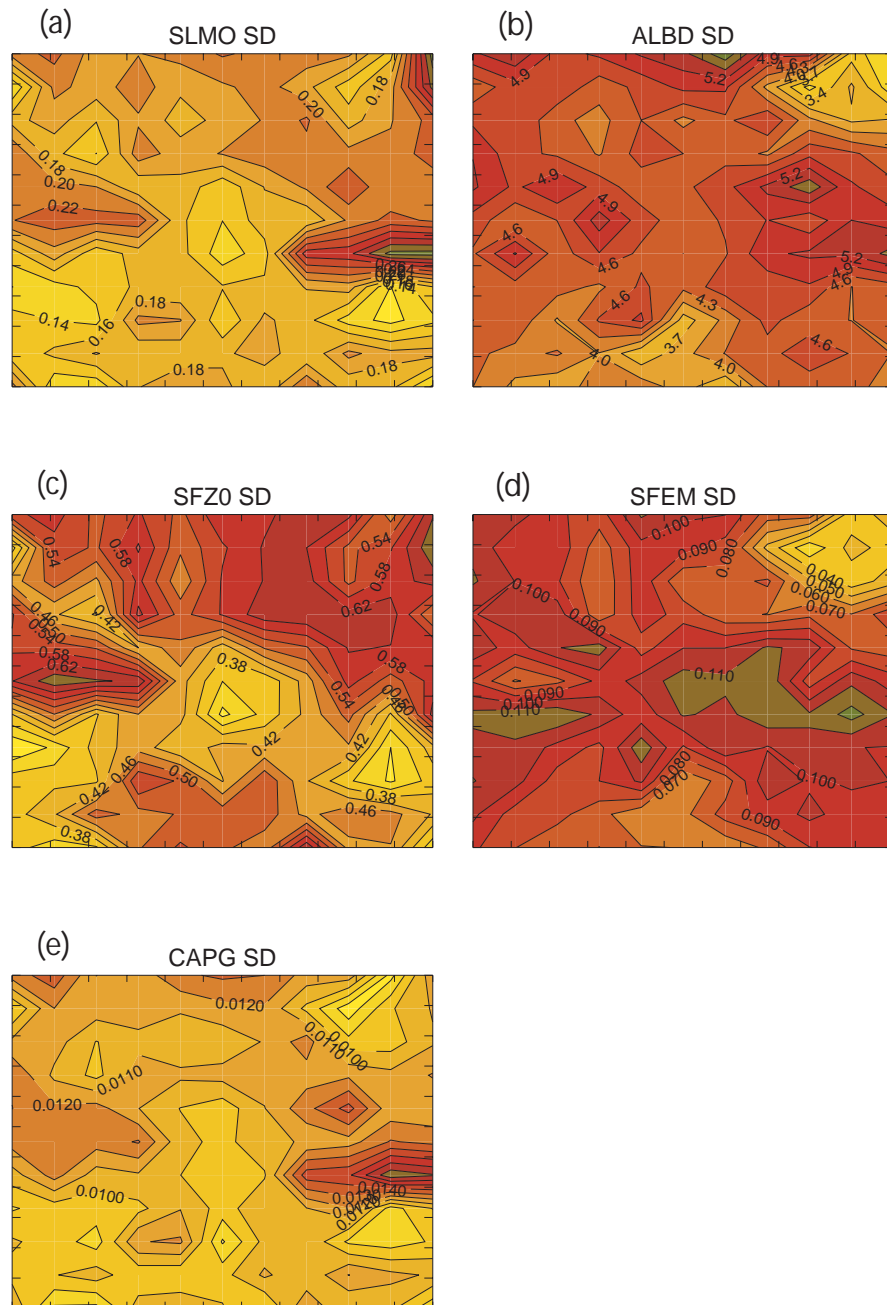


Figure 18. Distribution of the 4 km grid standard deviations of each surface parameter value in the HOU area: (a) SLMO, (b) ALBD (%), (c) SFZ0 (m) (d) SFEM, and (e) CAPG ( $*3.293e+6$  J/K/m<sup>3</sup>).

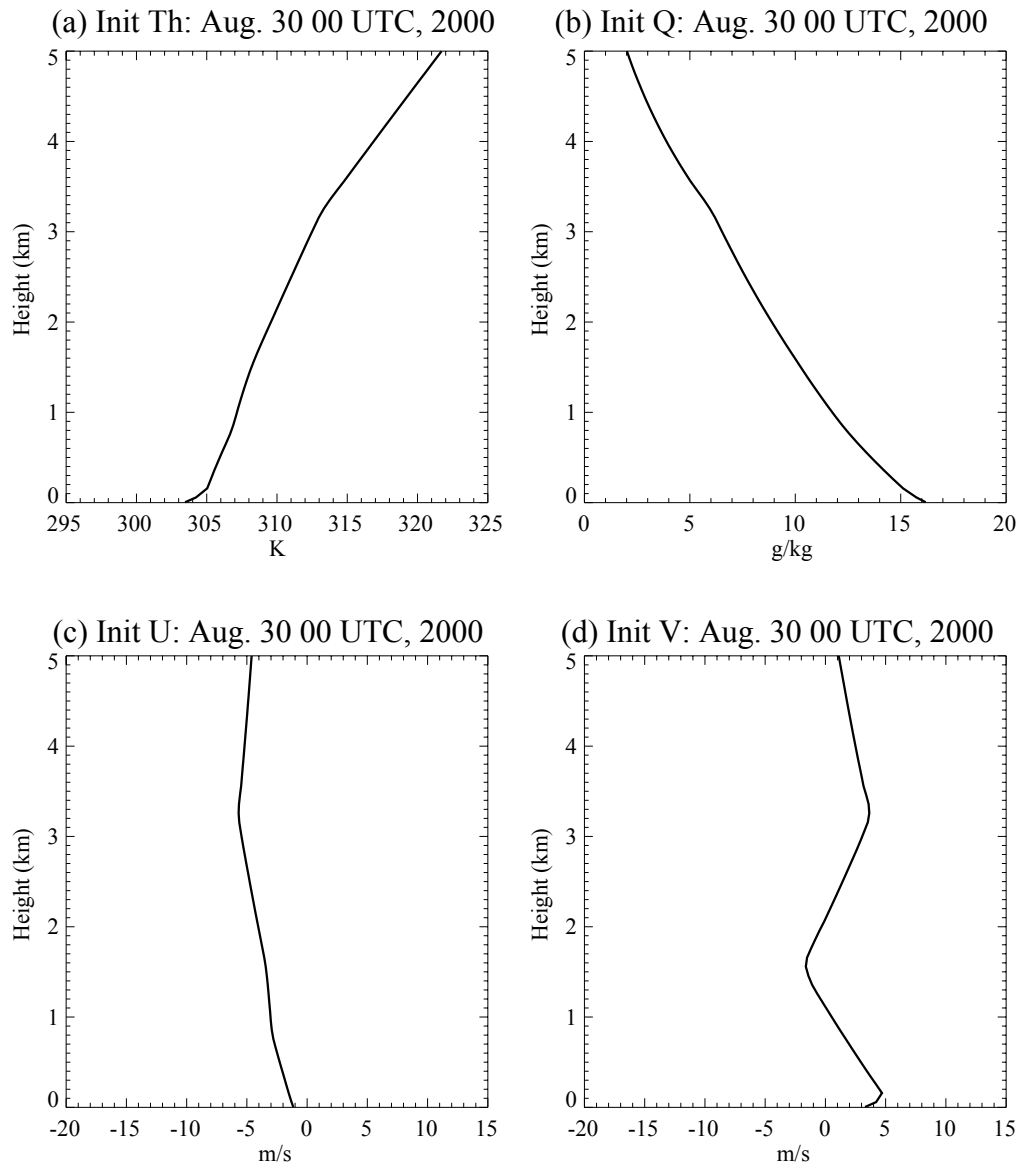


Figure 19. Profiles of (a) potential temperature, (b) specific humidity, (c) u-wind, and (d) v-wind used as the atmospheric initial conditions of the 1-d PBL simulations.

Upper boundary is fixed and no flux exchanges are allowed between the upper boundary and the layer below it by setting the vertical exchange coefficient with zero value at the highest full level.

There exist two uncertainty problems in analyzing the inhomogeneity impact from the 1-d simulations. First, the substrate temperature can not be determined from the 1-d model of this study since no soil model is coupled. Therefore, the substrate temperature needs to be prescribed as done for other variables mentioned above. Unlike the shortwave radiation, downward longwave radiation, and surface pressure, the substrate temperature is directly related to surface inhomogeneity via the soil heat capacity as expressed in Eq. (11). Because of that the subgrid-scale substrate temperature is necessary in order to compute subgrid-scale ground heat flux relevantly. However, the subgrid-scale substrate temperature is not available from the MM5 output. Therefore, we simplified the 1-d model such that the ground heat flux difference between the inhomogeneous and homogeneous runs is avoided. By that it is expected that the uncertainty of the inhomogeneity impact caused by the subgrid-scale ground heat flux might be avoided as well. During the integration the substrate temperature is kept 2 degree K lower than the slab (ground) temperature for both the inhomogeneous and homogeneous simulations. Then, since the area-weighted grid-mean of the subgrid-scale heat capacity ( $C_g$ ) of the inhomogeneous run is equal to the homogeneous run, no difference of ground heat flux is produced between the inhomogeneous and homogeneous runs. Preliminary simulations indicated that, on average, the homogeneous run with the 2 K lower substrate temperature produces ground temperature lower than the homogeneous run with the MM5-prescribed substrate temperature by about -1.0 K and about -0.5 K in the nighttime and daytime, respectively. Therefore, the inhomogeneity impact is not expected to be affected significantly.

Second, the geostrophic wind components in the momentum equation (3) and (4) can not be calculated in the 1-d model. Therefore, either geostrophic balance assumption or the prescribed geostrophic winds obtained from the MM5 outputs need to be used. The problem with that is that an accurate geostrophic wind is rarely possible to obtain from either the actual wind or pressure outputs of the MM5. According to Zhang and Anthes (1982), geostrophic wind is critical to the performance of an 1-d PBL model in simulating a realistic

atmospheric PBL. This implies there can be lots of uncertainty of the inhomogeneity impacts when the geostrophic wind is not accurately prescribed in the 1-d simulations. To avoid this problem we assumed that the Coriolis and pressure gradient forces are always balanced, thus contributing no forcing to the momentum tendency by those forces. Therefore, momentum changes in the 1-d PBL simulations of this study are enabled by only turbulent vertical mixing of momentum expressed by the last terms in Eqs. (3) and (4). This made it simpler to interpret the inhomogeneity impacts produced by the inhomogeneous 1-d simulation. That is, the inhomogeneity impacts, in particular, on momentum are made attributable to the surface inhomogeneities because the turbulent vertical mixing of momentum is directly affected from the inhomogeneities.

As presented in Table 4, the assumption of this study does not make simulation results significantly different from those of simulations without the assumption. The results in Table 4 were obtained from three homogeneous 1-d simulations with different representation of geostrophic winds: (a) idealized only in the surface layer, (b) fixed during the entire simulation at all heights, and (c) idealized in the surface layer and fixed at all heights above the surface layer. In (a), the geostrophic winds of the surface layer are defined as blowing 30° and 60° degree right of actual winds with the geostrophic wind speeds being given by a factor of 1.16 and 1.56 of the actual wind speeds under the conditions of stable and convective stability regimes, respectively (G1PBL). In (b), the geostrophic winds were fixed with initial actual winds during the entire simulation (G2PBL). In (c), the method (a) was applied in the surface layer and the method (b) was applied above the surface layer (G3PBL). The above simulations were conducted with the same initial conditions of this study using HOU-area-averaged surface parameter values.

Table 4. Differences of surface wind speed between the homogeneous 1-d simulation with idealized geostrophic winds (G1PBL, G2PBL, and G3PBL defined in the text) and the homogeneous 1-d with the balance assumption (BAPBL) during the stable (0400 UTC – 1400 UTC) and convective (1600 UTC – 2300 UTC) regimes.

	Stable	Convective
<b>G1PBL – BAPBL</b>	-0.005 ms <sup>-1</sup> (-0.3 %)	0.003 ms <sup>-1</sup> (0.1 %)
<b>G2PBL – BAPBL</b>	0.002 ms <sup>-1</sup> (0.1 %)	-0.7 ms <sup>-1</sup> (-23 %)
<b>G3PBL – BAPBL</b>	0.002 ms <sup>-1</sup> (0.1 %)	-0.7 ms <sup>-1</sup> (-23 %)
<b>Mean actual wind speed of BAPBL</b>	1.7ms <sup>-1</sup>	2.9ms <sup>-1</sup>

Later, the sensitivity of the inhomogeneity impact to wind speed will aid in understanding what the error in wind speed produced by the balance assumption implies for the resulting inhomogeneity impacts produced by inhomogeneous runs with the model assumption.

Both the homogeneous and inhomogeneous simulations were run at each grid in the HOU area shown in Figure 14a using the surface characteristics within each grid box. In this study, the homogeneous simulation means that the 1-d model was implemented with homogeneous representation of surface characteristics. That is, the area-weighted mean of surface parameter values calculated by Eq. (44) at each grid was used in the homogeneous simulation at the grid. Hereafter, we call the 1-d homogeneous and 1-d inhomogeneous simulations as HO1D and IN1D, respectively.

*d. Methodology of inhomogeneous simulation (IN1D)*

In the IN1D a grid box consists of 10 land cover types regrouped from subgrid-scale land patches of 30m size, all of which belong to at least one of 10 land cover types listed in Table 3. The size of each subgrid land cover is imagined to be proportional to its fractional area coverage (FAC) within the grid box. Accordingly, the atmospheric surface layer was

designed to have 10 subgrids corresponding to the subgrid land covers. The atmospheric layers above the surface layer were treated as being horizontally homogeneous.

At each subgrid of the 10 land cover types within a grid box, prediction and diagnosis of model variables are performed independently during the entire integration time. The surface parameter values listed in Table 3 are used for each subgrid. The grid mean of predicted and diagnosed model variables are computed by area-weighted average as expressed by Eq. (44) at every time step. The model processes above the surface layer are forced to sense the weight-averaged grid mean values of surface and ground. For comparative study with HO1D results the grid-mean model values were output.

This methodology is similar to Avissar and Pielke (1989) in that subgrid-scale surface forcings are computed independently, but is different in that subgrid-scale atmospheric forcings are expressed for the first atmospheric layer. Characteristic features of the inhomogeneous 1-d simulations are summarized in Table 5.

#### 4. Comparative study using the simulation results

We regard the difference between the IN1D and HO1D results as the impact induced by introducing surface inhomogeneity in the computation of model variables. Also, the impact can be interpreted as potential errors which any model could have when it does not include subgrid-scale parameterization of surface characteristics in the model.

In this study we compute the difference by subtracting HO1D from IN1D. Unless otherwise stated the difference means IN1D minus HO1D. The difference was calculated for all 121 grids in the area of interest (Fig. 14a). The model outputs were at 2-minute intervals for the surface variables and at 1-hour intervals for the variables above the surface layer.

##### *a. Distribution of time-averaged variable difference in HOU area*

We examine the differences separately during the stable regime in nighttime and the convective regime in daytime. In order to determine time ranges representative of both the stable and convective regimes from the 121 simulations of each of the IN1D and HO1D, initiation and end time of convective regime were examined and listed in Table 6.

Table 5. Characteristic features of inhomogeneous 1-d simulations.

	<b>Features of inhomogeneous land surface runs</b>	
	<b>Flux calculation</b>	<b>Exchange of flux between levels</b>
<b>Surface Layer</b>	Surface similarity following nondimensional gradient expression of Paulson (1970)	<ul style="list-style-type: none"> <li>- Top: Area-weighted grid-mean of subgrid fluxes and time mean of short time steps</li> <li>- Bottom: Subgrid-scale fluxes</li> </ul>
<b>Stable upper layers</b>	K-theory (Blackadar, 1976)	<ul style="list-style-type: none"> <li>- At the surface layer top: area-weighted grid-mean of subgrid-scale diffusivities and time mean of short time steps</li> <li>- Other layers: Grid-mean diffusivities</li> </ul>
<b>Unstable mixed layers</b>	Plume model (Blackadar, 1976, 1978) following Priestley's (1956) expression of heat flux at surface layer top	<ul style="list-style-type: none"> <li>- Heat flux at the surface layer top: area-weighted grid-mean of subgrid heat flux and time mean of those of short time steps</li> <li>- Positive area: area-weighted and time mean of subgrids</li> <li>- Mixed layer height: estimated using the area-weighted surface layer potential temperature and grid-mean profile of potential temperature</li> </ul>
<b>Stability regime determination</b>	Based on the grid-mean bulk Richardson number estimated from area-weighted grid-mean variables of ground potential temperature, surface layer potential temperature, and surface layer wind speed	
<b>Ground temperature</b>	Blackadar (1979) slab model is used to predict subgrid-scale slab (ground) temperatures. The subgrid substrate temperatures are forced to remain 2 K lower than those of subgrid slabs at every model time step.	
<b>Subgrid-scale predictive variables</b>	Wind components, specific humidity, and potential temperature at the surface layer and ground (slab) temperature	
<b>Subgrid-scale diagnostic variables</b>	<ul style="list-style-type: none"> <li>- Sensible and latent heat fluxes at the top and bottom of the surface layer, reflected short-wave radiation, absorbed and emitted long-wave radiation, and ground heat flux at the ground.</li> <li>- Positive area of buoyant subgrid-scale air parcel.</li> <li>- Diffusivity at the surface layer top.</li> </ul>	



Table 6. Initiation and end time of free convective regime from 121 simulations of IN1D and HO1D indicated by number of hours UTC into the integration.

	Initiation of free convection			End of free convection		
	Earliest	median	Latest	Earliest	Median	Latest
IN1D	14.12	14.37	15.57	23.50	24.00	24.00
HO1D	13.97	14.27	15.87	23.17	23.63	23.83

In general the IN1D reached the initiation time of free convection a few minutes later and maintained the regime longer than the HO1D (IN1D maintained the free convection regime until the end of forecasting time, 2400 UTC). This implies that the IN1D ground surface (slab) is heated and cooled slower following increase and decrease of solar radiation in the early and late afternoon, respectively. In order that the IN1D and HO1D simulations are comparable, time ranges for both regimes were determined so that different regimes are not concurrent in each time range. The selected two time ranges are from 0400 UTC to 1400 UTC and from 1600 UTC to 2300 UTC for stable and convective regimes, respectively.

The differences (IN1D – HO1D) were averaged in time from 2-minute interval outputs. The variables to be examined include ground temperature, 4m potential temperature, 4m wind speed, 4m specific humidity, sensible heat flux, and latent heat flux. Although the output from each 1-d simulation is mapped onto its corresponding location in the Houston area to give a sense of geographical variations, there is no advection or other communication of information between grid points.

#### 1) Stable regime

Figure 20 illustrates the difference of time-averaged fields in the HOU area for the stable regime in nighttime (0400 UTC – 1400 UTC). In general, due to weak radiation surface forcing during the stable nighttime, the inhomogeneity impacts are small.

Time-averaged ground temperatures decreased by about  $-0.4$  K in most parts of the area with maximum decrease of about  $-1.2$  K occurring around Houston Downtown (HDT) (Fig. 20a). This implies that more energy is escaping from the ground in the IN1D simulations.

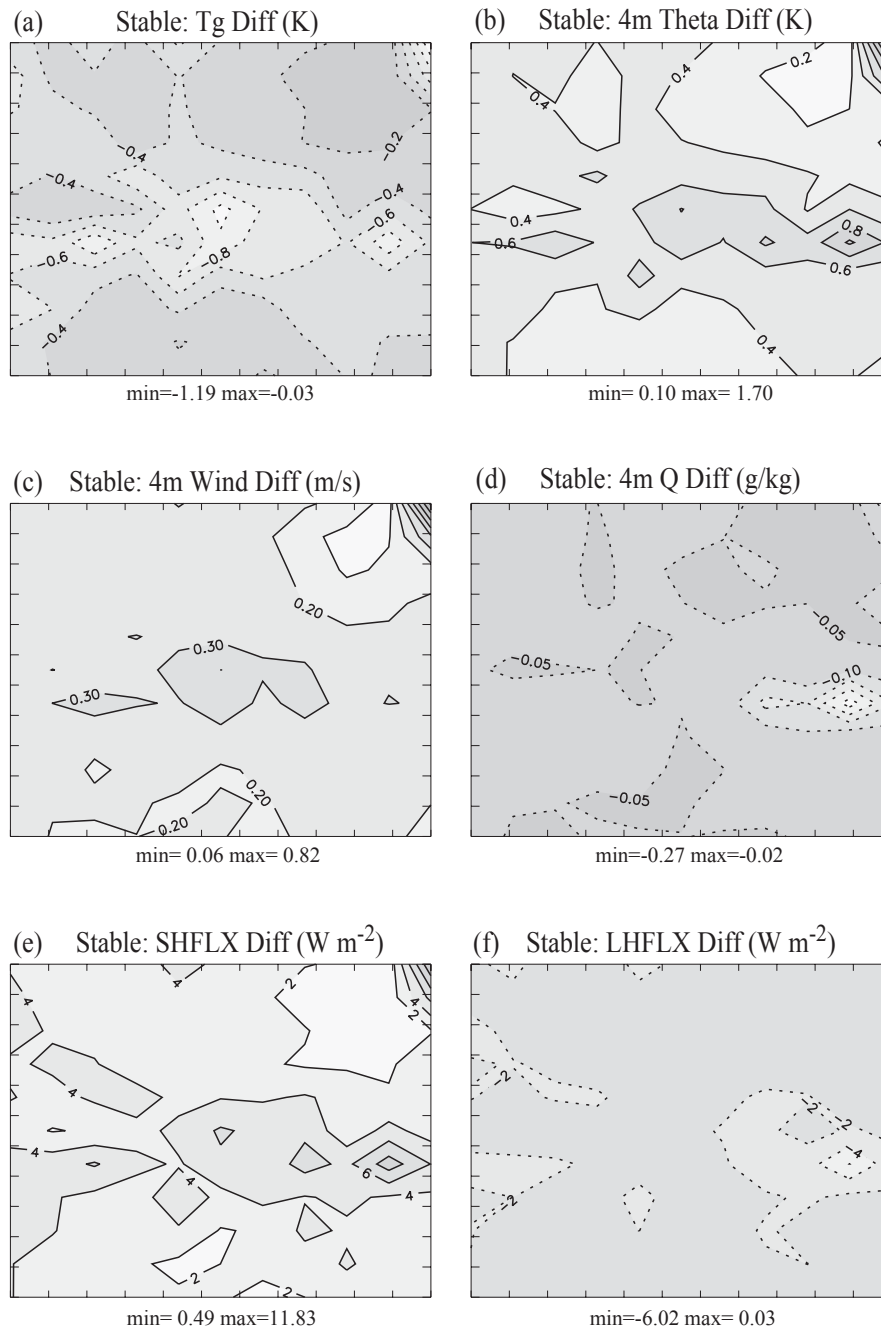


Figure 20. Distribution of the stable regime (0400 UTC - 1400 UTC) time-averaged differences (IN1D - HO1D) of (a) ground temperature, (b) 4m potential temperature, (c) 4m wind speed, (d) 4m specific humidity, (e) sensible heat flux, and (f) latent heat flux in HOU. Contour units are in each figure title.

Local maximum decreases around HDT and in the northeast corner of the HOU correspond to the areas in which roads and water bodies dominate, respectively (Fig. 16f and 16h). The area in which coniferous forest dominates (Fig. 16b) exhibited a local minimum decrease.

Time-averaged 4m potential temperatures showed increases of 0.4 K to 0.6 K in most areas (Fig. 20b) with a local maximum increase near central eastern boundary being coincident with the local maximum of impervious area coverage (Fig. 16j) and high standard deviation of soil moisture availability and emissivity (Fig. 18a and 18d). The local maximum in the northeast corner corresponds to relative dominance of water bodies (Fig. 16f) and high standard deviation of soil moisture availability and roughness (Fig. 18a and 18c). A local minimum increase is indicated in the northeast areas with local maximum coverage of coniferous forest (Fig. 16b) and low standard deviation of soil moisture availability (Fig. 18a). The increase of 4m potential temperature is indicative of positive biases of sensible heat flux of the IN1D simulations compared to the HO1D simulations.

Time-averaged 4m wind speed increased by about  $0.2 \text{ ms}^{-1}$  to  $0.3 \text{ ms}^{-1}$  in most area suggesting increased momentum flux in the surface layer of the IN1D simulations (Fig. 20c). Relatively smaller increase of the wind speed is indicated in northeast areas with relatively dominant coniferous forest (Fig. 16b) and lower standard deviation of soil moisture availability (Fig. 18a).

Time-averaged 4m specific humidity does not show a significant impact, with a slight decrease in most area (Fig. 20d). However, despite the insignificance, the decrease implies that latent heat flux of the IN1D became negatively-biased compared to the HO1D simulations. Relatively greater negative impact is indicated in the areas near the central eastern boundary with local maximum coverage of impervious (Fig. 16j) and high standard deviation of soil moisture availability and soil heat capacity (Fig. 18a and 18e).

Time-averaged sensible heat flux increased by about  $2 \text{ Wm}^{-2}$  to  $4 \text{ Wm}^{-2}$  in most area (Fig. 20e). Because positive sensible heat flux is directed toward the surface layer the increase of sensible heat flux is energetically consistent with the 4m temperature increase and ground temperature decrease mentioned above. As indicated in Figures 20a, 20b, and 20e, those impact patterns are similar to one another among the ground temperature, 4m potential

temperature, and sensible heat flux. Thus, local maximum and local minimum increases of the sensible heat flux correspond to local maximum magnitude of impacts of the 4m potential temperature and ground temperature.

The time-averaged latent heat flux slightly decreased by about 0 to  $-2 \text{ Wm}^{-2}$  in most areas (Fig. 20f). It is inferred that negative impacts on the ground temperature acted to reduce the saturated specific humidity of the ground, thus reducing the latent heat flux. In turn, the reduced latent heat flux would help in reduced surface layer specific humidity too. Even though the impact is negligible the negative impact is physically consistent with the sign of decrease in 4m specific humidity.

In general, even though the inhomogeneity impacts in the stable regime are small, the impacts exhibited consistency in sign and spatial variability in the HOU area. In summary, the inhomogeneity effects are 1) to decrease ground grid-mean temperature and 2) to increase surface layer grid-mean temperature by 3) increasing sensible heat flux into the surface layer, 4) to decrease surface layer grid-mean specific humidity induced by 5) decreasing latent heat flux, and 6) to increase momentum flux into the surface layer.

The inhomogeneity impacts involve many factors that are nonlinearly connected with one another, and those factors are quite variable depending on fractional area coverage (FAC) of each subgrid of 10 land types within a grid. Therefore, it is difficult to find a general explanation on the spatial variability of the impacts. However, as explained above, local minima and maxima of the impacts seem to be associated with relative dominance of certain land cover types and standard deviation of certain surface parameter values in the local area.

Maximum impacts occurred in the area where roads, impervious, and water bodies constitute relatively larger portion of the land cover compared to other areas. The roads are distinguished from other land types by zero soil moisture availability and smallest roughness length of 0.001 m. The impervious has smallest thermal inertia of the slab along with zero soil moisture availability. The water bodies are unique with 100 % soil moisture availability and greatest thermal inertia. Minimum impacts occurred in the area where coniferous forest is relatively dominant. The coniferous forest has a large roughness length of 1.3 m which is second to broad leaf forest of 1.6 m among the 10 land types. Intuitively, it makes sense that the areas with relatively larger portion of subgrids of extreme surface parameter values

exhibited maximum and minimum inhomogeneity impacts. Physical explanation will be provided in another section.

## 2) Convective regime

Figure 21 illustrates time-averaged difference fields in the HOU area for the convective regime in daytime (1600 UTC – 2300 UTC). Due to strong solar radiation the impacts are intensified for the sensible and latent heat fluxes and ground temperature. However, due to compensation of the fluxes at surface layer top, the impacts on surface layer variables are not intensified as much, but rather mitigated except for the area with relative dominance of impervious (structure).

Time-averaged ground temperature increased by up to about 4 K around HDT indicating increased energy flux into the slab or decreased energy flux out in IN1D simulations (Fig. 21a). As in the stable regime, the maximum and minimum impacts correspond to the areas in which roads and coniferous are relatively dominant, respectively (Figs. 16b and 16h).

Time-averaged 4m potential temperature resulted in very little increase, less than 0.2 K in most HOU areas (Fig. 21b) except for the small area of impervious local maximum near the central eastern boundary (Fig. 16j). Even a small decrease rather than an increase is indicated in some areas. In spite of the increased difference of sensible heat flux, which is greater by an order of magnitude compared to the stable regime (Fig. 21e), the impacts on potential temperature are mitigated compared to the stable regime. As will be clarified later, this can be attributed to the sensible heat flux at the surface layer top which compensates for the increase.

Time-averaged 4m wind speed (Fig. 21c) also showed a slightly lower increase of about  $0.1 \text{ ms}^{-1}$  in most areas compared to the stable regime except for the area of impervious local maximum. Inhomogeneity reduced the time-averaged specific humidity (Fig. 21d) in most areas except for slight increases in the areas of the roads and coniferous forest. In contrast to

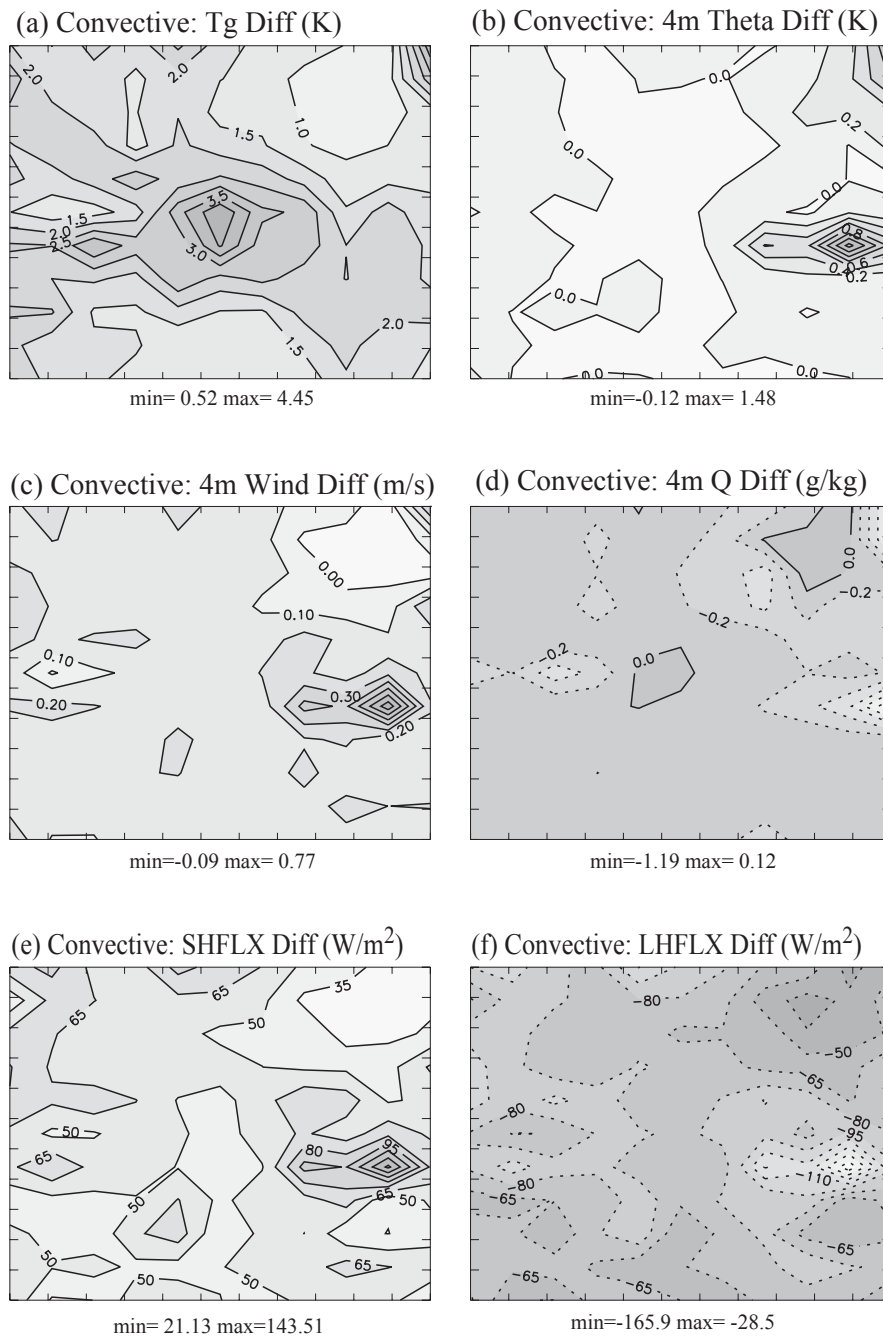


Figure 21. Same as Figure 20 but for the convective regime between 1600 UTC and 2300 UTC.

the 4m temperature and wind speed, the impacts are enhanced compared to the stable regime.

The inhomogeneity impacts on sensible and latent heat fluxes are both enhanced by more than an order of magnitude from those of stable regime as illustrated in figures 21e and 21f. The differences of the time-averaged sensible heat flux range from a minimum of  $21 \text{ Wm}^{-2}$  to a maximum of  $143 \text{ Wm}^{-2}$ . The decreases of time-averaged latent heat flux range from a minimum of  $-28 \text{ Wm}^{-2}$  to a maximum of  $-166 \text{ Wm}^{-2}$ . Even though the signs of the impacts are opposite, the impact patterns are similar to each other with local maximums being pronounced in the area of impervious local maximum (Fig. 16j) and local maximum of standard deviations of soil moisture availability and soil heat capacity (Figs. 18a and 18e). As a result of positive impact on sensible heat flux and negative impact on latent heat flux, the inhomogeneity effect is to increase the Bowen ratio in the IN1D simulations. This result is consistent with Seth and Giorgi (1994).

In general, except for the ground temperature, the signs of the inhomogeneity impacts are consistent with those of the stable regime. Positive impacts are mostly produced for the grid-mean ground temperature, 4m potential temperature, 4m wind speed, and sensible heat flux from the ground. Negative impacts are produced for the grid-mean specific humidity and latent heat flux from the ground with exceptions of negligible positive impacts on the specific humidity in the small areas of roads and coniferous forest.

Except for the ground temperature, while the impacts associated with roads are not as distinct as those of the stable regime around the HDT, impacts on the impervious local maximum area became more pronounced in the convective regime. This different feature may be caused by different behaviors of frictional velocity and frictional temperature between the regimes. While the frictional velocity is always positive, the frictional temperature is negative (positive) in the convective (stable) regime because of the temperature difference between the surface layer and ground (See Eqs. (14) and (15)). As will be explained later, this causes opposite impacts between  $U_*$  and  $T_*$  in the convective regime while same signs of the impacts are realized in the stable regime.

*b. Time variation of HOU area mean variables*

So as to examine the variation of the difference between IN1D and HO1D during the course of the day, HOU area means of variables were calculated as a function of simulation time. For each model variable, all grids in HOU were summed and divided by the grid total number every 2 minutes. As an aid for understanding the direction of fluxes, notice that all fluxes directed upward are positive. For example, positive sensible heat flux values indicate that the fluxes either enter the surface layer from the ground or leave into the layer above.

In figures 22a and 22b, the sensible heat flux at the ground (SHFLX) and that at the surface layer top (SHFLXT) are compared between the IN1D (solid line) and HO1D (dotted line) simulation. During the nighttime (stable regime) and for the first half of convective regime, the difference is not distinct. Obvious difference is seen from about 1800 UTC when maximum SHFLX is reached. Regardless of the difference amount in both the stable and convective regimes, the IN1D indicated greater SHFLX consistently during the entire simulation time. This result is consistent with those presented in the previous section. Maximum SHFLX difference of about  $90 \text{ Wm}^{-2}$  occurred around 2200 UTC. Similar differences are seen in Figure 22b for SHFLXT. As shown below, the simultaneous changes in SHFLX and SHFLXT yield little net change in surface air temperatures.

In figures 22c and 22d, the latent heat flux at the ground (LHFLX) and that at the top of the surface layer (LHFLXT) are compared. Unlike the SHFLX, LHFLX began to indicate obvious difference between IN1D and HO1D from about 1400 UTC which is close to the initiation time of free convection. In contrast to SHFLX the IN1D resulted in smaller LHFLX during the entire simulation time. This result also matches well to that found in the previous section. Maximum difference of about  $-110 \text{ Wm}^{-2}$  occurred at close to 2200 UTC. The LHFLXT also indicated reverse sign of the LHFLX.



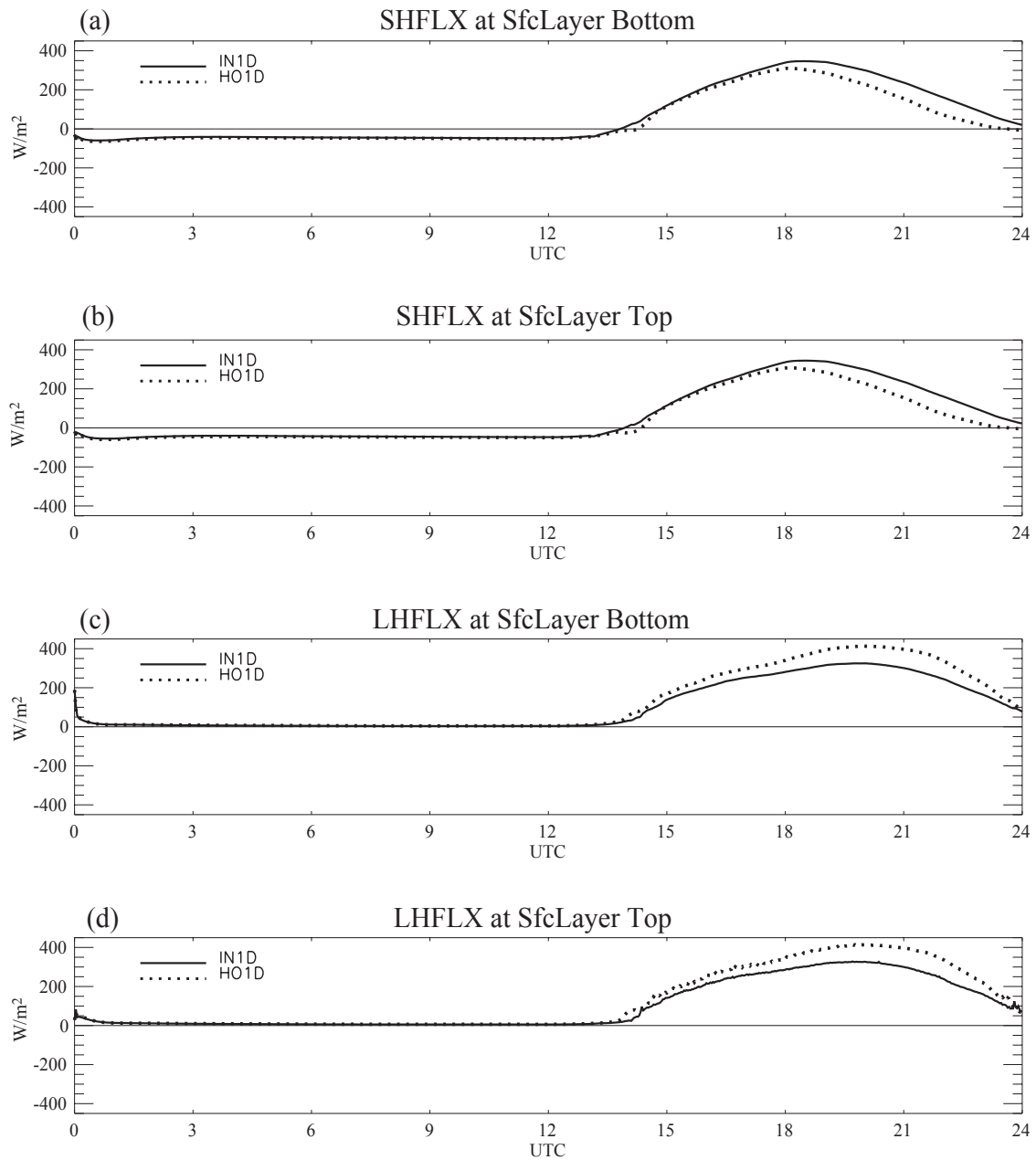


Figure 22. HOU-area-averaged sensible and latent heat fluxes in the surface layer as function of forecasting time: sensible heat fluxes at the (a) bottom (SHFLX) and (b) top (SHFLXT), latent heat fluxes at the (c) bottom (LHFLX) and (d) top (LHFLXT). Solid and dotted lines represent the IN1D and HO1D, respectively. The positive sign represents upward direction of the fluxes.

In Figure 23 ground potential temperature, 4m potential temperature, 4m wind speed, and 4m specific humidity are illustrated for both the IN1D (solid line) and HO1D (dotted line) simulations. The IN1D resulted in the ground potential temperatures which are about 0.5 K lower during the most stable nighttime and up to about 2.0 K greater in the convective daytime (Fig. 23a). The IN1D resulted in 4m potential temperatures which are about 0.3 K higher in the stable night time, average about -0.1 K lower during the first half of the convective regime, and average about 0.1K higher during the second half of the convective regime (Fig. 23b). As explained in previous section, compensatory SHFLXT made the inhomogeneity impact in the convective regime to be reduced despite more increases of SHFLX relative to those of stable regime.

The IN1D resulted in wind speeds which are about  $0.2 \text{ ms}^{-1}$  –  $0.3 \text{ ms}^{-1}$  higher during the most stable regime except for the slightly stable regime between about 1300 UTC and 1400 UTC. During the convective regime, the wind speed impacts showed variability but maintained mostly positive impacts of about 0 to  $0.5 \text{ ms}^{-1}$  (Fig. 23c). From the time of convective regime initiation (around 1400 UTC) to the time of maximum instability (around 1800 UTC), represented by minimum bulk Richardson number, the positive wind speed impact declined from about  $0.5 \text{ ms}^{-1}$  to  $0 \text{ ms}^{-1}$ . As the bulk Richardson number increased following the maximum the positive impact gradually increased again. This can be attributed to the opposite behavior of momentum flux to other fluxes. While the momentum flux decreases in the free convection regime as the instability increases, the sensible and latent heat fluxes increase.

The inhomogeneity impacts on the 4m specific humidity are opposite to those of 4m potential temperature, which is consistent with the results found in the previous section. The IN1D resulted in the 4m specific humidities which are in average 0.1 g/kg smaller during the stable regime and about 0.3 g/kg smaller during most of the convective regime (Fig. 23d). Opposite trends of the impacts were indicated in the transition regimes around 1400 UTC and 2200 UTC (slightly stable and slightly unstable).

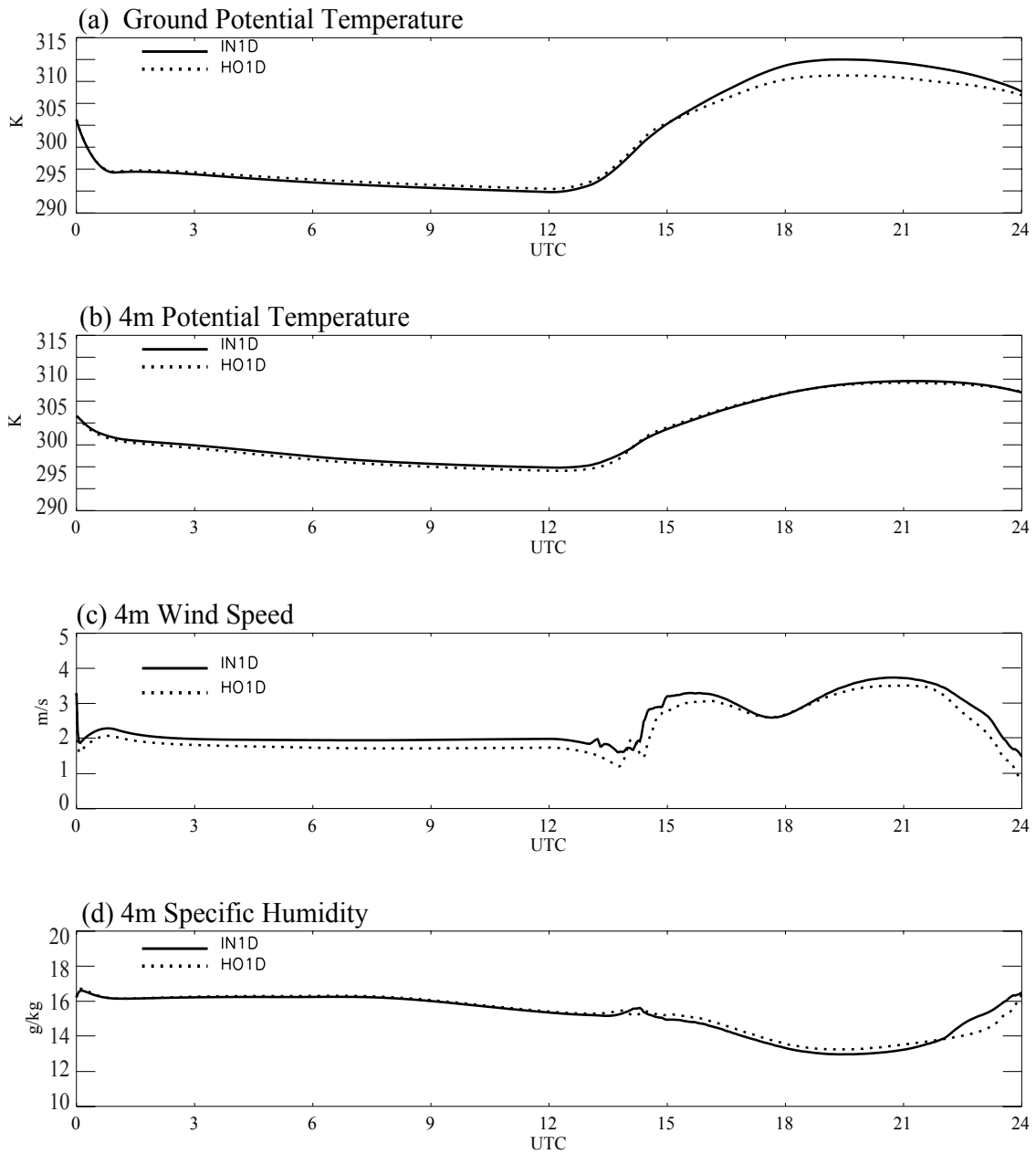


Figure 23. HOU-area-averaged (a) ground temperature, (b) 4m potential temperature, (c) 4m wind speed, and (d) 4m specific humidity for the IN1D (solid) and HO1D (dotted) as function of forecasting time.

In general the results of comparison of area-averaged variables presented above are fairly consistent with those from comparison of time-averaged variables presented in the previous section. In the transition regimes which were excluded in the comparison of time-averaged variables the inhomogeneity impacts seem to be enhanced and quite variable. This is probably due to the discontinuity of stability between the regimes and coexistence of the different regimes in the comparison between the IN1D and HO1D simulations.

*c. Comparison of HOU area mean PBL atmosphere*

In order to examine impacts of the inhomogeneity on the atmospheric PBL, profiles of HOU-area-averaged potential temperature, wind speed, and specific humidity were obtained at every forecasting hour. All grids in the HOU area were averaged using hourly outputs. The results from 1300 UTC to 0000 UTC are presented in figures 24, 25, and 26 for the potential temperature, specific humidity, and wind speed, respectively. In the figures the solid and dotted lines represent the profiles of IN1D and HO1D, respectively.

One General feature found from careful investigation of the profiles is that the inhomogeneity impacts in the surface layer are likely to be similar in the well mixed PBL as well, Near the PBL top (entrainment layer), the impacts are reversed from those of lower PBL due to increased vertical mixing coefficient (35). As summarized in Table 4, in the IN1D simulations, free convective vertical mixing is taken place between grid-mean PBL variables and fractional area weighted grid-mean surface variables. And the mixing coefficient is diagnosed from equation (35) with the outgoing sensible heat flux,  $H_1$ , being supplied by the fractional area weighted grid mean of those of subgrids. Based on the methodology of the inhomogeneity parameterization, the general feature mentioned above is fairly consistent with the results presented by the HOU-area-weighted mean variables (Figs. 22b, 23b, 23c, and 23d) in the previous section.

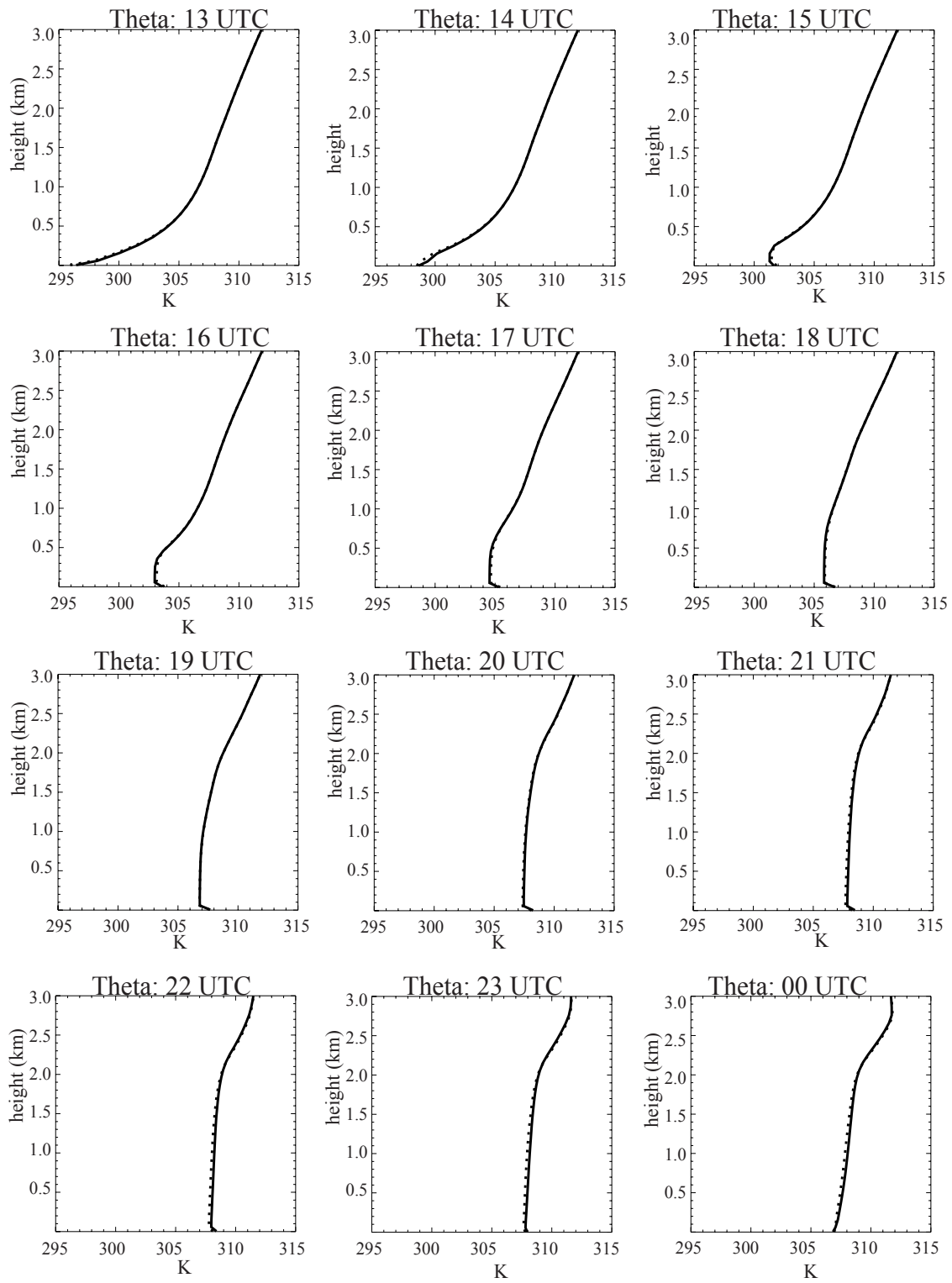


Figure 24. Profiles of HOU-area-averaged potential temperature for the IN1D (solid) and HO1D (dotted) from 1300 UTC to 0000 UTC. The x-axis is in K and y-axis is in km.

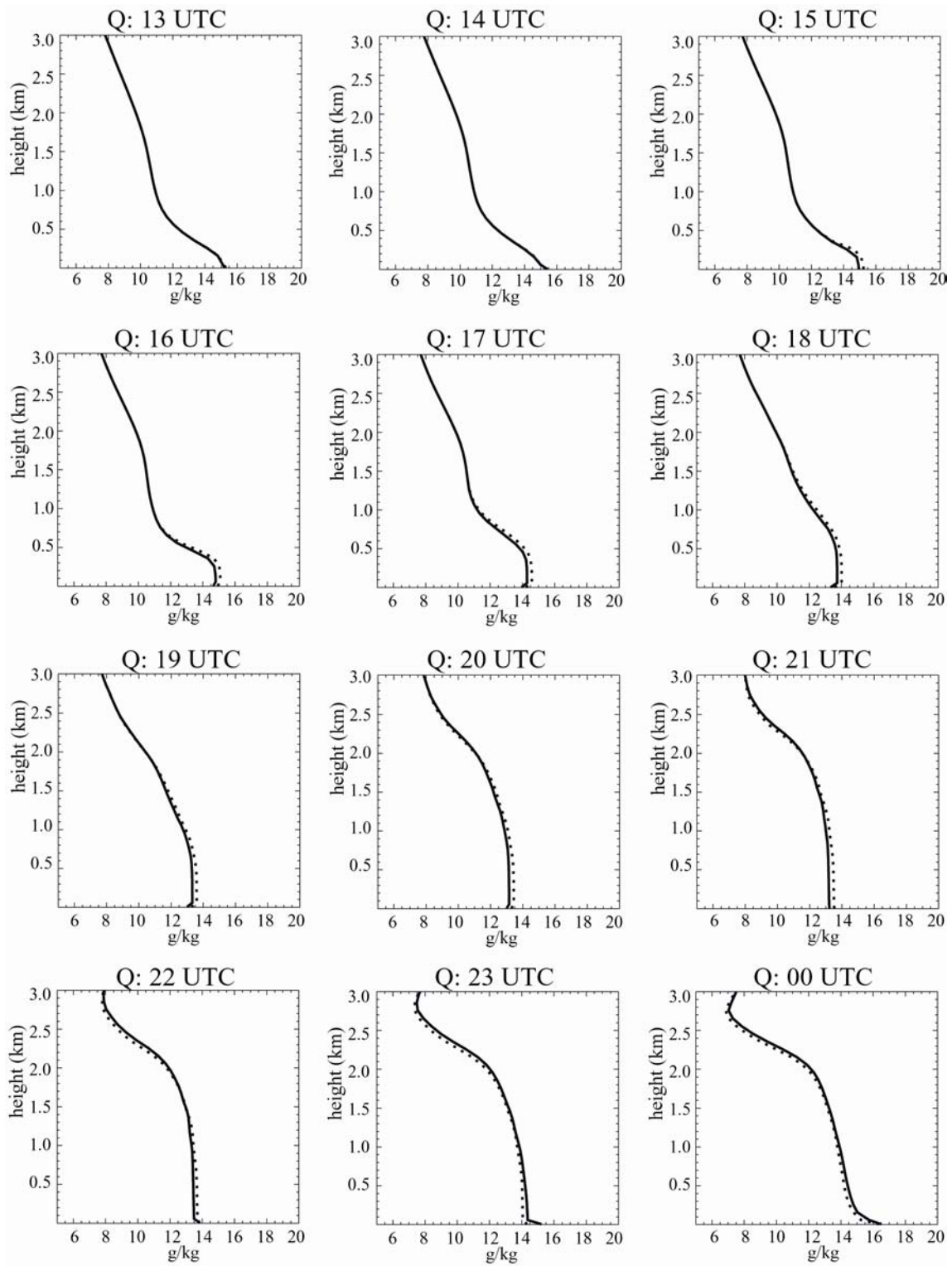


Figure 25. The same as Figure 24 but for specific humidity.

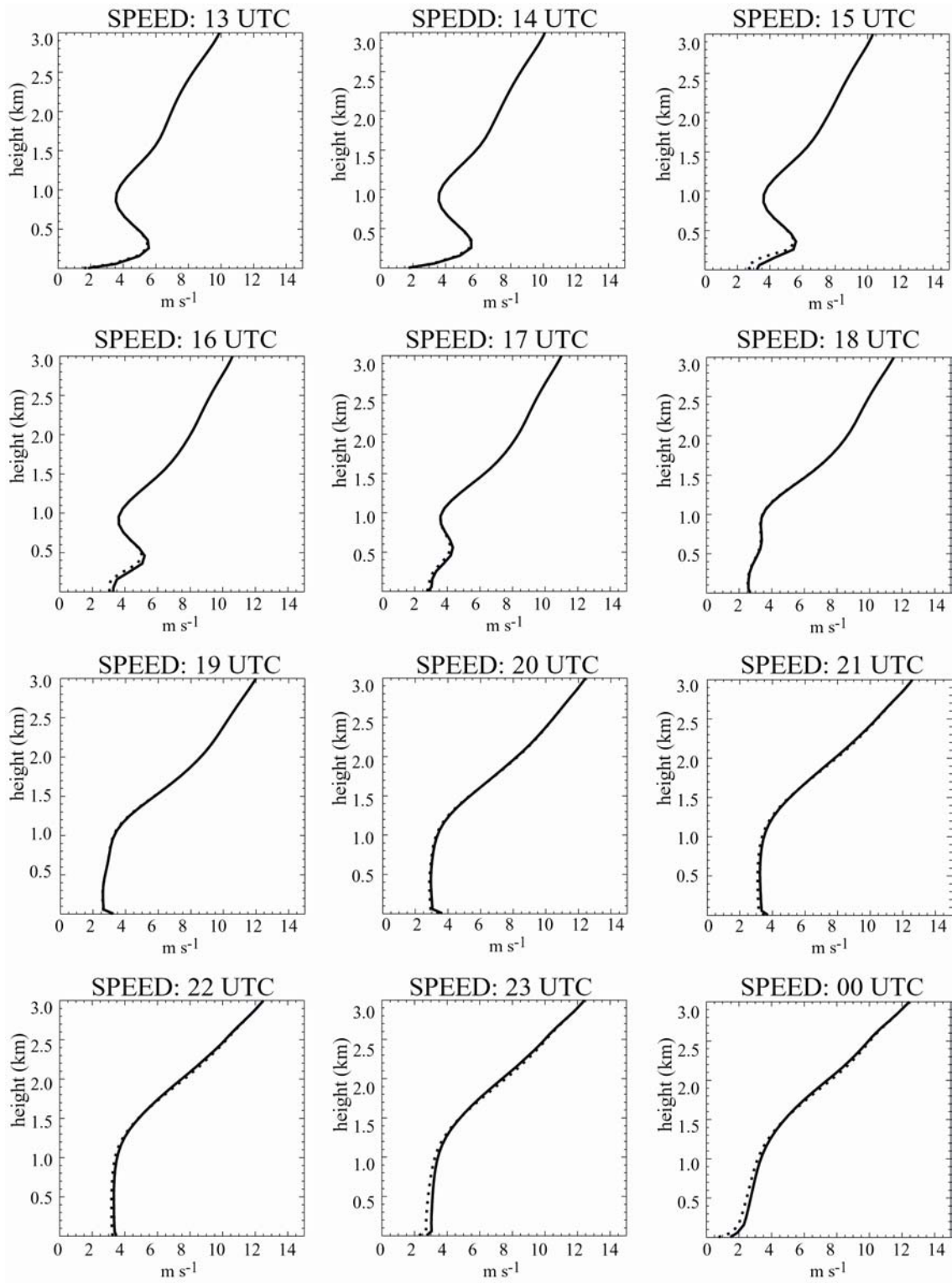


Figure 26. The same as Figure 24 but for wind speed.

As shown in Figure 22b the IN1D produced greater outgoing sensible heat flux,  $H_1$ , than the HO1D during the convective regime. And notice that during the first half of the regime the impact is negligibly small compared to that of second half. From this it is inferred that the vertical mixing coefficient, computed using Eq. (35), is relatively greater in the second half of the convective regime for the IN1D simulations.

As indicated in Figure 24, the potential temperatures of the IN1D are -0.1 K to -0.2 K lower in the PBL from 1500 UTC to 1800 UTC in accordance with the lower surface layer temperature of the IN1D as shown in Figure 23b. As the surface layer temperature became greater from about 1900 UTC (Fig. 23b) the impacts in the well mixed PBL got reversed accordingly. Thus, the IN1D resulted in greater well mixed PBL temperatures by about 0.2 K to 0.3 K during the second half of the convective regime. About -0.1 K lower temperatures near the PBL top of the IN1D from 2100 UTC were caused by the increased vertical mixing coefficients mentioned above.

As the result of reduced surface layer specific humidity from 1500 UTC to 2200 UTC (Fig. 23d), the IN1D resulted in specific humidity impacts ranging from -0.2 g/kg to -0.4 g/kg (Fig. 25). Near the PBL top, as the result of the increased vertical mixing coefficients during the second half of the convective regime, the humidity increased by about 0.1 g/kg to 0.4 g/kg from 2000 UTC.

The impacts on PBL wind speed (Fig. 26) are well represented according to those of surface layer wind speed (Fig. 23c). As can be seen in the figures positive impacts decrease from about  $0.8 \text{ ms}^{-1}$  near the surface at 1500 UTC to almost none at 1900 UTC following decreasing impacts of the surface layer wind speed during the time. The trend became reversed afterwards with maximum impact of about  $0.7 \text{ ms}^{-1}$  near the surface



occurring at 0000 UTC when the surface layer impact of wind speed is greatest. Because the vertical mixing is reduced by the weighting function (40) the impacts gradually decrease at higher levels in the well mixed layer compared to those of near surface. The impacts in the PBL top induced by the increased vertical mixing are discernable from 2000 UTC ranging from close to zero to about  $-0.2 \text{ ms}^{-1}$ .

In order to look at the spatial distribution in HOU, mean PBL variables at 2100 UTC were computed by averaging vertically in the well mixed PBL and illustrated in Figure 27a, 27b, and 27c for the potential temperature, specific humidity, and wind speed, respectively. As expected from the above arguments the impacts on the PBL are almost identical to those of surface layer (Figs. 21b, 21c, and 21d) in terms of spatial distribution.

Presented in Figure 27d is the spatial distribution of impacts on PBL height at 2100 UTC in HOU. Figure 28 represents time variation of the HOU-area-averaged PBL height during the convective regime. In the IN1D simulations the PBL heights were diagnosed using the grid-mean surface layer temperatures as mentioned in Table 5. Because the PBL height is determined at the height level of equilibrium with buoyant air parcel from the surface layer plus the entrainment depth, it is likely that the impacts correspond to those of surface layer temperature. Thus, on average, the IN1D resulted in about 50 m lower and up to about 300 m higher PBL heights during the first and second half of the convective regime, respectively.

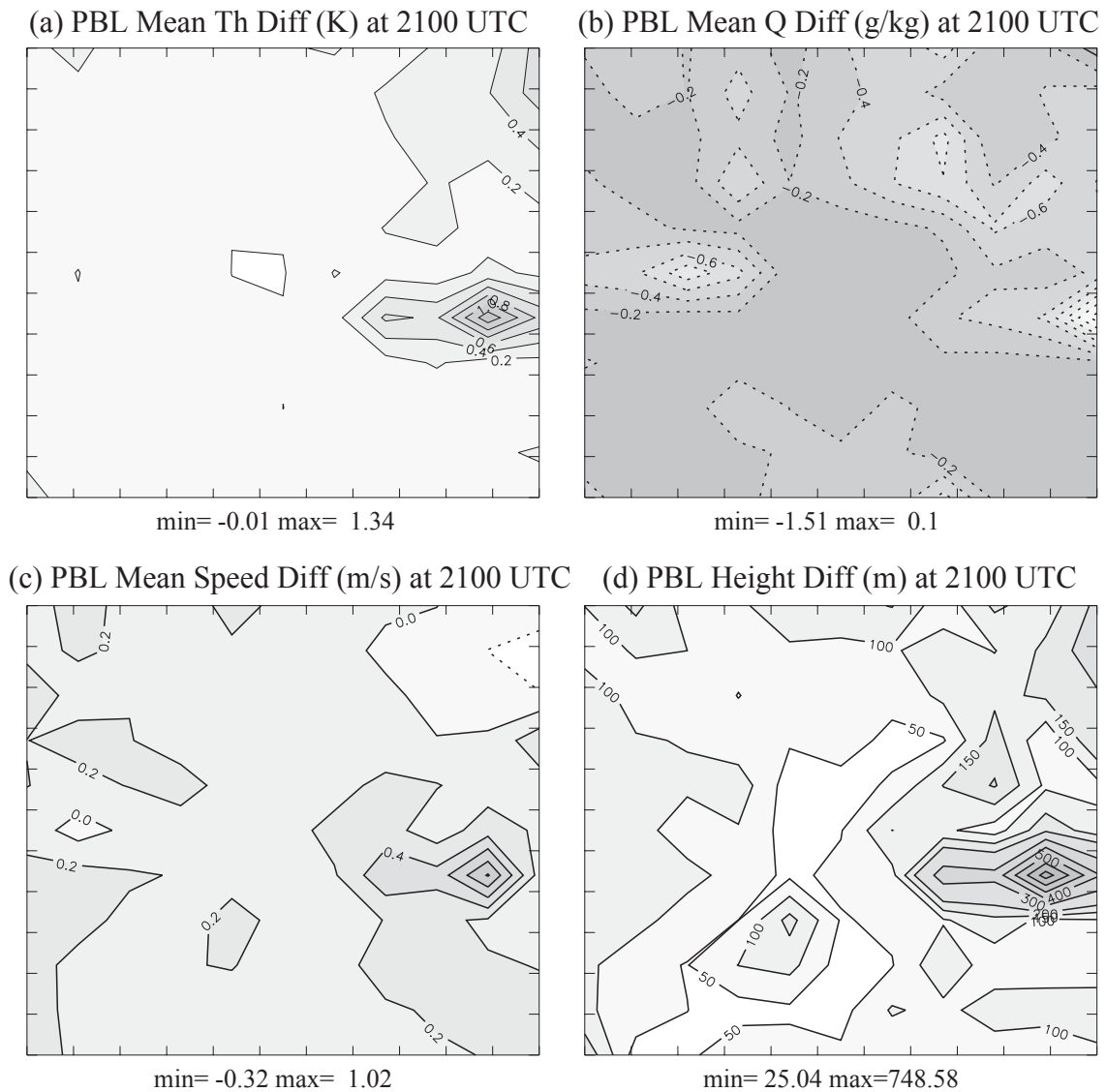
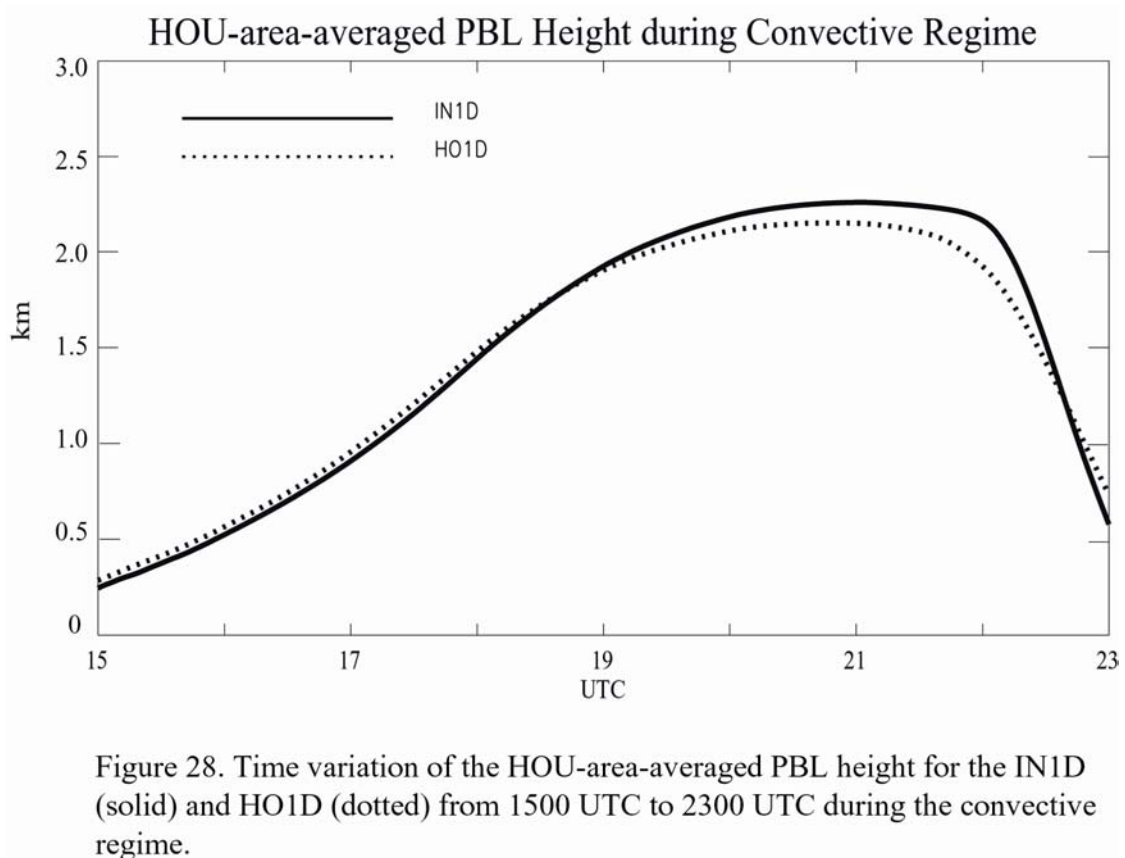


Figure 27. Distributions of differences (IN1D - HO1D) of the PBL-averaged (a) potential temperature, (b) specific humidity, (c) wind speed and (d) PBL height at 2100 UTC in HOU. The minimum and maximum values in the domain are indicated at the bottom of each figure. Units are indicated in each figure title.



## 5. Discussion

From the comparative studies presented in the previous section, it was revealed that the inhomogeneity parameterization applied in the IN1D simulations affected the boundary layer evolution. The impacts were variable both spatially and temporally. Notice again that the impacts and those variabilities are induced only by inhomogeneous representation of surface characteristics within each grid element. Within a grid element, the inhomogeneity impacts are induced by two factors. The first one stems from the grid-mean computation of subgrid-scale fluxes itself because the fluxes are non-linear functions of surface characteristics. The second factor is the difference of surface characteristics among the subgrids within the grid element. During the model integration the two factors combine in different ways due to time-variation of forcings and the different within-grid distributions of subgrid-scale surface characteristics among the grids.

### *a. Consideration of fundamental causes of inhomogeneity impacts*

In this study, the IN1D grids were segmented into 10 subgrids each of which has unique surface characteristic and fractional area coverage. For the HO1D grids the surface characteristics were obtained by the area-weighted average of the 10 subgrids as expressed by (44). While (a) the grid-mean fluxes of the HO1D are computed as function of the grid-mean surface characteristics, (b) those of the IN1D are obtained by fractional area-weighted sum of the 10 subgrid fluxes. Then, due to the non-linearity, the (a) and (b) are different even though the grid-mean surface characteristics are same, and even if the values of atmospheric variables are also identical.

For example, suppose that sensible heat flux is expressed by

$$H = -U_*(z_0)T_*(z_0),$$

where  $U_*$  and  $T_*$  are non-linear functions of roughness length  $z_0$  as expressed by (14) and (15). Then, the homo- and inhomogeneous computations of the sensible heat flux are expressed by

$$H^h(\bar{z}_0) = U_*(\bar{z}_0)T_*(\bar{z}_0)$$

and

$$\begin{aligned} H^i(z_0) &= \overline{H(z_0)} \\ &= -\overline{U_*(z_0)T_*(z_0)}, \text{ respectively.} \end{aligned}$$

From those expressions,  $H^h(\overline{z_0})$  and  $H^i(z_0)$  should be different since the  $U_*$  and  $T_*$  are non-linear function of  $z_0$  and since they are multiplied together to compute sensible heat flux.

Under identical atmospheric conditions, differences of variables among the subgrid-scale land types are induced by differences of surface fluxes. As expressed in Eqs. (13), (17), and (25) for sensible heat flux, latent heat flux, and ground stress, respectively, the surface fluxes are nonlinear function of frictional velocity ( $U_*$ ) and frictional temperature ( $T_*$ ). Therefore, as expressed in Eqs. (14) and (15), given initially identical atmospheric conditions and ground temperatures, flux differences will be initiated by differences of surface roughness existing among the subgrids. Differences of soil moisture availability will produce different latent heat fluxes for each of subgrid land types as expressed by Eq. (17). Both effects will in turn lead to inhomogeneities of ground temperature, further altering the fluxes.

As represented in the equations mentioned above, the computation of sensible heat flux directly involves the roughness length via  $U_*$  and  $T_*$ . Momentum flux directly involves the roughness length via  $U_*$  only. Latent heat flux directly involves the roughness via  $U_*$  and the soil moisture availability. Surface emissivity and albedo contribute to differences of net radiation in the energy budget equation (5), thus taking part in producing different ground temperatures among the subgrids. As expressed in Eq. (5) thermal inertia of the slab also contributes to different ground temperatures. Thus, the thermal inertia, surface emissivity, and surface albedo indirectly contribute to the different fluxes of sensible heat, latent heat, and momentum among the subgrids through different atmospheric stabilities induced by different ground temperatures.

*b. Turbulence characteristics from the perspective of grid-mean bulk Richardson number*

Figure 29 represents the time variation of the HOU-area-averaged grid-mean bulk Richardson number (Rb). The Rb is an atmospheric parameter defined by Eq. (20) and used

as a measure of turbulence characteristics in the PBL near the surface. For stable conditions  $R_b$  is greater than zero while for the unstable conditions the sign is reversed. In the simulations of this study, statically stable conditions with  $R_b$  less than 0.2 are characterized by mechanical turbulence where the turbulence is sustained by wind shear. In terms of grid-mean bulk Richardson number the IN1D favors greater turbulent vertical mixing in the surface layer in both the stable and free convective regimes. If this is the case the IN1D should produce greater surface fluxes all the time except for the narrow time range of near neutral condition. However, for example, latent heat flux decreased rather than increased during the convective regime as presented in figures 21f and 22c. From the grid-mean perspective, the inhomogeneity parameterization weakened the sensible heat and momentum fluxes in the stable regime and the latent heat flux in the free convective regime even though turbulence should have strengthened and air-land contrasts were greater. It is imagined that some subgrids within grid boxes produce fluxes which are dominant over and opposite to the rest of the subgrids. Based on the comparison study of time-averaged variables in the previous section, the subgrids which contribute to the counter-gradient fluxes are likely to correspond to the land types with extreme surface characteristics such as zero and 100 % soil moisture availability, or smallest and greatest roughness length.

*c. Sensitivity of inhomogeneity impacts to each surface parameter*

From the arguments provided above, it is inferred that the roughness length and soil moisture availability parameters play critical roles in producing the inhomogeneity impacts in the IN1D simulations. So as to examine the relative importance of each surface parameter in producing the inhomogeneity impacts, sensitivity runs of the IN1D were performed at an idealized single cell. In each sensitivity run the inhomogeneity was limited to one surface parameter with other parameters being assigned area-weighted grid-mean values. The 10 subgrid land types were allowed to have the fractional area coverage of 0.1 for each. Five sensitivity runs were conducted and the results were compared with the normal multi-inhomogeneity run (IN1D). Fractional area coverage of land cover types and area-weighted grid-mean of surface parameters at the grid are listed in Table 7 along with characteristic parameter values for each land cover types.

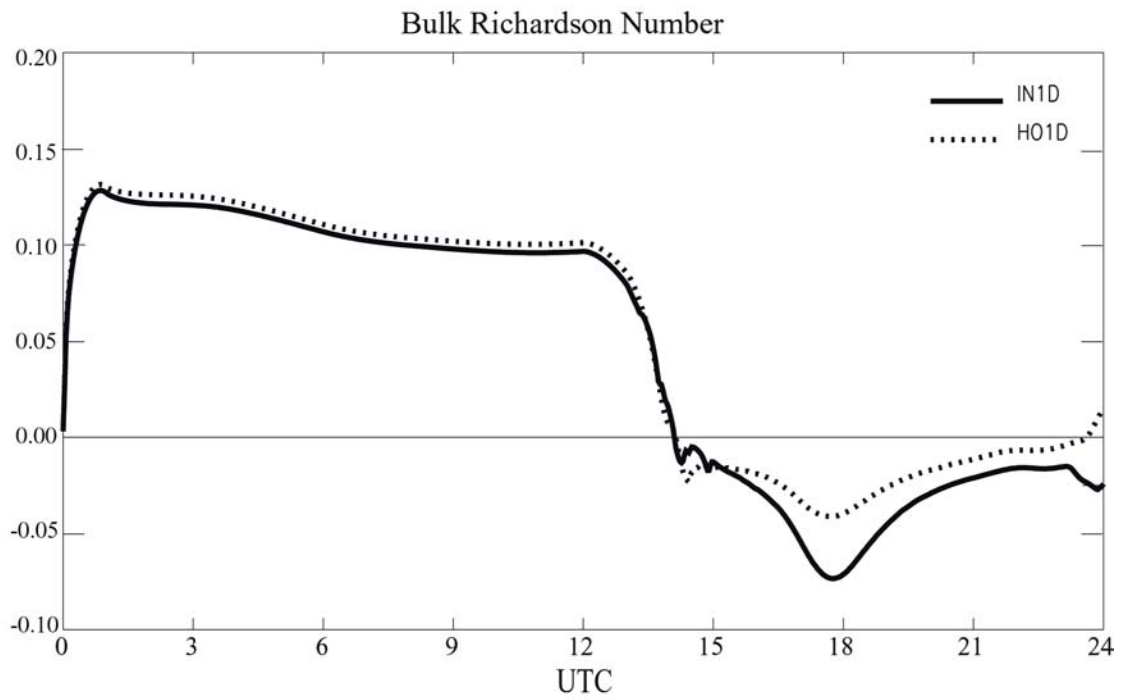


Figure 29. HOU-area-averaged grid-mean bulk Richardson number for the IN1D (solid) and HO1D (dotted) as function of forecasting time.

Table 7. Specification of surface parameters used in sensitivity runs. Column headings are defined on pages 47 and 50.

<b>Land cover types</b>	<b>FAC</b>	<b>SLMO</b>	<b>ALBD (%)</b>	<b>SFZ0 (m)</b>	<b>SFEM</b>	<b>CAPG (J/K/m**3)</b>
BroadLeaf Forest	<b>0.1</b>	0.58	11.38	1.6	0.95	2955700.
Coniferous Forest	<b>0.1</b>	0.35	9.81	1.3	0.95	2364560.
Mixed Forest	<b>0.1</b>	0.35	7.79	1.3	0.94	2364560.
Grass	<b>0.1</b>	0.17	16.0	0.2	0.92	1773420.
Wet Land	<b>0.1</b>	0.69	14.3	0.3	0.95	3546840.
Water Bodies	<b>0.1</b>	1.0	12.77	0.01	0.98	3546840.
Barren Land	<b>0.1</b>	0.02	21.37	0.15	0.85	1182280.
Roads	<b>0.1</b>	0.0	23.76	0.001	0.95	1714306.
Impervious Flat	<b>0.1</b>	0.0	25.2	0.01	0.69	754549.
Impervious Structure	<b>0.1</b>	0.0	25.2	0.7	0.69	754549.
<b>Area-Weighted Mean</b>		<b>0.32</b>	<b>16.7</b>	<b>0.72</b>	<b>0.89</b>	<b>2096072.</b>

The sensitivities of ground temperature and 4m surface layer temperature to each inhomogeneity during the stable regime are illustrated in figures 30a and 30b. The results of the roughness sensitivity run are similar to the IN1D run, with roughness inducing much bigger temperature changes than any other inhomogeneity. This implies that roughness inhomogeneity plays a major role in inducing the inhomogeneity impacts of the IN1D simulations during the stable regime.



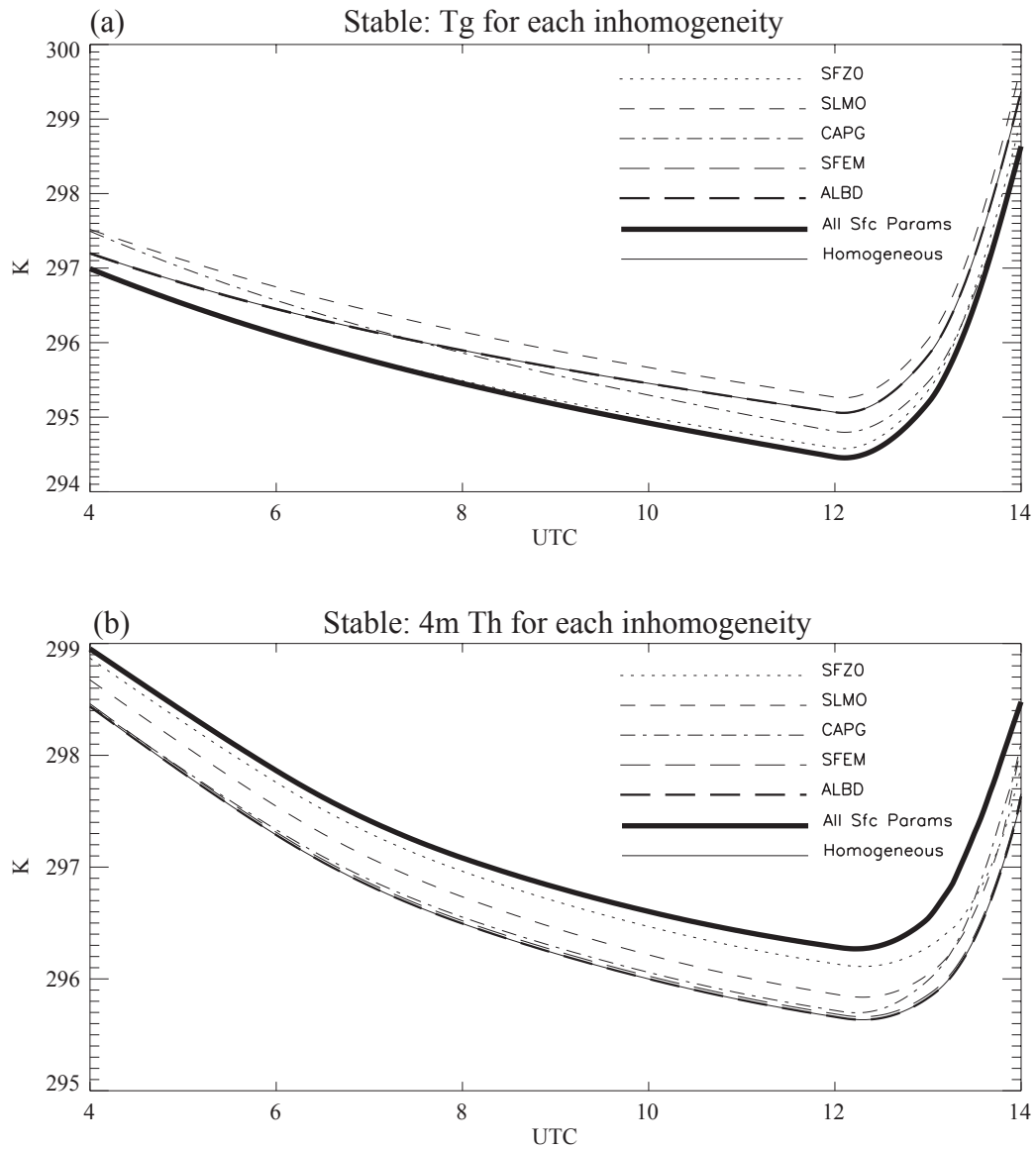


Figure 30. Comparisons of (a) ground temperatures and (b) 4 m potential temperatures from 5 different settings of surface inhomogeneities during the stable regime with respect to homogeneous and inhomogeneous (all surface params) runs. Each line indicated in panel denotes each inhomogeneity setting.

In the convective regime the roughness inhomogeneity again produced the ground temperature most closely matching the IN1D run (Fig. 31a). The sensitivity of the 4m temperature in the convective regime was not as distinct as the ground temperature (Fig. 31b). In Figure 32 the sensitivities of variables to each inhomogeneity were compared. In the figure the sensitivity values were defined by normalized time-averaged variable differences between the HO1D and each of inhomogeneity sensitivity runs. That is, the sensitivity is expressed by

$$\text{Sensitivity} = (In - HO1D) / |IN1D - HO1D|,$$

where  $In$  represents one of inhomogeneity runs. The variables used in the sensitivity calculation were time-averaged using the time ranges between 0400 UTC and 1400 UTC for the stable regime and between 1600 UTC and 2300 UTC for the convective regime. As can be seen in the figure, the sensitivity indicated substantial variability among the variables. Nonetheless, the roughness and soil moisture availability dominated other parameters in both the stable and convective regimes. In other words, the inhomogeneity impacts in the IN1D simulations were largely caused by the roughness and soil moisture availability inhomogeneities. In the stable regime, except for the latent heat flux and 4m specific humidity, the roughness inhomogeneity seemed to control the inhomogeneity impacts (Fig. 32a). In the convective regime, except for the ground temperature and 4m specific humidity, the soil moisture availability played a major role in inducing the inhomogeneity impacts (Fig. 32b).

*d. Implication of the frictional velocity ( $U_*$ ) and temperature ( $T_*$ ) impacts*

As explained earlier the frictional velocity ( $U_*$ ) and frictional temperature ( $T_*$ ) are key factors for surface flux calculations. The roughness, which is directly involved in the diagnosis of  $U_*$  and  $T_*$ , turned out to be a critical parameter that brings the inhomogeneity impacts (especially during the stable regime) to the IN1D simulations. With this in mind, the differences of  $U_*$  and  $T_*$ , between homogeneous and inhomogeneous representations of the roughness length were evaluated in HOU with other conditions being the same.

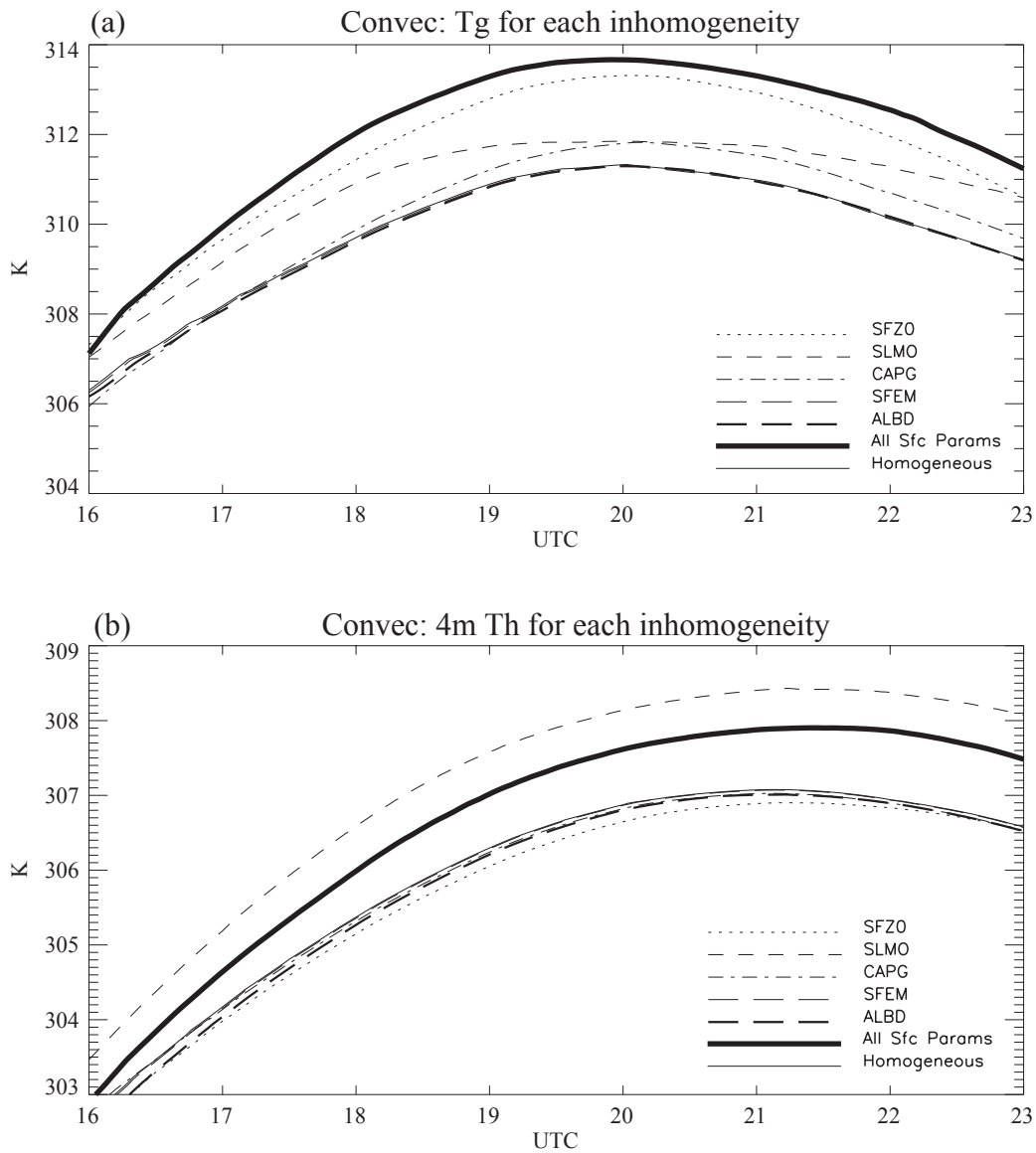


Figure 31. The same as Figure 30 but for the convective regime.

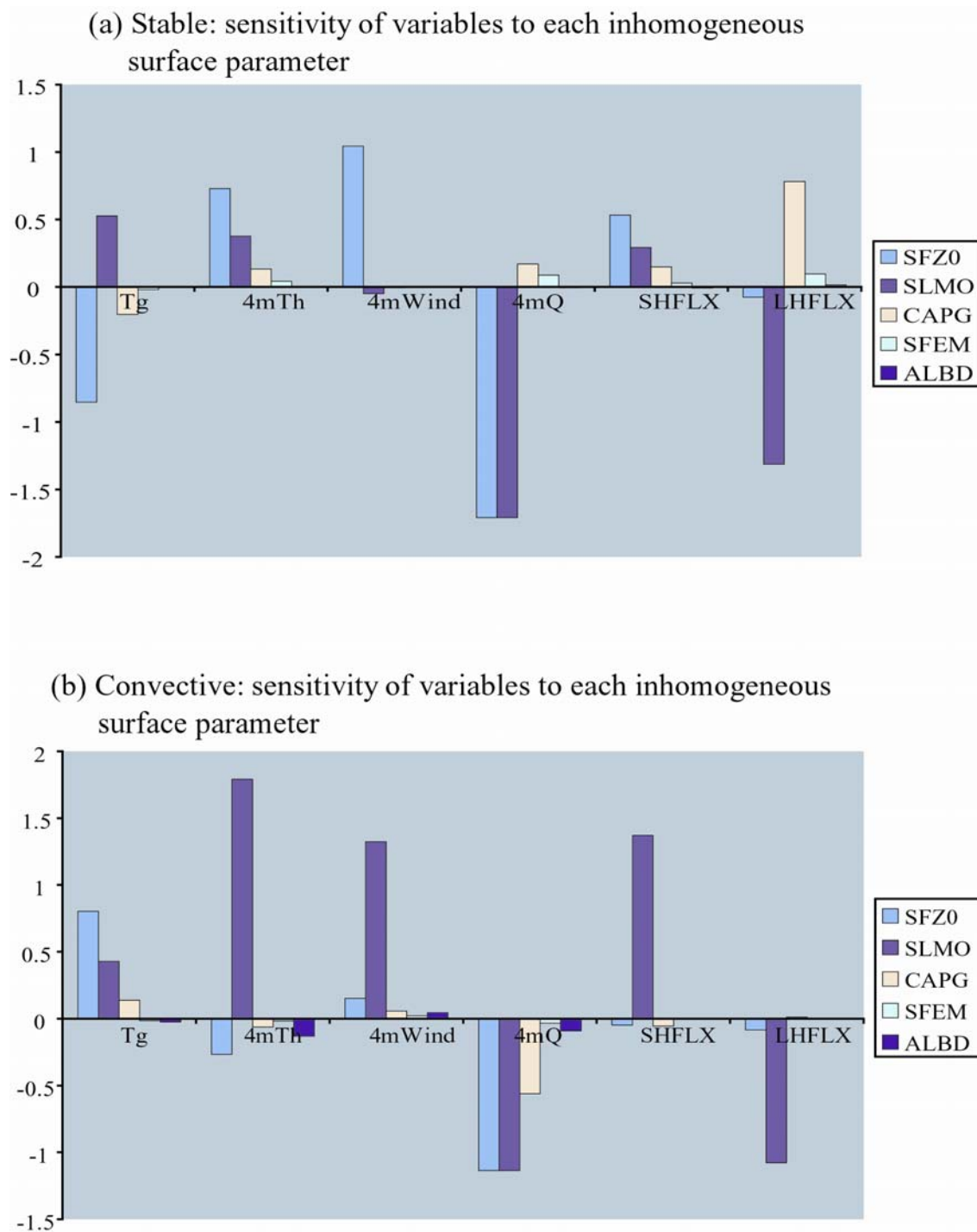


Figure 32. Bargraph showing the relative sensitivities of surface variables to the inhomogeneity defined by a single parameter with the fractional area coverage for each of 10 land cover types being given by 0.1. (a) stable regime and (b) convective regime.

The fixed values used in the  $U_*$  and  $T_*$  calculations were chosen to be representative of mean conditions in the stable and convective regimes. Thus, for the stable (convective) regime, the bulk Richardson number was given as 0.1 (-0.02), the surface layer wind speed was 2 m/s (4 m/s), and the potential temperature difference between the surface layer and ground surface was 3.0 K (-2.0 K). The differences were obtained by subtracting the homogeneous results from fractional area-weighted grid-mean values of inhomogeneous results at each grid in HOU. Figure 33 illustrates the distribution of the differences in HOU.

In the stable regime (Figs. 33a and 33b), the differences of the  $U_*$  and  $T_*$  between the inhomogeneous and homogeneous roughness have the same sign. Notice that areas with negative differences correspond to the areas with relatively smaller grid-mean roughness length. As expressed in Eqs. (13) and (17) for sensible and latent heat fluxes, respectively, decreased  $U_*$  and  $T_*$  implies decreased sensible heat exchange under stable conditions, and decreased  $U_*$  implies decreased latent heat flux. Also, decreased  $U_*$  implies decreased wind stress as expressed by Eq. (25), and then the decreased wind stress implies decreased momentum drag. These arguments are consistent with the results represented in figures 20c, 20e, and 20f in the roads and impervious area where local maximum negative  $U_*$  and  $T_*$  impacts occur.

In the convective regime the difference (Figs. 33c and 33d) of the  $U_*$  and  $T_*$  indicated opposite sign to each other. This is because the temperature contrast between the surface layer and ground is negative in the convective regime producing negative  $T_*$  from Eq. (15). With the negative  $T_*$  the positive impacts of  $T_*$  in Figure 33d implies negative impacts on the sensible heat flux expressed by Eq. (22). Thus, in the convective regime, even though those signs of impacts are reversed between the  $U_*$  and  $T_*$ , the same direction of impacts on the sensible heat flux is realized by the  $U_*$  and  $T_*$  impacts. The negative and positive impacts of the  $U_*$  and  $T_*$ , respectively, over the roads and impervious imply the negative impact on both the sensible and latent heat fluxes, and the positive impacts on wind speed in those areas. As shown in Figure 21e, the sensible heat flux is inconsistent with the above argument.

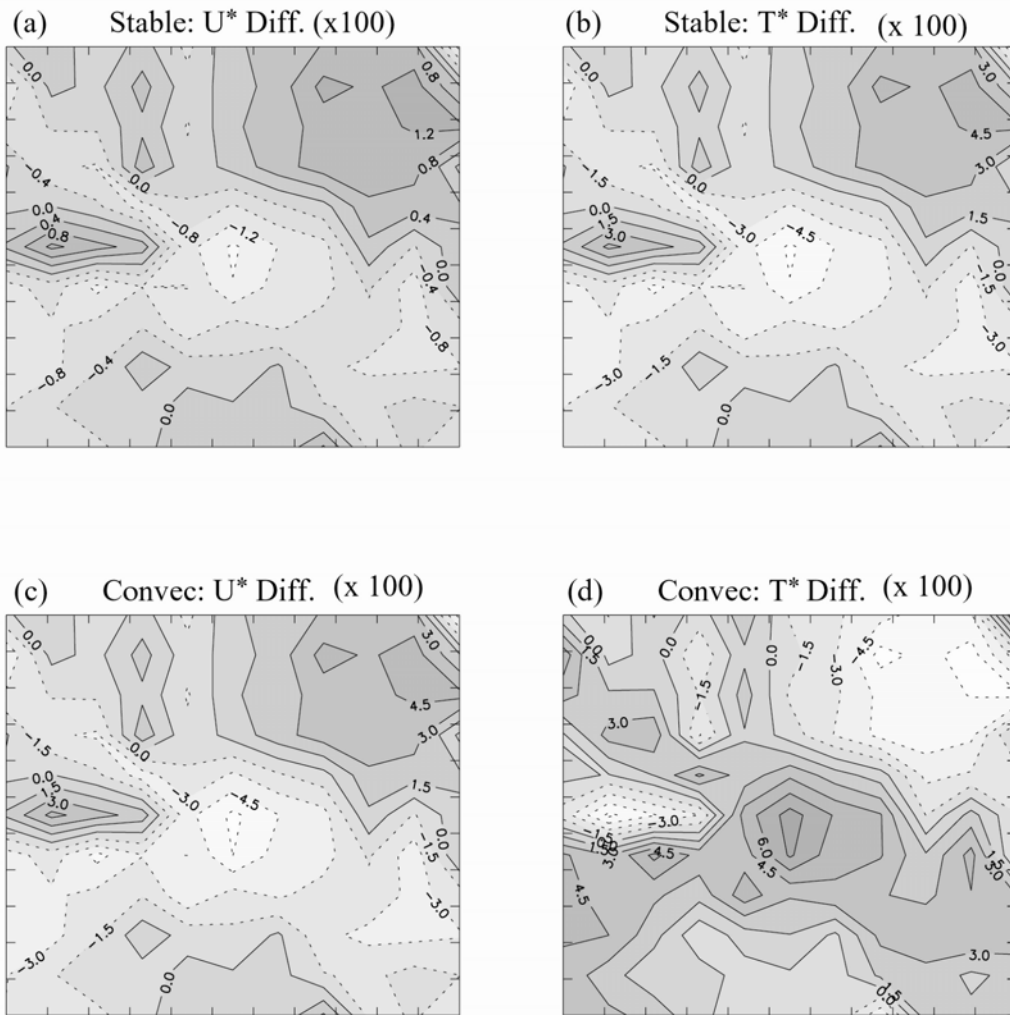


Figure 33. Distribution of  $U^*$  and  $T^*$  differences between homogeneous and inhomogeneous representation of surface roughness length in HOU for each regime: (a) and (b) for stable regime, (c) and (d) for convective regime in HOU.

Above, the  $U^*$  and  $T^*$  impacts, generated by the roughness inhomogeneity only, were compared with the results presented in figures 20 and 21 in order to examine the consistency of those impacts with the flux impacts. By the consistency it is implied that the roughness inhomogeneity plays a relatively important role in inducing the inhomogeneity impacts on the surface fluxes. From the examination, it is inferred that, except for the sensible heat flux during the convective regime, the inhomogeneity flux impacts are correlated well to the roughness inhomogeneity in the areas where grid-mean roughness is relatively smaller. For the sensible heat flux in the convective regime, points that are warm because of low latent heat flux have large negative bulk Richardson number (Eq. 20) too, so inhomogeneous fluxes are magnified.

*e. Relative importance of area coverage and different surface characteristics*

In order to examine the relative importance, in inducing the inhomogeneity impacts, of area coverage and different surface characteristic, the following set of experiment was performed. First, a grid is composed of two land surface types with fractional area coverages being given by  $F$  and  $1 - F$  and those surface characteristics being represented by

$$\alpha_1 = A\alpha_2,$$

where  $\alpha_1$  and  $\alpha_2$  represents each surface characteristic of the two land types and  $A$  is a proportional coefficient. Then, the grid-mean surface characteristics are obtained by

$$\bar{\alpha} = \alpha_1 F + \alpha_2 (1 - F).$$

Holding the grid-mean surface characteristics  $\bar{\alpha}$  constant, 83 inhomogeneous simulations were performed in the phase space  $(A, F)$ . The constant grid-mean values for the roughness, soil moisture availability, thermal inertia, emissivity, and albedo are determined as 0.5 m, 0.2, 0.03, 0.88, and 0.18, respectively. The homogeneous run to be compared was also performed with these values.

The percent differences of sensible and latent heat fluxes of the inhomogeneous simulations from the homogeneous were computed and contour-plotted on the A-F space. The computations were performed in the stable (ST) and convective (CO) regimes, separately. The results are presented in Figure 34. In the figures the asterisk marks designate

the position on the A-F space of the inhomogeneous simulations. The x- and y-axis represent the proportional coefficient A and fractional area coverage F, respectively. As can be seen in the figure, maximum magnitude of the percent differences occurs at the position of smallest A and greatest F values. This result implies that a greater impact is made possible when some subgrids within a grid element have relatively smaller surface characteristic values and larger area coverage. Thus, this argument is consistent with the results that the maximum impacts occurred in the areas where the roads with the smallest roughness and zero soil moisture availability and the impervious with zero soil moisture availability occupied relatively larger area coverage.

*f. Sensitivity of wind speed*

As mentioned earlier in the computational aspects, the 1-d simulations of this study excluded the momentum changes by the Coriolis and pressure gradient forces assuming those forcing terms are balanced during the integration period. Therefore, the simulated winds were induced only by the turbulent vertical mixing processes. It was explained that the 1-d simulations would have systematic wind speed errors due to the assumption as indicated in Table 4. In the stable regime, geostrophic winds cause negligible changes in wind speed from the balance assumption. In the convective regime, geostrophic winds produce the surface layer wind speeds 23 % lower than the balance assumption. Therefore, it is inferred that the simulated surface layer winds of this study might include at most about 23 % positive errors caused by the model assumption in the convective regime.

In order to understand what is implied by different wind speeds on the inhomogeneity impacts, wind speed sensitivity runs were performed. The method is to increase the initial wind components by factors listed in Table 8 for each sensitivity run. The representation of surface inhomogeneities is made using the HOU-area-averaged values for each sensitivity run. The impacts on sensible and latent heat fluxes are presented in Figure 35 as function of the wind increase factor for the stable (ST) and convective (CO) regimes, separately.



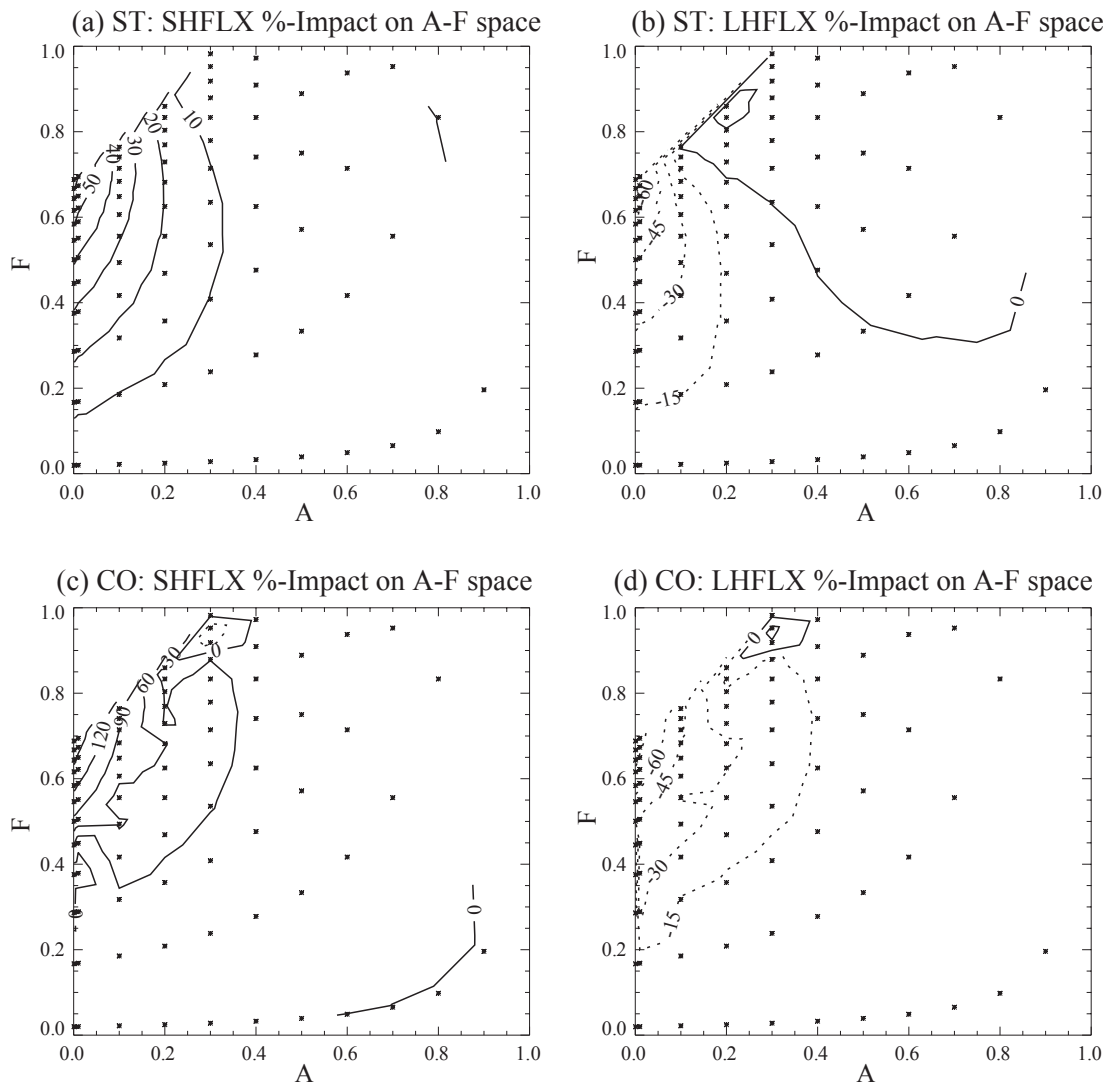


Figure 34. Percent impact distribution in the A-F space (defined in the text) of (a) sensible and (b) latent heat fluxes in the stable regime, and (c) sensible and (d) latent heat fluxes in the convective regime.

Table 8. The 4m wind speed and the percent impact of wind speed sensitivity runs of sensible and latent heat fluxes averaged for the stable (parentheses) and convective regime. Each row represents each sensitivity run with different initial wind speed.

<b>Initial wind increase factor</b>	<b>4m wind speed (ms<sup>-1</sup>)</b>	<b>Percent Impact of SHFLX (%)</b>	<b>Percent Impact of LHFLX (%)</b>
<b>1.0</b>	3.1 (1.9)	35 (7)	-24 (-22)
<b>1.2</b>	3.3 (1.9)	33. (6.)	-22. (-14.)
<b>1.4</b>	3.5 (1.9)	30. (5.)	-21. (-7.)
<b>1.6</b>	3.7 (2.0)	28. (3.)	-19. (-1.)
<b>1.8</b>	3.9 (2.2)	24. (-2.)	-16. (16.)
<b>2.0</b>	4.2 (2.3)	20. (-3.)	-13. (24.)
<b>2.2</b>	4.4 (2.4)	15. (-25.)	-10. (145.)
<b>2.4</b>	4.7 (2.8)	9. (-150.)	-6. (822.)
<b>2.6</b>	5.0 (3.3)	0.5 (-226.)	-1. (1266.)
<b>2.8</b>	5.4 (4.9)	-14. (-453.)	8. (2446.)
<b>3.0</b>	5.8 (5.8)	-25. (-571.)	15. (3100.)
<b>Reference CLIM</b>	2.9 ms <sup>-1</sup> (1.7 ms <sup>-1</sup> )	191 Wm <sup>-2</sup> (-46 Wm <sup>-2</sup> )	361 Wm <sup>-2</sup> (8 Wm <sup>-2</sup> )

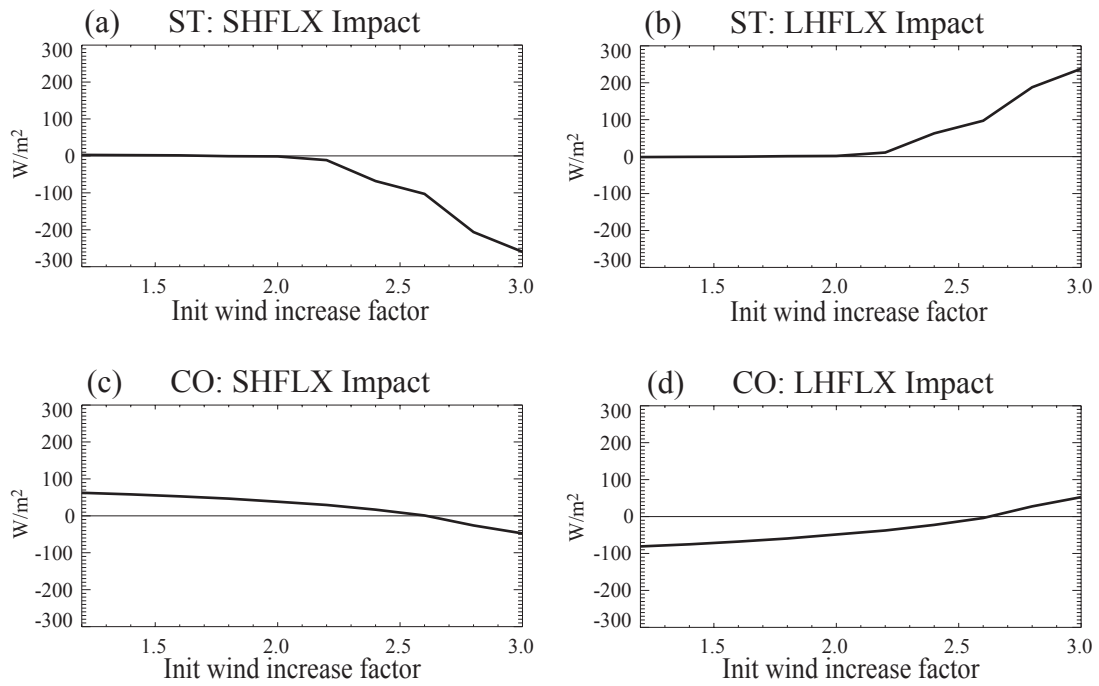


Figure 35. Inhomogeneity impacts of sensible and latent heat fluxes for (a) and (b) stable and (c) and (d) convective regimes as function of initial wind speeds. The impacts are defined as the wind speed sensitivity runs minus homogeneous CLIM.

The impacts were obtained by subtracting the results of climatological homogeneous run (*CLIM*), designated as reference in the Table 8, from each sensitivity run. Notice that *CLIM* is a single homogeneous simulation that was implemented with the HOU-area-averaged surface parameter values. For the sensible heat flux, as the wind speed increases from the reference value of  $1.7 \text{ ms}^{-1}$  (stable regime) and  $2.9 \text{ ms}^{-1}$  (convective regime), the impacts kept decreasing from the positive to negative impacts. For the latent heat flux, the impact trends are reversed. The impacts change sign at the increasing factor of 1.8 and 2.8 for the stable and convective regimes, respectively. This implies that the inhomogeneity impacts decrease in magnitude as the wind speed increases until the turning point of signs at the increasing factor 1.8 and 2.8 for the stable and convective regimes, respectively. From the turning points the inhomogeneity impacts will increase again with the impact directions reversed. In particular, for the stable regime, the rate of change of the impacts becomes steeper from the turning point implying much greater impacts opposite to the reference values. In Table 8, mean wind speed and percent impacts of the sensible and latent heat fluxes, compared with *CLIM*, for each sensitivity run are listed.

The percent impacts were computed by

$$PI = 100 \times (sen - CLIM) / |CLIM|,$$

where, *sen* and *CLIM* indicate each regime-averaged fluxes for the inhomogeneous sensitivity and homogeneous climatological runs, respectively.

With no changes in wind speed (factor 1.0 case), the inhomogeneous sensitivity run produced 35 % and -24 % impacts for the sensible and latent heat fluxes, respectively, in the convective regime, and 8 % and -22 % in the stable regime. As explained above the decreases of impacts are indicated as the mean wind speed increase and changes of impact sign occurs too as the winds further increase. The changes of sign occur at  $5.4 \text{ ms}^{-1}$  and  $2.2 \text{ ms}^{-1}$  for the convective and stable regimes, respectively.

With the 23 % wind speed error associated with the model's assumption in the convective regime, the inhomogeneity impacts approximately corresponds to those of the factor 1.2 sensitivity run in Table 8. The impact difference between the factor 1.0 and other factor sensitivities is interpreted as the inhomogeneity impact error caused by the wind speed

difference between the factor 1.0 and other sensitivities. Thus, between the factor 1.0 and 1.2, the difference of percent impacts for both the sensible and latent heat fluxes is 2 % implying that the model's assumption with regard to the geostrophic winds causes about 2 % underestimation of the inhomogeneity impacts for both the fluxes.

*g. Percent difference of the IN1D with respect to CLIM*

In order to understand how much significance the inhomogeneity impacts implicate in the model simulations over the HOU area, percent differences of the surface variables of the IN1D simulations were computed with respect to the homogeneous climatological simulation (CLIM) for the stable and convective regimes separately. The percent differences were computed by

$$PD = 100 \times (\overline{IN1D} - CLIM) / |CLIM|,$$

where, the overbar indicates spatial average in the HOU area. Also, in the computation, time-averages for each regime were applied for both the IN1D and CLIM simulations. For the temperature the denominator was normalized by the amplitude of diurnal temperature variation. The climatological simulation, CLIM, was run using the HOU-area-averaged surface parameters values with other conditions being given the same as in the HO1D. The results are presented in Table 9.

The ground temperature and sensible heat flux indicated more significance in the convective regime compared to the stable regime. Taking the systematic wind speed errors, which were explained above as being induced by model assumption, for the sensible heat flux, the percent differences would be about 10 % and 35 % for the stable and convective regimes, respectively. And, for the latent heat flux, the percent difference would be -29 % to -39 % and about -24 % for the stable and convective regimes, respectively. Thus, when the error corrections are considered, the latent heat flux impact is more significant in the stable regime in terms of the percent difference.

Table 9. The HOU-area-averaged percent differences of IN1D simulations with respect to CLIM simulation.

	Tg	4mTh	4mWind	4mQ	SHFLX	LHFLX
Stable Regime	-2.2	2.1	16.1	-0.5	8.2	-25.0
Convective Regime	11.0	0.7	11.2	-1.1	36.1	-24.6

**CHAPTER IV**  
**ESTIMATION OF GOES SKIN TEMPERATURE ERROR OVER HOUSTON**  
**URBAN AREA**

1. Introduction

It is expected that the daytime Houston urban heat island produces local variations in surface temperature, mixing height, and wind. To give simulations of this phenomenon a direct observational basis, satellite-observed changes in surface temperature are used in the NGMM5 simulations during the ozone episode to infer soil moisture availability compatible with the model and with the observed temperature changes. In order properly resolve the inhomogeneities within Houston itself, the method is applied at a resolution of 4-km for the first time.

One potential problem in applying the technology is that the large subgrid-scale variations in land surface characteristics may cause systematic errors which would be insignificant over more homogeneous surfaces. Using the sensitivity simulation results obtained from the 1-d PBL model simulations in the previous chapter, the magnitude of these errors is estimated for the future correctional development of the technology.

One such error is in the estimation of surface skin temperature itself. While the assimilation technique assumes that the satellite-observed skin temperature represents an average over the image pixel, the actual emissions at the relevant infrared wavelengths from surfaces within the pixel are strongly nonlinear function of temperature. This introduces a small bias in the satellite temperature estimates which depends on the degree of subpixel temperature inhomogeneity.

In addition to the error estimation, model impacts implicated by the errors in applying the satellite assimilation technique are examined using the 1-d PBL model developed in chapter III.

## 2. Brief description of the GOES satellite data assimilation technique

### a. Calculation of observed soil moisture availability

This technique couples the remotely sensed surface skin temperature to the land-surface forcing of a mesoscale atmospheric model using the surface energy budget equation of the model. Following McNider's notation the surface energy budget equation (5) for the surface skin temperature can be expressed

$$C_g \left( \frac{dT_G}{dt} \right) = R_n - H_m - H_g - E, \quad (45)$$

where  $\frac{dT_G}{dt}$  is the rate of change of the land surface temperature (LST),  $C_g$  the surface heat capacity,  $R_n$  is the net radiation,  $H_g$  is the sensible heat flux,  $H_m$  is the soil heat flux, and  $E$  is the latent heat flux.

In the actual application a composite representation of the surface characteristics of vegetation, soil, etc., was assumed for the energy budget of the model and satellite (McNider et al. 1995). Therefore,  $C_g$  represents a resistance to forcing. McNider et al. found that in the morning the LST change is most sensitive to errors in latent heat flux. By assuming that all of the terms in the model's surface energy budget are accurate except for the latent energy term,  $E$ , the difference of the surface energy budget for the model and satellite is

$$E_s = C_g \left[ \left( \frac{dT_G}{dt} \right)_s - \left( \frac{dT_G}{dt} \right)_m \right] + E_m, \quad (46)$$

where  $\left( \frac{dT_G}{dt} \right)_s$  is calculated from the hourly GOES-derived LST products retrieved at model grid points. The subscript s and m of each term in the above equation represent satellite and model respectively. The latent heat flux in the Blackadar boundary layer scheme in MM5 (Blackadar 1979; Zhang and Anthes 1982), for example, is given from equation (17) and (18) by



$$E_m = \frac{M\rho_a(q_s(T_g) - q_a)ku_*}{\ln\left(\frac{ku_*z_a}{K_a} + \frac{z_a}{z_l}\right) - \varphi_h} \quad (47)$$

where  $M$  is the soil moisture availability,  $q_s(T_g)$  is the saturation mixing ratio of the surface,  $q_a$  is the mixing ratio of the air immediately above the surface,  $k$  is the von Karman constant,  $u_*$  is the frictional velocity,  $z_a$  the height of the lowest model layer,  $z_l$  is the depth of the molecular layer,  $K_a$  is a background molecular diffusivity, and  $\varphi_h$  is a non-dimensional stability parameter for heat and water vapor. To obtain the satellite-inferred moisture availability, we solve above equation for  $M$  as follows:

$$M_s = E_s \frac{\ln\left(\frac{ku_*z_a}{K_a} + \frac{z_a}{z_l}\right) - \varphi_h}{\rho_a ku_*(q_s(T_g) - q_a)} \quad (48)$$

where  $E_s$  is the difference of the surface energy budget as given by equation (46). In order to meet the assumptions of the moisture recovery technique the GOES derived net solar radiation is also assimilated into the model via direct insertion. Thus, during the dynamical initialization period of the model the satellite skin temperatures are used to adjust the moisture availability and the satellite-derived insolation is inserted.

*b. Land Surface Temperature (LST) retrieval equation of the Physical Split-Window algorithm*

The upwelling radiance  $I$  observed at the satellite, assuming a nonscattering, plane-parallel atmosphere and an emissivity of unity, is expressed as

$$I = B(T_s)\tau_{ps} + \int_{ps}^0 B[T(p)] \frac{\partial \tau_p}{\partial p} dp, \quad (49)$$

where  $B$  and  $\tau$  are the Planck function and atmospheric transmittance, respectively, for a wavelength domain associated with a sensor spectral channel. The  $T$  and  $p$  are the temperature and pressure, respectively. The subscript ‘‘s’’ denotes surface and ‘‘ps’’ denotes

that the atmospheric parameter is evaluated at the surface pressure. Thus,  $T_s$  is surface or skin temperature and  $T_{ps}$  is the surface air temperature.

Expressing the observed temperature,  $T$ , and transmittance,  $\tau$ , with sum of first guess and perturbation part by

$$T = \bar{T} + \delta T \quad (50)$$

and

$$\tau = \bar{\tau} + \delta\tau, \quad (51)$$

and substituting (50) and (51) into (49), we get

$$I = \bar{I} + \delta I, \quad (52)$$

where  $\bar{I}$  is the upwelling radiance by the model first guess profile and  $\delta I$  is the perturbation in radiance.

$\bar{I}$  and  $\delta I$  are expressed by

$$\bar{I} = B(\bar{T}_s)\bar{\tau}_{ps} + \int_{ps}^0 B[\bar{T}(p)]\frac{\partial \bar{\tau}_p}{\partial p} dp \quad (53)$$

and

$$\delta I = C\delta T_s + D\delta U_{ps}, \quad (54)$$

where  $U$  is precipitable water, and  $C$  and  $D$  are expressed by

$$C = \bar{\tau}_{ps} \frac{\partial B(\bar{T}_s)}{\partial T} \quad (55)$$

and

$$D = \frac{\partial \bar{\tau}_{ps}}{\partial U} [B(\bar{T}_s) - B(\bar{T}_{ps})] - \frac{1}{\bar{U}_{ps}} \int_{ps}^0 \bar{U}(p) \frac{\partial \bar{\tau}(p)}{\partial U} \frac{\partial B[\bar{T}(p)]}{\partial p} dp. \quad (56)$$

The resulting perturbation Eq. (54) becomes linear in the unknowns  $\delta T_s$  and  $\delta U_{ps}$ . A solution for  $\delta T_s$  and  $\delta U_{ps}$  is obtained by formulating Eq. (54) for two or more different IR

sensor spectral window channels. Thus, for two different IR window sensor channels  $\lambda_1$  and  $\lambda_2$ , solutions are given by

$$\delta T_s = \frac{\delta I_{\lambda_1} D_{\lambda_2} - \delta I_{\lambda_2} D_{\lambda_1}}{C_{\lambda_1} D_{\lambda_2} - C_{\lambda_2} D_{\lambda_1}}, \quad (57)$$

$$\delta U_s = \frac{\delta I_{\lambda_1} C_{\lambda_2} - \delta I_{\lambda_2} C_{\lambda_1}}{D_{\lambda_1} C_{\lambda_2} - D_{\lambda_2} C_{\lambda_1}}. \quad (58)$$

Therefore, the retrieved skin temperature  $T_s$  is expressed by

$$T_s = \bar{T}_s + \delta T_s. \quad (59)$$

### 3. Estimation of GOES skin temperature error

#### a. Method

A simple idea is utilized to examine the skin temperature retrieval error produced by using homogeneous model ground temperature in the computation of first guess upwelling radiance expressed by Eq. (53). In applying the idea the fundamental assumption is that the inhomogeneities affecting the upwelling radiance variation are given only by subgrid-scale ground temperatures. This assumption is the same as for the 1-d PBL simulations in the previous chapter.

First, instead of observed radiance, first guess radiance from the grid mean ground temperature is regarded as the observed. Thus, Eq. (49) is now expressed as

$$I = B(\bar{T}_s) \bar{\tau}_{ps} + \int_{ps}^0 B[\bar{T}(p)] \frac{\partial \bar{\tau}_p}{\partial p} dp. \quad (60)$$

Next, the first guess upwelling radiance is computed from inhomogeneous surface as

$$\bar{I} = \sum_{i=1}^N FAC(i) B(T_{si}) \bar{\tau}_{ps} + \int_{ps}^0 B[\bar{T}(p)] \frac{\partial \bar{\tau}_p}{\partial p} dp, \quad (61)$$

where  $N$  is the number of subgrid-scale land types (in this study 10 land types are defined in the previous chapter) regrouped from surface patches within the grid box, and  $T_{si}$  denotes

the ground temperature for each subgrid land type. The  $FAC(i)$  denotes the fractional area coverage of the  $i$ -th land type in the grid box. The inhomogeneity of emissivity is not considered because the emissivity is assumed to be unity.

Then, from equation (52), the perturbation in radiance due to the inhomogeneous surface is given by

$$\delta I = [B(\bar{T}_s) - \sum_{i=1}^N FAC(i)B(T_{si})]\bar{\tau}_{ps} . \quad (62)$$

From Eqs. (55) and (56), it seems that the variation of coefficients  $C$  and  $D$  due to surface heterogeneity is smaller than that of Planck function by an order of magnitude. Therefore, neglecting the change of coefficients between homogeneous and inhomogeneous surface, the perturbation surface temperature is computed using Eq. (57). Notice that the perturbation temperature computed here should be interpreted as the skin temperature retrieval error produced by using homogeneous (grid mean) ground temperature without consideration of subgrid-scale temperatures,  $T_{si}$ .

Inhomogeneous ground temperatures,  $T_{si}$ , for each subgrid land type are supplied from the inhomogeneous 1-d PBL simulations (IN1D) as shown in Figure 36, and the retrieval error is computed following the above procedure. Table 10 illustrates specified values used in the skin temperature error calculation with respect to GOES-8 imager channel 4 and 5.

Table 10. Specified transmittance at the surface and coefficient values used in computation of skin temperature retrieval error for GOES-8 Imager channels 4 and 5.

<b>GOES-8 Imager</b>	<b>Coefficient <math>C</math></b> ( $mWm^{-2}sr^{-1}cmK^{-1}$ )	<b>Coefficient <math>D</math></b> ( $mWm^{-2}sr^{-1}cm \cdot mm^{-1}$ )	<b>Transmittance</b> $\tau_{ps}$	<b>Wavenumber</b> ( $cm^{-1}$ )
Channel 4	1.14	-0.15	0.9	936
Channel 5	0.99	-0.23	0.6	837

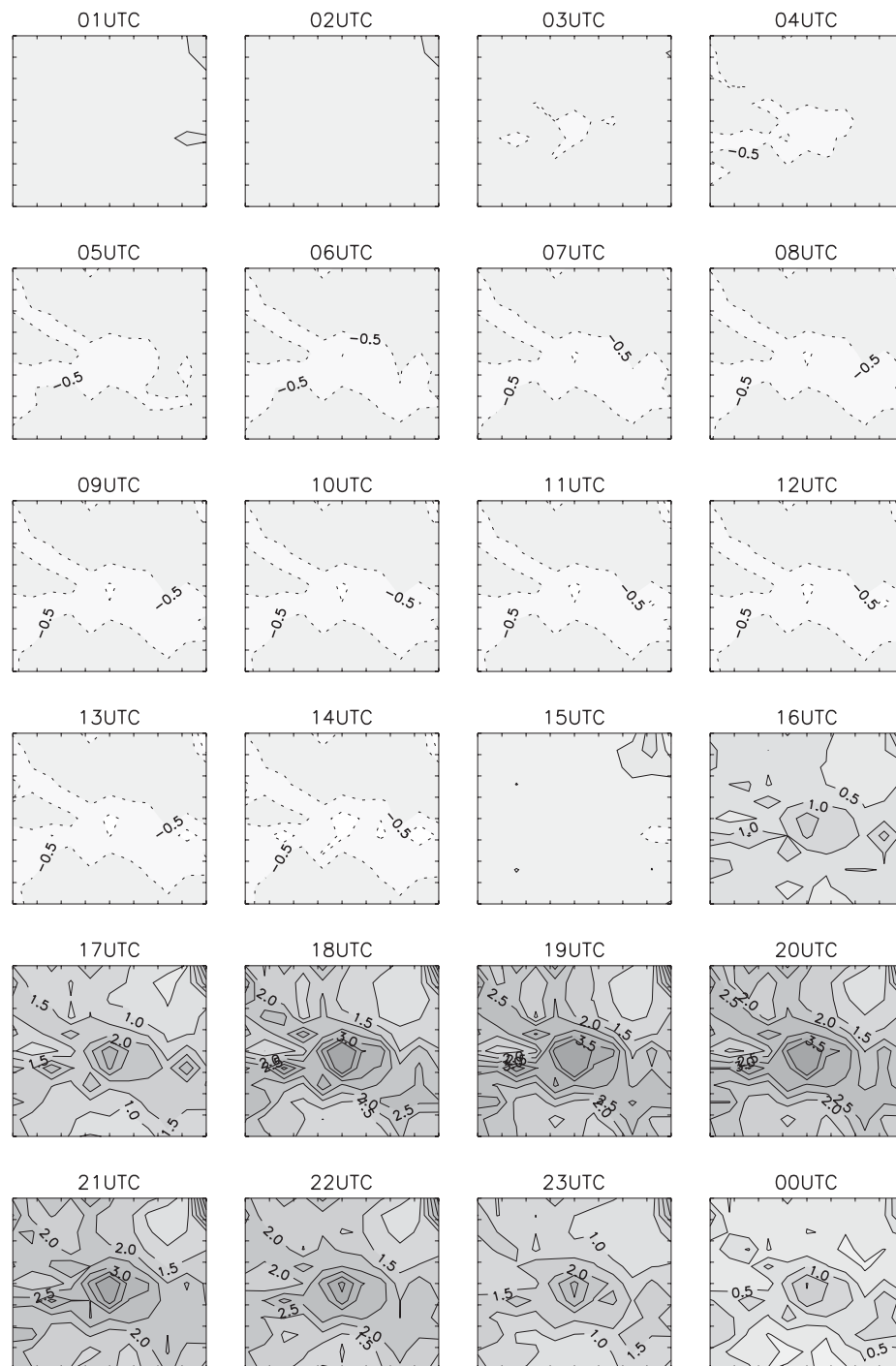


Figure 36. Distributions of ground temperature difference (IN1D - HO1D) in HOU from 0100 UTC to 0000 UTC. Contour intervals are 0.5 K.

*b. Results*

The GOES skin temperature retrieval errors caused by an inhomogeneous surface are estimated here. The estimation method explained above was applied in the HOU area which is the same area of interest investigated in the 1-d PBL simulations in the previous chapter. The IN1D simulations parameterized with 10 subgrid-scale land types resulted in the distribution of subgrid-scale ground temperatures in the HOU area illustrated in Figure 37 by the histogram. The IN1D simulated ground temperatures ranging from 290 K to about 334 K during the period of one day forecast. During the daytime of intense solar radiation between 1700 UTC and 2300 UTC, the model-simulated subgrid-scale ground temperatures indicated maximum about 334 K for hottest land types such as roads and minimum about 305 K for those of the coldest such as water bodies and wet land. With these distributions the skin temperature errors are estimated in the HOU during the course of the day as illustrated in Figure 38.

Notice that the sign of the estimated errors is chosen such that the values are of the inhomogeneous effects rather than retrieval error. This is the case for all figures in this section. During the nighttime no significant impacts are seen in the entire HOU area. Until 1400 UTC the effects are limited to 0.1 K. During the daytime the effects increased by up to about 0.6 K at 2000 UTC around the Houston downtown (HDT) where road and impervious land types are relatively dominant compared to other areas. From 1700 UTC to 2200 UTC, the effects remained between 0.2 K and 0.6 K in most areas except for the northeastern part where coniferous forest was more dominant.

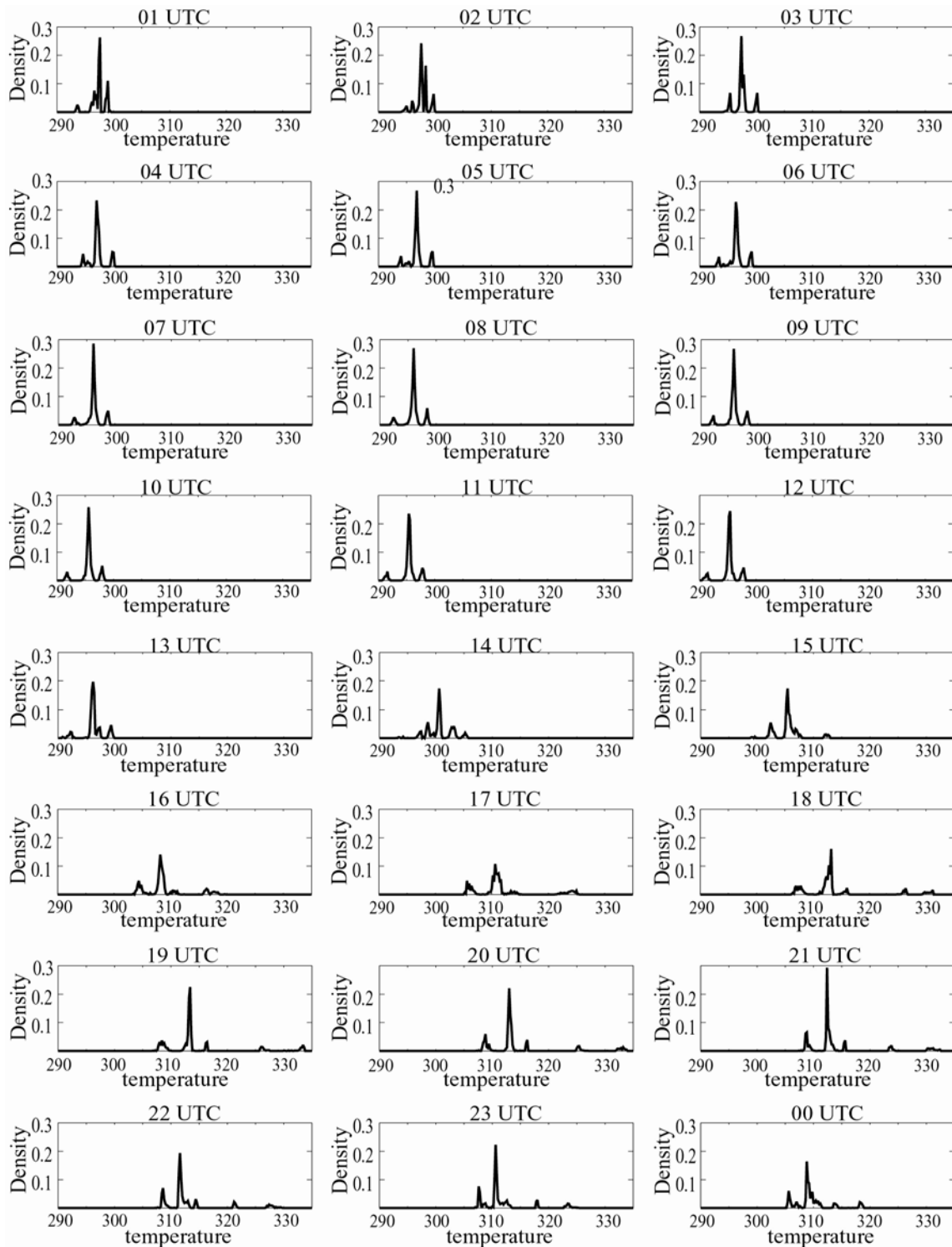


Figure 37. Histograms representing densities of the IN1D subgrid-scale ground temperatures with 0.2 K bin size in the HOU area.

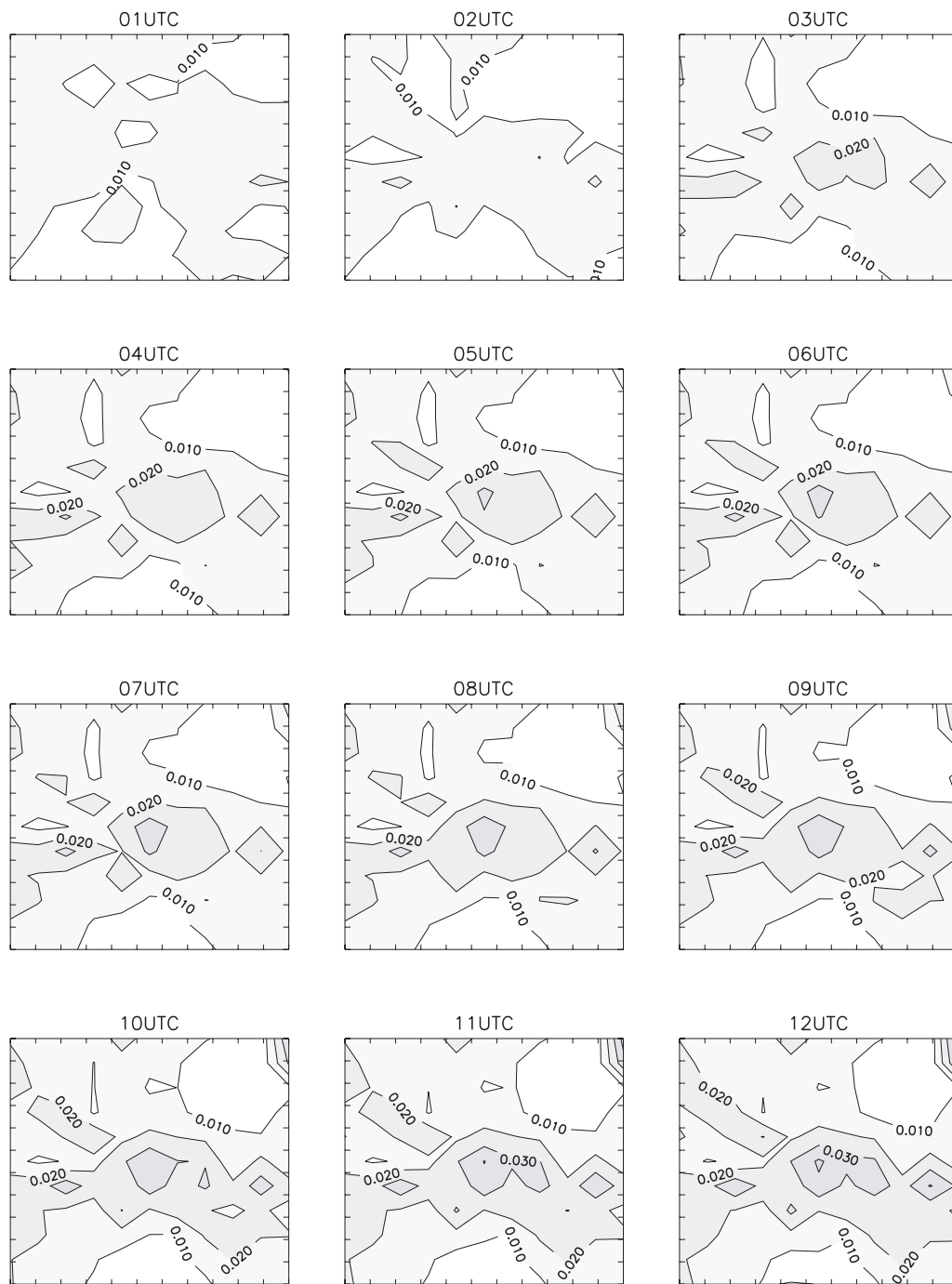


Figure 38. Distribution of the GOES skin temperature retrieval error induced by the inhomogeneous ground temperature within grid elements in the HOU area. Contour lines are in 0.01 K interval (0100 UTC - 1200 UTC) and 0.04 K interval (1300 UTC - 0000 UTC).



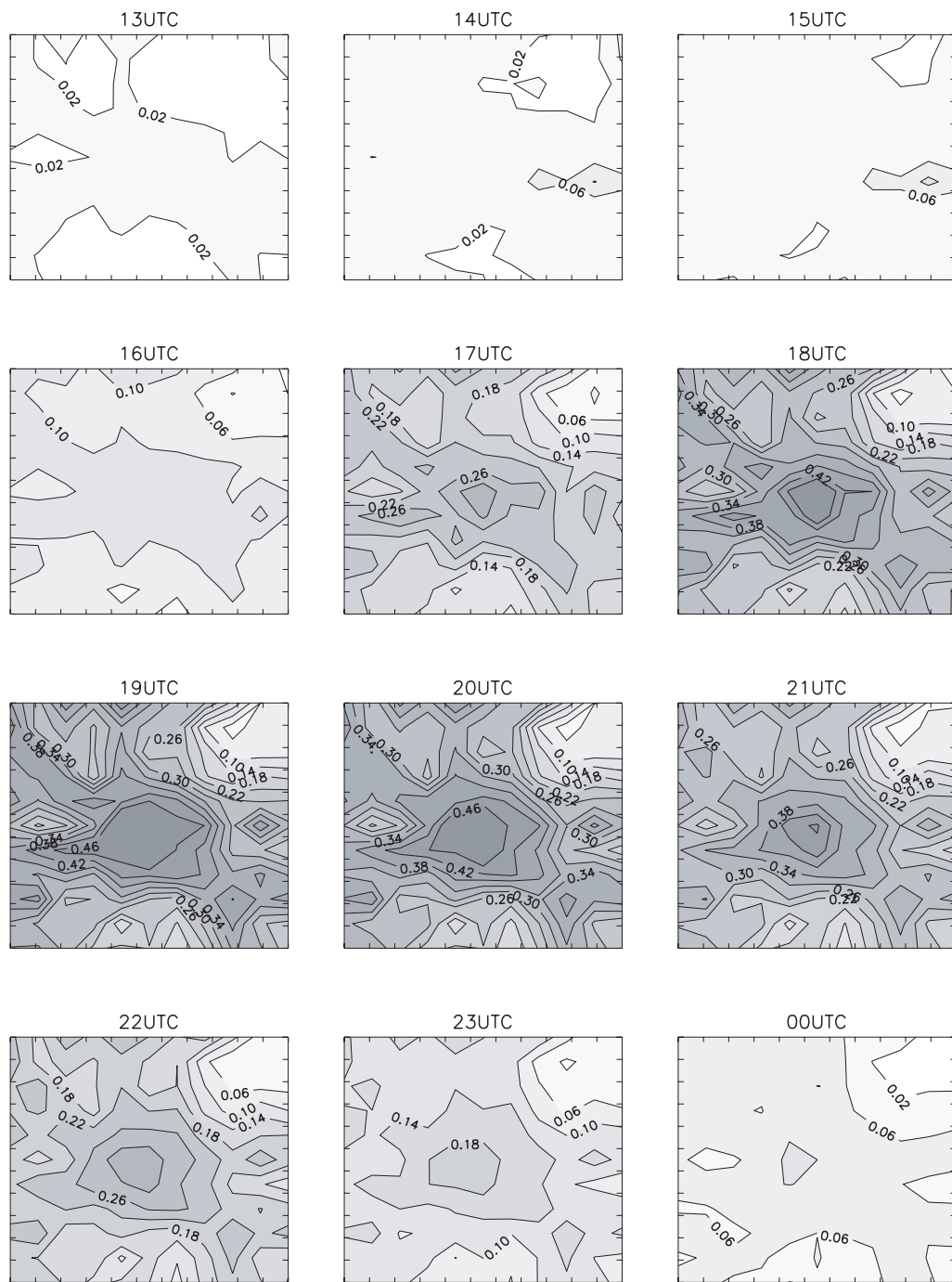


Figure 38. Continued.

#### 4. Investigation of model impacts caused by the GOES skin temperature error

##### *a. Method*

In order to examine model impacts implied by the inhomogeneity-caused GOES skin temperature errors, the GOES data assimilation technique was applied into the homogeneous 1-d PBL model simulations (HO1D) of the previous chapter with other simulation factors not changing. Here, we regard the ground temperature produced from the inhomogeneous run (IN1D) as GOES skin temperature, and the homogeneous run as the model. Thus, the ground temperature from the inhomogeneous run was assimilated (a) with and (b) without the error correction obtained from the error estimation in the previous section. The difference of model results between (a) and (b) is interpreted as the model impacts induced by the GOES skin temperature retrieval error.

The assimilation was implemented between 1400 UTC and 1800 UTC during the 24-h integration period started from 0000 UTC. From the end time of the assimilation cycle the soil moisture availability was kept at the value obtained from the assimilation until the end of model integration. In the assimilation cycle, the rate of change of the satellite-observed ground temperature,  $\left(\frac{dT_G}{dt}\right)_s$ , in Eq. (46), is computed at every time step using the temperatures linearly interpolated into the model time steps from hourly outputs of the inhomogeneous run. Also, the rate of change of the model ground temperature,  $\left(\frac{dT_G}{dt}\right)_m$ , is calculated at every time step as well. In this assimilation, in order to ensure computational stability, 100 s spanning time is used in the computation of the rate of change of the ground temperature for both the satellite and model. Using the satellite-observed latent heat flux,  $E_s$  calculated from (46), the satellite-inferred soil moisture availability is obtained from Eq. (48). Meanwhile, the model-diagnosed latent heat flux,  $E_m$  is replaced by  $E_s$ . Within the assimilation cycle (1400 UTC – 1800 UTC), when the fractional change of the soil moisture availability is less than 0.01, the model soil moisture availability was allowed to be updated. But at the end of the cycle the soil moisture availability was updated unconditionally.

Table 11. HOU-area-averaged soil moisture availability and percent difference of the GOES assimilation soil moisture availability from the model value.

	Model	GOES without correction	GOES with correction
Soil moisture availability	0.200	0.216	0.221
Percent difference		8 %	11 %

*b. Results*

Here, we call the GOES assimilation runs with the error correction GCOR and without the error correction GERR. First of all, at the end of the assimilation cycle, the GOES assimilations resulted in soil moisture availabilities of 0.215 and 0.221 for the GERR and GCOR, respectively, in the HOU area. Each value represents 8 % and 11 % increase from the HOU-area-averaged soil moisture availability (0.2) of the model (Table 11).

Model errors were obtained by subtracting the results of the GCOR from those of GERR. Figure 39 illustrates those errors, in the HOU area, of ground temperature, 4m potential temperature, 4m wind speed, 4m specific humidity, and surface sensible and latent heat fluxes. The errors were averaged in time between 1600 UTC and 2300 UTC.

In general, the error patterns indicate that local maxima of the absolute errors occurred around areas where the grid-mean surface parameter values are small except for the surface albedo (see Fig. 17). It is seen that the error distribution does not match well with those of the ground temperature errors during the assimilation cycle between 1400 UTC and 1800 UTC as indicated in Figure 38. This might be caused by the assumption of the assimilation technique that the difference of the rate of change of the ground temperature between the model and satellite is induced only by the latent heat flux term as expressed in (46). Further consideration of that issue is not given in this study. As a result of about 3 % lower

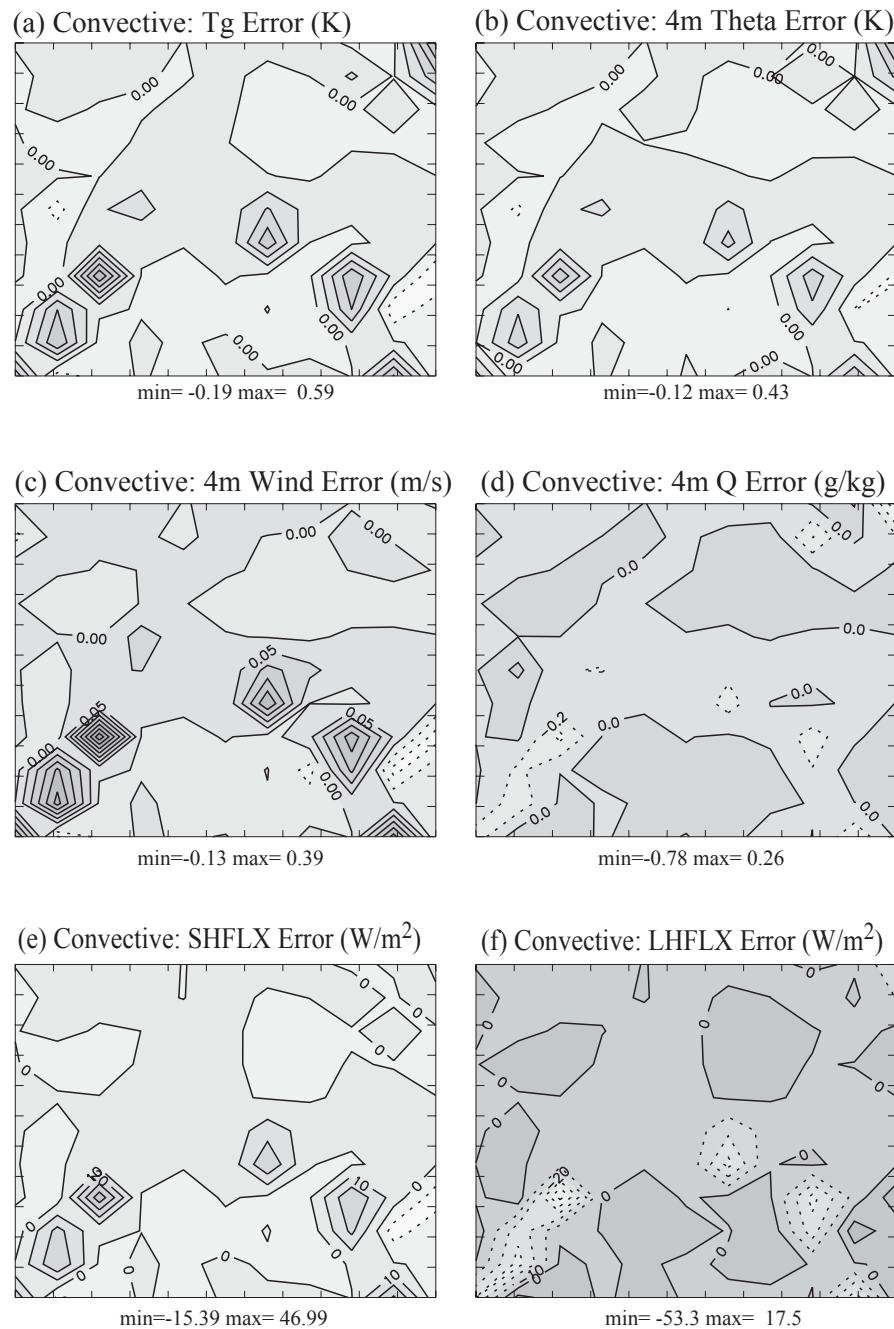


Figure 39. Distribution of time-averaged (between 1600 UTC and 2300 UTC during the convective regime) errors caused by the GOES ground temperature retrieval error in HOU: (a) ground temperature, (b) 4m potential temperature, (c) 4m wind speed, (d) 4m specific humidity, (e) sensible heat flux, and (f) latent heat flux. The maximum and minimum values in the domain are indicated at the bottom of each figure.

soil moisture availability than the GCOR, the GERR produced positive sensible heat flux errors and negative latent heat flux errors in most HOU areas (Figs. 39e and 39f). Due to the positive sensible heat flux errors, positive 4m potential temperature errors with a similar pattern were induced as illustrated in Figure 39b.

In order to examine the time variation of the errors, the HOU-area-averaged errors were calculated and provided in figures 40 and 41. It seems that the errors are very small until about 1700 UTC because the inhomogeneity-caused ground temperature errors are small. As the ground temperature error grows the model errors appeared to increase from 1700 UTC. From the end point of the assimilation cycle the model errors are produced by the soil moisture availability difference between the GCOR and GERR. The surface sensible and latent heat flux errors maintained at about  $4 \text{ Wm}^{-2}$  and  $-4 \text{ Wm}^{-2}$ , respectively, between 1800 UTC and 2100 UTC. Those errors gradually decreased after 2100 UTC (Figs. 40a and 40c). As illustrated in the figure, the errors of the surface variables gradually increased from about 1700 UTC until 2100 UTC, consistent with the flux errors. Even though the magnitudes of the errors are small, it is obvious that the GOES assimilation might result in the errors caused by the inhomogeneity-caused ground temperature retrieval error.

Figure 42 shows the assimilation errors induced by GOES ground temperature retrieval error in the PBL averaged in the HOU at 2200 UTC. As explained in the previous chapter, the errors in the surface layer caused almost the same magnitude of errors in the well-mixed layer. Near the PBL top, the direction of the errors was reversed due to vertical mixing exchange errors induced by the surface flux error.

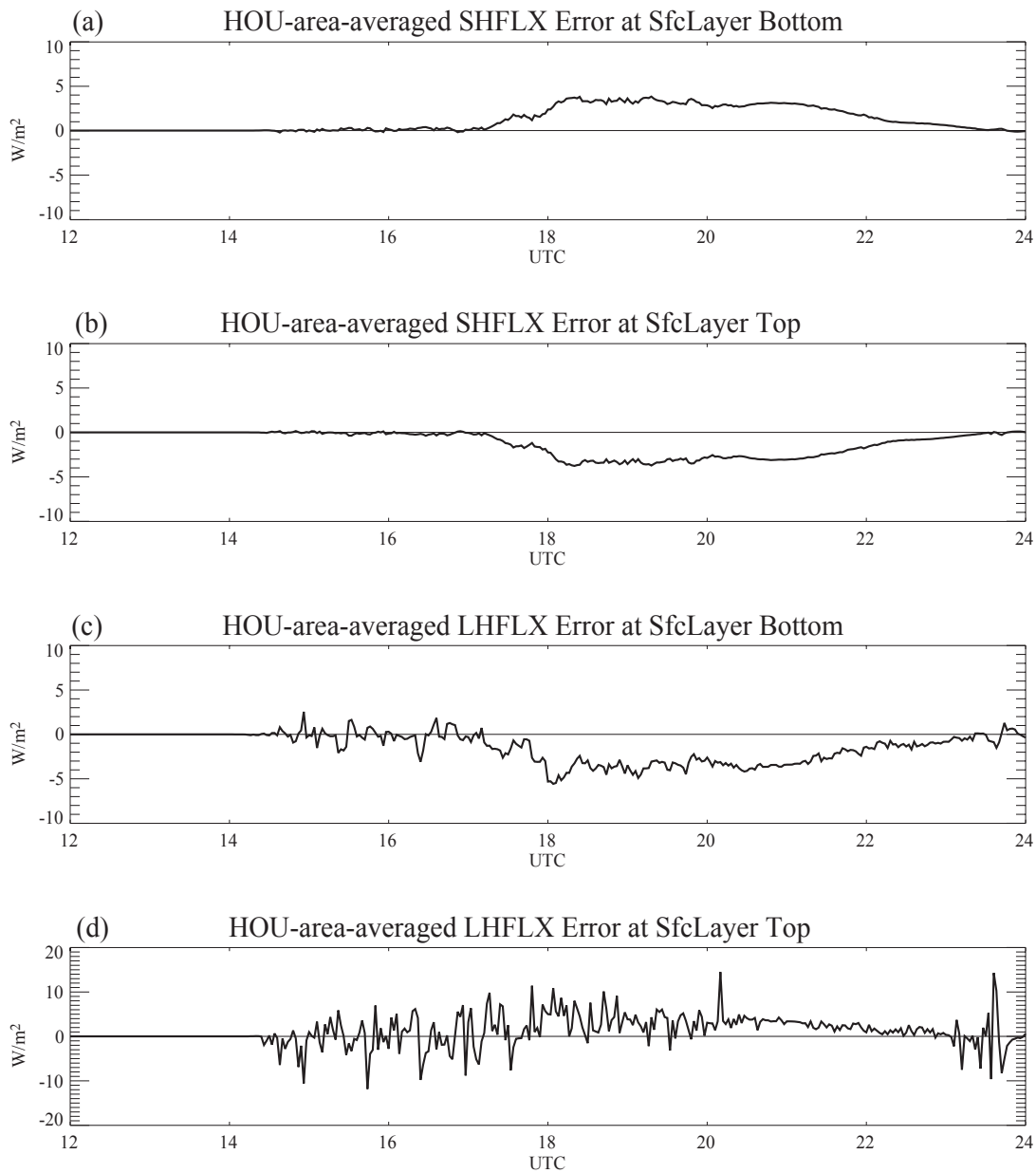


Figure 40. The HOU-area-averaged sensible and latent heat flux errors caused by GOES ground temperature retrieval error as function of forecasting time: (a) SHFLX error at the surface layer bottom, (b) those at the top, (c) LHFLX error at the surface layer bottom, and (d) those at the top.

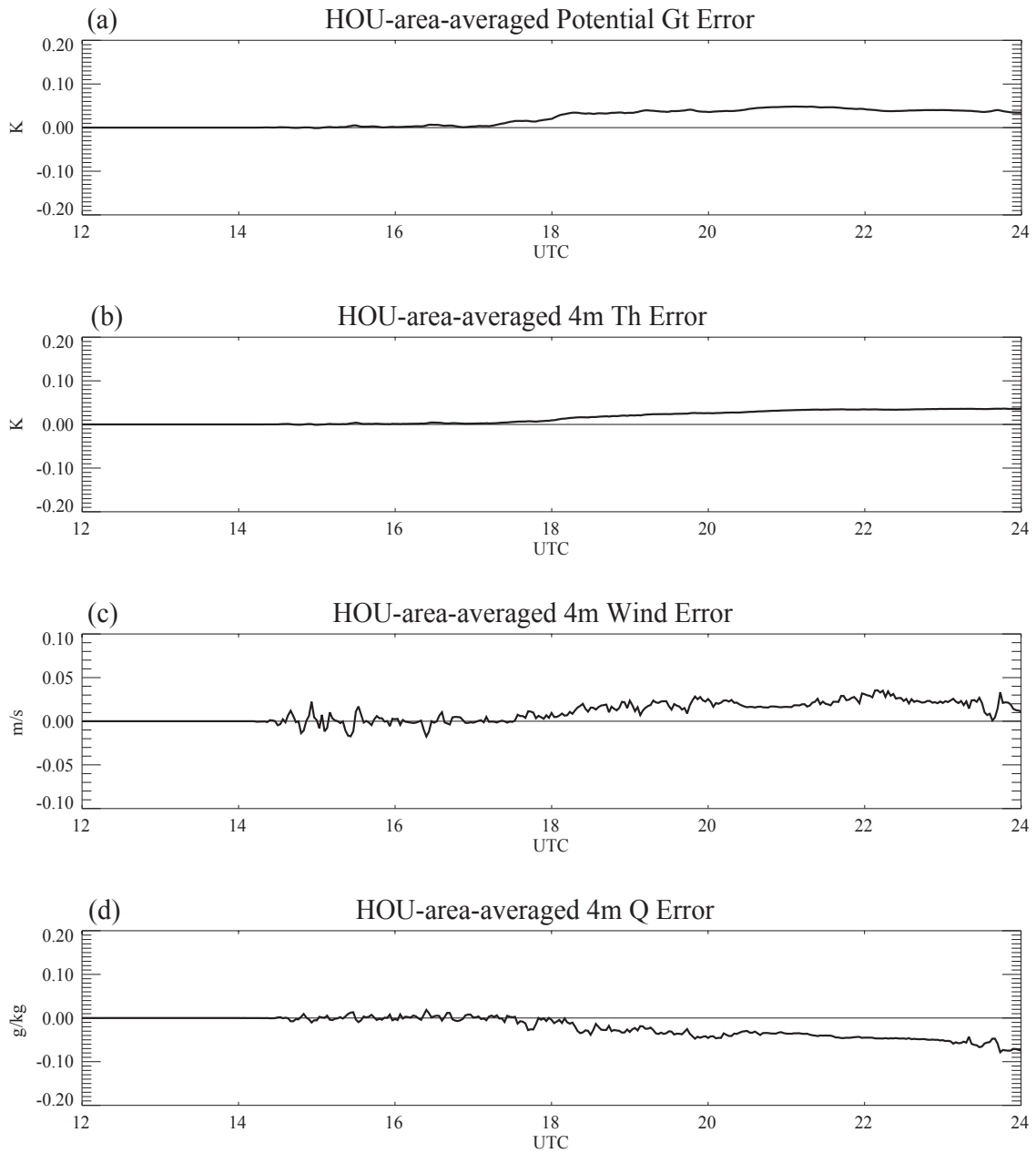


Figure 41. The HOU-area-averaged surface variable errors caused by GOES ground temperature retrieval error as function of forecasting time: (a) potential ground temperature, (b) 4m potential temperature, (c) 4m wind speed, and (d) 4m specific humidity.

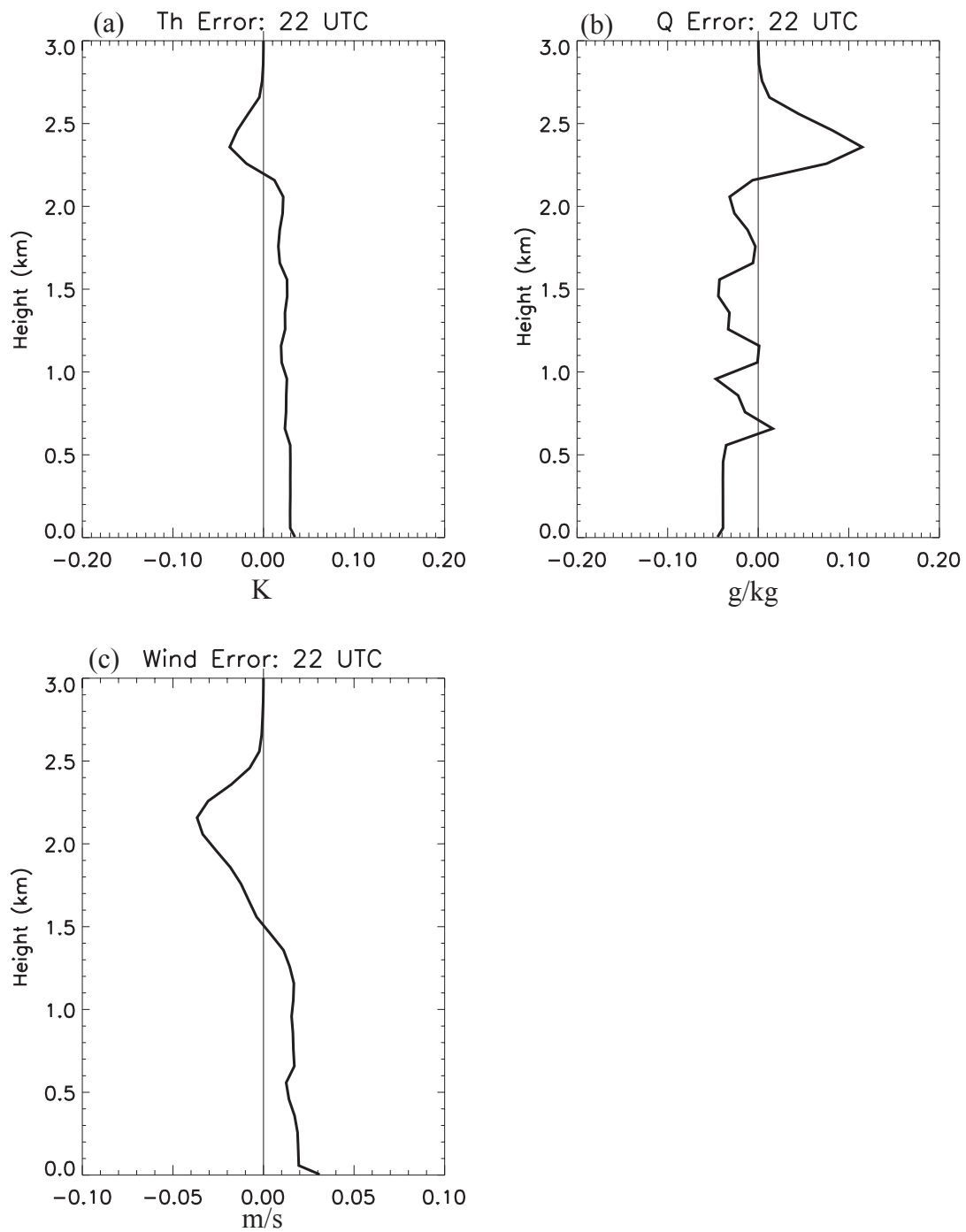


Figure 42. Error profiles of HOU-area-averaged PBL variables induced by GOES ground temperature retrieval error at 22 UTC: (a) potential temperature, (b) specific humidity, and (c) wind speed.



Table 12. Percent errors induced by inhomogeneous ground temperature in the 1-d PBL model of the GOES skin temperature assimilation technique (GERR).

SHFLX	LHFLX	4mQ	4mWind	4mTh	Tg
1.47	-0.83	-0.24	0.57	0.10	0.20

In summary, with the negative ground temperature errors induced by treating the surface homogeneously, the GOES assimilation run resulted in positive errors for the sensible heat flux, ground temperature, and well-mixed PBL temperature and wind and negative errors for the latent heat flux and well-mixed PBL humidity. In Table 12 the percent errors for those variables are listed. The percent errors were calculated using mean error values obtained by averaging in time between 1800 UTC and 2200 UTC and in the HOU area. The reference values are those of the GCOR. And the temperature reference values were normalized with the amplitude of the temperature diurnal cycle of the GCOR.

## 5. GOES assimilation errors associated with linear interpolation of hourly ground temperature into model time step

### *a. Method*

In the GOES skin temperature assimilation technique, the rate of change of the satellite ground temperature is calculated using temperatures linearly interpolated into the model time steps from the hourly observations within the assimilation cycle. The linear interpolation implies errors because the ground temperature varies non-linearly during the assimilation cycle (1400 UTC – 1800 UTC) in general.

In this section those GOES assimilation errors are estimated using the 1-d PBL model. The assimilation technique is applied in the same way as in the previous section. Methodologically, ground temperatures at hourly intervals obtained from the 1-d simulation without the assimilation are regarded as true values observed from GOES satellite. These ground temperatures are assimilated in the same 1-d model which produced the ground temperatures defined as true value. Due to the linear interpolation of the temperature, the

assimilated simulation (child simulation) results can not be the same as the original simulations (mother simulation) which supplied with the true hourly ground temperatures. The difference, between the child simulation with assimilation and the mother simulation without assimilation, is defined as the GOES skin temperature assimilation error caused by the linear interpolation error.

In order that homogeneous and inhomogeneous treatment of model surfaces can be compared, the homogeneous and inhomogeneous 1-d models are used as the ground temperature-supplying mother and to-be-assimilated child simulations. That is, each 1-d mother model produces the hourly ground temperatures defined as truth, then becomes the child model which assimilates the interpolated ground temperatures produced by itself.

*b. Results from homogeneous simulation*

In Figure 43, the distribution of assimilation errors in HOU (child simulation minus mother simulation) of the sensible and latent heat fluxes and the surface layer potential temperature and specific humidity are illustrated for the homogeneous 1-d simulation. The errors are averaged in time between 1800 UTC and 2200 UTC. The 1800 UTC is the assimilation ending time.

As can be seen in the figure, the distribution of errors indicates similar pattern among the variables. The error magnitude is distinctly bigger in forest area compared to the other areas. Except for the forest areas, positive errors for the sensible heat flux and surface layer temperature and negative errors for the latent heat flux and surface layer specific humidity are produced. The reason for the difference of errors between land types is not investigated further in this study.

In order to see how the assimilation errors evolve in time, area-averaged errors in two different sub-areas are presented in Figure 44. Because of the distinct difference the forest and downtown areas are chosen as the two sub-areas illustrated in Figure 14 as boxes. The

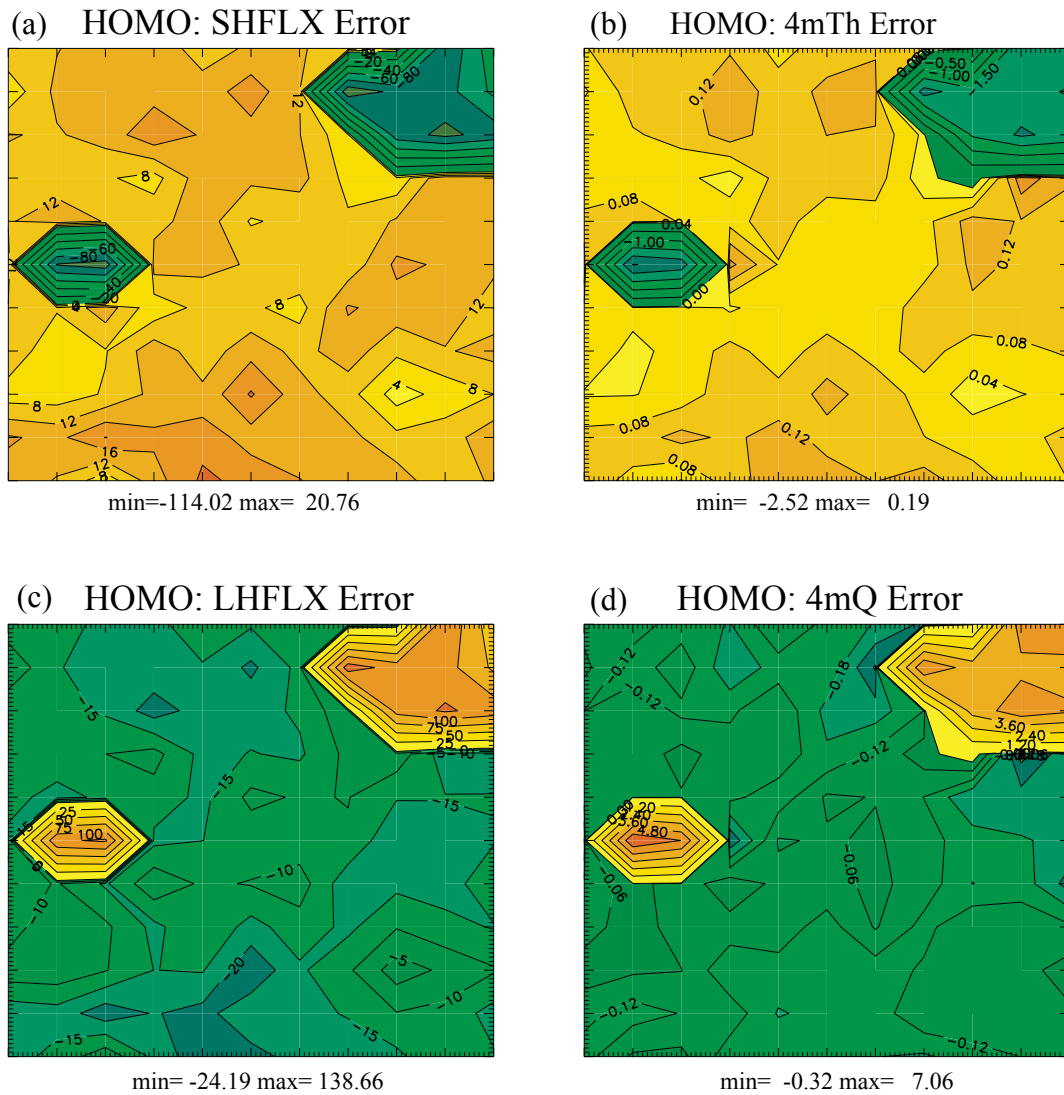


Figure 43. The GOES skin temperature assimilation errors of the homogeneous 1-d PBL model caused by the linear interpolation of hourly observed ground temperatures in HOU: (a) sensible heat flux ( $\text{W m}^{-2}$ ), (b) surface layer potential temperature (K), (c) latent heat flux ( $\text{W m}^{-2}$ ), and (d) surface layer specific humidity (g/kg). The errors are averaged in time between 1800 UTC and 2200 UTC.

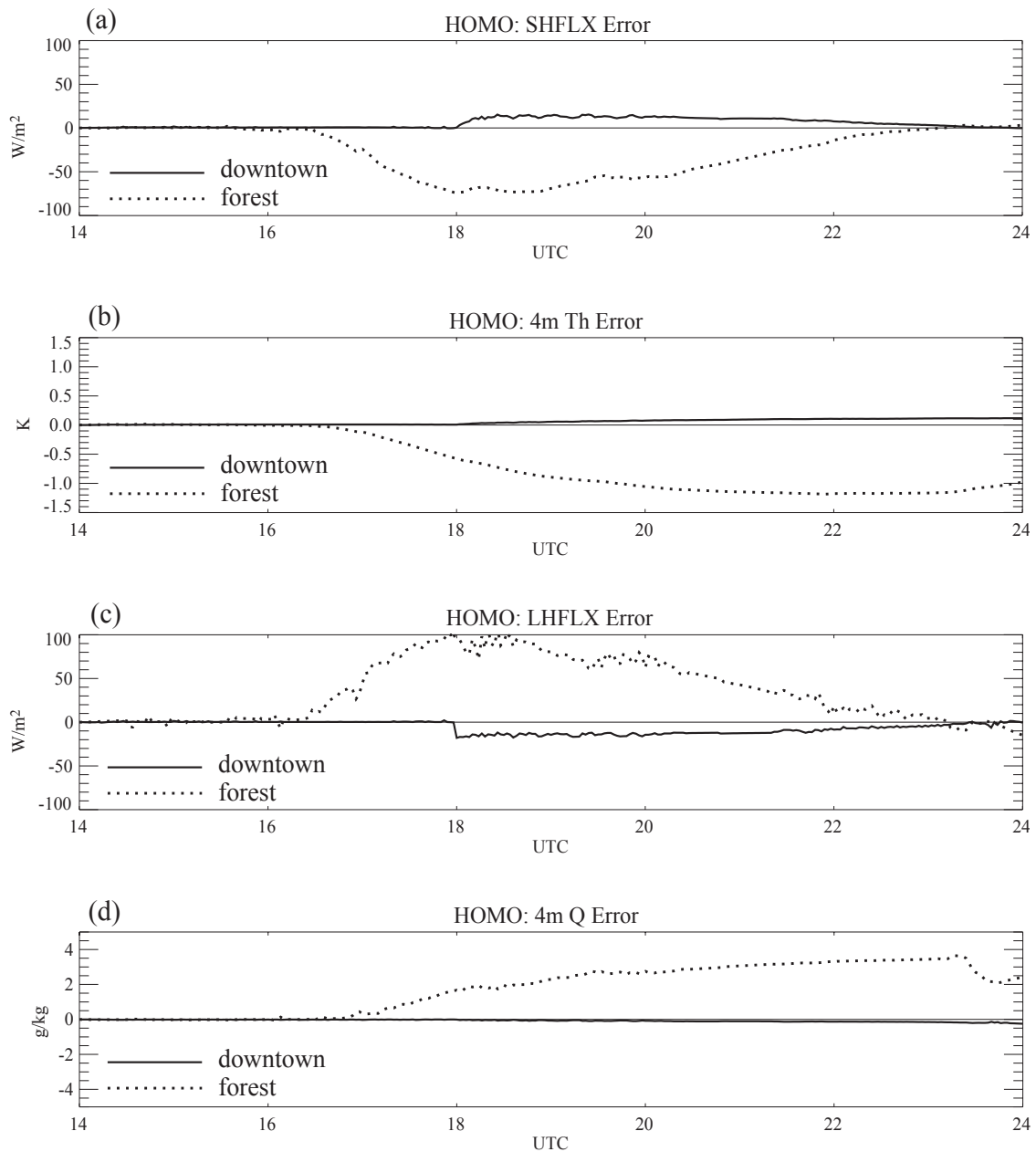


Figure 44. The HOU-area-averaged GOES skin temperature assimilation error of the homogeneous 1-d PBL model caused by the linear interpolation of the observed hourly ground temperature: (a) sensible heat flux ( $W m^{-2}$ ), (b) surface layer potential temperature (K), (c) latent heat flux ( $W m^{-2}$ ), and (d) surface layer specific humidity (g/kg).

error features that the forest area showed much bigger errors are as explained above from the spatial distribution between 1800 UTC and 2200 UTC. The characteristic features are that flux errors tend to peak within about two hours after the end of assimilation cycle (1800 UTC), then gradually decline recovering from the errors at close to 0000 UTC. In contrast to fluxes the errors of surface variables gradually grow until about 2200 UTC, then remain at that level afterwards. The reason for this feature is not known at present.

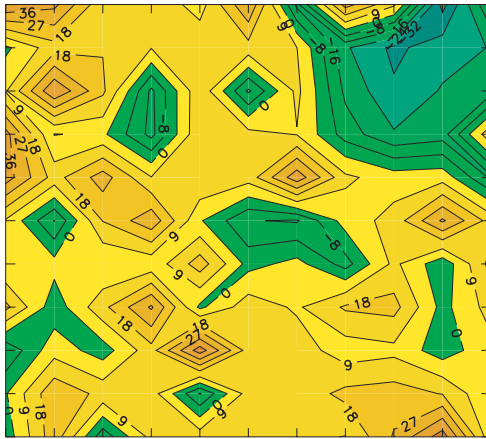
*c. Results from inhomogeneous simulation*

The assimilation errors (Fig. 45) obtained using the inhomogeneous 1-d model simulation shows some differences from those of homogeneous 1-d simulation. Though the overall feature seems to be similar to each other, much spatial variability of errors is indicated from the inhomogeneous simulation. As in the homogeneous simulation, the forest area shows the negative errors for sensible heat flux and surface layer temperature. As an additional characteristic feature there are negative error areas which are positive error areas in the homogeneous simulation. The downtown area is one such case. The error features for the latent heat flux and surface layer specific humidity are the same as those for sensible heat flux and temperature but for reversed sign.

Figure 46 shows the evolution of errors in time for the two sub-areas, forest and downtown. The characteristic features are as indicated in the homogeneous case. However, compared to the homogeneous simulation, amplitudes are much reduced. In particular, downtown errors is very small.

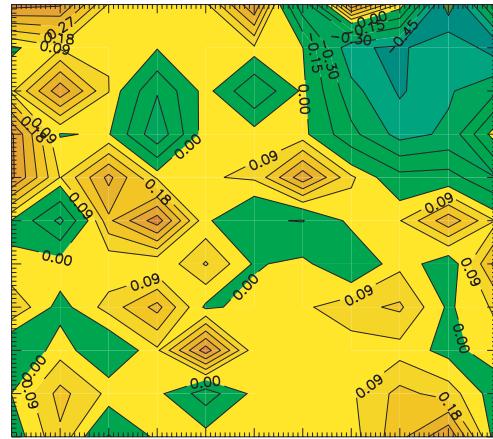
The percent errors for the fluxes and surface layer variables were calculated between 1800 UTC and 2200 UTC in the forest sub-area, downtown sub-area, and entire HOU, separately. The method is that  $\text{Percent error} = 100 \times (\text{child} - \text{mother}) / (\text{absolute mother})$ .

(a) INHOMO: SHFLX Error



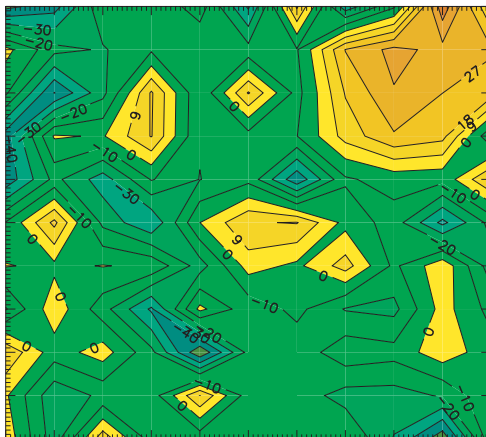
min= -42.89 max= 49.88

(b) INHOMO: 4mTh Error



min= -0.85 max= 0.50

(c) INHOMO: LHFLX Error



min= -58.49 max= 50.75

(d) INHOMO: 4mQ Error



min= -0.53 max= 2.53

Figure 45. The same as Figure 43 but for the inhomogeneous runs.

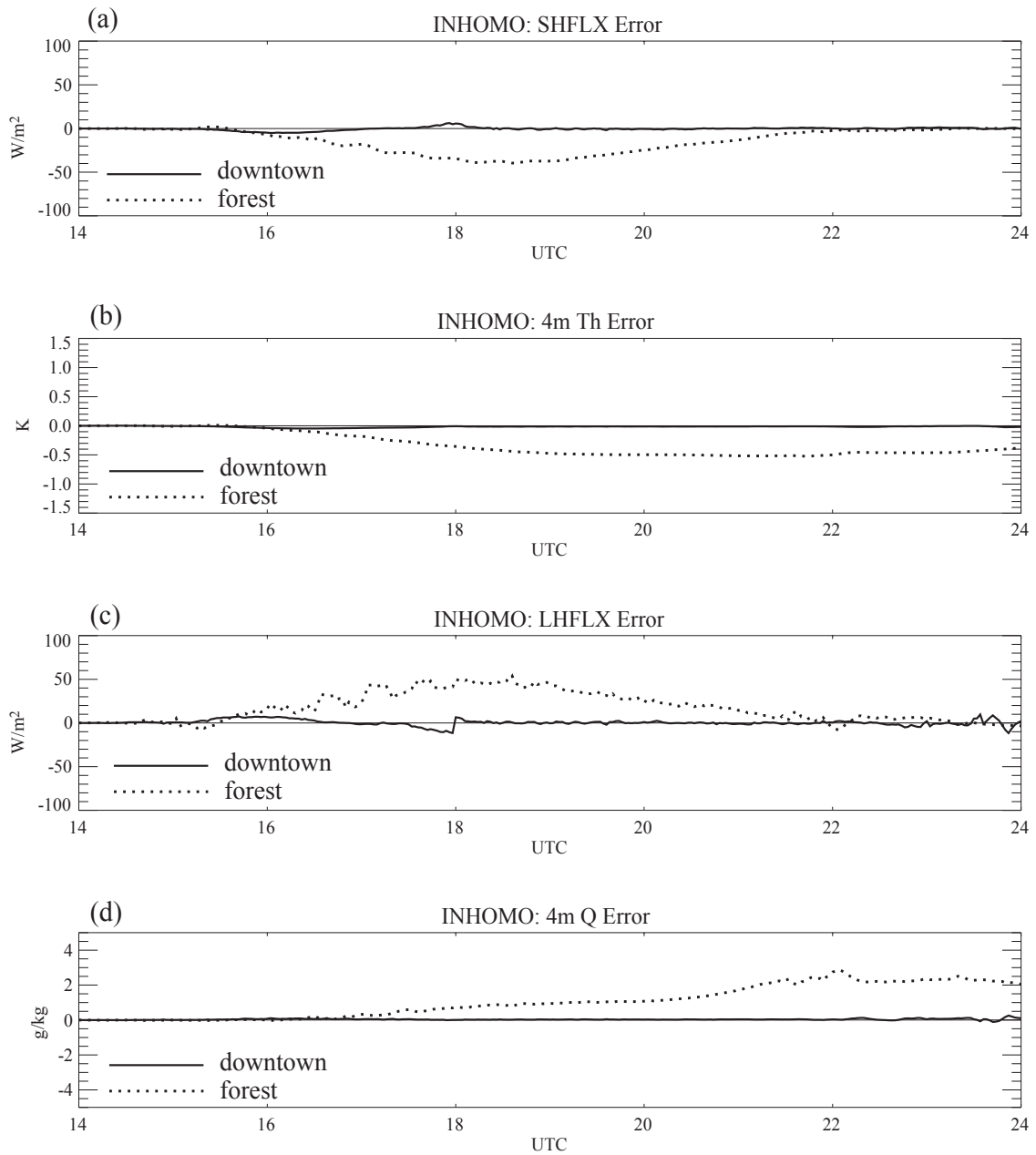


Figure 46. The same as Figure 44 but for the inhomogeneous 1-d model assimilation.

The results are in Table 13. From the Table, as explained above, the contrast between the forest and downtown is obvious for the homogeneous simulation. Because relatively much greater errors are in the local forest area the HOU area errors is not relevant for the representative mean assimilation errors from the homogeneous simulation. Therefore, from the inhomogeneous simulation, on average the assimilation errors induced by the linear interpolation error are to increase sensible heat flux by about 2.6 % and to decrease latent heat flux by about -2.7 %. The errors in the surface layer temperature is negligibly small.

Table 13. Percent errors of sensible (SHFLX) and latent (LHFLX) heat fluxes, surface layer potential temperature (4mTh), specific humidity (4mQ) and wind speed (4mWind), and ground temperature (Tg). Bold and plain numerals indicate errors obtained from inhomogeneous and homogeneous simulations, respectively.

	<b>SHFLX</b>	LHFLX	4mTh	4mQ	Tg	4mWind
Downtown Sub-area	<b>0.02</b> 4.36	<b>0.17</b> -4.05	<b>-0.05</b> 0.31	<b>0.24</b> -0.69	<b>-0.05</b> 0.68	<b>-0.37</b> 1.81
Forest Sub-area	<b>-11.83</b> -32.52	<b>6.28</b> 13.08	<b>-1.87</b> -3.87	<b>8.89</b> 17.08	<b>-2.90</b> -5.66	<b>-10.84</b> -3.17
Entire HOU Area	<b>2.55</b> 1.25	<b>-2.70</b> -0.65	<b>0.05</b> -0.39	<b>0.88</b> 2.76	<b>0.43</b> -0.46	<b>1.01</b> 1.91

## 6. GOES assimilation errors caused by using the model without surface inhomogeneity parameterization

### *a. Method*

From the results of chapter III, it is suggested that the homogeneous treatment of model grids caused negative ground temperature errors by up to about -4.0 K around HDT during the assimilation cycle (1400 UTC – 1800 UTC). Most other areas in HOU also experienced the negative errors ranging from -0.5 K to -3.0 K during the assimilation period. The negative ground temperature errors are likely to produce systematic errors in applying the GOES assimilation technique to the model with homogeneous treatment of surface characteristics over inhomogeneous areas such as in HOU.



In order to investigate those errors the same methodology as in the previous section was applied. Here, the assimilation of the inhomogeneous 1-d model is regarded to produce the true values. The assimilation of the homogeneous 1-d model produces the model errors induced by the ground temperature error. For both the inhomogeneous and homogeneous assimilations the ground temperatures produced by the inhomogeneous 1-d are used as the GOES skin temperature to be assimilated. The difference of variables between the two assimilations is defined as the model assimilation error. Thus, the homogeneous 1-d assimilations results subtracted by the inhomogeneous 1-d assimilation results are the GOES assimilation errors caused by the model's ground temperature error.

### *b. Results*

Figure 47 illustrates those errors, in the HOU area, of (a) sensible heat flux, (b) 4m potential temperature, (c) latent heat flux, and (d) 4m specific humidity. The errors were averaged in time between 1600 UTC and 2300 UTC. In general, the errors are opposite to those errors estimated in the previous two sections, that is, the errors associated with GOES ground temperature retrieval error and linear interpolation of the GOES ground temperature. Negative sensible heat flux and positive latent heat flux errors are indicated in the entire HOU area. Those errors range from  $-17 \text{ Wm}^{-2}$  to  $-185 \text{ Wm}^{-2}$  for the sensible heat flux and from  $28 \text{ Wm}^{-2}$  to  $227 \text{ Wm}^{-2}$  for the latent heat flux. Consistent with the flux errors in general, negative 4m potential temperature and positive 4m specific humidity errors with similar pattern to those of fluxes are produced in most HOU areas except for some exceptional areas. Compared to the flux errors it is seen that the errors in surface variables are not as significant as those of surface fluxes. Apart from two local maxima areas most HOU areas are confined to absolute errors of 0.5 for both the surface variables.

In order to examine the time variation of the errors, area-averaged-errors for the fluxes and surface layer variables were calculated between 1400 UTC and 0000 UTC in the forest sub-area and downtown sub-area, separately (Fig. 48). Typical differences between the two areas are not found. It is seen that, as the model's ground temperature error grows, the model assimilation errors appear to increase during the assimilation cycle (1400 UTC – 1800 UTC). From the end point of the assimilation cycle the model errors are produced by the combined

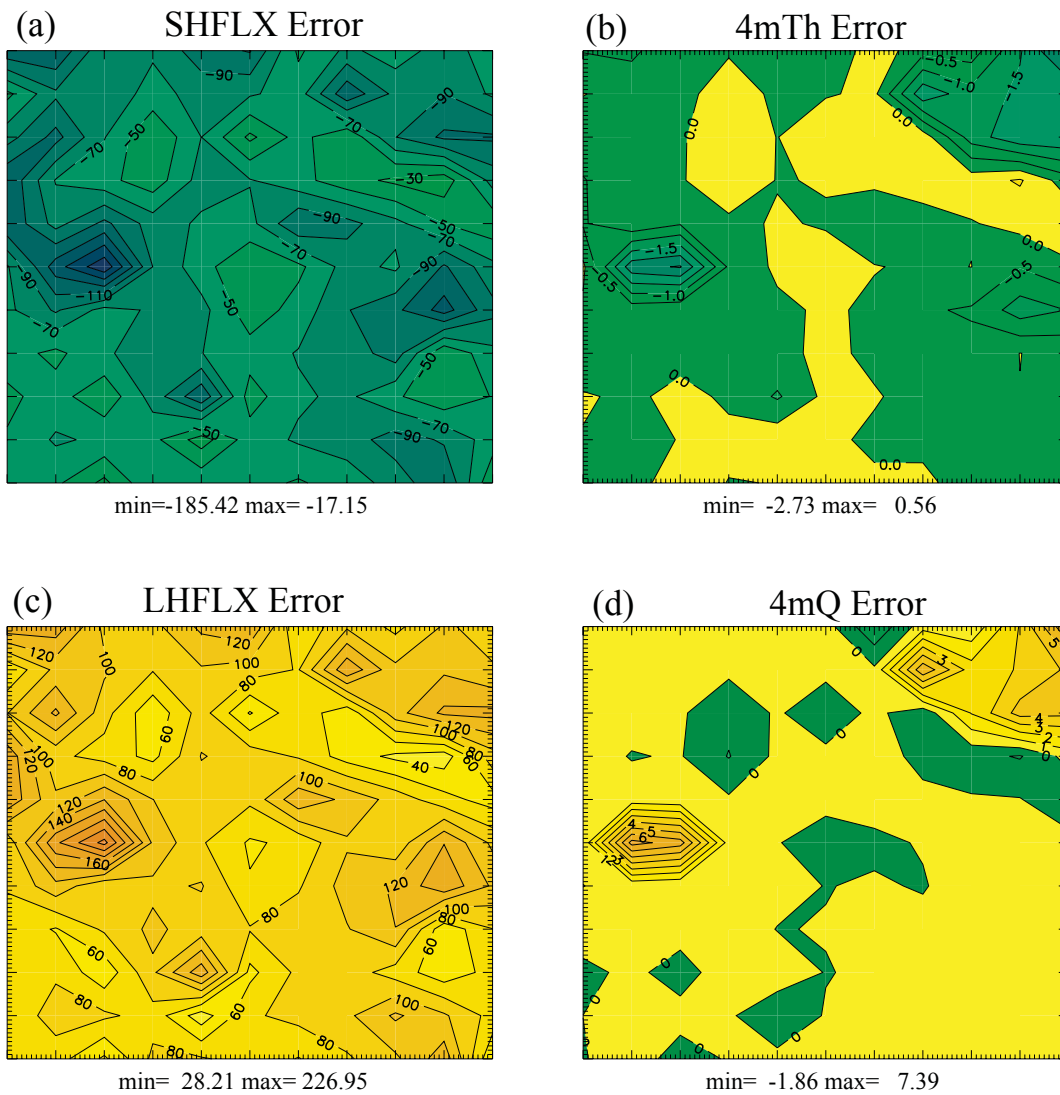


Figure 47. The GOES skin temperature assimilation errors of the homogeneous 1-d PBL model caused by the model ground temperature error in HOU: (a) sensible heat flux ( $\text{W m}^{-2}$ ), (b) surface layer potential temperature (K), (c) latent heat flux ( $\text{W m}^{-2}$ ), and (d) surface layer specific humidity (g/kg). The errors are averaged in time between 1800 UTC and 2200 UTC.

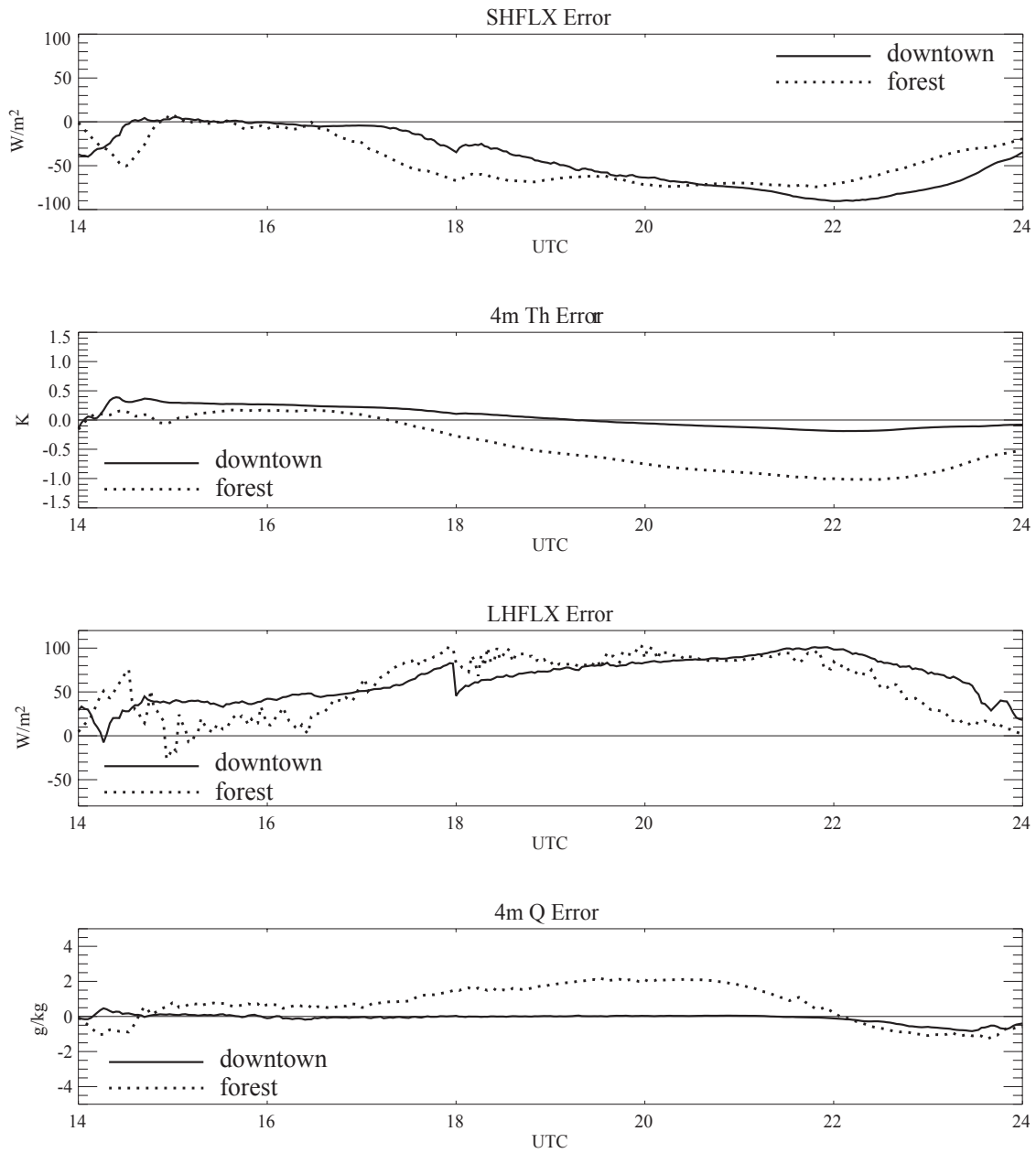


Figure 48. The HOU-area-averaged GOES skin temperature assimilation error of the homogeneous 1-d PBL model caused by the model ground temperature error: (a) sensible heat flux ( $\text{W m}^{-2}$ ), (b) surface layer potential temperature (K), (c) latent heat flux ( $\text{W m}^{-2}$ ), and (d) surface layer specific humidity ( $\text{g/kg}$ ).

effect of the soil moisture availability error, produced at the end of the assimilation cycle, and the assimilation model's homogeneous treatment of surface inhomogeneities. All variables show gradual increases of the error until about 2200 UTC, then the errors decline afterwards. Near the 2200 UTC the errors range from  $-60 \text{ Wm}^{-2}$  to  $-80 \text{ Wm}^{-2}$ ,  $-0.2 \text{ K}$  to  $-10 \text{ K}$ ,  $80 \text{ Wm}^{-2}$  to  $90 \text{ Wm}^{-2}$ , and 0 to  $1.0 \text{ g/kg}$  for the sensible heat flux, 4m potential temperature, latent heat flux, and 4m specific humidity, respectively.

As in the previous section, the percent errors for the fluxes and surface layer variables were calculated between 1800 UTC and 2200 UTC in the entire HOU area. The results designated by Model error are in Table 14. In the Table other percent errors caused by the GOES ground temperature retrieval error (GOES error) and the combined two errors (Total error) are also included in order to compare the Model and GOES errors and see the total errors. As mentioned earlier the opposite trends of the two assimilation errors are indicated. On average the errors caused by the GOES errors compensate for the Model errors by about 3 % to 10 % of the Model errors.

As a conclusive remark, from the investigation of the GOES assimilation errors presented in this chapter, it is visualized as follows. The surface inhomogeneity causes (a) the negative GOES skin temperature retrieval error and (b) the negative model ground temperature error. Then, the (a) and (b) factors induce the assimilation model errors opposite to each other. Thus, in this study the combined two errors produced 23 % decreased sensible heat flux, 30 % increased latent heat flux. Consistent with the flux errors, surface layer temperature decreased by about 0.9 % and surface layer humidity increased by about 3.6 %.

Table 14. Percent errors of sensible (SHFLX) and latent (LHFLX) heat fluxes, surface layer potential temperature (4mTh), specific humidity (4mQ) and wind speed (4mWind), and ground temperature (Tg) for two assimilation errors and their combination designated by Model error, GOES error, and Total error, respectively, in the first column.

	SHFLX	LHFLX	4mTh	4mQ	Tg	4mWind
<b>Model error</b>	-24.86	31.24	-0.99	3.82	-14.07	-3.32
<b>GOES error</b>	1.47	-0.83	0.10	-0.24	0.20	0.57
<b>Total error</b>	-23.39	30.41	-0.89	3.58	-13.87	2.75

**CHAPTER V**

**PRELIMINARY APPLICATION OF THE INHOMOGENEITY  
PARAMETERIZATION INTO A STANDARD MM5 SIMULATION IN USE OF  
MRF PBL SCHEME**

1. Introduction

In order to test the applicability of the inhomogeneity parameterization developed in the 1-d PBL model of chapter III, a preliminary application of the parameterization was implemented on a standard MM5 simulation to correct errors induced by the inhomogeneous surface characteristics in the Houston urban area. For this purpose, the parameterization method is integrated into the MM5's MRF scheme.

While the representation of surface fluxes in both the 1-d PBL model and MRF scheme is based on surface similarity theory, vertical mixing is estimated differently. In the 1-d PBL, assuming the eddy exchange coefficients for momentum, heat, and moisture to be equal to each other, the coefficients are determined as a function of local wind shear and local Richardson number derived by Blackadar (1976) for the case of stable conditions. For unstable conditions, the vertical mixing is visualized as taking place between the surface layer and each layer in the mixed layer (Blackadar, 1979) with the mixing coefficient being given by equation (35). As will be described later, the MRF scheme is based on formulations with bulk similarity for prescribing the exchange coefficients (turbulent diffusivity) in the boundary layer and includes nonlocal correctional terms in the computation of heat and moisture fluxes.

Therefore, effects of the parameterization applied into the MM5 simulation are likely to be quantitatively different from those of 1-d simulations. Furthermore, the horizontal diffusion and advection terms inherent with 3-d simulations may influence the parameterized inhomogeneity effects.

As in the 1-d simulations of chapter III, two MM5 simulations with and without the surface inhomogeneity parameterization are compared with each other to examine the impacts induced by the parameterization in the 3-d MM5 simulations.

## 2. Method of the inhomogeneity parameterization

Basically the same methodology as in the 1-d PBL model is applied into the MRF PBL scheme. That is, the urban grids in the model domain are imagined to be segmented into 10 subgrids of the 10 land cover types as classified in the chapter III over the Houston urban area. In Figure 49 the urban grids of Houston metropolitan area in the 4 km model domain are illustrated. While the 1-d simulation had different fractional area coverage of each land cover type for each grid element over the HOU area, the MM5 urban grids of the parameterization are expressed by unique fractional area coverage given by the HOU-area-averaged fractional area coverage in the HOU area. There is no other reason for that but for simplification purpose of the preliminary application. In this preliminary application, the HOU-area-averaged fractional coverage is assumed to be representative of urban surface type distribution. The averaged fractional area coverages are: broad leaf forest 0.15, coniferous forest 0.04, mixed forest 0.01, grass 0.45, wet land 0.01, water body 0.01, barren land 0.07, roads 0.07, impervious flat 0.06, and impervious structure 0.13. The characteristic surface parameter values for each of the land types are also listed in the Table 3. The fractional area-weighted average of each surface parameter value is used as the grid-mean value for the homogeneous MM5 simulations without the parameterization.

The grid-mean ground temperature and the first level (surface layer) atmospheric variables are obtained by the fractional area-weighted average of the predicted subgrid-scale variables at every time steps during the model integration. The subgrid-scale variables, ground temperature and surface layer variables in the first atmospheric level, are predicted independent of other subgrids during the entire integration time. While the subgrid-scale ground temperatures are predicted through the interaction of each subgrid land type with the corresponding subgrid-scale surface layer, the variables of the subgrid-scale surface layer interact with grid-mean variables above the surface layer at the top and with the subgrid-scale land type at the bottom. The variables above the surface layer are allowed to interact with the area-weighted grid-mean values of ground temperature and surface layer variables. The segmentation of the atmospheric surface layer into the corresponding subgrid-scale land

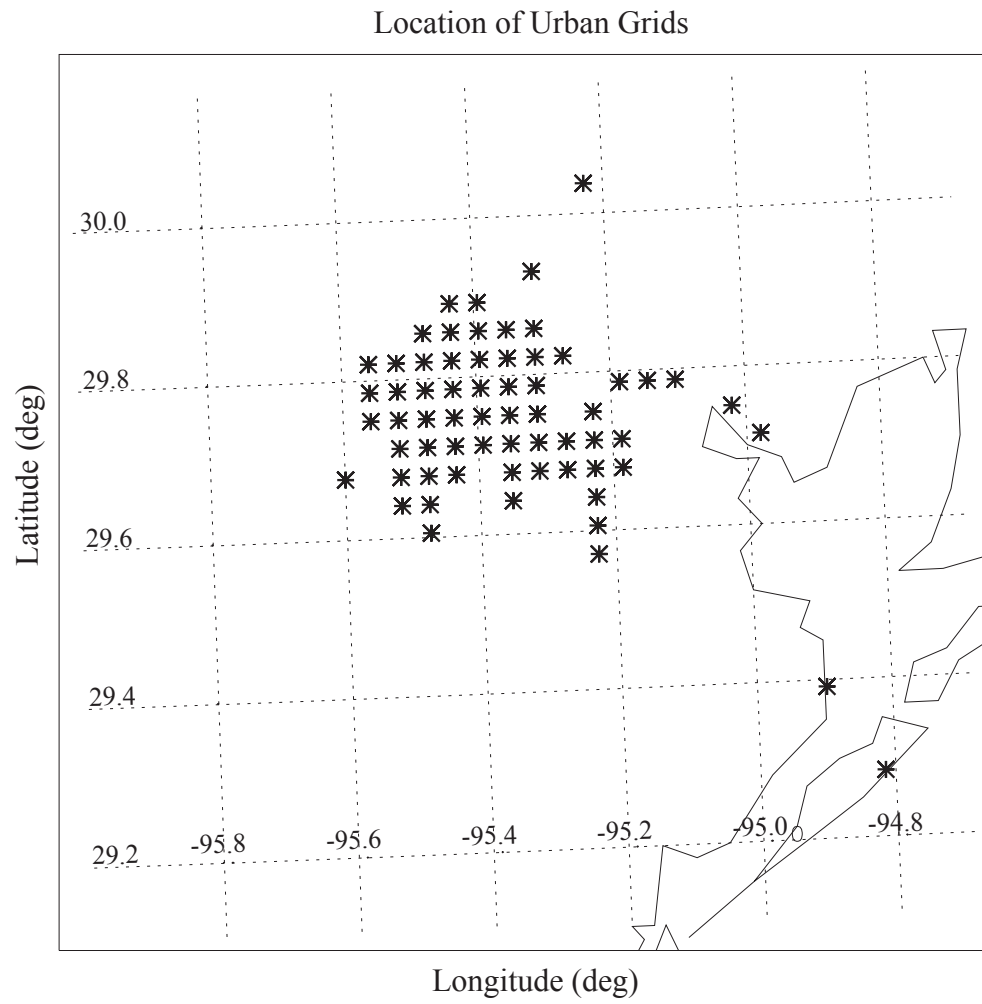


Figure 49. Location of the HOU urban grids in the 4 km domain of the MM5.



types is based on the assumption that the subgrid-scale surface layers are in equilibrium with the corresponding subgrid land surface.

In predicting the subgrid-scale ground temperatures, the five soil layers are also segmented accordingly in the slab model of the MM5. This is different feature of the 3-d MM5 parameterization of inhomogeneous land surface compared to the 1-d model in chapter III where the substrate temperatures were always kept 2 K lower than the slab (ground) temperature purposely to simplify the explanation of the inhomogeneous impacts. Hereafter, the MM5 simulations with and without the parameterization are called INHOMO and HOMO, respectively.

### 3. Description of MRF PBL scheme

The MRF PBL scheme was developed based on Troen and Mahrt (1986), coded by Hong at NCEP (Hong and Pan, 1996), and implemented by Dudhia at NCAR. One characteristic feature of this scheme is that it includes a correctional term in its flux computation in consideration of thermals and eddies of boundary-layer scale which are nonlocal. The correctional term is the counter-gradient term as discussed by Priestley and Swinbank (1947) and Deardorff (1966).

In the scheme, surface fluxes are represented in terms of similarity theory while turbulent diffusivities above the surface layer are formulated in terms of bulk similarity considerations and matching conditions at the top of the surface layer. The boundary layer depth is expressed in terms of a bulk Richardson number which is modified to include the influence of thermals (Troen and Mahrt, 1986).

#### *a. Determination of diffusivity profiles*

In the scheme, the layer between the surface and the lowest model level is assumed to be in equilibrium, obeying surface-layer similarity. Based on the equivalent assumption, the parameterization scheme devised by Louis (1979) is used to relate surface fluxes of heat, momentum, and water vapor to the values of temperature, wind components and specific humidity at the lowest model level.

Above the surface layer, the momentum diffusivity is expressed by

$$K_m = u_* k z \Phi_m^{-1} \left(1 - \frac{z}{h}\right)^p, \quad (63)$$

where  $u_*$  is the surface friction velocity,  $k$  is the von Karman constant (0.4),  $\Phi_m$  is the nondimensional shear,  $z$  is the height above ground, and  $h$  is boundary-layer height.

For stable conditions, the  $\Phi_m$  from Businger *et al.* (1971) is given as

$$\Phi_m = 1 + \frac{4.7z}{L}, \quad (64)$$

where  $L$  is the Monin-Obukhov length. For  $z \gg L/4.7$ , combining (63) and (64) yields the asymptotic expression:

$$K_m \cong (k/4.7) L u_* \left(1 - \frac{z}{h}\right)^p. \quad (65)$$

Thus, for the entire boundary layer of the stable condition,  $L$  and  $u_*$  become the relevant velocity and length scale, respectively.

For unstable conditions,

$$\Phi_m(z/L) = (1 - 7z/L)^{-1/3}, \quad z \ll h. \quad (66)$$

Considering the surface layer to extend upward to  $z = \varepsilon h$ , where  $\varepsilon = 0.1$  is chosen, and the relevant velocity scale to be constant above the surface layer, the velocity scale for the unstable case is given by

$$u_* \Phi_m^{-1} = (u_*^3 + 7\varepsilon k w_*^3)^{1/3} \equiv w_s, \quad (67)$$

where  $\Phi_m$  is evaluated at  $\varepsilon h$  and  $w_*$  is the convective velocity scale. Then, the momentum diffusivity expression (63) becomes for unstable conditions

$$K_m = w_s h k \frac{z}{h} \left(1 - \frac{z}{h}\right)^p, \quad z > \varepsilon h. \quad (68)$$

*b. Determination of boundary layer depth*

Consistent with the bulk approach in prescribing the diffusivity profile given above, the boundary layer top is determined by specifying the value of a modified bulk Richardson number such that

$$h = \text{Ri} \frac{T_0 |v(h)|^2}{g(\theta_v(h) - \theta_s)}, \quad (69)$$

where  $\theta_v(h)$  is the virtual potential temperature at the boundary layer top,  $\theta_s$  is the temperature of thermals near the surface,  $T_0$  is the potential temperature at height  $h$ , and  $v(h)$  is the wind speed at the top of the boundary layer.

In the MRF scheme, model levels are checked in a downward direction to find the level where the modified bulk Richardson number yields the specified critical value. If met this level is determined as the boundary layer top. The specified critical value in use is 0.5.

The  $\theta_s$  is defined as a measure of temperature of the thermals in the lowest part of the boundary layer as in Zhang and Anthes (1982). Thus, using the relevant velocity scale  $w_s$  given in (67), the scaled virtual temperature excess near the surface is defined as

$$\theta_T = C \frac{\overline{(w'\theta'_v)_0}}{w_s}, \quad (70)$$

where  $\overline{(w'\theta'_v)_0}$  is the surface heat flux and  $C$  is a coefficient of proportionality chosen as 7.8. In the MRF scheme, the temperature excess (70) is assumed to occur at the lowest model level  $z_1$ , then

$$\theta_s = \theta_v(z_1) + \theta_T. \quad (71)$$

For the stable case, the surface virtual temperature is defined as  $\theta_s$  since the first model level may be above the nocturnal boundary layer.

*c. Diffusivities for heat and water vapor*

Diffusivities for heat and water vapor are assumed to be equal to each other. In the mixed layer, fluxes become more related to bulk gradients because the local gradients may vanish. In order to include this nonlocality, the counter-gradient term as discussed by Priestley and Swinbank (1947) and Deardorff (1966) is incorporated in the heat flux computation as expressed by

$$\overline{w'\theta'} = -K_h \left( \frac{\partial \theta}{\partial z} - \gamma \right). \quad (72)$$

The  $\gamma$  is expressed, consistent with the temperature excess for thermals, (70), as

$$\gamma = C \frac{(\overline{w'\theta'})_0}{w_s h}. \quad (73)$$

As in equation (70), the proportionality coefficient,  $C$  is specified as 7.8 in the scheme.

The correctional counter-gradient term for the moisture flux is given by

$$\gamma_q = C \frac{(\overline{w'q'})_0}{hw_s}, \quad (74)$$

where  $(\overline{w'q'})_0$  is the surface moisture flux.

The heat and momentum fluxes are matched at the top of the surface layer so that

$$u_* \theta_* = K_h \left( \frac{\partial \theta}{\partial z} - \gamma \right), \quad u_*^2 = K_m \frac{\partial u}{\partial z}, \quad (75)$$

where  $\theta_* \equiv -(\overline{w'\theta'})_0 / u_*$ . Combining these two relationships and solving for the Prandtl number using the definitions given above,

$$\text{Pr} = \frac{K_h}{K_m} = \left[ \frac{\Phi_h}{\Phi_m} \left( \frac{z}{L} \right) + k \frac{z}{h} C \right]^{-1}, \quad (76)$$

where  $z$  is the level where the matching is applied taken as  $0.1h$ . The Prandtl number is assumed to be independent of height above  $0.1h$ .

## 4. Simulation aspects

### *a. Configuration of MM5*

The MM5 system is configured with 2 domains, a coarse domain with 12-km grid-spacing and a nested domain with 4-km grid-spacing. The two domains are allowed to interact with each other in 2-way mode. The 4-km domain encompassing the HOU area is the target domain of this study. The parameterization explained above is applied in both domains.

The 44 full sigma levels defined from the model top to the surface are: 0.0, 0.010, 0.025, 0.045, 0.065, 0.090, 0.115, 0.145, 0.175, 0.210, 0.250, 0.290, 0.330, 0.370, 0.405, 0.440, 0.475, 0.510, 0.540, 0.570, 0.600, 0.630, 0.660, 0.690, 0.720, 0.750, 0.775, 0.800, 0.825, 0.850, 0.865, 0.880, 0.895, 0.910, 0.920, 0.930, 0.940, 0.950, 0.960, 0.970, 0.980, 0.990, 0.996, 1.0. The lowest half sigma level (0.998) is about 15 m above the ground level in the model domains.

The choices of physical processes and key parameters are listed in Table 15. Initial and boundary conditions are obtained from the Eta Data Assimilation System (EDAS) analyses. The forecast length for each simulation is 24 hours starting from 0000 UTC Aug. 30, 2000 for each run.

### *b. Simulation case*

A case on Aug. 30, 2000 was chosen for the simulation during the ozone regime-II (Aug. 30 – Sep.1, 2000). On Aug. 30, surface winds were tended to be lightest during the afternoon and disorganized especially over land. The winds were predominantly westerly flow. Most locations in the HOU area had high temperatures in the low to mid 100s (Fahrenheit). By choosing the same day as in the 1-d simulation of chapter III, it is intended that the results from the preliminary application can be comparable with the 1-d simulation, minimizing possible differences associated with different ambient atmospheric conditions between the two simulations.

Table 15. MM5 model parameter settings used in the inhomogeneity test run.

Model aspect	Settings	
	Fine	Coarse
<b>Model version</b>	3.4	3.4
Grid-spacing	4 km	12 km
Grid number	82 by 82	43 by 43
Time step	6 seconds	18 seconds
Vertical half levels	43	43
Cumulus parameterization	None	None
Shallow convection	Yes	Yes
PBL scheme	MRF	MRF
Cloud physics	Simple ice	Simple ice
Radiation scheme	RRTM	RRTM
Radiation update frequency	30 min	30 min
Fake dry	Yes	Yes
Soil scheme	5-layer	5-layer

## 5. Comparison of simulation results between the INHOMO and HOMO

### *a. Spatial distribution of simulated PBL variables*

The INHOMO and HOMO results were compared at 3 half sigma levels; 1) lowest sigma level sigma9980 (15 m above the ground) which represents the surface layer, 2) sigma8575 (about 1160 m), and 3) sigma7050 (2570 m) at 1500 UTC, 1800 UTC, 2100 UTC, and 0000 UTC. Prior investigation indicated gravity wave features of inhomogeneity impacts (not shown) from 2100 UTC. The gravity wave seems to have been excited by increased sensible heat flux over HOU area in the model domain. The increased sensible heat flux may cause a change of divergence around HOU resulting in imbalance of flows around HOU area, thereby generating the gravity waves. In order to avoid obscuring other inhomogeneity impacts by the gravity waves, the impacts (INHOMO – HOMO) with wave length less than 60 km were filtered out. But other model variables presented below were left unfiltered.

#### 1) Temperature

At 1500 UTC (Fig. 50), INHOMO resulted in surface layer (sigma9980) temperatures which were up to  $-0.2$  K lower than HOMO over Houston (HOU) area. The same impact direction and similar degree of impacts were also produced in the 1-d simulations. At this time no differences were found between INHOMO and HOMO in the upper levels (sigma8575 and sigma7050) above the surface layer.

At 1800 UTC (Fig. 51), INHOMO resulted in up to  $0.5$  K and  $0.1$  K greater temperatures in the surface layer and sigma8575 level, respectively. At this time the 1-d began to produce positive impacts too. No differences were yet found in the sigma7050 level because free convective mixed height has not reached that level. The INHOMO-generated PBL heights, from 1600 UTC to 0000 UTC, are 1200 m (1600 UTC), 1500 m (1700 UTC), 2000 m (1800 UTC), 2200 m (1900 UTC), 2300 m (2000 UTC), 2500 m (2100 UTC), 2500 m (2200 UTC), 2400 m (2300 UTC), and 2000 m (0000 UTC). At 2100 UTC (Fig. 52), the temperature differences in the surface layer had increased to up to  $0.5$  K near Houston Downtown (HDT).

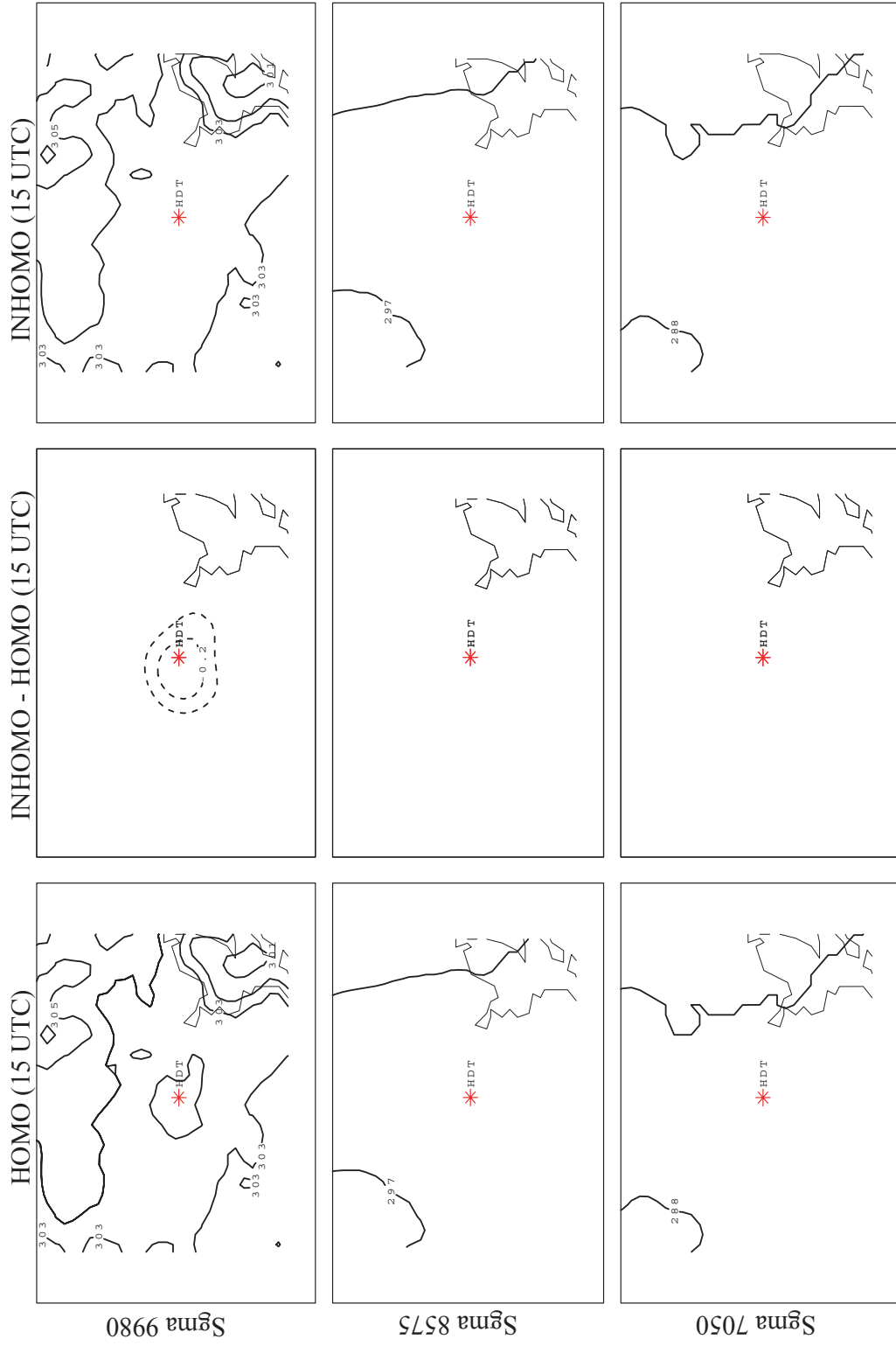


Figure 50. Temperature contour plots of the HOMO (left) and INHOMO (right) and those differences (center), INHOMO - HOMO, at 15 m □ lowest sigma level (upper), 1160 m sigma8575 level (middle), and 2570 m sigma7050 level (lower) at 1500 UTC. Contour intervals are 1 K □ and 0.1 K for the temperature and difference, respectively.



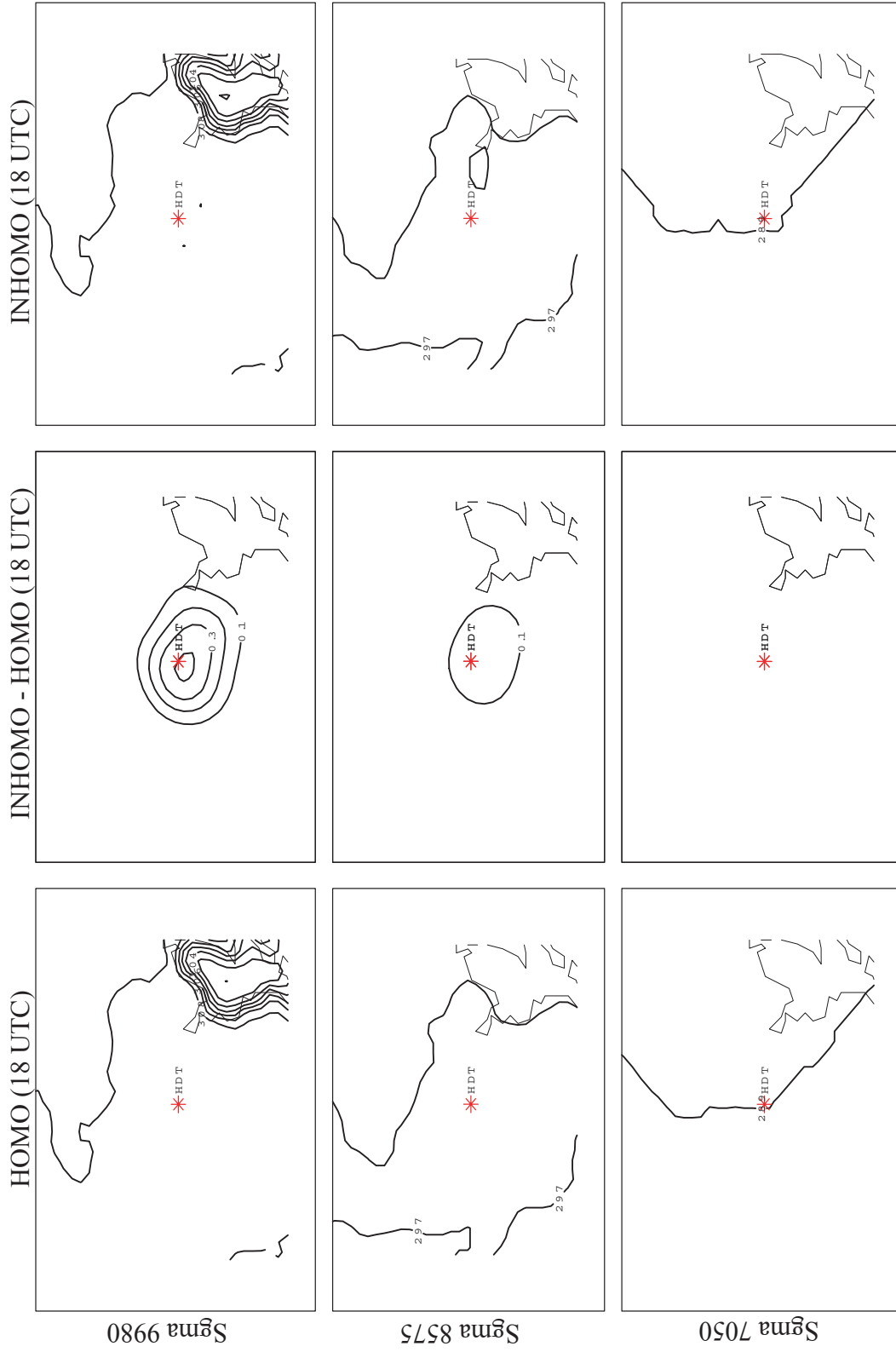


Figure 51. The same as Figure 50 but for at 1800 UTC.

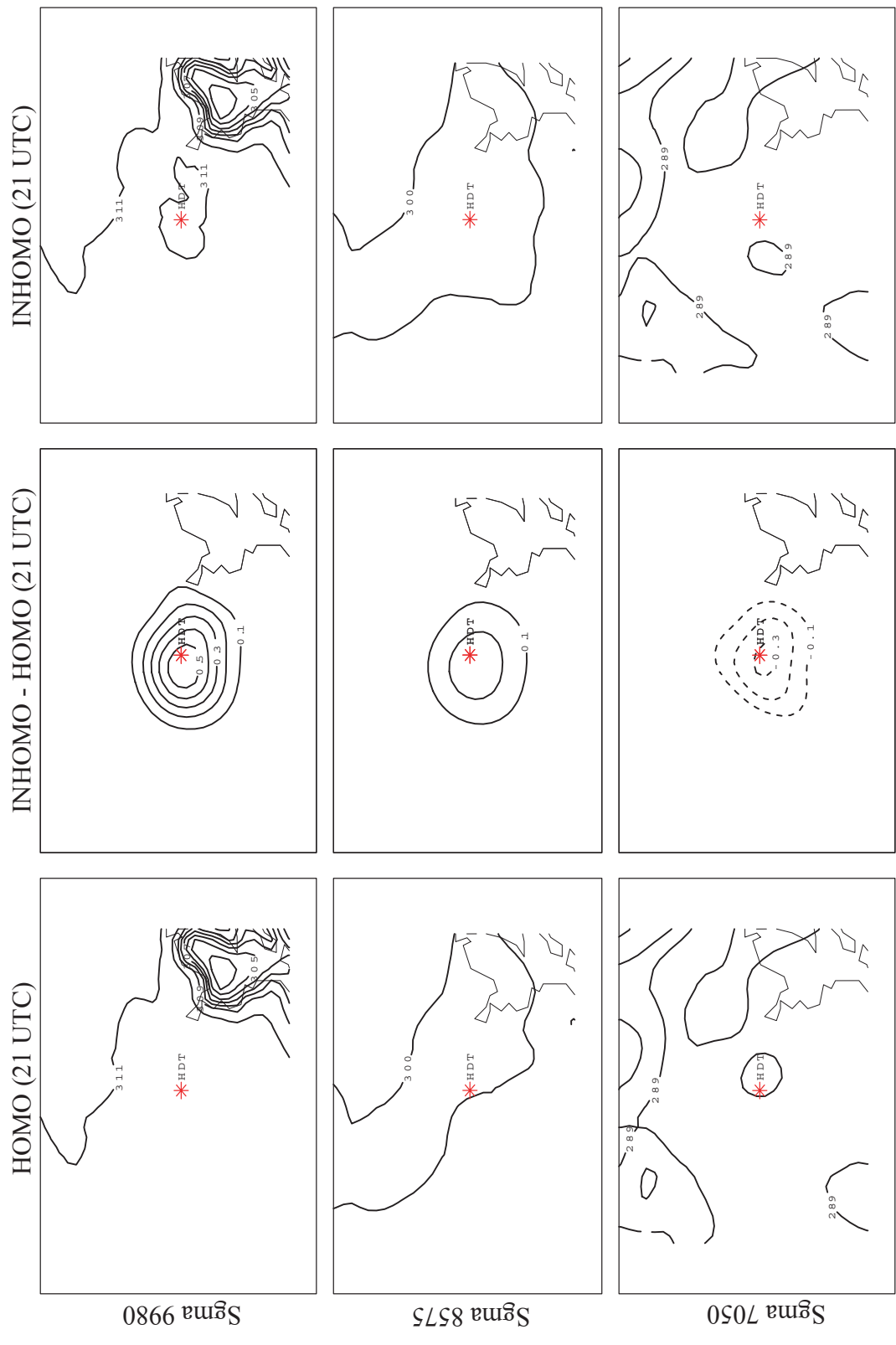


Figure 52. The same as Figure 50 but for at 2100 UTC.

At the sigma8575 level the temperature differences remained up to about 0.2 K but the area of differences had become enlarged. At that time INHOMO resulted in up to  $-0.4$  K lower temperatures over HOU area at the sigma7050 level implying that the mixed layer reached that level by this time. As explained from the 1-d PBL simulations in the chapter III, the negative trend near the PBL top of the temperature impacts of INHOMO seems to be induced by the greater heat diffusivity of INHOMO.

At 0000 UTC (Fig. 53), evidence of advection of the temperature difference is found in the surface layer and sigma7050 level. As will be illustrated later southeasterly winds from Galveston Bay advect the temperature difference field over the HOU toward northwest direction in the surface layer. Likewise, at the sigma7050 level, east-southeasterly winds moved the lower temperatures toward the west-northwest. In the meantime, the area and magnitude of temperature differences became enhanced in both the surface layer and sigma7050 level. Maximum impacts were 0.7 K and  $-0.4$  K in the surface layer and sigma7050 level, respectively. At the sigma8575 level, the positive impact declined but the positive impact of 0.1 K spread more widely in horizontal space. In the surface layer, negative impacts southeast of the positive difference field are likely to be the result of temperature advection by the modified wind circulation of INHOMO.

Generally, the inhomogeneity parameterization in INHOMO produced temperatures which were up to 0.9 K greater in the surface layer, 0.1 K to 0.2 K greater at the sigma8575 level (within the well mixed PBL), and up to about  $-0.5$  K lower in the sigma7050 level (near the PBL top) over the HOU. The results were consistent with those of the 1-d simulations in the chapter III except that the advection effects are produced in the 3-d INHOMO simulation. The increased PBL temperature implies increased sensible heat fluxes in the surface layer. And the opposite trend in the PBL top can be accounted for by the increased diffusivity of heat.

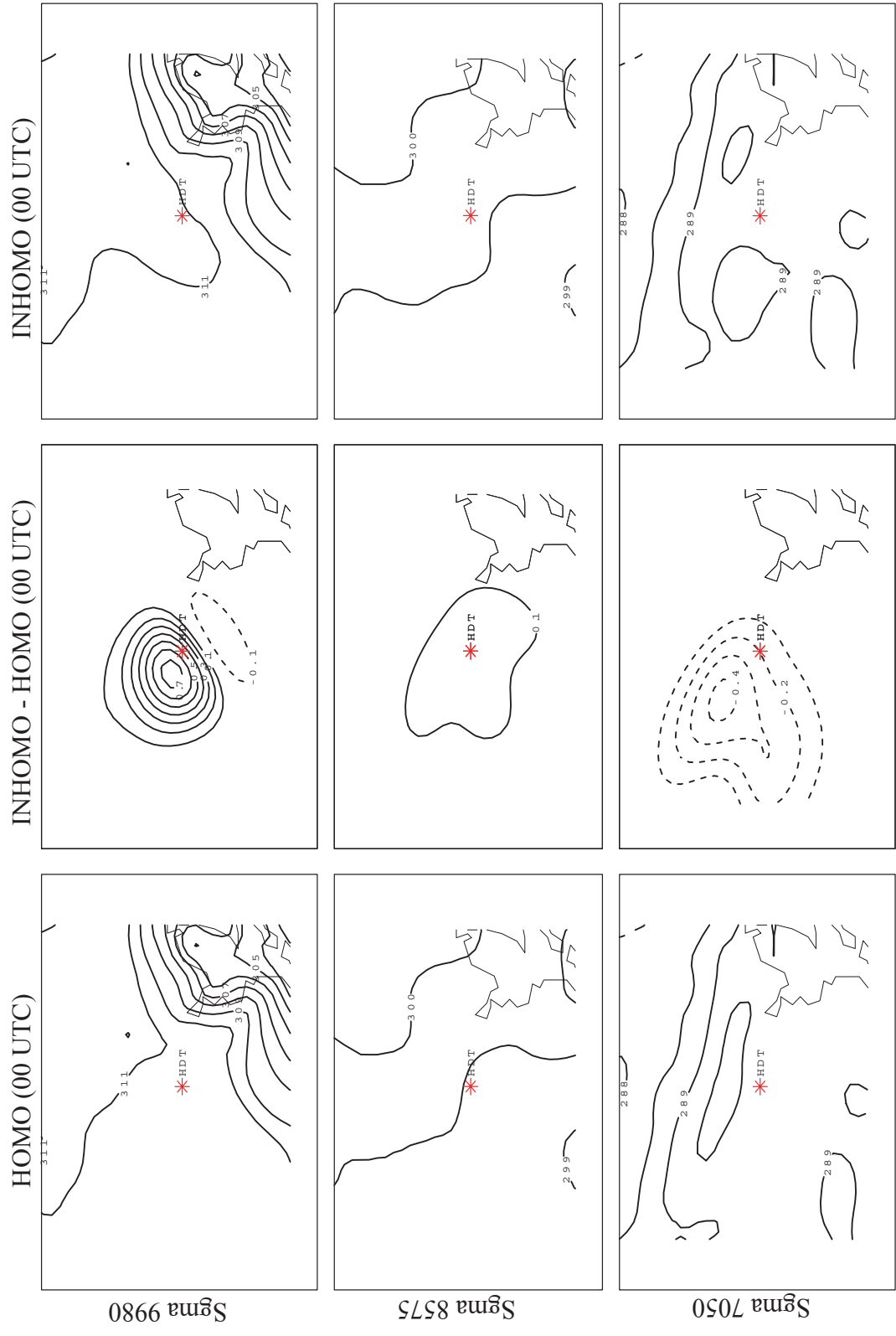


Figure 53. The same as Figure 50 but for at 0000 UTC.

## 2) Dewpoint temperature

INHOMO produced inhomogeneity impacts on dewpoint temperature which are opposite to those on temperature except for 1500 UTC. At 1500 UTC (Fig. 54), INHOMO resulted in an up to  $-0.6$  K lower dewpoint temperature in the surface layer over the HOU. Since the mixed layer could not reach the  $\sigma_{8575}$  level by the time, no differences are found at the  $\sigma_{8575}$  and  $\sigma_{7050}$  levels. As a result of free convection growth impacts occurred at the  $\sigma_{8575}$  level as well at 1800 UTC (Fig. 55). The impacts are about  $-0.2$  K in the surface layer and  $\sigma_{8575}$  level over HOU. At 2100 UTC (Fig. 56) the impacts are seen at all levels. The surface layer and  $\sigma_{8575}$  level maintained a  $-0.2$  K impact over HOU. At the  $\sigma_{7050}$  level the impact is positive with a maximum of about  $0.8$  K occurring near HDT. At 0000 UTC (Fig. 57), the impacts became most pronounced and advected in the same direction as those of temperature impacts in the surface layer and  $\sigma_{7050}$  level. The impacts were up to about  $-0.8$  K and  $1.4$  K in the surface layer and  $\sigma_{7050}$  level, respectively.

Apart from the sign of the impacts, the inhomogeneity impacts on the dewpoint temperature were similar to those of temperature. Because a lower dewpoint temperature implies a drier atmosphere, the results presented above indicated that INHOMO produced less latent heat flux from the surface.

## 3) Winds

At 1500 UTC (Fig. 58), positive impacts of about  $0.1$  m/s were indicated in the surface layer. No impacts were found in the upper levels at the time. Since the impact area over the HOU was fairly coincident with that of temperature and dewpoint temperature, the wind impact appeared to be caused by the difference of vertical momentum flux. The differential local circulation did not develop by this time. At 1800 UTC (Fig. 59), because the surface layer winds were calm over the HOU, impacts were avoided in the surface layer. At the  $\sigma_{8575}$  level differential local circulations of  $0.1$  m/s and  $-0.1$  m/s were weakly indicated southwest and northeast of HDT, respectively. The  $\sigma_{7050}$  level was not affected by this time.

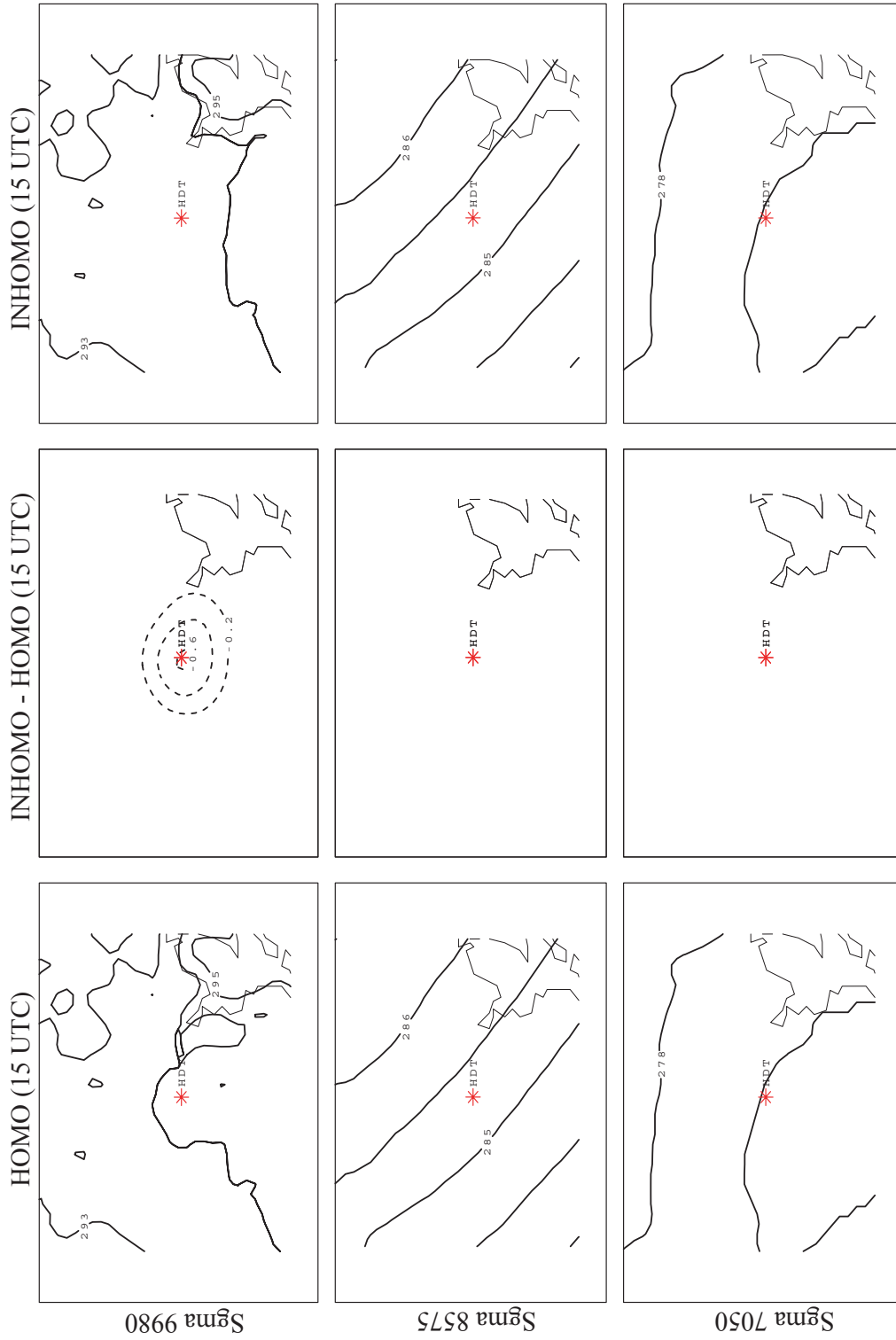


Figure 54. Dewpoint temperature contour plots of the HOMO (left) and INHOMO (right) and those differences (center), INHOMO - HOMO, at 15 m lowest sigma level (upper), 1160 m sigma8575 level (middle), and 2570 m sigma7050 level (lower) at 1500 UTC. Contour intervals are 1 K for the lowest level and 0.5K at sigma8575 and sigma7050 levels. Contour interval of the difference is 0.2 K.

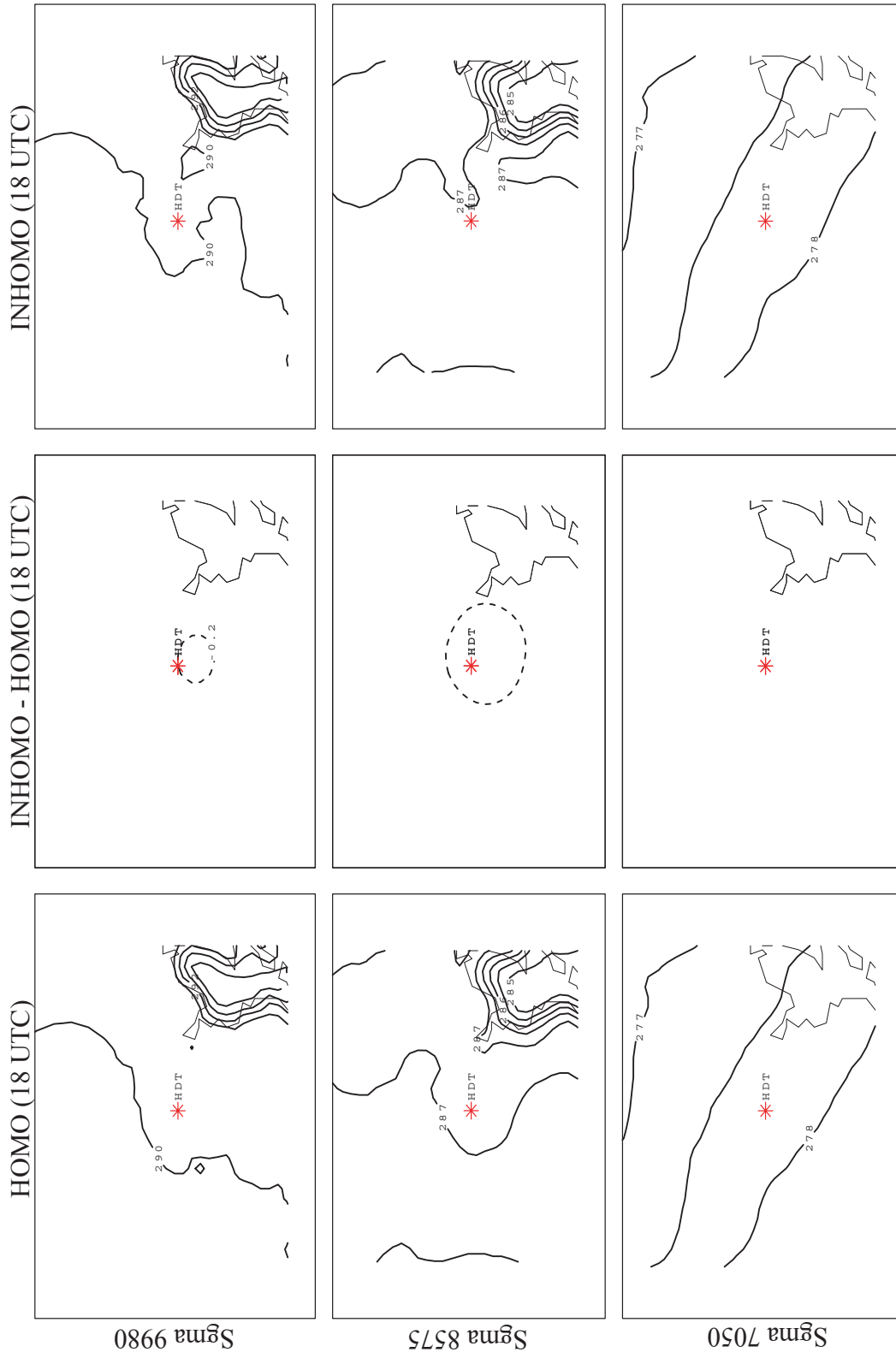


Figure 55. The same as Figure 54 but for at 1800 UTC.

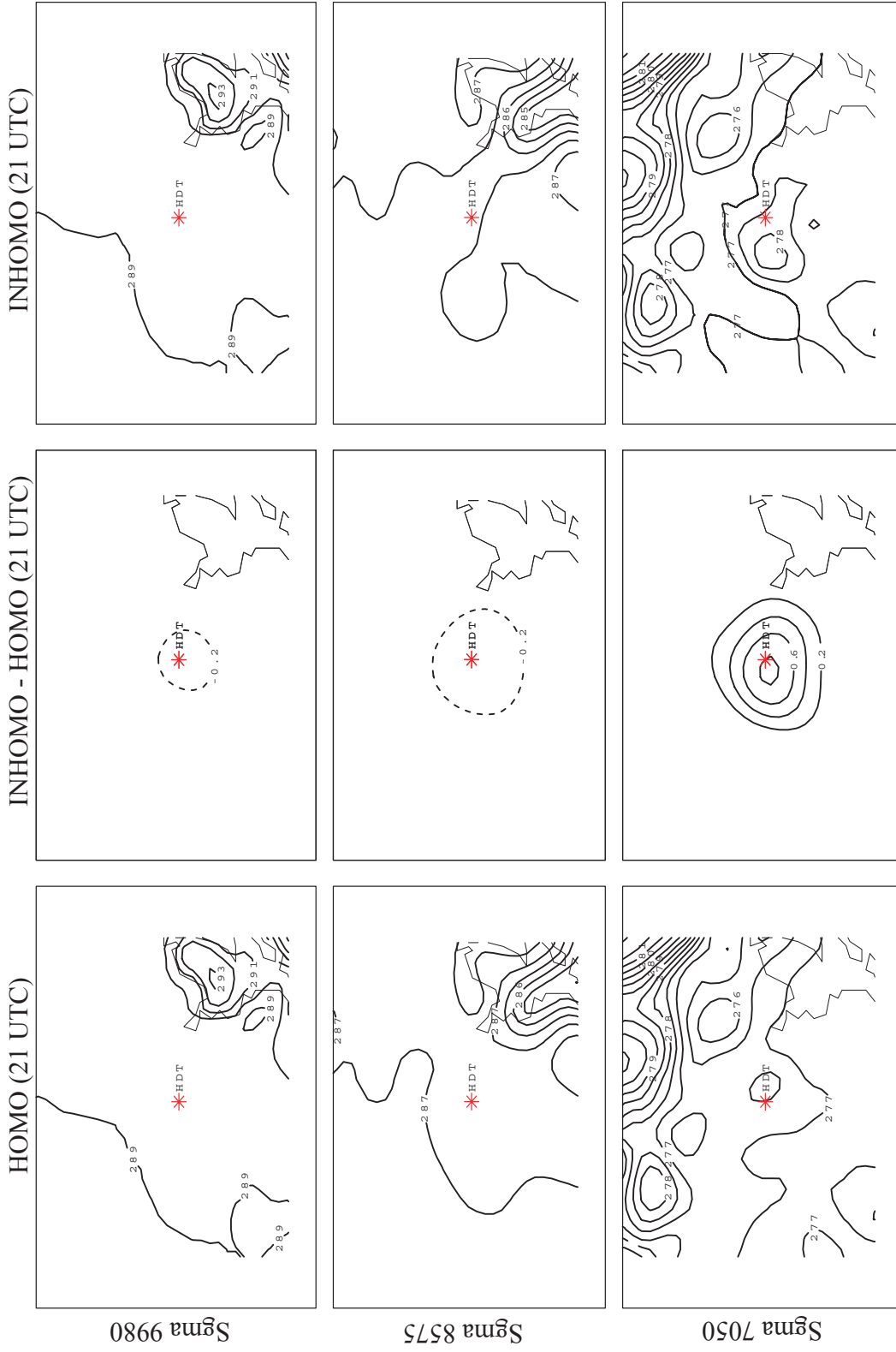


Figure 56. The same as Figure 54 but for at 2100 UTC.





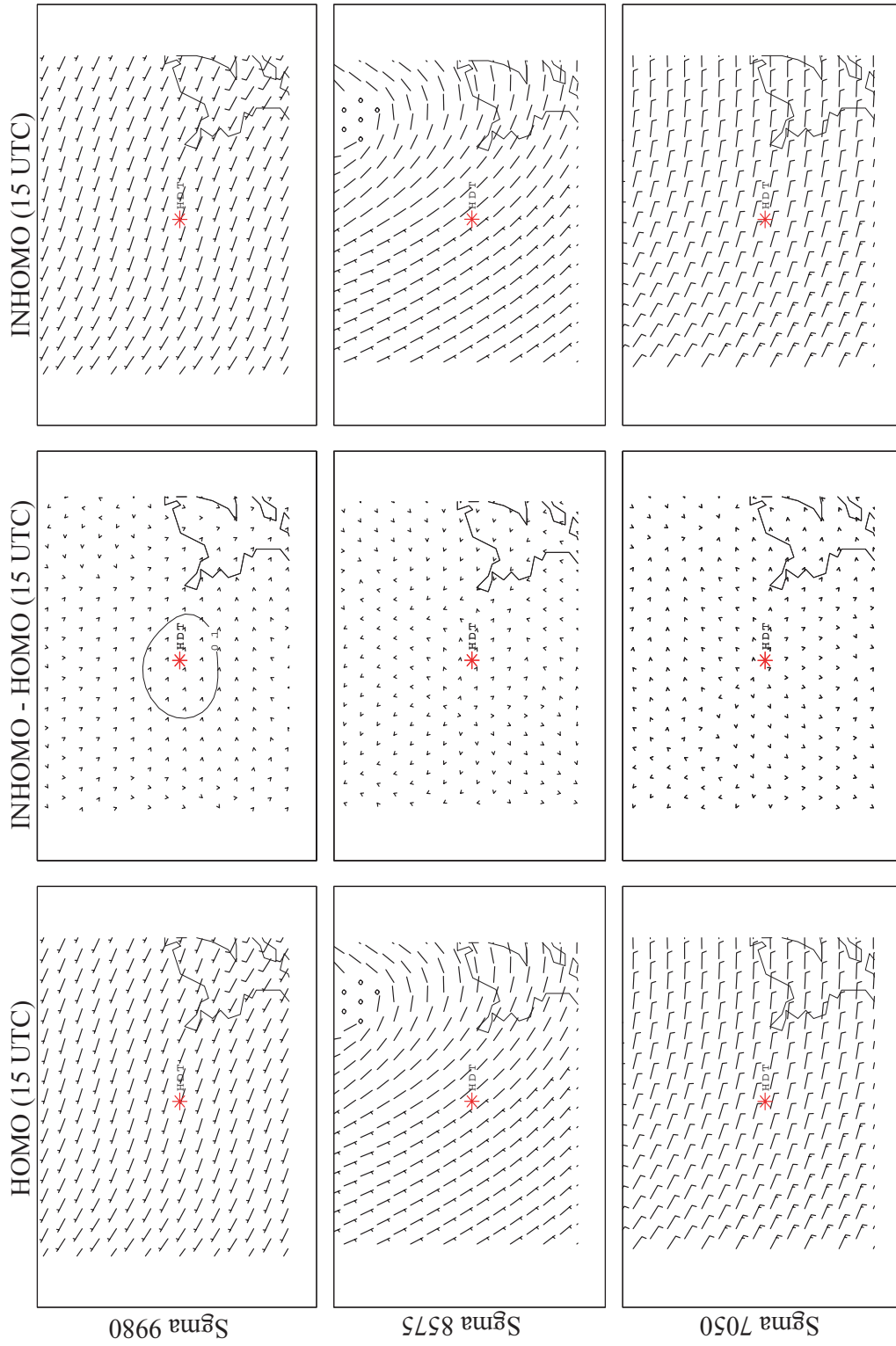


Figure 58. Wind barb plots of the HOMO (left), INHOMO (right), and those wind vector and speed difference (center), INHOMO - HOMO, at 15 m lowest sigma level (upper), 1160 m sigma8575 level (middle), and 2570 m sigma7050 level (lower) at 1500 UTC. Wind barbs are in knots and the wind speed differences are in 0.2 m/s intervals.

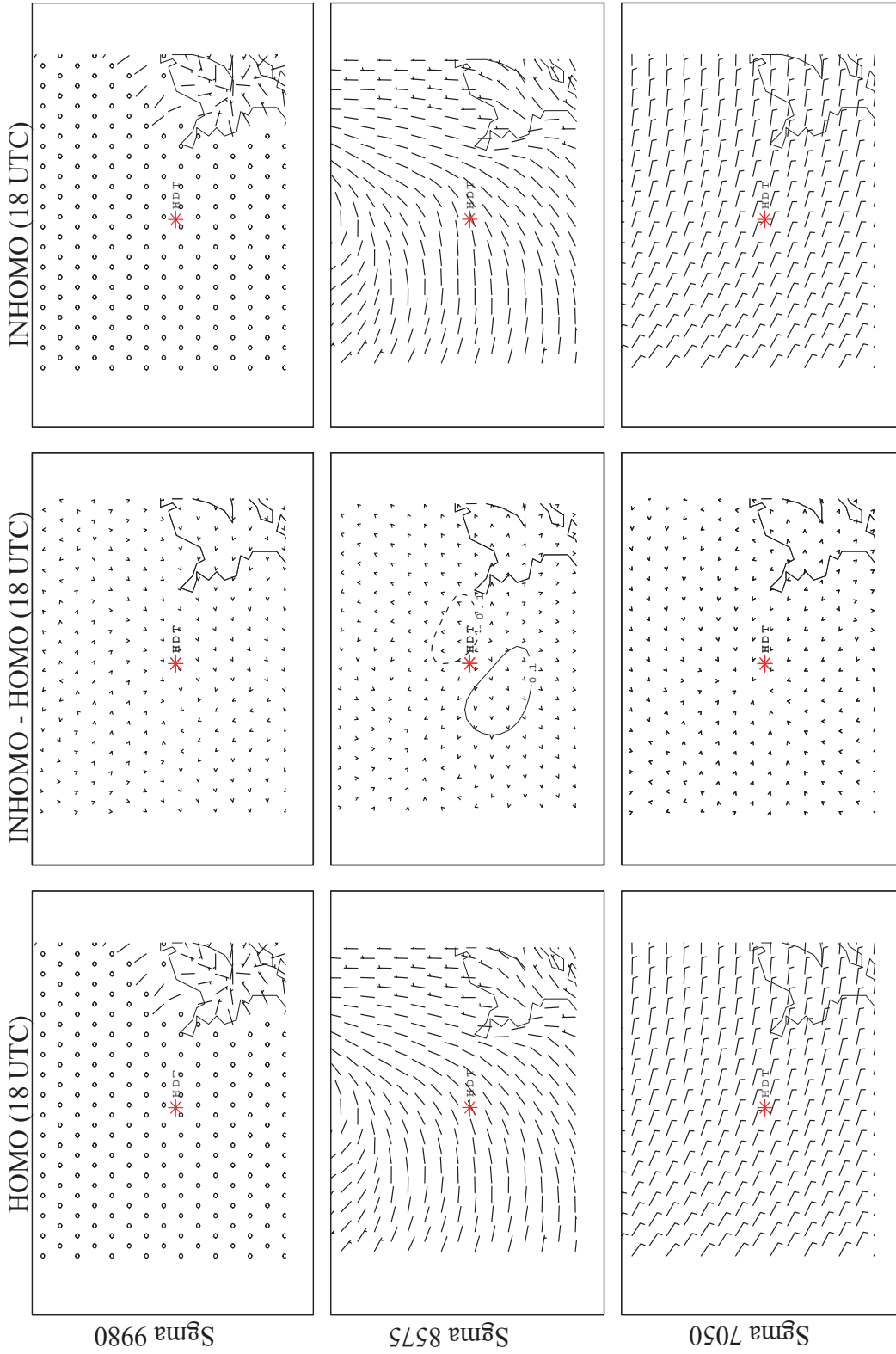


Figure 59. The same as Figure 58 but for at 1800 UTC.

At 2100 UTC (Fig. 60), the differential local circulation produced impacts of up to  $-0.3$  m/s northwest of HDT and about  $0.1$  m/s southeast of HDT in the surface layer. At this time impacts appeared at the sigma7050 level as well. The dipole pattern with positive impact of  $0.1$  m/s to the west and negative impact of  $-0.3$  m/s to the east of HDT indicated the differential local circulation in the sigma7050 level. At 0000 UTC (Fig. 61), impacts induced by the local circulation seemed to be significant. Also, in accordance with the advection of the temperature impacts, the dipole pattern of the differential local circulation was similarly displaced as indicated in the surface layer and sigma7050 level. In the surface layer negative impacts with maximum values of about  $-2.0$  m/s were seen to be widely spread north of HOU, and positive impacts with maximum values of about  $1.3$  m/s were south of HOU. Apparent changes of wind vectors occurred around HDT and north of HOU in the surface layer as illustrated by vector wind differences in Figure 61.

From examination of the wind barb plots for INHOMO and HOMO and those differences of the wind speed and vector, the inhomogeneity impacts on winds seemed to be complicated due to the combined effects of vertical momentum flux and the thermally driven differential local circulation. Because of thermal differences, differential local circulations were likely to be generated. The impacts of the differential local circulation induced by thermal difference between the INHOMO and HOMO were clearly indicated at 2100 UTC (Fig. 60) and 0000 UTC (Fig. 61). As shown from the 1-d simulations in chapter III the inhomogeneity acts to increase existing wind speed in the well mixed layer and to decrease it near the PBL top. The impacts of differential local circulation on wind speeds were characterized by a dipole pattern (e.g. Fig. 61) depending on the existing wind direction. That is, while wind speeds on one side of the thermal difference area were positive, they were negative on the other side. The winds downwind of the temperature difference weakened and vice versa as indicated in Figure 61.

As a result of warmer air over HOU a more rapid inland advance of the sea breezes from Galveston Bay were indicated in the surface layer as can be seen from wind barb plots. As an evidence of the inland sea breeze, cooling over part of the HOU area (south of HDT) occurred and a vertical dipole of wind impact could be seen at 00000 UTC when the sea breeze reached HDT.

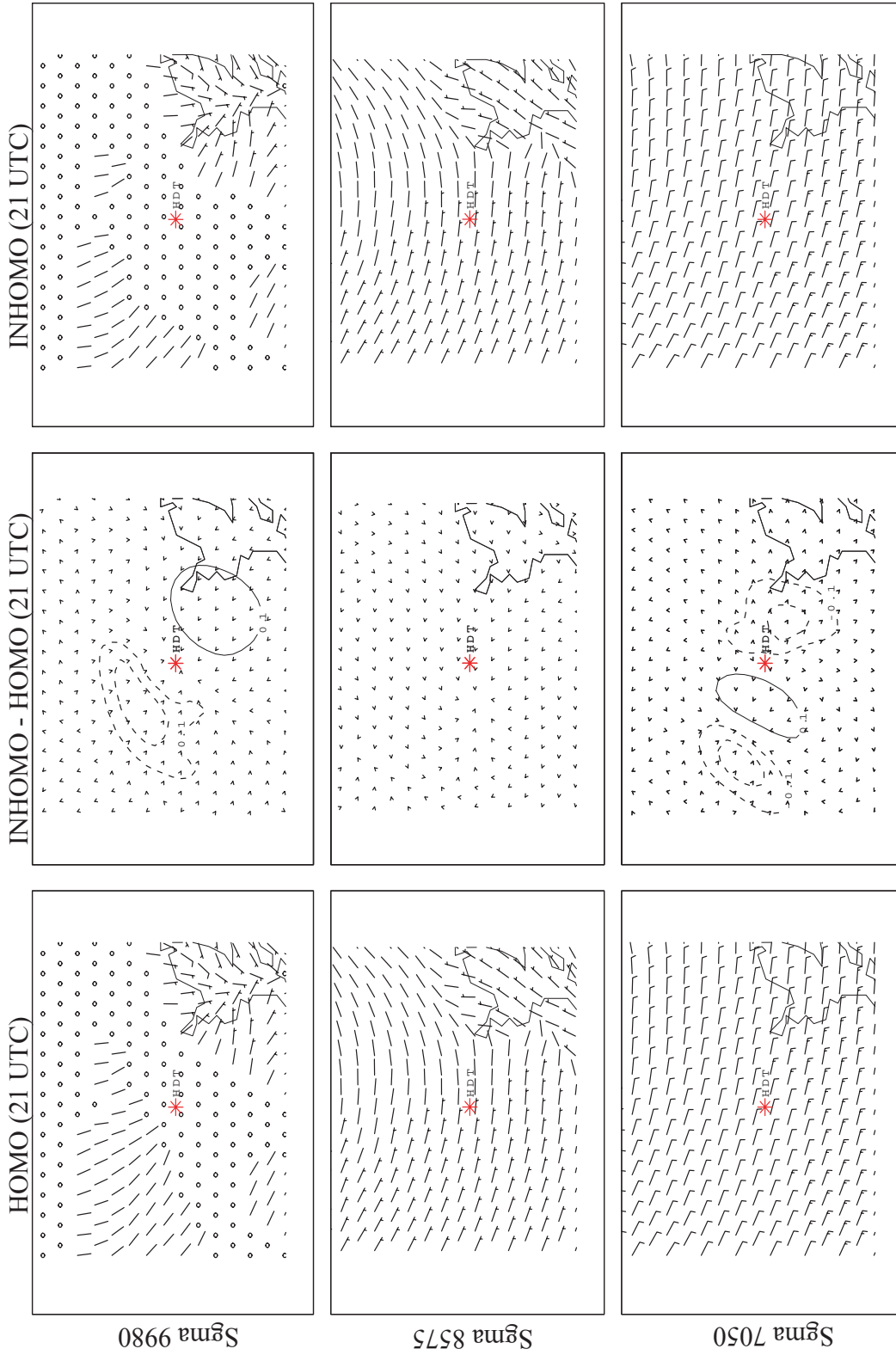


Figure 60. The same as Figure 58 but for at 2100 UTC.

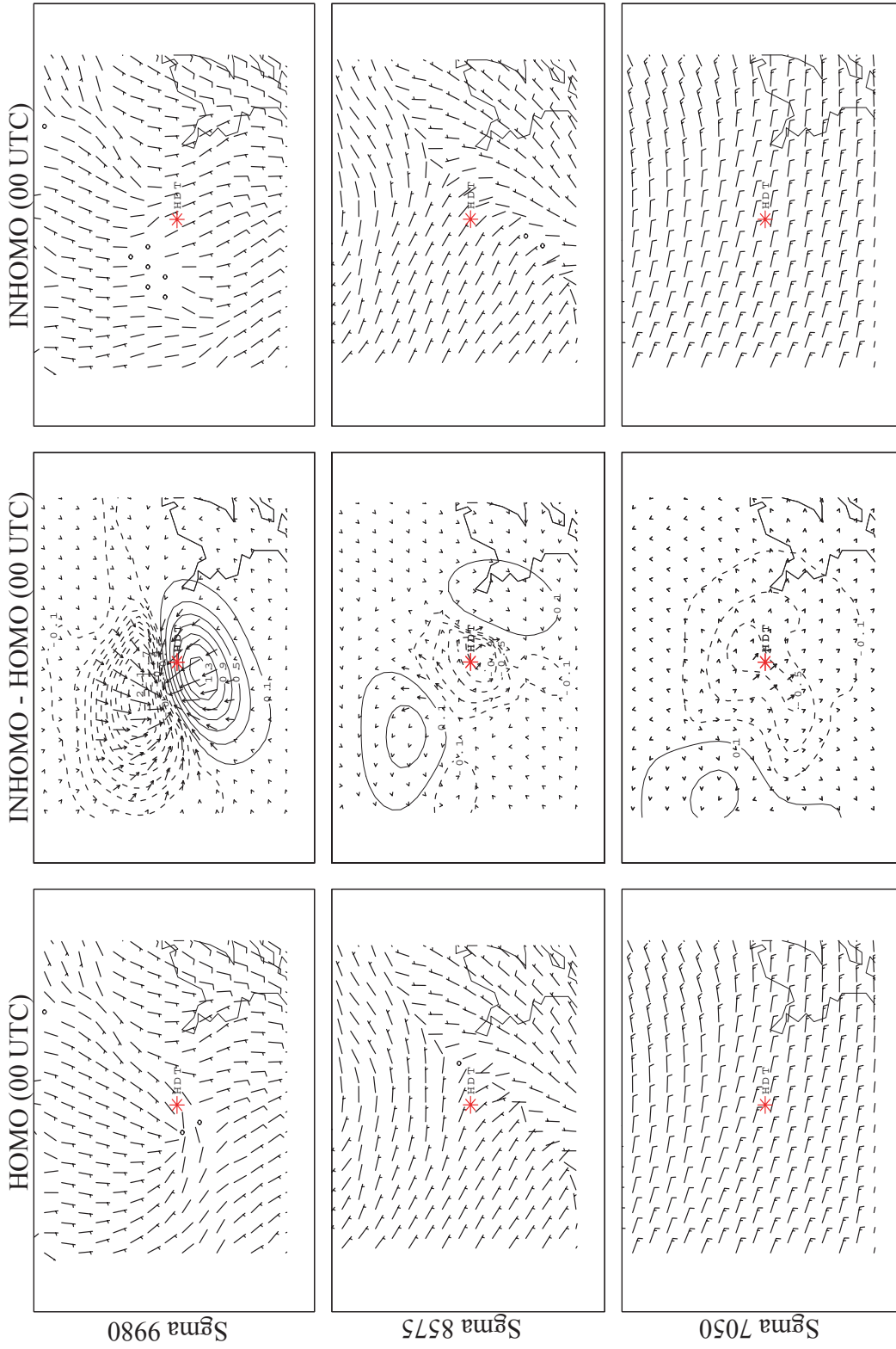


Figure 61. The same as Figure 58 but for at 0000 UTC.

*b. Comparison of surface variables at HDT as function of time*

In order to examine time variation of the inhomogeneity impacts, variables of the surface layer and ground around HDT were averaged and compared between INHOMO and HOMO during the model integration time.

The INHOMO run produced ground temperatures which are lower by about -0.1 K during most of stable nighttime (0000 UTC – 1200 UTC) and greater by about 0.9 K during the convective daytime (1200 UTC – 0000 UTC) as shown in Figure 62a. This implies the inhomogeneity parameterization caused more energy to escape from the ground surface during the nighttime and less energy to escape from the ground surface during the daytime. Those results are consistent with the 1-d simulations in chapter III.

Surface layer (lowest sigma level sigma9980, 15 m above the ground) temperature of INHOMO resulted in slight impacts of 0.1 K and -0.05 K between 0000 UTC and 0700 UTC and between 0700 UTC and 1300 UTC, respectively (Fig. 62b). During most of the convective daytime, INHOMO produced 0.2 K to 0.4 K higher surface layer temperatures. From this it is inferred that the surface layer of INHOMO experienced more influx of sensible heat during the convective daytime and first half of the stable nighttime and less influx between 0700 UTC – 1500 UTC. Compared to the 1-d results INHOMO was about 0.1 K to 0.3 K greater in the second half of convective day time and about 0.2 K lower in the first half of stable nighttime. While the 1-d showed negative impact between 1500 UTC and 1800 UTC, INHOMO showed it between 0700 UTC and 1500 UTC. Apart from the negative impact timing and impact magnitude, INHOMO is generally consistent with the 1-d simulation.

The INHOMO resulted in negligibly small impacts on the surface layer dewpoint temperature during the stable nighttime and negative impacts of -0.1 K to -0.4 K during the most of convective daytime (Fig. 62c). As will be clarified later the negative impacts of the dewpoint temperature implies that the surface layer of the INHOMO experienced less latent heat flux during the convective day time. The result is also consistent with the 1-d simulations.

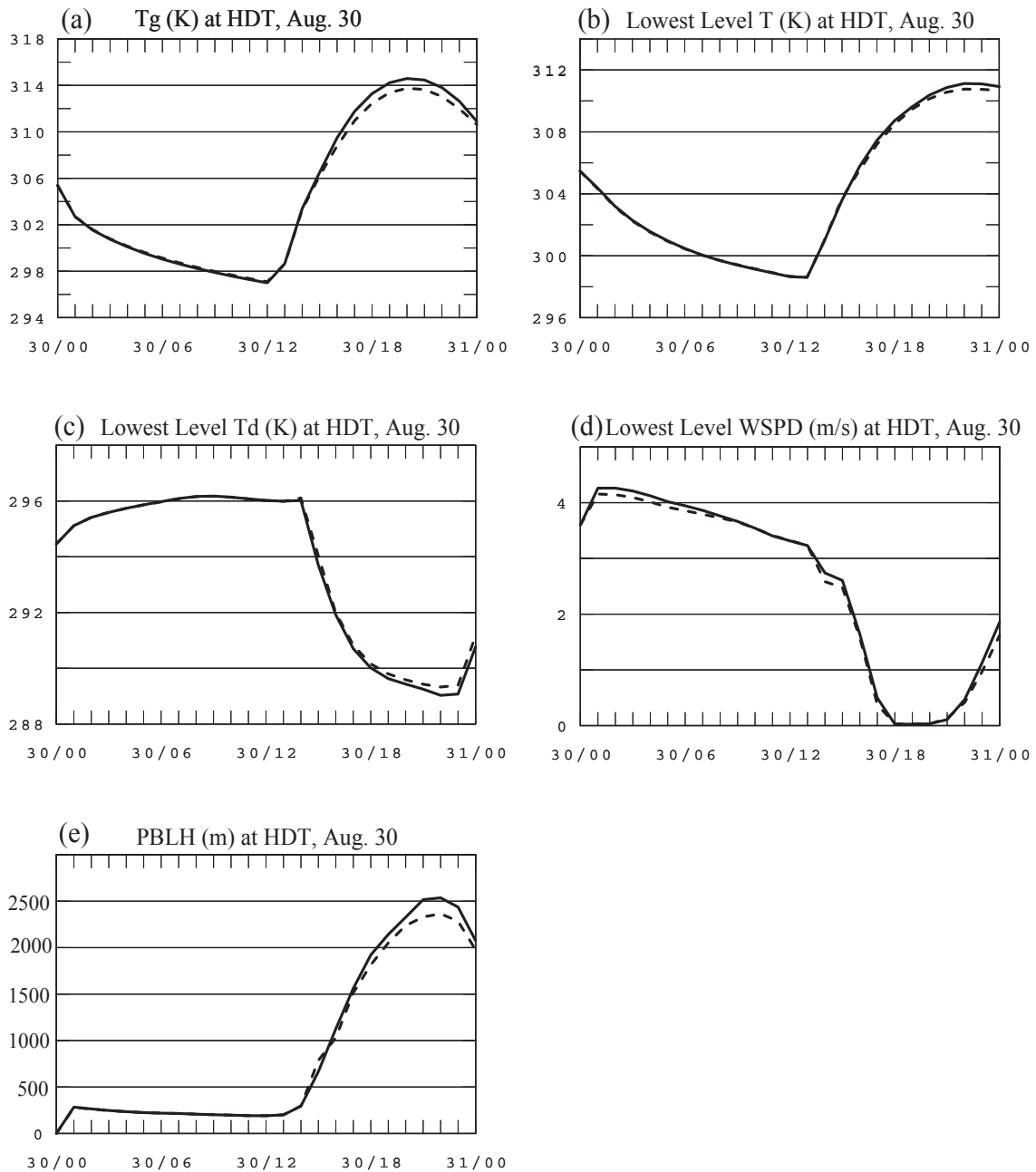


Figure 62. Plots comparing HOU-area-average of (a) ground temperature and lowest sigma level (b) temperature, (c) dewpoint temperature, and (d) wind speed and (e) PBL height between the INHOMO (solid) and HOMO (dashed). X-axes indicate time in UTC expressed by "date/UTC". Y-axes indicate values of each variable with units appearing in each figure title.



On average, INHOMO produced about 0.1 m/s greater wind speed between 0000 UTC and 0800 UTC and almost zero impact between 0800 UTC and 1300 UTC during the stable nighttime (Fig. 62d). During the convective daytime, except for from 1800 UTC to 2100 UTC in which impacts were negligible, INHOMO produced about 0.1 m/s to 0.2 m/s greater wind speed. Especially during the convective regime INHOMO showed a variability pattern similar to the 1-d simulation. As explained from the 1-d simulations, smaller frictional velocity ( $U_*$ ) implies weaker momentum drag under the same atmospheric conditions, thereby generating positive wind speed impacts. From this INHOMO seems to have produced smaller frictional velocity most of time except between 1800 UTC and 2100 UTC. Those exceptional times are likely to correspond to the times in which bulk Richardson numbers are indicative of most turbulent vertical exchange of surface fluxes. Relatively large impact at 0000 UTC seems to have been induced by the differential local circulation explained earlier.

In Figure 62e, PBL heights were compared. Between 1600 UTC and 0000 UTC during the convective daytime, in which positive surface layer temperature impacts occurred, the INHOMO produced 100 m to 200 m higher PBL heights. As expressed in equation (69), the increase (decrease) of surface layer temperature is expected to increase (decrease) the boundary layer depth. The negative impact of -100 m at 1500 UTC is coincident with about -0.1 K temperature impact at that time. Those exceptions seem to be associated with slightly stable or unstable near neutral stability regime.

In Figure 63, HOU-area-averaged sensible and latent heat fluxes are compared so as to support the results explained so far. From the investigation of the atmospheric temperature and dewpoint temperature, it was argued that the inhomogeneity parameterization brought positive and negative impacts to INHOMO simulation for the sensible and latent heat fluxes, respectively, in the surface layer during the convective daytime. As expected INHOMO resulted in greater sensible heat fluxes between 1800 UTC and 0000 UTC by up to about  $20 \text{ Wm}^{-2}$  (Fig. 63a) and less latent heat fluxes between 1300 UTC and 2300 UTC by up to about  $-20 \text{ Wm}^{-2}$  (Fig. 63b) during the convective regime.

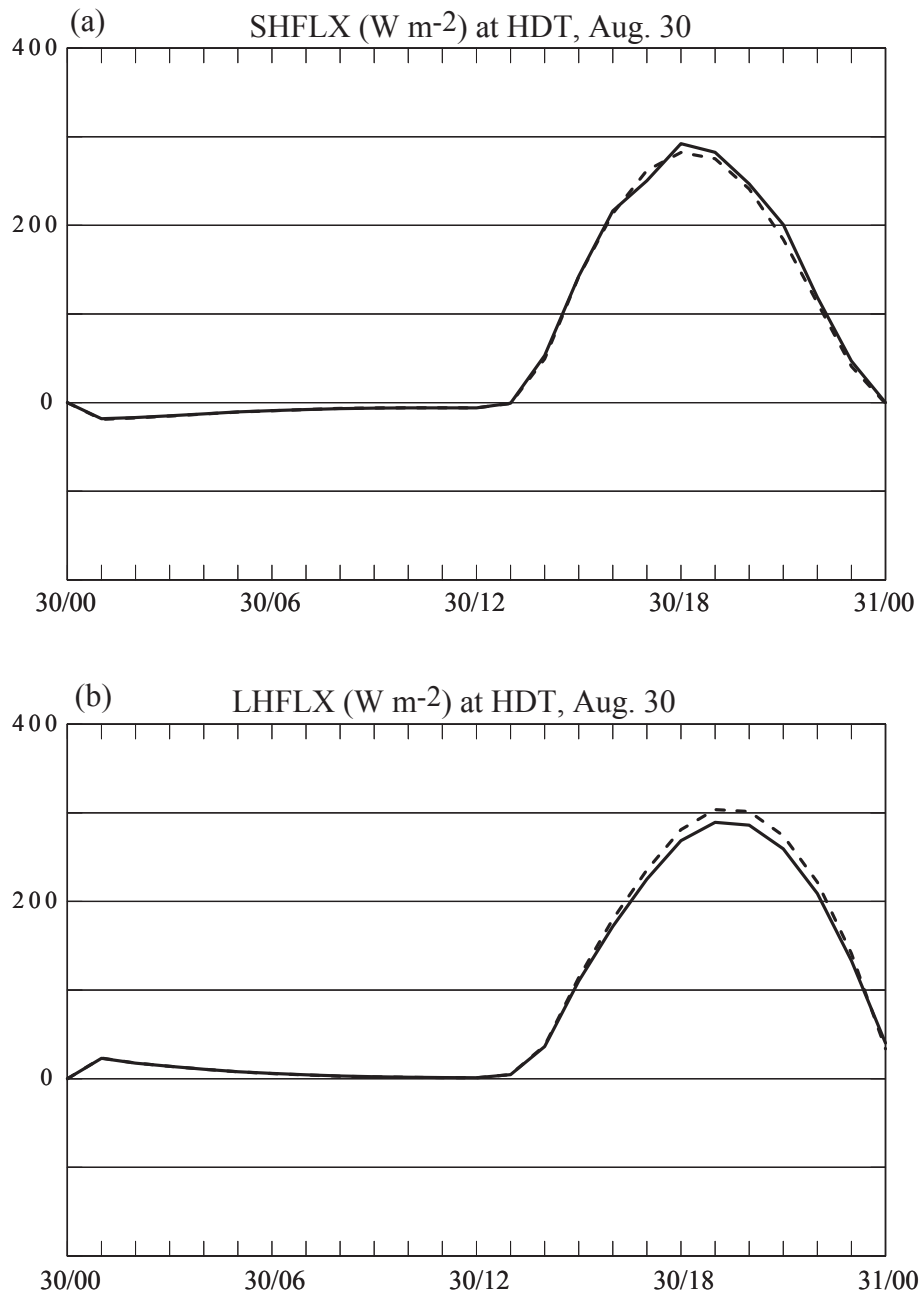


Figure 63. Plots comparing HOU-area-average of (a) sensible heat flux and (b) latent heat flux between the INHOMO (solid) and HOMO (dashed). X-axes indicate the time expressed by "date/UTC" and y-axes indicate values with units appearing in the figure titles.

*c. Comparison of variable profiles at HDT*

Profiles of atmospheric variables are provided in figures 64, 65, and 66 in order to illustrate the PBL impacts induced by the inhomogeneity parameterization. The variables are potential temperature, relative temperature, and wind speed at HDT. Comparison times are from 1600 UTC to 0000 UTC at one hour intervals.

During the convective daytime, as a result of the increased surface layer temperature and sensible heat flux of INHOMO as presented above, greater diffusivity of fluxes was induced in INHOMO. This is physically similar to the 1-d simulation. From equation (68) the velocity scale  $w_s$  and PBL height  $h$  are key factors to determine the momentum diffusivity in unstable condition. Then, according to Troen and Mahrt (1986), for  $h \gg -L$  the velocity scale is approximately  $w_s \cong 0.65w_*$ , where convective velocity scale  $w_* = (g / T_0 \overline{w'\theta'_0} h)^{1/3}$ . The PBL height  $h$  is expressed in (69). Thus, greater value of either convective velocity  $w_*$  or PBL height  $h$  will produce greater diffusivities. From the expression of the convective velocity scale and PBL height, it can be inferred that INHOMO should produce greater diffusivities because  $h$  is greater due to the greater  $\theta_s$  in (69), and  $w_*$  is bigger due to both the greater heat flux  $\overline{w'\theta'_0}$  and  $h$ .

Once the momentum diffusivities are determined, those of heat and water vapor are obtained from the relation defined as Prandtl number (76) assuming the Prandtl number is independent of height in the PBL. Thus, increased momentum diffusivities imply increased diffusivities of heat and water vapor as well. The arguments above are represented well in the PBL results of the INHOMO. The positive impacts of surface layer temperature (0.2 K – 0.4 K between 1600 UTC and 0000 UTC) resulted in positive impacts throughout the PBL by convective vertical mixing. Negative impacts of the potential temperature near the PBL top were produced by the increased diffusivities of heat.

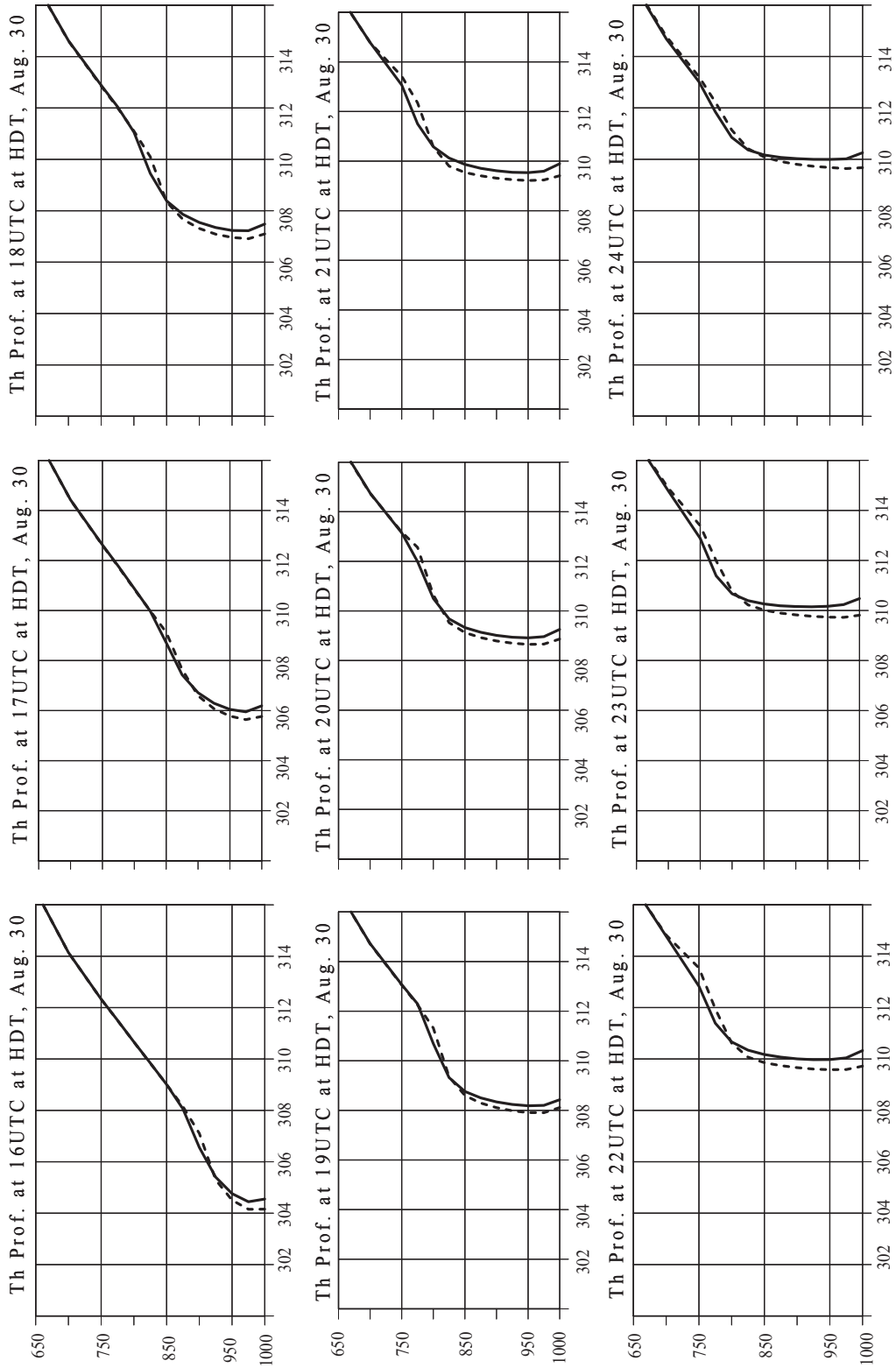


Figure 64. Profile plots comparing potential temperature between INHOMO (solid) and HOMO (dashed) at HDT from 1600 UTC to 0000 UTC. The x-axes are in degree K and y-axes are in mb.

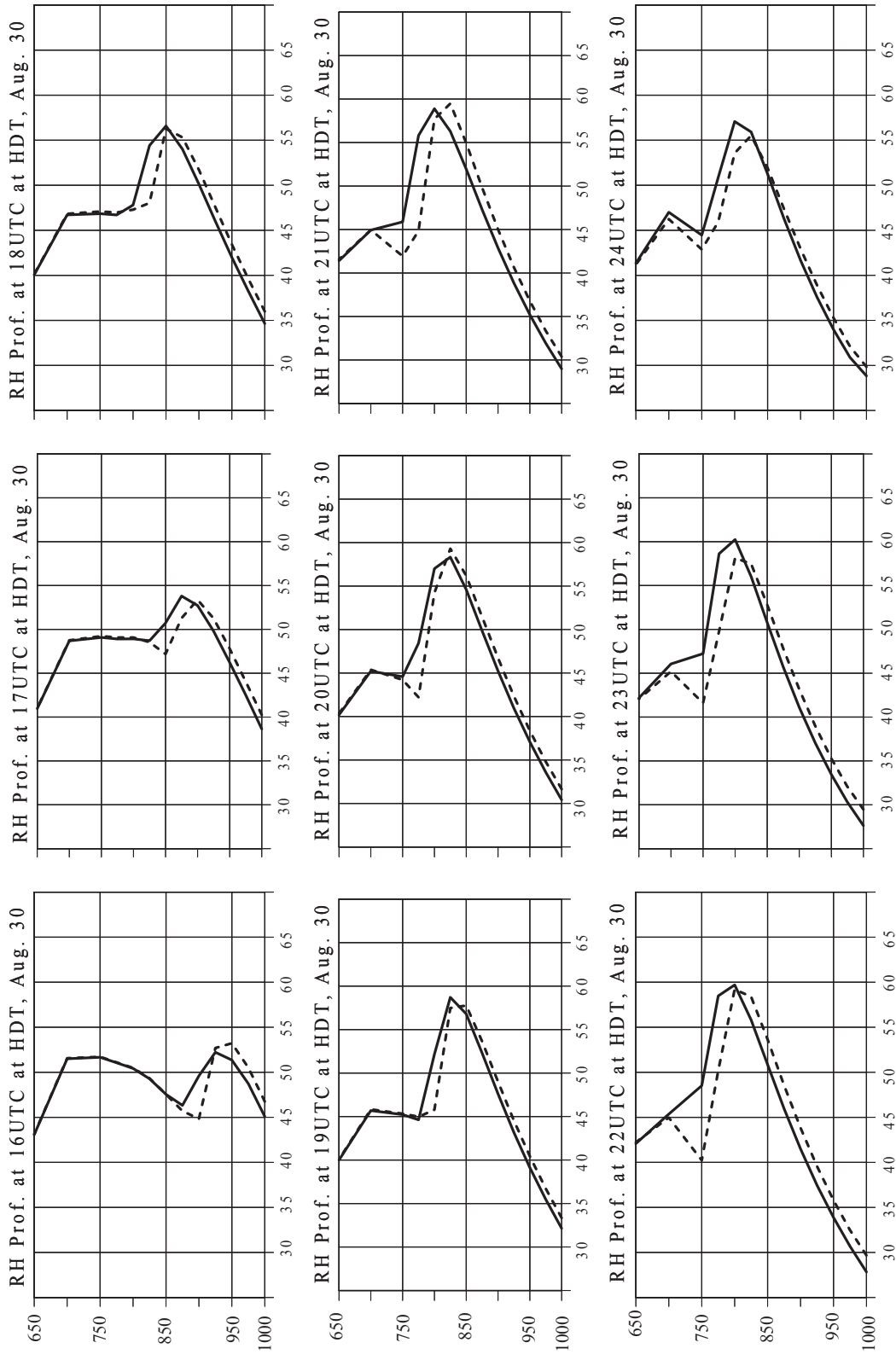


Figure 65. The same as Figure 64 but for Relative Humidity. The x-axes are in percent and y-axes are in mb.

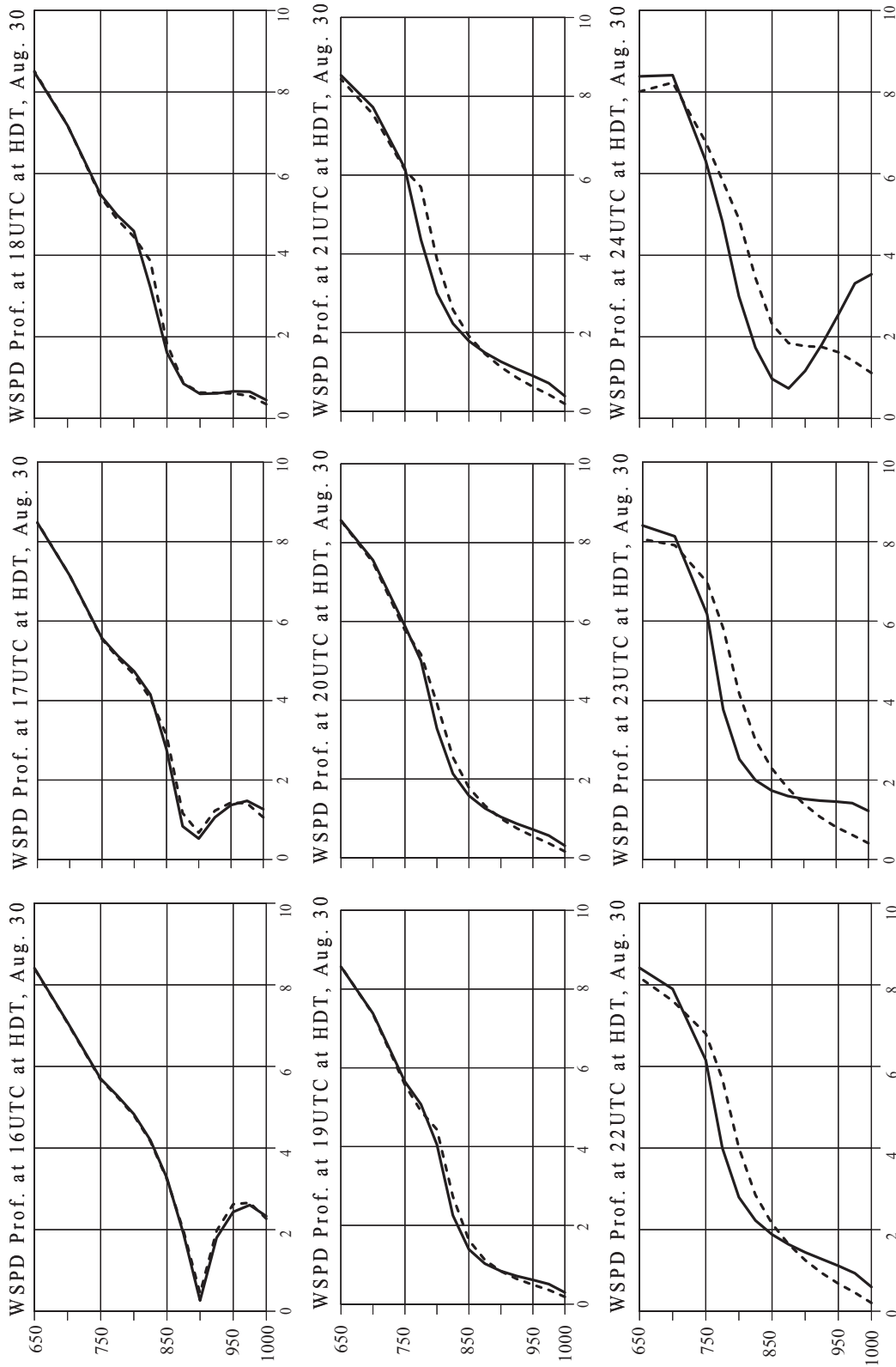


Figure 66. The same as Figure 64 but for wind speed. The x-axes are in m/s and y-axes are in mb.

Those results are presented in Figure 64. At the times presented in the Figure INHOMO produced well mixed PBL potential temperatures which average about 0.3 K to 0.4 K greater than HOMO. Near the PBL top, maximum negative impacts ranged from about  $-0.4$  K to  $-0.7$  K for the times (from 1600 UTC to 0000 UTC) in the figure. Thus, the effects of inhomogeneity in the convective daytime are to make the well mixed layer warmer and the entrainment layer near the PBL top colder.

In the same manner INHOMO brought impacts to the PBL relative humidity (Fig. 65). In contrast to the potential temperature, the impacts on the relative humidity are opposite to those of the potential temperature. The negative impacts of about  $-1$  % to  $-2$  % in the surface layer brought on average about  $-2$  % impacts to the well mixed PBL through the process of convective vertical mixing. Entrainment of drier air from above helped the negative impacts. The increased diffusivity of moisture near the PBL top induced positive impacts. Maximum positive impacts ranged from about 3 % to about 10 % for the times in the figure. Those results imply that the inhomogeneity parameterization produced a drier well mixed PBL and more humid PBL top during the free convective regime.

As mentioned earlier the impacts on the PBL wind speed became complicated too due to the differential local circulations which were generated by the impacts on temperature. Since the differential local circulations were not developed distinctly by 2100 UTC, the impacts between 1600 UTC and 2000 UTC illustrated in Figure 66 are believed to have been mainly caused by the difference of vertical momentum fluxes between INHOMO and HOMO. Thus, during this time, positive impacts up to about 0.2 m/s were produced generally in the well mixed PBL. Meanwhile, negative impacts of  $-0.4$  m/s to  $-0.6$  m/s induced by the increased diffusivity of momentum were produced near the PBL top. As the differential local circulations began to occur from 2100 UTC (see Fig. 60), the combined effects of the vertical momentum flux and local circulation resulted in up to 2.4 m/s impacts near the surface and up to about  $-1.8$  m/s impacts near the PBL top at 0000 UTC. Consequently, the inhomogeneity in the INHOMO produced more momentum in the lower PBL and less momentum in the upper PBL.

*d. Illustration of the PBL atmospheric differences in cross sections*

In order to illustrate the above results, the cross section lines were determined so as to cross the HOU area from northwest to southeast as indicated in Figure 67. The cross sections of potential temperature, relative humidity, and tangential winds are provided in figures 68, 69, and 70. The end points of the cross section line are at about equal distance from the HDT. The times presented are from 1600 UTC to 0000 UTC at every hour.

The findings so far presented can be seen consistently in the figures. From the difference figures (center panels), warm air pockets above the surface can be seen around the center of the cross section, the HOU area (solid red lines). Cold areas are clearly indicated at the levels of the PBL top just above the warm air pockets (dashed red line). Drying and moistening of the PBL corresponding to the warm pockets and cold areas, respectively, are well indicated.

As a result of vertical momentum flux and differential local circulation, enhanced vertical motions are distinct in the urban PBL especially from 2100 UTC onward. Due to the differential local circulation the winds became reduced and intensified to the left (downwind) and right (upwind) of the warm air pockets, respectively, in INHOMO from about 2100 UTC when the PBL became fully-grown. As mentioned earlier, the advection of the inhomogeneity impacts toward the left are also recognizable at 0000 UTC.



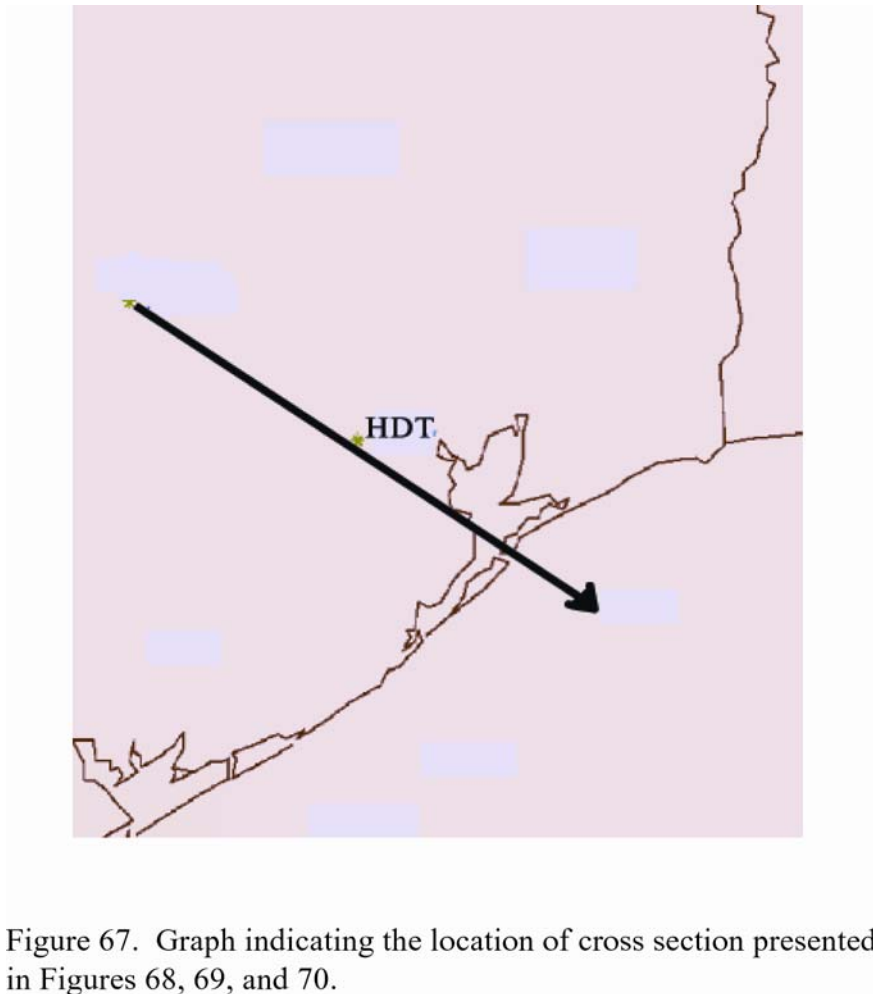


Figure 67. Graph indicating the location of cross section presented in Figures 68, 69, and 70.

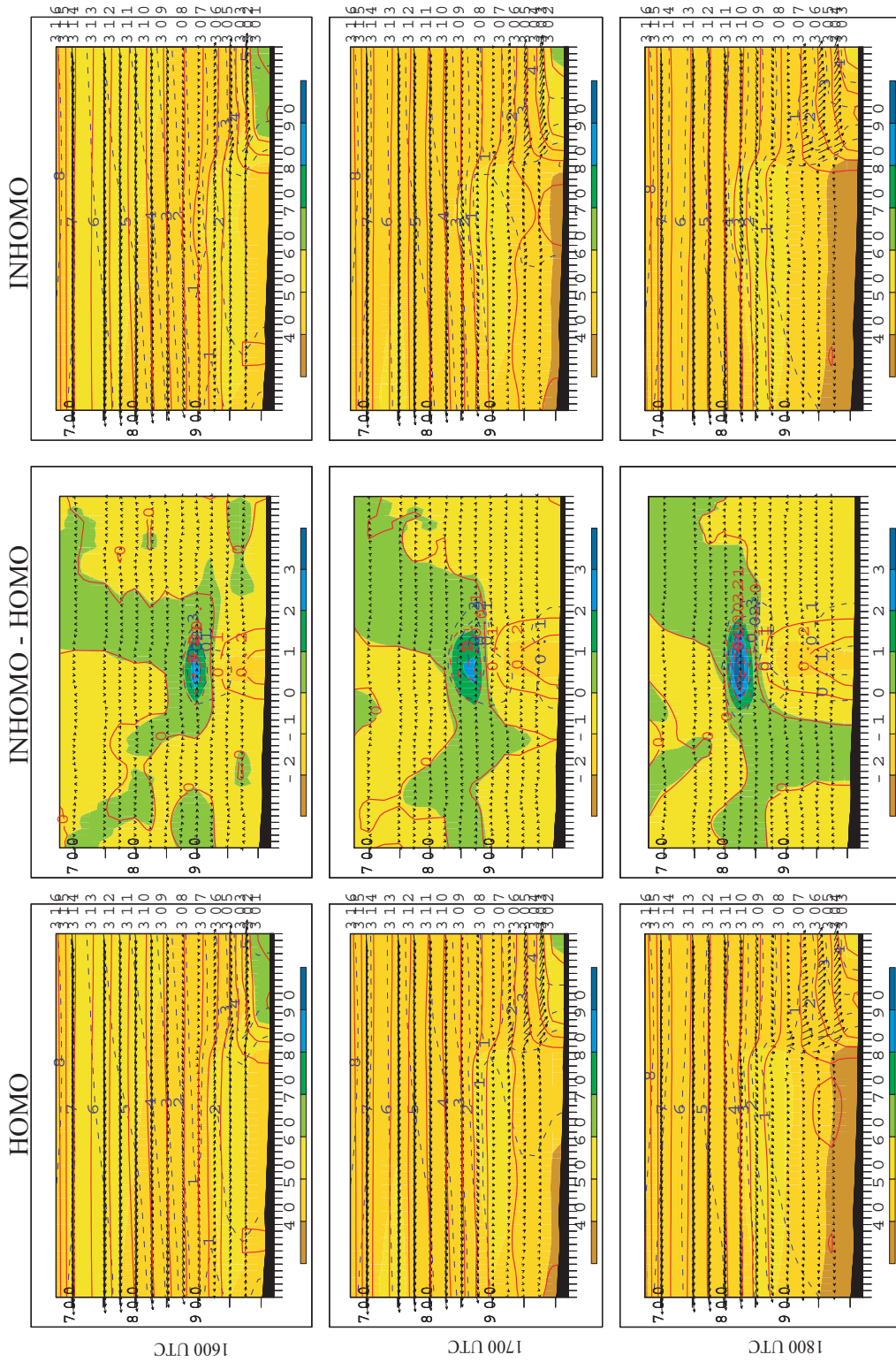


Figure 68. Cross section plots of relative humidity in color, potential temperature (K) in red lines, and section plane tangential winds (m/s) in arrow for the HOMO and INHOMO, and those variable differences at 1600 UTC (upper), 1700 UTC (middle), and 1800 UTC (lower). Color bars in each panel designate the relative humidity.

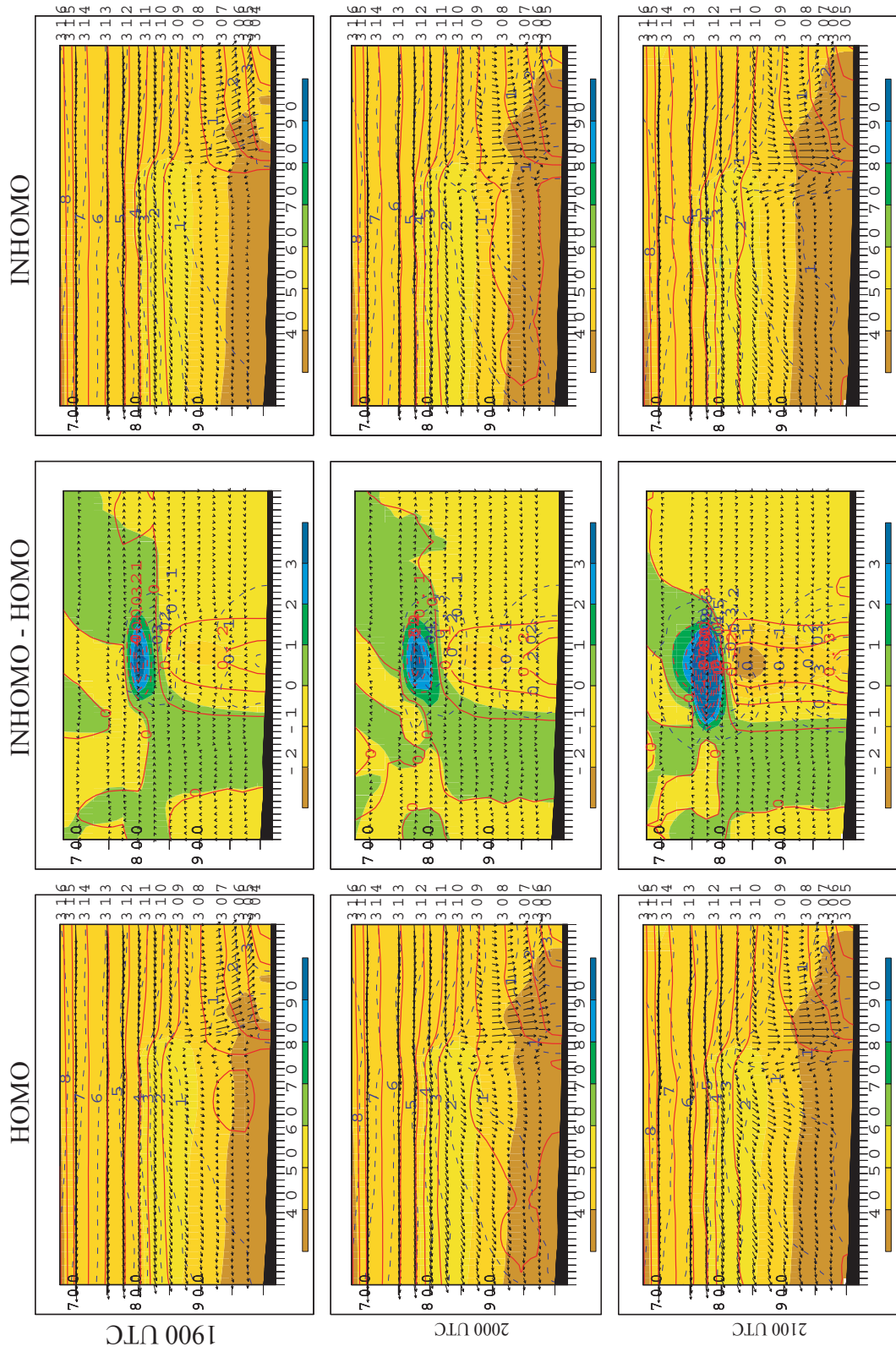


Figure 69. The same as Figure 68 but for at 1900 UTC (upper), 2000 UTC (middle), and 2100 UTC (lower).

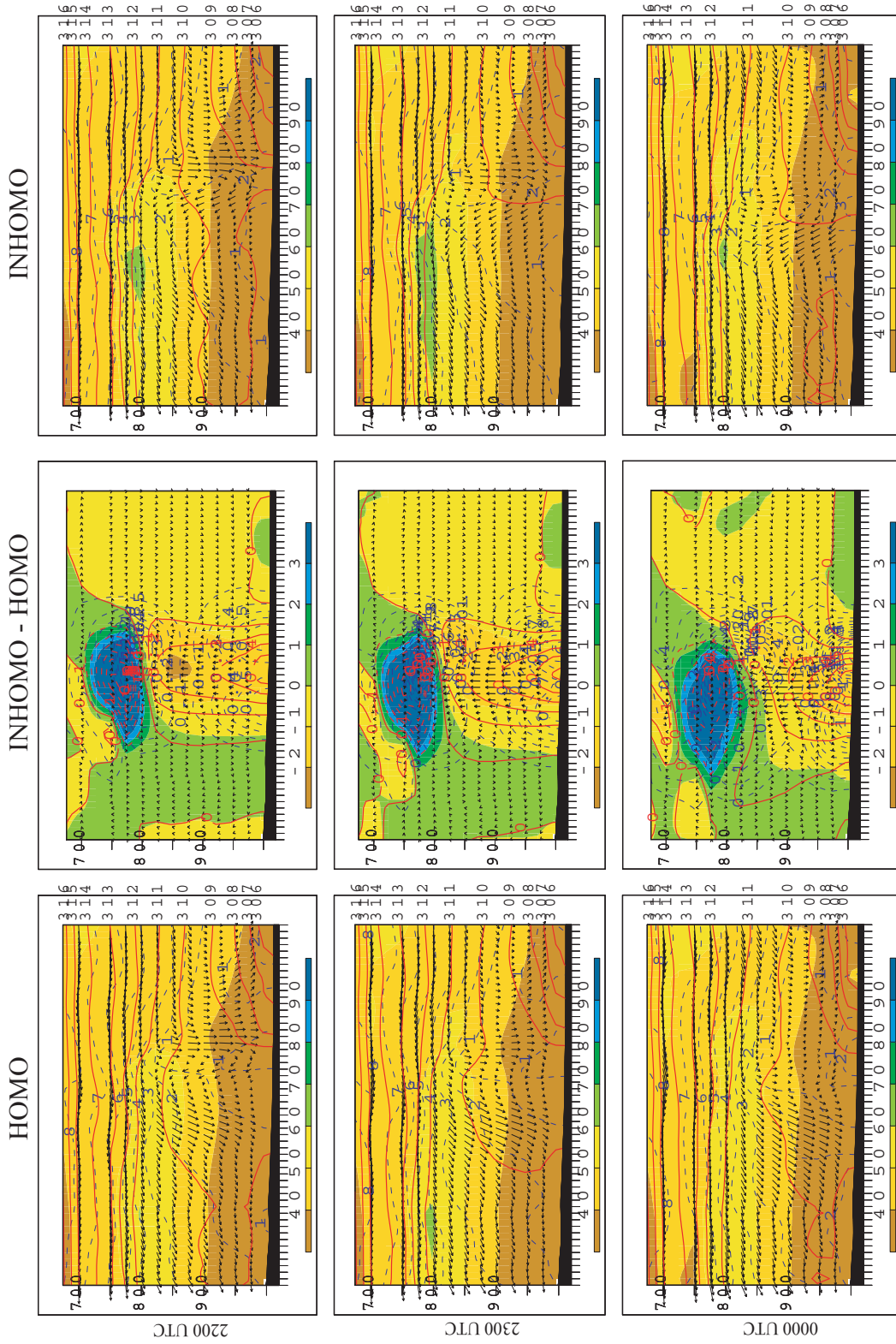


Figure 70. The same as Figure 68 but for at 2200 UTC (upper), 2300 UTC (middle), and 0000 UTC (lower).

## CHAPTER VI

### CONCLUSIONS

Originally, this study was motivated from the scientific issue that the inhomogeneous surface characteristics in the Houston urban area may cause a systematic error in GOES skin temperature on which GOES data assimilation, which is applied to MM5 simulations over the area, is based. In pursuit of this issue, the GOES skin temperature needed to be evaluated against ground-based true observations. However, at the moment, those observations are not available. Therefore, this study uses the 1-d PBL model-generated ground temperatures to estimate the GOES skin temperature retrieval errors induced by the inhomogeneous land surfaces in the HOU area. While this study was motivated by the GOES skin temperature issue, the investigation and correctional method of model errors associated with the inhomogeneous surface became a bigger portion of this study. Actually, those efforts are required not only to correct the GOES skin temperature in the HOU, but to improve mesoscale model performance in general.

First, this study compared the performance of NGMM5 simulations over the inhomogeneous HOU area to its performances over the homogeneous surrounding areas in the 4km model domain, using the MTP observations as a reference. In doing so characteristic MM5 features were searched for over the HOU area. The results indicated that in general, the model biases (against MTP) of PBL height and potential temperature over the HOU were different from those of surrounding areas. Over HOU the NGMM5 seemed to produce those biases in such ways to make the lower PBL warmer (+0.7 K), the upper PBL colder (-0.2 K), and the PBL height higher (+80 m) relative to the composite surrounding areas during the free convective daytime. For example, those results imply that if the MM5 has systematic warm (cold) bias in the lower PBL the HOU will experience enhanced warm (mitigated cold) biases relative to surrounding areas.

According to the results of both the 1-d and 3-d parameterization of the inhomogeneous surface in chapter III and V, the inhomogeneous surfaces in the HOU cause warmer lower PBL, colder near-PBL top, and higher PBL height during the convective daytime. Those results implicate that the NGMM5 without the inhomogeneous parameterization should have

resulted in the opposite trends (that is, colder lower PBL, warmer near-PBL top, and lower PBL height relative to the homogeneous surrounding areas) if the surface inhomogeneities over the HOU mainly contributed to differences of the relative performances between the HOU and surrounding areas. But the results are not consistent with the expectation. Even if the results came out as expected it is unreasonable to attribute those to the surface inhomogeneity without the evidence that the errors came from no other source. Therefore, from the results, at least, it is inferred that the relative performance of the NGMM5 over the HOU was likely to be induced by errors included in the representation of grid-mean surface parameter values relative to the surrounding areas. Of the grid-mean surface parameters the soil moisture availability is most suspicious because model PBL is known to be most sensitive to the soil moisture availability (Zhang and Anthes, 1982). Based on the above arguments, it is suggested that the GOES satellite data assimilation technique resulted in the soil moisture availability errors which are relatively greater in HOU when the technique has systematic dry bias, or relatively smaller when the technique has systematic moist bias.

From the comparative study of the NGMM5 relative performances the inhomogeneous surface impacts on the model performance were not appreciated. In order to extensively investigate the impacts of the surface inhomogeneities in the HOU, the 1-d PBL model was constructed with the inhomogeneity parameterization which is similar to Avissar and Pielke (1989) and implemented using the realistic surface characteristics obtained from the GEM land cover data of 30m resolution. The differences produced by the 1-d simulations with the inhomogeneity parameterization were regarded as the impacts caused by the subgrid-scale inhomogeneities within a 4km grid element.

In general, the surface inhomogeneity enhanced the sensible heat flux, reduced the latent heat flux, and enhanced the momentum flux in both the stable nighttime and convective daytime over most HOU areas. Those impacts were realized consistently in the surface layer variables except for temperature during first few hours of the convective regime. That is, on average the inhomogeneity produced surface layer temperatures which are about 0.3 K and 0.1 K greater during the stable night time and during the second half of convective daytime, respectively. The impacts on the surface layer humidity were about -0.1 g/kg and -0.3 g/kg for the stable and convective regimes, respectively. The impacts on the surface layer wind speed were around 0.2 m/s to 0.3 m/s during the stable regime. During the convective

regime the surface layer wind impacts were variable ranging from about 0 m/s to about 0.5 m/s. During the first few hours of the convective regime, the enhanced sensible heat fluxes, which are inconsistent with the negative impacts (-0.1 K) of grid-mean surface layer temperature, can be interpreted to be the result of counter-gradient subgrid-scale heat fluxes. During the convective regime the impacts in the surface layer were realized in the well mixed layer as well in almost the same direction and degree through convective vertical mixing processes with reversed impacts occurring in the layers near the PBL top. The impacts near the PBL top were induced by the increased vertical mixing coefficients which were produced by the increased sensible heat flux from the surface layer top. As results of the combined surface fluxes the ground potential temperature resulted in about -0.5 K and about 2.0 K impacts during the stable nighttime and convective daytime, respectively.

The inhomogeneity impacts indicated spatial variability in degree as well as temporal variation. In the areas in which land cover types with extreme surface parameter values occupied a relatively larger fractional area, the inhomogeneity impacts were pronounced. Particularly, in the grid elements which include subgrid-scale land types with much lower surface values than grid-mean and occupying most grid area, the inhomogeneity impacts are maximized. In the HOU, the local areas that have such land surface characteristics are roads, impervious, and water bodies. Of the surface parameters, surface roughness length and soil moisture availability played distinctly important roles in inducing the inhomogeneity impacts. During the convective daytime, soil moisture availability dominates over other parameters. This is consistent with the study by Wetzal and Boone (1995). The wind speed sensitivity indicates that inhomogeneity impacts would be enhanced as the winds become weaker than those of this study (on average  $2 \text{ ms}^{-1}$  during the convective regime). As the winds gradually get strengthened the degree of impacts declines and eventually comes to zero impacts around  $2 \text{ ms}^{-1}$  and  $5 \text{ ms}^{-1}$  wind speeds for stable and convective regimes, respectively. Further increase of wind speeds from the zero impact point increases the impacts in the reversed direction with steeper rate of change of the impacts than before the zero impact point. During the convective regime, the inhomogeneity impacts are significant for the ground temperature, sensible and latent heat fluxes, and surface layer temperature. The percent impacts for those variables are 11 %, 36 %, -25 %, and 11 %, respectively. The positive impact of sensible heat and negative impact of latent heat are indicative of the

energy partitioning toward the increase of Bowen ratio. This is consistent with previous studies (Seth and Giorgi, 1994).

Subgrid-scale ground temperatures, which were simulated from the parameterized 1-d PBL model in chapter III, were used for the estimation of the GOES skin temperature retrieval errors. The estimation method was established using the land surface temperature retrieval equations of the physical split-window algorithm (Suggs et al., 1998). By applying the GOES skin temperature assimilation technique to the 1-d PBL model, two kinds of error in applying the assimilation technique in the model were estimated. One was the error pertaining to the GOES skin temperature retrieval error caused by inhomogeneous ground temperature. The other was the error pertaining to the model ground temperature error caused by the homogeneous treatment of the inhomogeneous surface characteristics within a grid box.

Within the assimilation cycle of NGMM5 between 1400 UTC and 1800 UTC, the retrieval error ranged from about -0.04 K up to -0.5 K around HDT. With that much error the model implied errors of 1.5 % sensible heat flux, -0.8 % latent heat flux, 0.1 % surface layer temperature, and -0.2 % surface layer specific humidity between 1800 UTC and 2200 UTC in terms of HOU-area-average. During the same period the homogeneous 1-d simulations indicated the assimilation errors, caused by the model ground temperature error, of -24.9 % sensible heat flux, 31.2 % latent heat flux, -1.0 % surface layer temperature, and 3.8 % surface layer specific humidity. If combined the two errors the total assimilation errors are -23.4 % sensible and 30.4 % latent heat fluxes, -0.9 % surface layer temperature, and 3.6 % surface layer specific humidity. Thus, it is inferred that, from the GOES skin temperature assimilation, models using GOES will generally experience cold and moist biases in the PBL atmosphere over the Houston urban area.

The preliminary application of the inhomogeneity parameterization developed in the 1-d PBL model into the standard MM5 simulation was successful. Unlike in the 1-d simulations, in the MM5 the parameterization was applied with the fractional area coverages for each subgrid land type within an urban grid being given by the HOU-area-averaged value uniquely. In general the inhomogeneity impacts were similar to those of 1-d simulations. Unlike the 1-d results, advection of the impacts can be seen and the differential local circulations induced by positive impacts of the PBL temperature were produced when the



PBL was fully-grown during the second half of convective regime. Due to the differential local circulations, winds around HOU area significantly changed between 2100 UTC and 0000 UTC, mitigated downwind and intensified upwind.

From the findings of this study, it is inferred that the NGMM5 seems to experience warm and dry PBL biases aided by the GOES assimilation error pertaining to the GOES ground temperature error, and hindered by both the GOES assimilation error pertaining to the model ground temperature error and surface inhomogeneity-caused errors during the convective daytime over HOU. This inference is made possible from the results that the inhomogeneity impact (errors) is to increase (decrease) sensible heat flux and to decrease (increase) latent heat flux, and that the combined assimilation errors of both kinds are to reduce the sensible heat flux and to enhance the latent heat flux. Previous model studies with respect to inhomogeneous surfaces using the inhomogeneity parameterization methods similar to this study indicated results consistent with this study (e.g., Seth and Giorgi, 1994; Wetzel and Boone, 1995). In spite of similarity of this study to the previous studies in terms of inhomogeneity impact and methodology, this study is unique in that urban inhomogeneity was investigated using high resolution (30 m) satellite land cover data. So far it is seen that no attempt to research the model impacts of the inhomogeneous surface over a metropolitan area is made.

At the moment the application of the inhomogeneity parameterization to the MM5 simulation would adversely affect the model performance because the inhomogeneity impacts will act to help the already existing warm and dry biases in the model. Therefore, consideration of the surface inhomogeneities in the urban area should be confined to the GOES skin temperature retrieval. In order that the inhomogeneity parameterization can be useful for the improvement of MM5 model performance the corrections for the warm and dry biases in the model should be made first.

## REFERENCES

- Allen, D. D., C., G. McGaughey, and J. W. Nielsen-Gammon, 2002: Accelerated science evaluation of ozone formation in the Houston-Galveston area. *A report to the Technical Analysis Division, Texas Natural Resource Conservation Commission*, Version 2.0.
- Asselin, R., 1972: Frequency filter for time integrations. *Mon. Wea. Rev.*, **100**, 487–490.
- Avissar, R., 1992: Conceptual aspects of a statistical-dynamical approach to represent landscape subgrid-scale heterogeneity in atmospheric models. *J. Geophys. Res.*, **97**, 2729–2742.
- Avissar, R., and R. A. Pielke, 1989: A parameterization of heterogeneous land surfaces for atmospheric numerical models and its impact on regional meteorology. *Mon. Wea. Rev.*, **117**, 2113–2136.
- Avissar, R. and T. Schmidt, 1998: An evaluation of the scale at which ground-surface heat flux patchiness affects the convective boundary layer using large-eddy simulations. *J. Atmos. Sci.*, **55**, 2666–2689.
- Blackadar, A. K., 1976: Modeling the nocturnal boundary layer. Preprints, *3rd Symp. on Atmospheric Turbulence, Diffusion and Air Quality*, Raleigh, NC, Amer. Meteor. Soc., 46-49.
- Blackadar, A. K., 1978: Modeling pollutant transfer during daytime convection. Preprints, *4th Symp. on Atmospheric Turbulence, Diffusion and Air Quality*, Reno, NV, Amer. Meteor. Soc., 46-49.
- Blackadar, A. K., 1979: High resolution models of planetary boundary layer. *Advances in Environmental Science and Engineering*, J. R. Pfaflin and E. N. Ziegler, Eds., Gordon and Breach, 50-85.
- Businger, J. A., 1971: Comments on “free convection in the turbulent Ekman layer of the atmosphere”. *J. Atmos. Sci.*, **28**, 298–299.
- Businger, J. A., J. C. Wyngaard, Y. Izumi, and E. F. Bradley, 1971: Flux-profile relationships in the atmospheric surface layer. *J. Atmos. Sci.*, **28**, 181–189.
- Carlson, T. N. and F. E. Boland, 1978: Analysis of urban-rural canopy using a surface heat flux/temperature model. *J. Appl. Meteor.*, **17**, 998–1013.
- Chen, F. and J. Dudhia, 2001a: Coupling an advanced land surface-hydrology model with the Penn State-NCAR MM5 modeling system. Part I: model implementation and sensitivity. *Mon. Wea. Rev.*, **129**, 569–585.

- Chen, F. and J. Dudhia, 2001b: Coupling an advanced land surface-hydrology model with the Penn State-NCAR MM5 modeling system. Part II: preliminary model validation. *Mon. Wea. Rev.*, **129**, 587-604.
- Chen, F., D. N. Yates, H. Nagai, M. A. LeMone, K. Ikeda, and R. L. Grossman, 2003: Land surface heterogeneity in the Cooperative Atmosphere Surface Exchange Study (CASES-97). Part I: Comparing modeled surface flux maps with surface-flux tower and aircraft measurements. *J. Hydrometeorology*, **4**, 196–218.
- Chen, T. H., A. Henderson-Sellers, P. C. Milly, A. J. Pitman, A. C. Beljaars, and coauthors, 1997: Cabauw experimental results from the project for intercomparison of land-surface parameterization schemes. *J. Climate*, **10**, 1194–1215.
- Colle, B. A., B. Olson, S. Joseph, and J. Tongue, 2003: Multiseason verification of the MM5. Part II: evaluation of high-resolution precipitation forecasts over the northeastern United States. *Wea. Forecasting*, **18**, 458–480.
- Coulter, R. L., 1979: A comparison of three methods for measuring mixed-layer height. *J. Appl. Meteor.*, **18**, 1495–1500.
- Dalu, G. A. and R. A. Pielke, 1993: Vertical heat fluxes generated by mesoscale atmospheric flow induced by thermal inhomogeneities in the PBL. *J. Atmos. Sci.*, **50**, 919–926.
- Deardorff, J. W., 1966: The counter-gradient heat flux in the lower atmosphere and in the laboratory. *J. Atmos. Sci.*, **23**, 503–506.
- Deardorff, J. W., 1977: A parameterization of ground-surface moisture content for use in atmospheric prediction models. *J. Atmos. Sci.*, **16**, 1182–1185.
- Dickinson, R. E., 1988: The force–restore model for surface temperatures and its generalizations. *J. Climate*, **1**, 1086–1098.
- Dickinson, R. E., A. Henderson-Sellers, P. J. Kennedy, and M. F. Wilson, 1986: Biosphere Atmosphere Transfer Scheme (BATS) for the NCAR community climate model. NCAR Tech. Note, NCAR TN275 + STR, 69 pp.
- Doran, J. C., W. J. Shaw, and J. M. Hubbe, 1995: Boundary layer characteristics over areas of inhomogeneous surface fluxes. *J. Appl. Meteor.*, **34**, 559–571.
- Doran, J. C. and S. Zhong, 1995: Variations in mixed-layer depths arising from inhomogeneous surface conditions. *J. Climate*, **8**, 1965–1973.
- Dornbrack, A., T. Birner, A. Fix, H. Flentje, A. Meister, H. Schmid, E. Browell, and M. J. Mahoney, 2002: Evidence for inertia-gravity waves forming polar stratospheric clouds over Scandinavia. *J. Geophys. Res.*, **107**(D20), 8287.

- Essery, R. L. H., M. J. Best, R. A. Betts, P. M. Cox, and C. M. Taylor, 2003: Explicit representation of subgrid heterogeneity in a GCM land surface scheme. *J. Hydrometeorology*, **4**, 530–543.
- Estoque, M. A., 1968: Vertical mixing due to penetrative convection. *J. Atmos. Sci.*, **25**, 1046–1051.
- Gary, B. L., 1981: An airborne remote sensor for the avoidance of clear air turbulence. *AIAA Pap.*, AIAA-81-0297.
- Gary, B. L., 1984: Clear Air Turbulence avoidance using an airborne microwave radiometer. *AIAA Pap.*, AIAA-84-0273.
- Gopalakrishnan, S. G. and R. Avissar, 2000: An LES study of the impacts of land surface heterogeneity on dispersion in the convective boundary layer. *J. Atmos. Sci.*, **57**, 352–371.
- Hong, S.-Y. and H.-L. Pan, 1996: Nonlocal boundary layer vertical diffusion in a medium-range forecast model. *Mon. Wea. Rev.*, **124**, 2322–2339.
- Kondo, Y., M. Koike, H. Ikeda, B. E. Anderson, K. E. Brunke, and coauthors, 1999: Impact of aircraft emissions on NO<sub>x</sub> in the lower most stratosphere at northern Midlatitudes. *Geophys. Res. Letters*, **26** (20), 3065-3068.
- LeMone, M. A., R. L. Grossman, F. Chen, K. Ikeda, and D. Yates, 2003: Choosing the Averaging Interval for Comparison of Observed and Modeled Fluxes along Aircraft Transects over a Heterogeneous Surface. *J. Hydrometeorology*, **4**, 179–195.
- Lin, C.-L., and J. W. Glendening, 2002: Large eddy simulation of an inhomogeneous atmospheric boundary layer under neutral conditions. *J. Atmos. Sci.*, **59**, 2479–2497.
- Louis, J. F., 1979: A parametric model of vertical eddy fluxes in the atmosphere. *Boundary-Layer Meteorol.*, **17**, 187-202.
- Mahrt, L., 1987: Grid-averaged surface fluxes. *Mon. Wea. Rev.*, **115**, 1550–1560.
- Mahrt, L. and D. H. Lenschow, 1976: Growth dynamics of the convectively mixed layer. *J. Atmos. Sci.*, **33**, 41–51.
- Mahrt, L., J. Sun, D. Vickers, J. I. Macpherson, J. R. Pederson, and R. L. Desjardins, 1994: Observations of fluxes and inland breezes over a heterogeneous surface. *J. Atmos. Sci.*, **51**, 2484–2499.
- Manabe, S., 1969: Climate and the ocean circulation. *Mon. Wea. Rev.*, **97**, 739–774.
- McNider, R. T., A. J. Song, D. Casey, P. J. Wetzel, W. Crosson, and R. M. Rabin, 1994: Toward a dynamic-thermodynamic assimilation of satellite surface temperature in numerical atmospheric models. *Mon. Wea. Rev.*, **122**, 2784-2803.

- McNider, R. T., J. A. Song, and S. Q. Kidder, 1995: Assimilation of GOES-derived solar insolation into a mesoscale model for studies of cloud shading effects. *Int. J. Remote Sens.*, **16**, 2207-2231.
- Mellor, G. L. and T. Yamada, 1974: A hierarchy of turbulence closure models for planetary boundary layers. *J. Atmos. Sci.*, **31**, 1791-1806.
- Mölders, N. and A. Raabe, 1996: Numerical investigations on the influence of subgrid-scale surface heterogeneity on evapotranspiration and cloud processes. *J. Appl. Meteor.*, **35**, 782-795.
- Monin, A. S. and A. M. Obukhov, 1954: Basic laws of turbulent mixing in the atmosphere near the ground. *Tr. Akad. Nauk SSSR Geofiz. Inst.*, **24**(151), 163-87.
- Nielsen-Gammon, J. W., 2002a: Meteorological modeling for the August 2000 Houston-Galveston ozone episode: PBL characteristics, nudging procedure, and performance evaluation. *A report to the Technical Analysis Division, Texas Natural Resource Conservation Commission.*
- Nielsen-Gammon, J. W., 2002b: Meteorological modeling for the August 2000 Houston-Galveston ozone episode: Improved data assimilation and statistical evaluation. *A report to the Technical Analysis Division, Texas Natural Resource Conservation Commission.*
- Nielsen-Gammon, J. W., 2003: Meteorological modeling for the August 2000 Houston-Galveston ozone episode: Implementation and initial evaluation of GOES skin temperature assimilation. *A report to the Technical Analysis Division, Texas Natural Resource Conservation Commission.*
- Oke, T. R., 1987: *Boundary Layer Climates*. 2d ed., University Press, Cambridge, 450 pp.
- Oncley, S. P. and J. Dudhia, 1995: Evaluation of surface fluxes from MM5 using observations. *Mon. Wea. Rev.*, **123**, 3344-3357.
- Orville, R. E., G. R. Huffines, J. Nielsen-Gammon, R. Zhang, B. Ely, S. Steiger, S. Phillips, S. Allen, and W. Read, 2001: Enhancement of cloud-to-ground lightning over Houston, Texas. *J. Geophys. Res.*, **28**, 2597-2600.
- Paulson, C. A., 1970: The mathematical representation of wind speed and temperature profiles in the unstable atmospheric surface layer. *J. Appl. Meteor.*, **9**, 857-861.
- Pielke, R. A., G. A. Dalu, J. S. Snook, T. J. Lee, and T. G. F. Kittel, 1991: Nonlinear influence of mesoscale land use on weather and climate. *J. Climate*, **4**, 1053-1069.
- Priestley, C. H. B., 1956: Convection from the earth's surface. *Proc. Roy. Soc. London*, **A238**, 287-304.

- Priestley, C. H. B. and W. C. Swinbank, 1947: Vertical transport of heat by turbulence in the atmosphere. *Proc. Roy. Soc. London*, **A189**, 543-561.
- Pyles, R. D. and coauthors, 2003: Coupling between the University of California, Davis, Advanced-Canopy-Atmosphere-Soil algorithm (ACASA) and MM5: preliminary results for July 1998 for western north America. *J. Appl. Meteor.*, **42**, 557-569.
- Ronda, R. J., B. J. J. M. van den Hurk, and A. A. M. Holtslag, 2002: Spatial heterogeneity of the soil moisture content and its impact on surface flux densities and near-surface meteorology. *J. Hydrometeorology*, **3**, 556–570.
- Segal, M., and R. W. Arritt, 1992: Nonclassical mesoscale circulations caused by surface sensible heat-flux gradients. *Bull. Amer. Meteor. Soc.*, **73**, 1593–1604.
- Sellers, P. J., Y. Mintz, Y. C. Sud, and A. Dalcher, 1986: A Simple Biosphere Model (SIB) for use within General Circulation Models. *J. Atmos. Sci.*, **43**, 505–531.
- Sellers, W. D., 1974: *Physical Climatology*. University of Chicago Press, 272 pp.
- Seth, A. and F. Giorgi, 1994: Simulating fluxes from heterogeneous land surfaces: explicit subgrid method employing the biosphere-atmosphere transfer scheme (BATS). *J. Geophys. Res.*, **99**, 18651-18667.
- Stull, R. B., 1976: Mixed-layer depth model based on turbulent energetics. *J. Atmos. Sci.*, **33**, 1268–1278.
- Suggs, R. J., G. J. Jedlovec, and A. R. Guillory, 1998: Retrieval of geophysical parameters from GOES: evaluation of a split-window technique. *J Appl. Meteor.*, **37**, 1205-1227.
- Tennekes, H., 1975: Reply. *J. Atmos. Sci.*, **32**, 992–994.
- Troen, I. and L. Mahrt, 1986: A simple model of the atmospheric boundary layer; sensitivity to surface evaporation. *Bound.-Layer Meteor.*, **37**, 129-148.
- Westphal, D. L., 1981: The interaction between radiative and boundary layer processes in stratus clouds. M. S. thesis, The Pennsylvania State University, University Park, 138 pp.
- Wetzel, P. J. and A. Boone, 1995: A parameterization for Land-Atmosphere-Cloud Exchange (PLACE): documentation and testing of detailed process model of the partly cloudy boundary layer over heterogeneous land. *J. Climate*, **8**, 1810-1837
- Zhang, D. and R. A. Anthes, 1982: A high-resolution model of the Planetary Boundary Layer-sensitivity tests and comparisons with SESAME-79 data. *J. Appl. Meteor.*, **21**, 1594–1609.
- Zhong, S. and J. C. Doran, 1995: A modeling study of the effects of inhomogeneous surface fluxes on boundary-layer properties. *J. Atmos. Sci.*, **52**, 3129–3142.

Zhong, S. and J. Fast, 2003: An evaluation of the MM5, RAMS, and meso-Eta models at subkilometer resolution using VTMX field campaign data in the Salt Lake Valley. *Mon. Wea. Rev.*, **131**, 1301–1322.

## VITA

Sang-Ok Han was born in the city of Namwon, Korea on June 10 1964. He grew up there until he graduated from the Namwon Middle School. Then, he entered the Kunsan Jae-il High School which is in the city of Kunsan, about 120 km away from Namwon. He graduated from the high school in February, 1982, and entered Seoul National University in March of that year. After graduating from the university with a Bachelor of Science in meteorology in 1986, he served a 3-year term of compulsory military service in the Korean Army. He got a job as a meteorologist in the Korean Meteorological Administration in 1989. Through the program funded by the Korean government for 2-year overseas study by governmental officials, he came to Texas A&M University in June, 1996, and began the program of study for the Master of Science. After he finished his M. S. in December 1998, he continued his education in the Ph. D. program at the same department.

He was married to Eun-Kyoung Seo on the first of June, 1996. She gave a birth to their only son, Isaac, in 2001. Their permanent address is 629 Fulton Rd. APT. 34, Tallahassee, FL 32312.